Understanding biological networks to identify regulatory points under perturbation

Thesis submitted to Jadavpur University
for the award of the degree of
Doctor of Philosophy

Submitted by
Suvankar Halder

Under the supervision of
Dr. Samrat Chatterjee

Translational Health Science and Technology Institute
NCR Biotech Science Cluster, 3rd Milestone
Faridabad-Gurgaon Expressway
Faridabad-121001, India
February 2023

Declaration

I, Suvankar Halder, solemnly declare that this thesis represents my own work which has been done after registration for the degree of PhD at Jadavpur University and has not been previously included in any thesis or dissertation for the purpose of earning a degree, diploma, or any other credential.

Suvankar Halder
16/02/2023

Suvankar Halder

iii

thsti
ट्रांसलेशनल स्वास्थ्य विज्ञान
एवं प्रौद्योगिकी संस्थान
TRANSLATIONAL HEALTH SCIENCE
AND TECHNOLOGY INSTITUTE
An autonomous institute of the Deptt. of Biotechnology, Ministry of Science & Technology, Govt. of India
NCR Biotech Science Cluster
3rd Milestone, Faridabad-Gurgaon Expressway,
P O Box No. 04, Faridabad-121001
Haryana, India

CERTIFICATE FROM THE SUPERVISOR

This is to certify that the thesis entitled "**Understanding biological networks to identify regulatory points under perturbation**" submitted by **Sri Suvankar Halder**, who got his name registered (**Ref. No.: D-7/SC/30/2018** and **Index No.: 72/18/Maths./25**) on 20/02/2018 for the award of Ph. D. (Science) Degree of Jadavpur University, is absolutely based upon his own work under the supervision of myself, and that neither this thesis nor any part of it has been submitted for either any degree / diploma or any other academic award anywhere before.

16/2/2023

Dr. Samrat Chatterjee

(Signature of the Supervisor date with official seal)

डॉ. सम्राट चटर्जी, पीएच.डी / Dr. Samrat Chatterjee, Ph.D.
सह-आचार्य / Associate Professor
ट्रांसलेशनल स्वास्थ्य विज्ञान और प्रौद्योगिकी संस्थान
Translational Health Science and Technology Institute
(भारत सरकार के जैव-प्रौद्योगिकी विभाग का एक स्वायत्त संस्थान)
(An autonomous institute of the Dept of Biotechnology, Govt. of India)
एन.सी. आर. जैव प्रौद्योगिकी विज्ञान समूह / N. C. R. Biotech Science Cluster
3rd Milestone, Faridabad-Gurugram Expressway,
Faridabad-121001 Haryana, India

Phone: +91-129-2876300, Fax: +91-129-2876402, Email: info@thsti.res.in, Website: www.thsti.res.in

Dedicated to my beloved parents

Acknowledgement

The most satisfying part of the *Acknowledgement* is to get a chance to express my appreciation towards the people involved throughout this journey. First and foremost, I want to convey my sincere gratitude to my supervisor Dr. Samrat Chatterjee. Under his supreme guidance, I got to learn the ABCs of research. His ultra-supportive nature towards every member of his group makes him stand out from others. His passion and unique approach towards research and solving problems have always inspired me. My interest in doing research and dream of pursuing a Ph. D started in the classroom of Jadavpur University. The classes of Prof. Nandadulal Bairagi were the primary motivation and inspiration. His discipline and dedication towards Mathematics, especially in the field of Mathematical Biology, are a big inspiration. I am fortunate to have Prof. Nandadulal Bairagi and Dr. Bhabatosh Das as my Research Advisory Committee members. I thank them for their valuable suggestions and feedback during my doctoral research. The preparation of this thesis would not be possible without their constant support, time and encouragement not only in the field of Mathematical Biology but also in various aspects of life.

I am grateful to the Translational Health Science and Technology Institute (THSTI), Faridabad and Jadavpur University, Kolkata, for providing me with the platform to complete this work. I am thankful to the Council of Scientific and Industrial Research (CSIR), Govt. of India, for financial support throughout this journey.

I express my appreciation to my co-authors and collaborators, Prof. Joydev Chattopadhyay, Indian Statistical Institute, Kolkata, Dr. Phonindra Nath Das and Dr. Sumana Ghosh, for their sincere contributions to this research. I am very thankful to Dr. Sumana Ghosh for her constant

support and insightful discussions.

The friendly environment of Complex Analysis Group made this journey a very memorable and pleasurable one. It is a blessing to have helpful and motivating lab mates who offered not only research-related help but also provided emotional support during this journey. From coding to biology, I have learnt something new every day from Rajat sir, Ankur da, Dipanka da, Abhijit, Shivam, Garhima, and Suman da. I also thank all the juniors, Joy, Dev, Krishna, Mimansa and Poulomi, for creating a cheerful and vibrant lab environment.

I also thank seniors and friends, Mitul, Lovika, Anita and Mrityunjay da for their constant motivation and advice. I thank my Jadavpur friends Chittaranjan, Abhijit, Rajkumar, Rakibul, Sahadev, Tapan and Arindam for helping me in this journey. It will be incomplete without thanking my badminton group Raj, Harsh, Deepak, Kunal, Mani sir, Oinam and Shiv, for providing much-needed fun breaks from the monotonous research life.

The journey to pursue higher education started a long way back when I left the comfort of home to join *Jawahar Navodaya Vidyalaya Kalyani, Nadia*, for Higher Secondary education. I owe most of my early education to Manoj Kumar Das sir, Mintu Chakraborty sir and R Nagabhushanam sir, who not just offered me the formal education but also created a solid foundation for life. I thank all my Navodayan friends for their never-ending encouragement and support throughout this journey.

This doctoral thesis is a product of countless sacrifices, struggles and prayers of my parents and family. Their unconditional love and care always pushed me to have high hopes. Their faith has given me the strength to fly high and achieve my goals in life. This thesis belongs to them as much as it belongs to me.

Suvankar Halder

Abstract

In the era of high throughput approaches, cell signalling research has made significant advances in interdisciplinary fields. However, treatment approaches that target important molecules have yet to perform up to their expected promises for most common malignancies. Incomplete understanding brought on by single-pathway targeted techniques is one of the main challenges. Signal transduction is not linear, and they involve molecular cross-talks. To address these cross-talks, we must consider the system as a complicated network of interconnecting components. This shift from the conventional paradigm of focusing on a specific pathway to a broader strategy will help develop innovative treatments.

The current thesis combined a systems biology approach with mathematical modelling (based on ordinary and stochastic differential equations) to comprehend the intricate mechanisms underlying cell signalling networks globally. The presence of densely coupled modules controlling cellular processes makes signalling networks complicated. These signalling systems must be sensitive enough to capture the variations in the input stimuli. At the same time, they must be robust enough to execute their cellular activities. The inclusion of inherent noise adds more complicity to these input-output relations and is much more challenging to comprehend. We have considered the more compact functional subunits known as network motifs to help uncover this complexity. The motif organisation affects the network's sensitivity, robustness, and trade-off in a signalling network. This thesis focused on developing new mathematical models and tools. With the help of mathematical models, we have created analytical formulas that can classify and rank motifs according to their sensitivity to random

perturbations.

Bistability, the simultaneous existence of two outputs for a single input, emerged from a pilot study of two frequently observed two-node motifs. The inherent randomness of the signalling network disrupts emerged bistability. These complex phenomenons are extremely important to explain the intricate cellular signalling systems of cancer, diabetes and autoimmunity. The emergence of bistability and the effect of randomness on it demands an in-depth study of the association of network motifs and the input-output relation under random perturbation. To get a global view of the association, we have considered all possible two-node network motifs that can construct any biological network. The study reveals the significance of network motifs in maintaining cell signalling in a noisy environment and provides a methodology for screening potential drug targets. The dependency of the input-output relation on motif structure was applied to design a quantitative scoring formula to identify critical nodes in a protein-protein interaction network. Potential drug targets from cancer networks were identified using the tool and were validated by existing databases. The study reveals that potential drug targets also can be identified using a mathematical tool based on the emergence of bistability in the motif structures. Through hysteretic switching, signalling systems maintain robust signals in noisy conditions, which can also be used to identify drug targets. Existing techniques to identify drug targets are dependent on the data structure. They are mainly based on centrality and differentia. Differential networks compare different networks to identify therapeutic targets that heavily rely on data, whereas centrality-based methods identify targets using centrality measures. Targeting these central positions helps to disintegrate the networks but has detrimental side effects. Our study overcomes these drawbacks by proposing methods to identify prospective drug targets independent of the data and network structure.

The significance of bistability and randomness was further explored through two biological processes. The emergence of bistability was observed in the tumour necrosis factor (TNF) signalling network in T regulatory cells that helps in the decision-making processes. The complex behaviour of cell survival and death of T regulatory cells was explained through bistable switching. The model demonstrates that the primary contributor to cell death is the elevated TNF concentration and increased c-Jun N-terminal kinase (JNK) phosphorylation. The results

suggest that cell death can be controlled by reducing the TNF concentration. The bistable region can be reduced by intrinsic randomness, thus affecting the cell's normal functioning. Calcium signalling in diabetic cardiomyocytes was studied to investigate the significance of randomness in the complex case of diabetic cardiomyopathy. Altered calcium oscillation is a major contributor to the insulin-resistant cardiomyocytes that mimic the diabetes condition. The study proposed several strategies to restore the physiological calcium oscillations, which signify normal functioning. Early oscillation was observed when we incorporated the random translocation of the GLUT4 into the plasma membrane that controls glucose uptake, facilitating the restoration mechanisms.

Overall, the early part of the thesis was devoted to developing novel methods and tools to identify regulatory points of complex biological networks based on the association of network motifs and signal-noise relationships. Mathematical tools were constructed by exploring the emergence of bistability and the presence of intrinsic randomness in the system. Unlike existing methods, these methods are independent of data and network structures that can be used to identify potential drug targets. In the later part, we further explore the significance of noise in various biological processes through mathematical models. The significance of bistability in decision-making processes was captured by studying a small-scale kinetic model of TNF signalling. The random translocation of GLUT4 in diabetic cardiomyocytes was studied to comprehend the importance of randomness in the cell signalling system. The study reveals that randomness facilitates the restoration mechanism of physiological calcium oscillations.

Contents

List of Figures **xxi**

List of Tables **xxv**

1 Introduction **1**

1.1 Biological networks 1

1.2 Types of biological networks 3

1.3 Cell signalling 4

1.4 Types of cell signalling 6

1.5 Cell signalling defects and diseases 8

1.6 Presence of noise in cell signalling 9

1.7 Regulatory points in a biological network 10

1.8 Methods to find the regulatory points: Modelling cell signalling networks . . . 11

1.9 Mathematical modelling of cell signalling systems 13

1.9.1 Mathematical models based on ordinary differential equations 14

1.9.2 Mathematical models based on stochastic differential equations 14

1.10 Emergence of complex qualitative properties: ultrasensitivity, bistability and oscillation 15

1.11 Effect of stochasticity on ultrasensitivity, bistability and oscillation 19

1.12 Different tools used to study mathematical models 20

1.12.1 Mathematical tools to study deterministic models 20

1.12.2 Mathematical tools to study stochastic models 22
1.13 Statistical tools 24
1.13.1 Curve fitting 24
1.13.2 Sensitivity analysis 25
1.13.3 Latin Hypercube Sampling (LHS) 26
1.13.4 Partial Rank Correlation Coefficient (PRCC) 26
1.14 Overview 27

2 Unravelling the sensitivity of two frequently observed motif structures under random perturbations 33

2.1 Introduction 33
2.2 Construction of the deterministic models 36
2.2.1 Analytical results 38
2.2.1.1 Positive invariance and boundedness 38
2.2.1.2 Equilibrium points of the system (2.1) and their stability properties 39
2.2.1.3 Equilibrium points of the system (2.2) and their stability properties 40
2.2.2 Simulation results 41
2.2.2.1 Numerical analysis for the system (2.1) 41
2.2.2.2 Numerical analysis for the system (2.2) 44
2.3 Construction of the stochastic models 47
2.3.1 Stochastic stability of interior equilibrium 49
2.3.2 Stochasticity induces loss of bistability 55
2.4 Discussion 56

3 Understanding noise in cell signalling in the prospect of drug-targets 59

3.1 Introduction 59
3.2 Model formulation 61
3.2.1 Two-node motifs and their nomenclature 61

3.2.2 The general model for two-node topology 63
3.2.3 Stochastic model of two-node topology 64
3.3 Analytical results 65
3.3.1 Stochastic stability around interior equilibrium point 65
3.3.2 Analysis for the motif PF_2 67
3.4 Numerical results 70
3.4.1 Vulnerability of two-node network motifs under systemic noise 70
3.4.2 Significance of sensitive motifs 73
3.4.3 Identification of sensitive nodes 75
3.4.4 Sensitive nodes and drug targets 75
3.4.5 Biological significance of sensitive nodes as drug targets 78
3.5 Discussion 80

4 Bistability in cell signalling and its significance in identifying potential drug targets 83
4.1 Introduction 83
4.2 Mathematical model of general topology with two-node motif structure 85
4.3 Existence of possible two-node bistable structures in a signalling network . . . 87
4.4 Sensitivity of parameters towards the occurrence of bistability 88
4.5 Robustness of sensitive parameters towards the maintenance of bistability . . . 90
4.6 Bistable property of a motif structure can be applied to identify potential drug targets through hysteresis 91
4.7 Validation of the model predictions using existing drug information 93
4.8 Disruption of bistability due to the introduction of random perturbations 98
4.9 Discussion 100

5 Bistability regulates TNFR2-mediated survival and death of T-regulatory cells 103
5.1 Introduction 103
5.2 Construction of the deterministic model 106
5.3 Analytical results 108
5.3.1 Positive invariance and boundedness of the solutions 108

5.3.2 Equilibrium point and stability analysis . . . 111
5.4 Construction of the stochastic model . . . 112
5.4.1 Stochastic stability of the interior equilibrium point . . . 114
5.5 Numerical results . . . 118
5.5.1 Model validation with experimental data . . . 118
5.5.2 Global sensitivity analysis . . . 119
5.5.3 Existence of bistability . . . 120
5.5.4 Robustness of bistability . . . 120
5.5.5 Bistability determines cell's fate: survival or death . . . 121
5.5.6 TNF concentration regulates cell death . . . 123
5.5.7 Addition of randomness triggers loss of bistability . . . 126
5.5.8 Effect of saturated synthesis of S, J and A on model results . . . 128
5.6 Discussion . . . 129

6 Studying the role of random translocation of GLUT4 in cardiomyocytes on calcium oscillations 133

6.1 Introduction . . . 133
6.2 Construction of deterministic model . . . 137
6.3 Analysis of the deterministic model . . . 140
6.3.1 Positivity and boundedness . . . 140
6.3.2 Equilibrium point and its stability . . . 142
6.3.3 Hopf bifurcation analysis . . . 145
6.4 Analysis of the stochastic model . . . 146
6.4.1 Construction of the stochastic model . . . 146
6.4.2 Stochastic stability of interior equilibrium . . . 148
6.5 Numerical analysis . . . 153
6.5.1 Parameter choice and model validation . . . 153
6.5.2 Effect of parameter variations on the Ca^{2+} oscillation . . . 154
6.5.3 Global sensitivity analysis . . . 158
6.5.4 Robustness analysis of the sensitive parameters . . . 159

6.5.5 Effect of randomness on Hopf bifurcation 160
6.5.6 Restoration strategies and potential drug-targets 162
6.6 Discussion 164

7 Conclusions and future directions **169**
7.1 Conclusions 169
7.2 Future directions 173

References **175**

List of Publications **201**

List of Other Publications **203**

List of Conferences **205**

List of Figures

1.1 General biological network 2

1.2 Cell signalling 6

1.3 Response curve modification due to varying feedback strength 17

2.1 Schematic diagram of two frequently observed two-node motifs 36

2.2 Bistability in structure 1 42

2.3 Robustness analysis for structure 1 43

2.4 Global sensitivity analysis for structure 1 44

2.5 Bistability in structure 2 44

2.6 Robustness analysis for structure 2 45

2.7 Global sensitivity analysis for structure 2 47

2.8 Time series analysis 53

2.9 Phase plane of structure 1 54

2.10 Phase plane of structure 2 55

2.11 Effect of randomness on bistability 56

3.1 Schematic diagram of the general two-node motif 61

3.2 All biologically feasible two-node topologies and their nomenclature 62

3.3 Association of noise and input stimulus with stochastic stability 70

3.4 Methodology to calculate stochastic stability 72

3.5 Ranking of the two-node motifs 73

3.6 Collective behaviour of the motif groups under systemic noise 73
3.7 Druggability test 74
3.8 Sensitive and robust nodes vs drugs 76
3.9 Significance and application of cumulative score 79
3.10 GO annotation and KEGG pathway enrichment analysis of the highly sensitive nodes 80

4.1 All possible bistable two-node motifs 86
4.2 Bistable two-node motifs 88
4.3 Global sensitivity analysis 89
4.4 Robustness analysis 90
4.5 Bistable properties through hysteresis 92
4.6 Feedback and reversible hysteresis 92
4.7 Abundance of bistable nodes (proteins) in PPI networks 93
4.8 Drug targets and reversible hysteresis 95
4.9 Effect of stochasticity on model prediction 98

5.1 Map of the TNFR2 pathway 107
5.2 Model validation with experimental data 118
5.3 Global sensitivity of the system parameters 119
5.4 Existence of bistability 120
5.5 Robustness analysis 121
5.6 Hysteresis: the hallmark of bistability 122
5.7 Response and feedback strength 124
5.8 Time evolution of TNF-TNFR2 and JNK in the presence of noise 125
5.9 Change of stochastic stability with variation in feedback strength 127
5.10 Global sensitivity analysis and robustness analysis 129

6.1 Calcium signaling in cardiomyocytes 137
6.2 Time series analysis 154
6.3 Physiological and non-physiological oscillations patterns 155

6.4 Existence of periodic solution through Hopf bifurcation 155
6.5 Global sensitivity analysis 159
6.6 Robustness analysis 160
6.7 Population distribution for low and high noise intensities 161
6.8 Comparison of Hopf bifurcation results for the deterministic and stochastic systems 161
6.9 Parameter recalibration 163

List of Tables

2.1 Parameters description and the initial values for structure 1 42

2.2 Parameters description and the initial values for structure 2 46

3.1 Table containing the cumulative score and total frequency of the highly impact drug-targets of pancreatic, ovarian and breast cancers 77

4.1 Example of bistable proteins and their corresponding structure 88

4.2 Frequency distribution of bistable motifs in three cancer networks 96

4.3 List of bistable proteins and drugs targetting them 97

4.4 List of drug targets and associated bistable output nodes 97

4.5 List of bistable parameter sets 99

5.1 Kinetic parameters involved in the system 117

6.1 Parameter description along with default values and references 140

6.2 Impact of individual parameters on the overall performance of the system . . . 157

6.3 Restoration of cytosolic calcium by adjusting the sensitive parameters 162

1

Introduction

1.1 Biological networks

Biology, the science of life and living things, is derived from the Greek words "bios", which means life, and "logos", meaning study [1]. The processes necessary for an organism to survive and interact with its surroundings are referred to as biological processes. These consist of the biochemical reactions, or the events involved in the persistence and evolution of living forms [2]. Body homeostasis, structural organisation, metabolism, growth, reproduction, response to stimuli etc., are some of the fundamental biological processes. A biological network is a way of expressing systems as intricate webs of binary relationships or interactions between different biological elements. In general, relationships between entities or objects are represented by networks or graphs [3]. A graph typically consists of a collection of nodes connected by edges.

In the case of biological networks, the nodes consist of biological entities, and the relations between them define the edges.

The basis of graph theory was laid by Leonhard Euler's analysis of the Seven Bridges of Königsberg in 1736. The subject of random graphs was established between 1930 and 1950. It was found in the middle of the 1990s that many distinct kinds of "real" networks have structural characteristics very dissimilar from random networks [4]. Scale-free and small-world networks started influencing the development of systems biology, network biology, and network medicine in the late 2000s [4]. In order to simulate the complex mechanism of a cell, different forms of information might be displayed as networks. When analysing a network representation, it is important to remember that the significance of the nodes and edges depends on the type of data used to create the network. In terms of connection, complexity, and structure, different data types will also result in networks with varied edges and nodes capable of carrying information across several levels. Fig. 1.1 gives a general network illustrating various biological interactions.

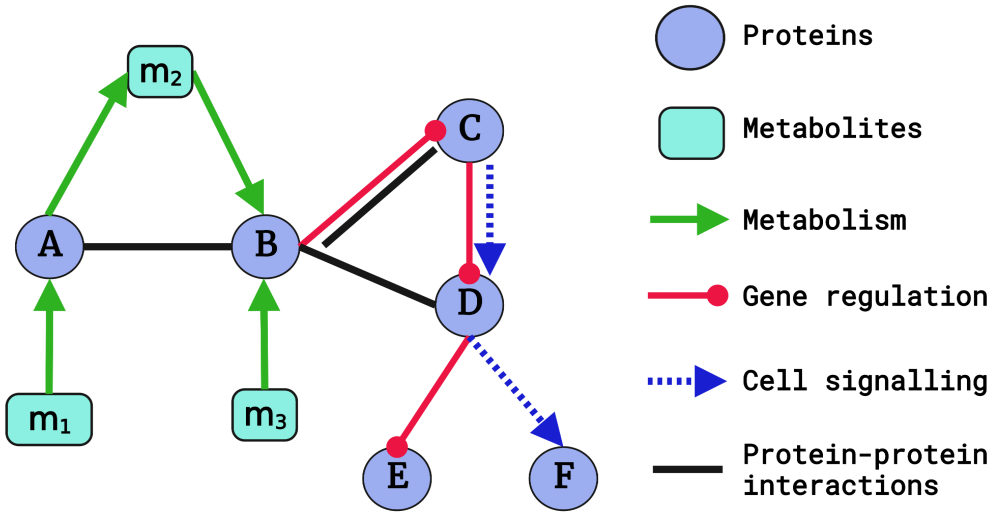

Figure 1.1: **General biological network.** The figure depicts the network representations for several kinds of biological interactions.

1.2 Types of biological networks

When the biological entities used to construct the networks are at the population level, some of the most common biological networks can be categorised are:

- *Food webs:* Feeding interactions bind all living things together. A complex food web of interactions between predators and prey connects species when one consumes or is consumed by another.

- *Inter-species interaction networks:* Ecological networks involving several species constructs these inter-species interaction networks. Plant-pollinator interactions are advantageous to both species and frequently involve a wide variety of plant and pollinator species. The success of plant reproduction depends on these interactions.

- *Intra-species interaction networks:* Social network is a kind of intra-species interaction network consisting of only one species. The study of social networks can also highlight significant variations in animal behaviour in changing environments.

Based on the data used to construct the network of the cell, biological networks can be categorised into several popular categories, including:

- *Protein-protein interaction (PPI) networks:* PPI networks represent the physical or functional relationship between the proteins. Proteins are represented as the nodes that are linked by directed or undirected edges representing their relationship. Practically every process occurring inside the cell depends on PPIs.

- *Metabolic networks:* Metabolic networks represent the biochemical processes that enable an organism to develop, reproduce, adapt to its surroundings, and preserve its structural integrity. In metabolic networks, enzymes and metabolites operate as nodes, and the reactions that describe their transformations are shown as directed edges. The direction of metabolic flow or the regulatory effects of a particular reaction also can be represented by edges.

- *Genetic interaction networks:* The phenotype that results from simultaneous mutations in two or more genes is markedly different from the phenotype that would follow from summing the effects of the individual mutations. This type of interaction is a synergistic phenomenon known as genetic interaction. Genetic interaction networks show a functional rather than a physical relationship between several genes. Nodes represent genes, while the connections between them are shown as edges. Based on the interaction evidence, the edges' directionality can be determined.

- *Gene / transcriptional regulatory networks:* Gene regulatory networks can model gene expression control. Genes and transcription factors are shown as nodes, and various kinds of directional edges show how they are related to one another. For instance, the directed edge between genes A and B shows that A controls the expression of B. Therefore, these directional edges represent the activation and the inhibition of gene regulation.

- *Cell signalling networks:* Signals are transduced within or between cells, forming intricate signalling networks crucial to the tissue's structure. Signalling pathways simulate the flow of information within the cell and depict the sequential order of occurrences. Gene regulatory networks are a subtype of cell signalling networks that concentrate on a particular signalling event that is frequently the last stage of a signalling cascade. Gene regulatory, metabolic, and protein-protein interaction networks are commonly incorporated into the signalling networks [5].

The cell signalling network represents the cell signalling processes and pathways, which is an essential aspect of all cellular life in both prokaryotes and eukaryotes. Every cellular activity is coordinated through cell signalling networks, and since it involves other interaction networks, the current thesis is mainly focused on cell signalling networks.

1.3 Cell signalling

The ability of a cell to receive, process, and transmit messages with its surroundings and with itself is known as cell signalling or cell communication in biology. Cell signalling is an intricate

process that coordinates the proper cellular response by transmitting diverse cellular inputs to effector molecules through a signalling cascade. Critical cellular decisions like development, cell growth and division, differentiation, migration, and apoptosis are influenced by cell signalling. Homeostasis is preserved through the coordinated control of these cellular processes. In all cases, the cell responds to chemical, mechanical or electrical signals, including hormones, neurotransmitters, mechanical stretch, shear and ion currents. Cell signalling also provides the coordination needed for multicellular creatures to function. Development, tissue repair, immunity, and normal tissue homeostasis are based on cells' capacity to recognise and appropriately respond to their micro-environment [6–8]. Numerous disorders, such as cancer, autoimmunity, and diabetes, are caused by errors in cellular information processing [9, 10]. Therefore cell signalling becomes the most extensively studied area in the case of human diseases. The relay information to effectors that alter sub-cellular processes is activated by signalling pathways.

Typically, there are three components of a cell signalling process, signal reception, signal transduction, and response. When a ligand binds to the cell's receptor, it sends the signal to the cell's interior, where the chemical messengers send the signal to the cell's nucleus, which accordingly responds. In the multicellular system, cell signalling produces signals that serve as inputs for the other cells. Figure 1.2 illustrates a schematic diagram of the cell signalling process. Every component of a cell's signalling pathways works together to form a complicated network. Network analysis enables us to comprehend the fundamental design of cell signalling networks and the potential effects of alterations to these networks on information transmission and flow. According to their organisation, networks can display various emergent traits, such as bistability and ultrasensitivity [11–14]. According to a review of signalling pathways in mammalian systems by Eungdamrong and Iyengar [11], cellular signals do not necessarily propagate linearly. Instead, cellular signalling networks are composed of densely coupled modules that can be utilised to control various functions in a context-dependent way [15]. Thus, mathematical models must be created to comprehend the overall behaviour of signalling networks and to forecast higher-order functions [11]. Additionally, as the combination of inputs often affects the behaviour of the output in a non-linear way, dynamical models of these signalling networks in the form of differential equations are commonly employed to sup-

plement experimental studies [16]. There are numerous publications where researchers used a system of ordinary differential equations to examine the network's structural topologies and their relationships to the signalling process [17, 18].

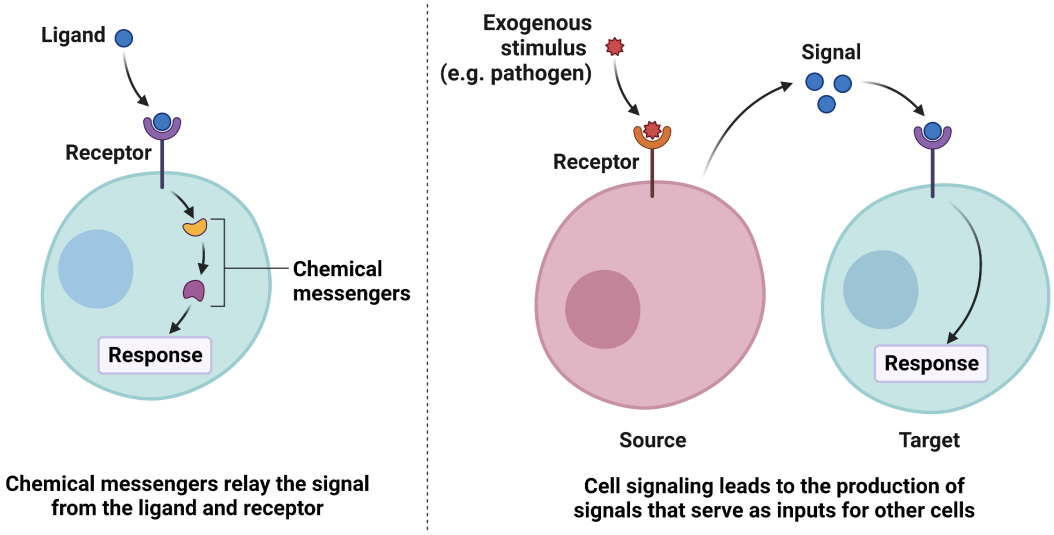

Figure 1.2: **Cell signalling.** The figure depicts the schematic representation of the simple steps involved in the cell signalling processes.

1.4 Types of cell signalling

Mechanical signals and biochemical signals are the two broad classifications of cell signalling. Cells can sense and react to mechanical signals, which are only the forces that are applied to and produced by the cell [19]. Signals produced by biological substances, including proteins, lipids, and ions, are referred to as biochemical signals. These signals can be classified as signalling within, between, or among the cells depending on the distance between the signalling and responder cells or between two signalling molecules. Here are some examples of classified signalling:

- *Intracrine signalling*: In this situation, the target cell generates signals that are internal to the target cell. It is possible to classify steroid hormones as intracrine since they have an effect on intracellular receptors. Example: Parathyroid hormone-related protein

- *Autocrine signalling*: Here, the target cell generates and secretes signals that interact with receptors on the target cell to affect it directly. Example: cytokine interleukin-1.

- *Juxtacrine signalling*: These signals can influence either the emitting cell or cells next to it because they are transferred along cell membranes via protein or lipid components that are essential to the membrane. It is essential for the growth of the brain and cardiac function in particular. Example: Signaling through Gap Junctions.

- *Paracrine signalling*: Paracrine signalling, which modifies the behaviour or differentiation of surrounding cells, is the mechanism used by cells to communicate with one another. Example: Neurotransmitters signalling.

- *Endocrine signalling*: Endocrine signalling is the phenomenon whereby biochemical processes work to control distant tissues by secreting substances right into the circulatory system. Hormones produced by endocrine cells circulate throughout the body via the blood. Example: beta cells insulin secretions.

Cells can communicate with each other by making physical contact or by releasing a signalling molecule that is subsequently received by another cell. For example, direct cell-to-cell contact is necessary for the functioning of the heart. Heart cells use gap junctions to connect their cytoplasm to the cytoplasm of neighbouring cells [20]. They combine two cells' cytoplasms directly, allowing different chemicals, ions, and electrical impulses to travel through a controlled gate between cells. Gap junctions between neighbouring cells in cardiac muscle enable action potentials to travel from the heart's cardiac pacemaker region and stimulate the heart's contraction [21]. Cell-to-cell communication via signalling molecules plays an essential role in the body's immune response. For example, signalling molecules like cytokines, a group of small proteins, are crucial in controlling the growth and activity of other immune system cells and blood cells. Cytokines produced by one cell can affect the growth and development of other immune and non-immune cells that helps in the body's immune and inflammatory responses. Cytokines support the body's natural ability to fight cancer by transmitting signals that can cause abnormal cells to die and normal cells to live longer [22, 23].

1.5 Cell signalling defects and diseases

Defects in signalling pathways are the root cause of many disorders. These malformations come in various types, and their reasons are also very diverse. Some of these defects can be brought on by pathogenic organisms and viruses, which can interfere with signalling events. For example, numerous viruses and pathogenic microorganisms alter the signalling mechanisms, causing defects in the signalling system and leading to different diseases [10]. Like, *Shigella flexneri*, a gram-negative bacteria can interfere with PtdIns4,5P_2 regulation of actin remodelling, causing bacillary dysentery. Cholera, caused by *Vibrio cholerae*, secrets the cholera toxin, which activates the cyclic AMP signalling pathway and causes severe water loss, vomiting and muscle cramps [10]. Other diseases, such as tuberculosis, listeriosis, peptic ulcers, etc., are also caused by pathogens that alter the signalling system [10].

Deficiencies in the operation of cell signalling pathways are responsible for a number of other illnesses. The majority of the significant illnesses that affect people, including high blood pressure, heart disease, diabetes, and many types of mental illness, appear to be caused by minute phenotypic changes in signalling pathways. Such phenotypic remodelling modifies cell behaviour and subverts normal cellular processes, resulting in disease [10]. Cancer, one of the most dreaded illnesses affecting people, is a multi-step process developed by multiple mutations in various signalling components. Firstly, the unbounded growth caused by oncogenes can alter the signalling pathways related to proliferation, making them constitutively active and causing cells to divide repeatedly. Secondly, the tumour suppressors' mutations can reduce inhibitory effects on cell proliferation. Thirdly, the mutations in the signalling system can identify aberrant cells and eliminate them by causing senescence or apoptosis. Therefore, numerous combinations of oncogene activation, tumour suppressor gene inactivation, and the emergence of various anti-apoptotic pathways might result in cancer development [10]. Several autoimmune diseases are also caused due to defective signal processing. Like, in the case of Inflammatory Bowel Disease (IBD), chronic intestinal inflammation is brought on by releasing inflammatory mediators such as tumour necrosis factor (TNF), IL-6, IL-8, and MCP-1. In the case of Multiple sclerosis (MS), an inflammatory response is initiated in the central nervous system (CNS) due to the recognition of oligodendrocytes as foreign cells by T cells [10].

Several other prevalent diseases, like insulin resistance and diabetes, are also caused due to alterations in the signal processing or the defects in the cell signalling system [10]. The enormous redundancy built into cell signalling pathways creates a wide range of opportunities for creating fresh approaches to treating numerous diseases.

1.6 Presence of noise in cell signalling

Random fluctuations of a signal are defined as noise. In the case of cell biology, cellular noise is the random fluctuations in quantities of biological entities (e.g. gene, protein etc.) [24]. Cell signalling noise can be categorised into two types, intrinsic and extrinsic noise. Intrinsic noise describes the fluctuation in identically-regulated genes within a single cell. In comparison, extrinsic noise defines the variability of identically-regulated genes between different cells [25]. For instance, even within the same tissue, genetically identical cells are frequently found to have variable sizes, shapes, and amounts of protein expression [25–27]. Elowitz *el al.* [25] showed that the presence of intrinsic noise in *Escherichia coli* exhibits phenotypic variations in the bacteria population. These seemingly arbitrary changes may have significant biological and physiological repercussions.

Cells use biochemical networks of interacting genes and proteins to sense and process information, which involves a sequence of molecular processes [28]. The whole process is carried out through a network of proteins known as the protein-protein interaction (PPI) network. PPI network is the mathematical representation of the physical contacts between proteins in the cell [29]. These physical contacts are specific, have a particular biological meaning, and serve a specific biological function. The intrinsic promiscuity of PPI introduces noise in signalling networks [30]. Randomness at the intracellular level is caused due to low copy numbers of chemical reactants and their heterogeneous distribution inside the cell [31]. Chemical reactions, diffusion, homologous recombination, gene expression, and many other fundamental biological processes are regulated to a large extent by the inherently stochastic interactions of molecules [32].

There are biological circuits where the input signal governs the flow of information, and ran-

dom fluctuations [33]. So the response-specificity is subjected to the input signal and stochastic perturbation, causing a change in the steady-state output value. This change in steady-state level could influence many biological processes, including adaptation, immunological memory, development, and cell differentiation[30, 31]. In the presence of molecular signalling noise, the signal transmission becomes a probabilistic rather than a linear view [30]. Multiple outputs are produced due to the sensitivity of the intracellular system. These variations are induced by the extracellular noise, or random perturbation of the intracellular components [8, 34–39]. The noise caused by stochastic fluctuations plays a significant role in cell function and phenotypic behaviour[30]. These fluctuations in biological systems can either improve the sensitivity of the biological process or decrease its accuracy. The presence of noise alters central regulatory switches of cellular processes. Thus, noise may have a role in human diseases [30].

1.7 Regulatory points in a biological network

Complex biological systems can be modelled as networks in the real world to understand the relationships between biological entities. A subset of the nodes that can significantly affect or regulate the outcome and function of the whole network can be called regulatory nodes. Identifying and ranking these regulatory points in a complex network, such as a biological network, is one of the most important and fundamental problems in network research [40–44]. Studying regulatory nodes in complex networks has important theoretical and practical implications for the structure, transmission, and synchronisation of complex networks. Based on the datasets used to construct the network, the identification of the key regulatory nodes can significantly help us to stop network attacks [45], to prevent the transmission of computer viruses across networks [46], to prevent the spread of misleading information throughout society [47], to guard against an outbreak of infectious diseases in the population [48], to highlight the key genes that might influence the phenotypes of diseases [42] and so on. Accurate estimation and evaluation of the importance of the node are relevant to enhance the robustness and design principle of the system structure. On the one hand, these crucial nodes can increase the network's overall dependability and resilience. On the other hand, the entire network can also be destroyed by

purposefully targeting these essential nodes. [40].

A common trait shared by all species is the ability to adapt to ongoing environmental changes. Numerous routes that receive and process signals from various parts of the cell and the external environment are used to interact with the environment [15]. The signals that regulate specific cell functions are transmitted via distinct signalling pathways. These cellular signalling pathways do not work independently but are part of a more extensive complex system. To understand the integrated cellular functions, we need to recognise and investigate the characteristics of the functional organisations of these complex cell signalling networks [15]. Cell signalling governs the cell's activities and coordination of multiple cell actions. Cell signalling regulates most of the cellular responses in our body [7, 8]. Defects in the signalling system may lead to complicated diseases such as autoimmunity, cancer and diabetes [9, 10]. The present thesis focused on identifying the regulatory points that potentially led to disease phenotypes in the cell signalling systems.

1.8 Methods to find the regulatory points: Modelling cell signalling networks

It is crucial to comprehend the statistical and mathematical techniques used to find the regulatory points from a complex biological network, such as a cell signalling network. Techniques that reveal the associations, communities, and centrality of the nodes can be used to determine the relationships. The development of these techniques straddles disciplinary borders and strongly incorporates ideas from Bioinformatics, Computer Science, and Mathematics. Some of the most common principles used to find the regulatory points are discussed below:

- *Association:* When analysing a network, there are numerous techniques to determine the association between nodes. The method to find the association between the nodes is chosen based on our interests. One of the most common methods used to find the association between nodes is to find the correlation between the nodes. The correlation coefficient is the numerical metric used to measure the correlation between two entities. It gives a statistical relationship between the two variables.

- *Centrality:* The most frequently used centrality measures are degree centrality, closeness centrality, betweenness centrality, and Katz centrality. But these centrality measures are heavily dependent on the topology of the network. Every kind of centrality technique has the potential to reveal significant features about the nodes in a specific network. Still, they all have one thing in common: they aim to quantify a node's importance inside a network. In a study by Joy *et al.* [49], they used centrality measures to find the important proteins from a yeast protein interaction network. Proteins with high betweenness centrality measures were more crucial and translated closely to the evolutionary age of a particular protein.

- *Communities:* A network is considered to have a community structure if its nodes can be easily categorised into (sometimes overlapping) sets of nodes, with each set being densely connected to the others. In real networks, community structures are fairly prevalent. Social networks are made up of community groups that share a common location, common hobbies, common occupations, etc. In the case of protein interaction networks, communities may correspond to a group of proteins in a cell with comparable functionality.

The biological systems do not work individually, but they operate in unison. Thus, developing efficient treatment methods necessitates a system-level knowledge of the molecules affected by disease and their complicated relationships. The systems biology approach is the best way to gather system-level knowledge of complex biological systems. The cell signalling system is based on hierarchy: the proteins on the edges (cell membrane) and the proteins in the core (nucleus) differ in their characteristics and functions. The linkages connect these hierarchical structures. Systems biology uses a holistic approach that incorporates the knowledge of the structures and their linkages. In other words, systems biology can recognise every component of a biological system and aims to create a complete system model by quantifying its components and their relationships. Network analysis and mathematical modelling are two fundamental elements of systems biology. Network analysis is mainly based on statistical tools, thus unable to capture the dynamics of the system's components. However, we need a dynamic approach to capture the effect of intrinsic noise on the system components. So, in this thesis,

we have opted for a systems biology approach based on mathematical modelling to identify the regulatory points accurately and efficiently under perturbation.

1.9 Mathematical modelling of cell signalling systems

Cell signalling systems are very complex in nature. This complexity arises due to the existence of hierarchy in the system. Each hierarchy adds different dynamics to the signalling system. The class of proteins that reside on the cell membrane (periphery) have different kinetics than the proteins/genes in the nucleus (core) of the cells. Although they may follow some regular dynamical patterns, the inherent stochasticity may change the dynamics abruptly. These sudden change in dynamics is hard to capture in experimental studies. Even if they can capture the outcome of the stochastic processes, it is hard to track the underlying mechanism. For example, by doing a knock-out study of a gene, biologists try to predict the functionality of the gene [50]. But these experiments may overemphasise the functionality of the single gene over a pool of numerous genes that are highly connected to a very complex system. Mathematical models, on the other hand, can portray these complexities abstractly. These models have the audacity to identify crucial parameters deriving the outcome of the system. However, the hypotheses from the mathematical studies need to be validated experimentally.

Mathematical models have the perfect balance between simplicity and complexity. They are composed of a well-defined set of equations capable of producing the complex dynamical properties of the signalling system. At the same time, they are simple enough to demonstrate the underlying mechanisms. In the disciplines of drug discovery and pharmacokinetics, mathematical models have been frequently constructed to investigate receptor-ligand interactions and pharmacokinetics [51, 52]. Metabolic networks have also been studied for a long time to assess the flow of metabolites in vast networks with several regulatory loops using sophisticated mathematical methods [53, 54]. Mathematical network analysis can enrich our knowledge of signalling pathways in three ways [11]. First, modelling reveals information about how distinct operational pathways operate in relation to one another. Second, modelling makes it possible to estimate variables that are currently technologically impractical to measure experimentally,

and it frequently confirms the validity of suggested molecular mechanisms. Third, modelling helps find potential targets for the pharmacological treatment of disorders by identifying the main regulatory hubs of signalling networks. That way, the mathematical model also reduces the time and saves ample resources required for the study.

1.9.1 Mathematical models based on ordinary differential equations

Mathematical models based on differential equations are frequently used to portray complex cell signalling systems. Chemical kinetics models based on ordinary differential equations (ODEs) are the most widely used modelling frameworks among the diverse models available to analyse cell signalling processes. This method's fundamental presumption is that the cell functions as a well-stirred reactor and that the governing equation describing the dynamics of a signalling component has the following structure:

$$\frac{dx_i}{dt} = production/activation - consumption/deactivation/degradation. \tag{1.1}$$

The above equation indicates that the rate at which every molecule's concentration (x_i) changes is equal to the rate at which it is produced and/or consumed/degraded. This equation is merely the mathematical representation of the actual biological phenomenon. The production or degradation terms can be constants, first order, or non-linear based on the biological phenomenon the equations are representing [55]. One of the significant drawbacks of the ODE-based model is that it assumes that the cell is a well-stirred reactor. Although this assumption may be true for some cases, it will be incompetent in case of biochemical reactions which are spatially restricted or where factors like noise are involved in the system.

1.9.2 Mathematical models based on stochastic differential equations

ODE-based models translate the kinetics of biological entities into a system of differential equations. But this is deterministic, which is unable to capture the effect of random fluctuation inherently present in the cell signalling systems. Adding stochastic effect or noise to such systems is one method of modelling them. Stochastic models must be used to accurately depict

the various types of variability needed for the realistic modelling of cell signalling systems. However, these stochastic models are much more computationally demanding than deterministic models and challenging to fit into experimental data. We can represent the general form of a stochastic differential equation (SDE) as

$$dy_t = f(t, y_t)dt + G(t, y_t)dw_t,$$

or with the equivalent integral form

$$y_t = y_{t_0} + \int_{t_0}^{t} f(s, y_s)\, ds \; + \int_{t_0}^{t} G(s, y_s)\, dw_s,$$

with an initial value, y_{t_0}. Here, $f : [t_0, t] \times R^n \to R^n, G : [t_0, t] \prod R^n \to R^{n \times m}$ and $\{w_t\}_{t \in [t_0, t]}$ denote an m-dimensional Wiener process (Brownian motion). R^n and $R^{n \times m}$ are n-dimensional and $n \times m$-dimensional Euclidean space, respectively.

1.10 Emergence of complex qualitative properties: ultrasensitivity, bistability and oscillation

Information relays to the effectors through signal transduction, which alters the sub-cellular processes. The information processing system must detect the input signal's amplitude and duration to generate an output signal of proper strength and duration. This relation is called the input-output (I/O) relation in the cell signalling network. Numerous studies demonstrated that multiple outputs are produced at the level of changes in gene expression and cellular activities [8, 34–39]. These provide strong evidence that intracellular signalling systems are sensitive to input stimuli changes like mutations, protein turnover rates, etc. However, for these inappropriate and non-specific responses, the system has its safeguards. In complex biological processes like adaptation, immunological memory, development, and cell differentiation, the changes in steady-state levels determine the outcome [13, 56, 57]. The complexity in the biological systems comes due to the presence of non-linear interactions between the cell signalling components [16], which arises from the presence of feedbacks [58]. Autoregulation is the most

basic form of positive feedback and is one of the most prevalent architectural components in signalling networks [59]. Also, the gene networks frequently use both positive and negative feedback as a control mechanism [60]. Prokaryotic gene circuits primarily use negative feedback to maintain homeostasis [61, 62]. Eukaryotic transcriptional activators frequently control their expression through positive and negative feedback [63]. The presence of non-linearity and the feedbacks make ideal ingredients for the emergence of complex qualitative properties like ultrasensitivity, bistability, and oscillations [14, 64–68].

The term ultrasensitivity refers to the stimulus/response curve that is steeper than the hyperbolic Michaelis-Menten curve. Cooperativity is the most common mechanism to generate ultrasensitive responses. For positively cooperative entities, we get sigmoidal stimulus/response curves. They require significantly less stimulus to drive from a very low response to a high response. But, when the stimulus is low, the ultrasensitive curve is less steep than Michaelis-Menten. Thus, this ultrasensitive curve moves towards all-or-none, switch-like responses [64]. One such ultrasensitive curve is shown in Fig. 1.3 (c). The all-or-none switch-like responses may be particularly well suited for mediating processes like mitogenesis, cell fate induction, and oocyte maturation when a cell flips from one discrete state to another due to the form of the MAPK stimulus/response curve [64]. Similar responses were reported by Bagowski *et al.* [12, 69] that the JNK's reactions to sorbitol and progesterone are virtually all or none. They observed that JNK activity was either extremely high or extremely low in each individual oocyte.

Another crucial part of the I/O relation is the existence of bistability, where the output signal can attain any of the two alternative stable-activity states that persist under identical parametric/experimental conditions [70]. Highly ultrasensitive responses become bistable when the feedback strength increases beyond some threshold value [71]. One of the hallmarks of bistability is that they often exhibit a kind of memory known as hysteresis [71, 72]. Hysteresis is the phenomenon where bistable switching is observed for different stimulus-response [71, 73, 74]. The two response curves representing two discrete stable steady states form a loop known as the hysteresis loop [75]. Thus the I/O relation becomes a loop rather than a curve. This hysteretic switching can be categorised into two types, reversible and irreversible [75]. In reversible hysteresis, the system can return to its previous steady state only by changing the input

stimulus, whereas in irreversible hysteresis, it can not. Whether a system will have reversible or irreversible hysteresis depends on the strength of the feedback parameter. By increasing the strength of the feedback parameter, a reversible hysteresis can be transformed into an irreversible one [71].

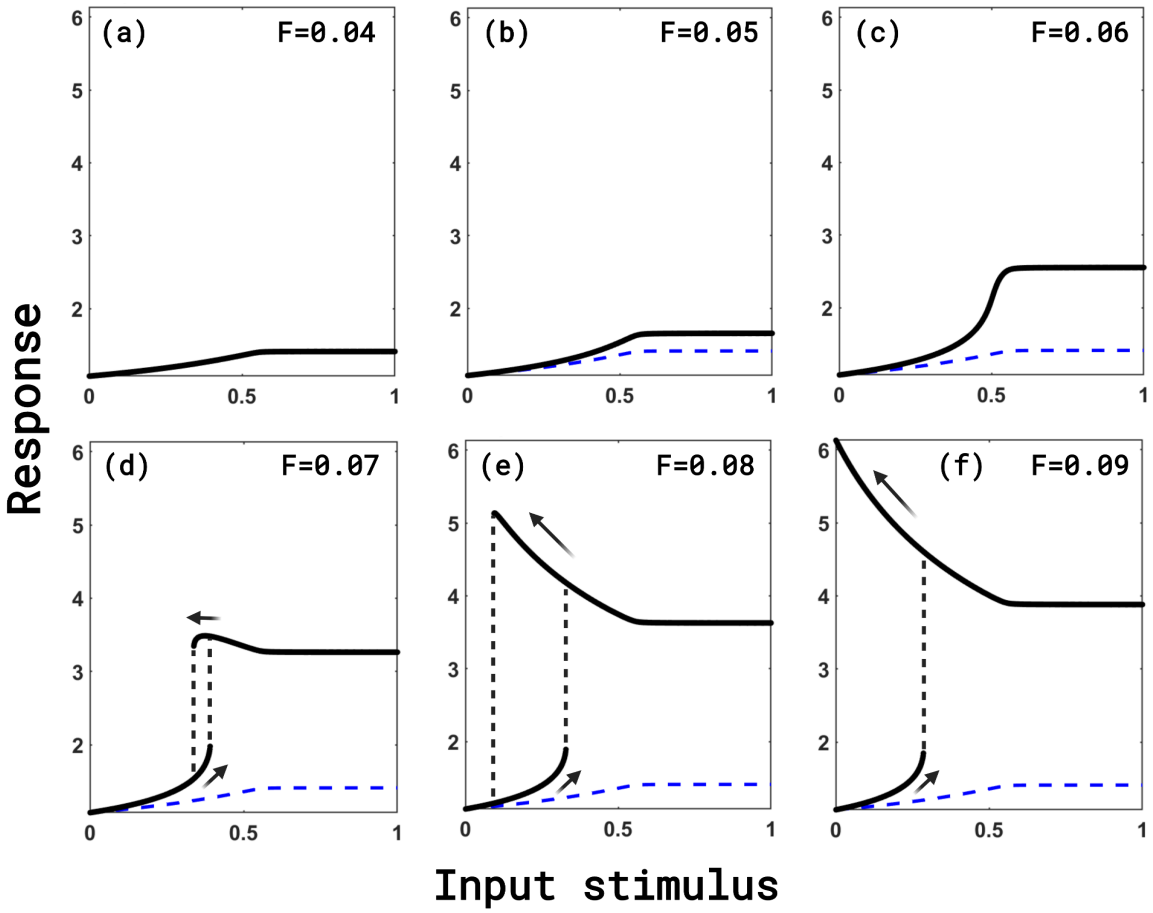

Figure 1.3: **Response curve modification due to varying feedback strength.** The figure depicts the emergence of ultrasensitivity, bistability and hysteresis (reversible & irreversible) upon changing the feedback strength (F). The response is a smooth curve when the feedback strength is low (F = 0.04). It becomes sigmoidal (ultrasensitive) when F is increased slowly to 0.06 (but still monostable). Upon further increasing, the response curve splits into two curves and becomes bistable at F = 0.07. It shows reversible hysteresis for F = 0.07 & 0.08. Eventually, the curve shows irreversible hysteresis when F is 0.09. The blue lines (response with F = 0.04) are included for comparison. The unit-free figure is adopted from [95] only used for depiction.

Fig. 1.3 depicts different stimulus/response curves showing various stages of ultrasensitivity and bistability. With a low feedback strength (F = 0.04), the response is a smooth curve, Fig. 1.3 (a). When F is gradually increased to 0.06, it becomes sigmoidal (ultrasensitive) but still monostable (see Fig. 1.3 (c)). Upon further increasing the feedback strength to 0.07, the

response splits into two curves and becomes bistable (see Fig. 1.3 (d)). And the system shows reversible hysteresis for F = 0.07 & 0.08 (see Fig. 1.3 (d-e)). Eventually, when the feedback becomes too large (F = 0.09), the response shows irreversible hysteresis (see Fig. 1.3 (f)). Even when the input concentration varies, the system can retain its current state through this hysteresis. Hence, these hystereses make the system robust against fluctuations in the input stimuli [75].

It is well recognised that ultrasensitivity and bistability play a crucial role in biological systems, particularly in cell signalling and functioning [71, 76–80], differentiation [71, 76, 77] and cell cycle progression [79–81]. By conserving the cellular memory of previous stimuli, it can improve adaptability in various organisms, including bacteria and humans [82, 83]. In positive feedback networks, where the input to the MAPK cascade is positively regulated by the activated MAPK, Ferrell and colleagues demonstrated that bistability might be driven by ultra-sensitivity [71, 77, 78]. Kholodenko *et al.* [84] establishes the possibility of bistability at the level of a single stage of the MAPK cascade. Bistability also plays a vital role in diseases like cancer and prion disease [85]. In cancer, bistability is mainly involved in the loss of cellular homeostasis associated with the beginning of the disease. The self-perpetuated activation of a signalling circuit is a declaration of its bistability. Alam *et al.* [86] have demonstrated the existence of self-perpetuated activation mechanisms for ERK1/2 in bronchial epithelial cells. ERK1/2 bistability arises from repetitive stimulation of the cell. They have hypothesised that this self-perpetuated ERK1/2 signal plays an important role in the pathogenesis of asthma. Kheir Gouda *et al.* [87] used a mathematical model on bistability to understand evolutionary reversibility.

Oscillation is another qualitative behaviour generated by the non-linearity in the signalling system. These oscillations are common in biological systems. Circadian rhythm is a well-known example of oscillation. Feedback appears to be essential for generating oscillations in gene networks [88]. Negative feedback is well-acknowledged as crucial for preserving oscillations in the rate of gene transcription. A negative feedback loop develops if a gene product inhibits the transcription of its own gene either directly or indirectly. Negative feedback loop systems frequently enter a steady state that can be either stable or unstable. If it is stable, the

result is generally a damped oscillation, tending towards the stable state; if it is unstable, the result is a sustained oscillation [89]. Circadian rhythmicity models frequently rely on cyclic inhibition of their own transcription by one or more genes (e.g., *per* and *tim* in Drosophila, or *freq* in Neurospora) [88].

Various systems showing circadian rhythms have been modelled using negative feedback of genes involved in circadian rhythm. They are as diverse as the fungus Neurospora [90], the plant Arabidopsis thaliana [91], and the fruit fly Drosophila [92]. In general, oscillation cannot be produced by positive feedback alone. Positive feedback allows the system to reach an upper steady state, but there is no counterbalancing negative feedback process to reduce the concentration. The addition of a limiting rate can cause oscillations to be produced by positive feedback [88]. Gene network models that include both positive and negative feedback can easily oscillate. The cardiomyocytes are another system where oscillation is significant. Cardiomyocytes' cytoplasmic calcium oscillations are fuelled by calcium ion exchange between the cytoplasm, extracellular environment, and sarcoplasmic reticulum (SR). This ion exchange is accomplished by several ionic channels and pumps embedded into the extracellular membrane, and the SR [93]. Oscillations can also emerge from single-stage bistability. The necessary condition for the oscillatory behaviour at the cascade level is single-stage bistability was studied computationally by Qiao *et al.* [94].

1.11 Effect of stochasticity on ultrasensitivity, bistability and oscillation

A highly complex signalling network usually displays extensive dynamic control in response to disturbances. Furthermore, it is well established that stochastic fluctuations or randomness are inherently present in the signalling network [96]. Numerous intriguing effects of random fluctuations have recently been theorised and experimentally verified [25, 97–99]. Stochasticity can alter the emergence of complex behaviours like bistability and oscillations, some of which are mentioned here. Artyomov *et al.* [100] observed that the deterministic system has a single steady state for all parameter values, but the stochastic response is bimodal. Arkun *et al.* [101]

investigated the emergence of bistability and oscillation by the presence of positive and negative feedback loops in the ERK signalling pathway. They have also shown how negative feedback combats uncertainty that arises from extracellular fluctuations and internal perturbations. Similar results for negative feedback were obtained in other studies also [102, 103]. Another study reported the interplay of negative and positive feedback in TCR signalling results in bistability. Bistability combined with stochastic fluctuations allows for switch-like responses to signals [104]. It is known that an increase in stochastic perturbation may affect the cellular signalling memory. In other words, it can switch the system from one steady state to another steady state [99, 105–107]. In the case of oscillations in biological networks, it is well known that intrinsic noise can have an impact on the frequency and amplitude of sustained oscillations [108]. It has been seen that biological oscillators can utilise stochastic noise by channelling it into oscillatory power [102]. Marchena *et al.* [109] observed that adding a small amount of noise to the RyR behaviour increases the oscillatory regime of calcium oscillations. Wang *et al.* [110] demonstrated how the self-repressing *Hes1* gene exploits the stochastic oscillations induced by the intrinsic fluctuations to generate robust oscillations. Thus, in the case of bistability, stochasticity may play a dual role; however, oscillatory systems benefit from the inherent stochasticity of biological systems.

1.12 Different tools used to study mathematical models

This section discusses several fundamental definitions and theorems that are used to study mathematical models.

1.12.1 Mathematical tools to study deterministic models

Definition 1.12.1. (Autonomous system) Let us consider a system of differential equations of the following form

$$\frac{dy}{dt} = \dot{y} = g(y) \tag{1.2}$$

where $y \in \mathbb{R}^n$, $g = (g_1, g_2, ..., g_n)^T$ and $g_i = g_i(y_1, y_2, ..., y_n)$. The initial value problem

$$\dot{y} = g(y)$$

with

$$y(0) = y_0$$

will have a unique solution if the partial derivatives of $g_1, g_2, ..., g_n$ are C^1 functions. Since the function g does not contain t explicitly, the system (1.2) is called an autonomous system. Otherwise, it is called a non-autonomous system.

Definition 1.12.2. (Equilibrium point) If the following equality holds true for a point $\hat{y} = (\hat{y_1}, \hat{y_2}, ..., \hat{y_n})$,

$$\dot{y} = f(\hat{y}) = 0,$$

then the point $\hat{y}$ is said to be the equilibrium point of the system (1.2).

Definition 1.12.3. (Local stability) An equilibrium point $\hat{y}$ of (1.2) is said to be locally stable if for each $\varepsilon > 0$ there exists a $\delta > 0$ such that every solution $y(t)$ of (1.2) with initial condition $y(t_0) = y_0$, $||y_0 - \hat{y}|| < \delta \ \Rightarrow \ ||y(t) - \hat{y}|| < \varepsilon$ for all $t \geq t_0$, where $||.||$ is the Euclidean norm.

Definition 1.12.4. (Local asymptotic stability) An equilibrium point $\hat{y}$ of (1.2) is said to be locally asymptotically stable if it is locally stable and if there exists a $\zeta > 0$ such that $||y_0 - \hat{y}|| < \zeta \ \Rightarrow \ \lim_{t\to\infty} ||y(t) - \hat{y}|| = 0$.

Definition 1.12.5. (Global asymptotic stability) An equilibrium solution $\hat{y}$ of (1.2) is said to be globally asymptotically stable if it is locally asymptotically stable and if $||y_0 - \hat{y}|| < \infty \Rightarrow \lim_{t\to\infty} ||y(t) - \hat{y}|| = 0$.

Definition 1.12.6. (Instability) If the equilibrium point $\hat{y}$ of (1.2) is not stable, then it is called unstable.

Theorem 1.12.1. ***(Hopf bifurcation theorem)*** *Let us consider an autonomous system of ordinary differential equations*

$$\dot{y} = h(y, \mu), \ y \in \mathbb{R}^n, \ \mu \in \mathbb{R}, \tag{1.3}$$

where h is continuously differentiable. Suppose, the system (1.3) has an equilibrium $\hat{y}(\mu)$. *Moreover, the Jacobian matrix evaluated at* $\hat{y}(\mu)$ *has one pair of complex eigenvalues*

$$\xi_{1,2}(\mu) = A(\mu) \pm iB(\mu)$$

such that for some $\mu = \mu^*$ *it becomes purely imaginary, i.e.,*

$$A(\mu^*) = 0 \text{ and } B(\mu^*) \neq 0.$$

Then the eigenvalues will cross the imaginary axis with nonzero speed if (transversality condition)

$$\left.\frac{dA(\mu)}{d\mu}\right|_{\mu=\mu^*} \neq 0.$$

Then the system of differential equations (1.3) will undergo a Hopf bifurcation around $\hat{y}(\mu)$ *for* $\mu = \mu^*$ *and will possess a periodic solution with approximate period* $T = \frac{2\pi}{B(\mu^*)}$ *as* μ *crosses* μ^*. *The parameter* μ *is called the bifurcation parameter, and the value* μ^* *is called the bifurcation point.*

1.12.2 Mathematical tools to study stochastic models

Let us consider a general stochastic differential equation

$$dy_t = f(t, y_t)dt + G(t, y_t)d\xi_t. \tag{1.4}$$

The equivalent integral form is given by

$$y_t = y_{t_0} + \int_{t_0}^{t} f(s, y_s)\, ds + \int_{t_0}^{t} G(s, y_s)\, d\xi_s,$$

with an initial value, y_{t_0}. Here, $f : [t_0, t] \times R^n \to R^n, G : [t_0, t] \prod R^n \to R^{n\times m}$ and $\{\xi_t\}_{t\in[t_0,t]}$ denote an m-dimensional Wiener process (Brownian motion). R^n and $R^{n\times m}$ are n-dimensional and $n \times m$-dimensional Euclidean space, respectively. Here, the stochastic perturbations of the state variables around their steady-state values $\hat{E} = (\hat{y_1}, \hat{y_2}, ..., \hat{y_n})$ are Gaussian white noise

that is proportional to the distances of $y_1, y_2, ..., y_n$ from their steady-state values $\hat{y_1}, \hat{y_2}, ..., \hat{y_n}$ respectively.

Stochastic stability of interior equilibrium

The stochastic differential system (1.4) can be centred at its positive equilibrium points $\hat{E} = (\hat{y_1}, \hat{y_2}, ..., \hat{y_n})$ by introducing the variables $u_1 = y_1 - \hat{y_1}, u_2 = y_2 - \hat{y_2}, ..., u_n = y_n - \hat{y_n}$. The linearised version of (1.4) around $\hat{E}$ is given by

$$du(t) = f(u(t))dt + G(u(t))d\xi(t)\,, \tag{1.5}$$

where

$$\begin{aligned} u(t) &= (u_1, u_2, ..., u_n), \\ G(u(t)) &= \begin{bmatrix} \sigma_1 u_1 & 0 & ... & 0 \\ 0 & \sigma_2 u_2 & ... & 0 \\ . & . & ... & . \\ 0 & 0 & ... & \sigma_n u_n \end{bmatrix}, \end{aligned}$$

$$f(u(t)) = \begin{bmatrix} \left(\frac{\partial f_1}{\partial y_1}\right) u_1 + \left(\frac{\partial f_1}{\partial y_2}\right) u_2 + ... + \left(\frac{\partial f_1}{\partial y_n}\right) u_n \\ \left(\frac{\partial f_2}{\partial y_1}\right) u_1 + \left(\frac{\partial f_2}{\partial y_2}\right) u_2 + ... + \left(\frac{\partial f_2}{\partial y_n}\right) u_n \\ ..... \\ \left(\frac{\partial f_n}{\partial y_1}\right) u_1 + \left(\frac{\partial f_n}{\partial y_2}\right) u_2 + ... + \left(\frac{\partial f_n}{\partial y_n}\right) u_n \end{bmatrix}, \tag{1.6}$$

and σ_i, $i = 1, 2, ..., n$ are real constants and known as the intensity of the fluctuations. Note that, in (1.5) the positive equilibrium $\hat{E}$ corresponds to the trivial solution $(u_1, u_2, ..., u_n) =$

$(0,0,...,0)$. Let Ω be the set defined by $\Omega = [(t \geqslant t_0) \times \mathrm{R}^n, t_0 \in \mathrm{R}^+]$. To define stability following theorem [111] can be used,

Theorem 1.12.2. *Suppose there exist a differentiable function $V(u,t) \in \mathrm{C}^n(\Omega)$ satisfying the inequalities*

$$K_1|u|^\alpha \leq V(u,t) \leq K_2|u|^\alpha \tag{1.7}$$

$$LV(u,t) \leq -K_3|u|^\alpha, \quad K_i > 0, \quad i = 1,2,3, \quad \alpha > 0\,. \tag{1.8}$$

Then the trivial solution of (1.5) is exponentially α stable for all time $t \geq 0$.

Note that, if in (1.7), (1.8), $\alpha = 2$, then the trivial solution of (1.5) is exponentially mean square stable. Furthermore, the trivial solution of (1.5) is globally asymptotically stable in probability.

Here, following (1.5),

$$LV(t,u) = \frac{\partial V(t,u(t))}{\partial t} + f^T(u(t))\frac{\partial V(t,u)}{\partial u} + \frac{1}{2}Tr\left[G^T(u(t))\frac{\partial^2 V(t,u)}{\partial u^2}G(u(t))\right] \tag{1.9}$$

where

$$\frac{\partial V}{\partial u} = \begin{pmatrix} \frac{\partial V}{\partial u_1} & \frac{\partial V}{\partial u_2} & \cdots & \frac{\partial V}{\partial u_n} \end{pmatrix}^T, \quad \frac{\partial^2 V(t,u)}{\partial u^2} = \left(\frac{\partial^2 V}{\partial u_j \partial u_i}\right)_{i,j=1,2,...,n}$$

and T means transposition.

1.13 Statistical tools

1.13.1 Curve fitting

Curve fitting is the process of developing a mathematical function or curve that best fits a set of data points. It is required when we need a specific mathematical function to describe a set of data or to estimate the value of a particular parameter from a mathematical function when the values of the other parameters are known. In statistics, there are two well-known varieties of curve fitting: linear or first-order polynomial curve fitting and parabolic or non-linear polynomial curve fitting. When fitting data linearly, we consider first-order polynomials

of the form

$$y = ax + b,$$

which is a line with a slope of a. The polynomial of the form

$$y = \sum_{i=1}^{n} a_i x^i + b$$

is considered for the non-linear curve fitting, where n is the degree of the polynomial and should be smaller than the number of data points. Several methods are used to evaluate the approximations required for curve fitting. One of the most used methods is the least square method. The polynomial coefficients can currently be calculated using a number of software programmes, such as Matlab, Mathematica, Gnuplot, etc., to give us the best-fit curve.

1.13.2 Sensitivity analysis

Sensitivity analysis (SA) is a technique for quantifying uncertainties in complex mathematical models. SA mainly helps to find the critical inputs, including the model parameters and the initial conditions and helps quantify the impact of input uncertainty on the model outcome(s). A limited number of parameters usually govern the output behaviour of high-dimensional systems, and SA provides a mechanism for identifying these parameters. SA can be applied locally and globally. The first strategy is the simplest and requires changing each parameter separately while keeping the others constant. The drawback of this approach is that it cannot analyse the impact of all parameters simultaneously. These techniques are useful when there is little to no uncertainty in the model inputs or when there are few interactions between the inputs [112]. Global sensitivity analysis (GSA) techniques capture the variations in model outputs when input parameters are allowed to change simultaneously within predetermined ranges [113]. Despite being computationally demanding, these techniques offer more information than the local SA. Partial rank correlation coefficient (PRCC) is a frequently used GSA technique.

1.13.3 Latin Hypercube Sampling (LHS)

Latin hypercube sampling (LHS) is a sampling method introduced by McKay *et al.* [114] and belongs to the Monte Carlo class of sampling methods. This method has the advantage of using fewer samples than simple random sampling to attain the same accuracy while still allowing an unbiased estimate of the average model output [114]. This approach samples N equal probability intervals that have been partitioned into N random parameter distributions, where N is the sample size. The value of this number N should be more than or equal to $k+1$, where k is the number of varied parameters, and bigger values of N should be used to assure accuracy [114, 115]. For a wide range of variation for a parameter to avoid under-sampling at the outer ranges of the interval where the parameter assumes very small values, the sampling might be calculated on a log scale.

1.13.4 Partial Rank Correlation Coefficient (PRCC)

In statistics, correlation is a statistical method used to assess how closely a model's input and output measurements are related. Partial correlation describes the linear relationship between the LHS parameters and the outcome measure using the residuals acquired from the regression technique after discounting the linear effects of the LHS parameters (inputs) x_j on the outcome measure (outputs) y [113]. As long as there is little to no correlation between the inputs, PRCC is a reliable sensitivity measure for non-linear but monotonic relationships between x_j and y. [113]. A correlation coefficient (CC) between x_j and y is calculated as follows:

$$r_{x_j y} = \frac{Cov(x_j, y)}{\sqrt{Var(x_j), Var(y)}} = \frac{\sum_{i=1}^{N}(x_{ij} - \bar{x})(y_i - \bar{y})}{\sqrt{\sum_{i=1}^{N}(x_{ij} - \bar{x})^2 \sum_{i=1}^{N}(y_i - \bar{y})^2}}, j = 1, 2, ...k,$$

which varies between -1 and +1 [113]. In the above expression, $Cov(x_j, y)$ is the covariance between x_j and y, $Var(x_j)$ and $Var(y)$ are, respectively the variance of x_j and y with $\bar{x}$ and $\bar{y}$ as the respective sample means and N is the sample size. We may evaluate the model's sensitivity to parameter variation using the combination of uncertainty analysis and PRCC [113].

1.14 Overview

Therapeutic strategies that target key molecules have yet to fulfil expected promises for most common malignancies. Major difficulties include the incomplete understanding and validation of these targets in patients due to single-pathway targeted approaches. A departure from the traditional paradigm of studying a single pathway to a more global approach will help to overcome the shortcomings of the existing therapeutic strategies. Recent research has emerged with substantial progress in systems biology with emerging high throughput techniques for detecting protein-protein interactions. This vast data leads to the emergence of network modelling to understand the mechanisms underlying a biological process. These networks are composed of smaller functional subunits known as network motifs of defined topology. The networks become more complex in the presence of inherent noise that might arise because of a low copy number of mRNA molecules, slight differences in protein turnover rates etc. Due to the complexity of the networks, it becomes necessary to develop new mathematical models and tools. As biological systems are inherently noisy, there is a trade-off between network sensitivity and robustness influenced by the motif organization. The system has to be robust enough for the proper execution of its cellular activities. It also needs to be sensitive to variations in input stimuli leading to changes in gene expression and cellular activities. This thesis focused on developing analytical formulas using mathematical models (consisting of ordinary and stochastic differential equations) to dissect the network and understand the importance of motif structure in determining the cellular function in the presence of noise and their distribution in a signalling network. Mathematical tools helped us quantitatively measure the sensitivity of a motif in the signalling network under noise and allowed us to capture sensitive nodes in that network. Eventually, that knowledge was used to identify potential drug targets. Complex qualitative behaviours of the non-linear interactions between the cell signalling systems were used to understand complicated disease mechanisms. The effect of inherent stochasticity was also evaluated in these studies. The whole thesis is divided into seven chapters. The first chapter covers the background and importance of the thesis. The middle chapters elaborate on the mathematical tools and techniques developed in the study. The thesis ends with the conclusions from the study and possible future possibilities.

In Chapter 2, we considered two frequently observed two-node motif structures. These motifs consisted of two nodes, the input node, which receives the signal and affects the other node, the output node. Both structures are based on negative feedback, where the negative effect is supplemented with positive autoregulation. Bistability was observed for arbitrary parameter sets for both motifs. Depending upon the initial conditions, the outcome can take any of the two steady-state values. We analysed the signal-noise relation for both of them. We observed that the output signal range depends on the structure, but the parameter's sensitivity is independent of the structure. In both structures, the downstream node is more sensitive to the outcome of the output signal. We also observed that under random perturbation with high noise intensity, the system loses its stability, and the bistable points are scattered, leading to an unwanted output signal. Further, we found that bistability may be disrupted due to the introduction of randomness to the bistable system. This chapter describes a pilot study focusing on only two specific structures, but it shows the importance of the structure and the noise in the signalling mechanism. So, to study the emergence of bistability and the effect of randomness on the motif structures, a detailed analysis was done containing all possible two-node motifs in the consequent chapters.

A system-level understanding of the molecules involved in disease and their complex interactions are necessary to create effective treatment techniques. Understanding the relationship between noise and network motifs has been a point of contention for many years. It is widely recognised that noise can change the central regulatory processes of cellular processes. All the existing network-based methods to identify regulatory points are mainly data-dependent or based on centrality and differentia. Targeting these central positions helps to disintegrate the network. However, identifying the targets using the disintegration methods leads to serious side effects. So, Chapter 3 presents a study that introduced a methodology independent of data and network structure that could be used to identify potential drug targets. This chapter aims to apply the dependency of the I/O relation on motif structure in designing a quantitative scoring formula that will help to identify critical nodes in a PPI network. Here we tried to understand the importance of motif structures in determining cellular function in the presence of noise. To capture the noise tolerance of network motifs, we developed a stochastic differential equation

(SDE) based mathematical model for different two-node motif structures. We studied the association between motif structure and input-noise relation. The vulnerability of a node to noise could be a significant factor in causing signalling error and need to be controlled. We classified and ranked these motifs according to their sensitivity toward noise and signal. The ranks of the motifs were used to develop a tool that identifies sensitive nodes in a network, which we hypothesised as potential targets. The significance of the tool was validated through cancer networks and drug bank databases.

The association between the motif structures in the existence of bistability in a signalling network using theoretical models is captured in Chapter 4. Bistability is a crucial characteristic of dynamical systems applied in various all-or-nothing decision-making processes. It is a phenomenon where two distinct stable steady states coexist in a given set of experimental conditions. An essential factor in the I/O relationship is the presence of bistability in a signalling network. Here, we have examined the circumstances in which bistability occurs using a theoretical model. We investigated the relationship between network motifs and the occurrence of bistability in a signalling network. With a focus on bistability, we looked at how the choice of motif structure affects the I/O relationship between two nodes. We systematically explored parameter space for several two-node motifs to understand their role in preserving bistability. We also studied bistable switching through hysteresis. The findings were used to identify potential drug targets and validate them with the existing data. It is also well known that the signalling network contains noise inherently. Stochastic differential equations were used to study the system to probe the issue of maintenance of bistability.

In Chapter 5, we tried to capture the disease mechanism of autoimmunity using bistability in TNFR2 signalling. T-regulatory cells (Tregs) regulate the body's immune responses to maintain homeostasis and self-tolerance and are crucial for preventing illnesses like cancer and autoimmunity. However, different autoimmune disorders show varied patterns of Treg frequency. Defects in TNFR2 signalling also characterise numerous autoimmune diseases. We investigated the TNFR2 signalling pathway in Treg cells due to the prevalence of TNFR2 signalling defects and the variety of patterns associated with Treg frequency seen in autoimmune disorders. TNF-mediated apoptosis is a complex and precisely regulated cellular process in-

duced by activating both pro- and anti-apoptotic signalling pathways. So, to facilitate targeted disease treatment, we want to understand the mechanism driving Treg cell survival and death. An ordinary differential equation (ODE) based model was constructed and analysed to capture the process of cell survival and death in Treg cells via TNFR2 signalling. The system exhibits bistability and strives to adapt to changing stimuli through hysteretic switching. We compute bifurcation diagrams and construct cell fate maps to examine how stimulus and feedback strength affect cell survival and death. The study revealed that increased JNK phosphorylation and raised TNF levels are the key factors that lead to Treg mortality. The system was then examined under stochastic perturbation to determine the effect of inherent noise on the system's dynamics. Bistability was disrupted by noise which reduced the system's bistable zone, and thus noise may impact the system's normal functioning.

The calcium oscillations are studied in Chapter 6 to understand the complex aetiology of diabetic cardiomyopathy (DCM). One of the factors contributing to the contractile dysfunction associated with DCM is defective excitation-contraction coupling (ECC). The primary cause of this ECC is the dysregulation of calcium (Ca^{2+}) oscillations in cardiomyocytes due to prolonged elevated blood glucose levels. For the normal functioning of the heart, cytosolic calcium ($[Ca^{2+}]_c$) of cardiomyocytes should oscillate in the physiological range (PO) (frequency: 40 to 180 bpm (beats per minute) & amplitude: $\geq 0.4\ \mu M$) and avoid NPO (non-physiological oscillations) & stability. This $[Ca^{2+}]_c$ oscillation is driven by the exchange of calcium ions (Ca^{2+}) between the extracellular region, cytoplasm and sarcoplasmic reticulum (SR), which is accomplished through a variety of ionic channels and pumps implanted in the extracellular membrane and the SR. Variations in free cytosolic calcium impact cardiac functioning. Glucose concentration in cardiac cells is vital in altering calcium oscillations in DCM. To gain insight into the complexities of metabolic insulin signalling pathways in cardiac cells, we develop a mathematical model in the current study that explicitly represents many of the known signalling elements mediating translocation of the insulin-responsive glucose transporter type 4 (GLUT4). We explored the conditions at which the system moves from a stable state to an oscillatory state. Here, we were interested in observing the impact of GLUT4's random translocation on calcium oscillation. We captured the calcium oscillations in PO and NPO circumstances through

mathematical modelling. System parameters were perturbed to induce insulin resistance (IR) in cardiomyocytes to mimic diabetic conditions. We suggested various potential restoration procedures to restore the PO of $[Ca^{2+}]_c$. When we added randomization to the system, we noticed an early bifurcation. The randomness facilitates the restoration mechanisms.

Finally, the thesis concludes in Chapter 7 by summarising the research done in this study. It also covers the contribution of the research to the field of identification of regulatory points and potential future opportunities.

2

Unravelling the sensitivity of two frequently observed motif structures under random perturbations[1]

2.1 Introduction

Cell signalling network is built from frequently occurring patterns, called network motifs [116, 117]. These network motifs embedded in the network define the dynamical properties of signalling networks [118–120]. The regulatory characteristics of a network are described by an analysis of the network using motifs formed from its components and modules. These

[1]The bulk of this chapter has been published in *Trends in Biomathematics: Modeling, Optimization and Computational Problems*, 2018, pp.245-263.

network motifs play an essential role in the propagation of signals in a network. Different motif structures are identified to date, collectively constituting the building blocks of biological networks [121–123]. A very frequently observed motif is the feedback loop. The negative feedback loop can give rise to adaptation and desensitization, while the positive feedback loop can lead to emergent network properties such as ultrasensitivity and bistability [12–14]. The pattern of motif organization defines the information processing capabilities of the signalling network, influencing the specificity and plasticity of input-output (I/O) relationships [56, 121]. The motif organization can affect the sensitivity, robustness, and trade-off between the I/O relation in a signalling network [56, 121].

Numerous studies demonstrated that multiple outputs produced at the level of changes in gene expression and cellular activities [8, 34–39]. These are clear evidence of the sensitivity of the intracellular signalling systems to input stimuli variations, which may be induced through extracellular noise or intracellular stochastic perturbations of the intracellular components (e.g. mutations, alterations in protein turn-over rates etc.). However, the system has its safeguards for these inappropriate and non-specific responses, which still need further investigation. Ghosh et al. [96] were amongst the first to study the noise characteristics of the motif with feed-forward loops. Guantes et al. [124] considered a simple detection process (a signal acting on a two-component module in a genetic circuit) to analyse how the performance of these circuits is affected by molecular noise. They showed that the presence of a feedback interaction in the motif imposes a trade-off on amplitude and frequency detection, whose intensity depends on feedback strength. Molecular noise restricts the ability of an individual cell to resolve input signals of different strengths and gather information about the external environment [125]. Jesan et al. [126] demonstrated long-range communication through retrograde propagation between branches of signalling pathways whose molecules do not directly interact. Despite such studies on motifs, more work is needed on motif structures in deciding the I/O signal relation, especially in the presence of noise.

The present study aims to capture the I/O relation in the structure and how they are influenced by parameter variation, especially under random perturbation. To probe the issue of maintenance of response-specificity, we selected a condition wherein cells were subjected

to varying levels of stochastic perturbations and evaluated the consequent steady-state value, rather than the kinetic features, of the output attained [34, 56, 118, 127]. The change in steady-state levels has been shown to govern the outcome in complex biological processes such as adaptability, immune memory, development, and cell differentiation [13, 56, 57]. So, in an extensive signalling network, we seek steady state I/O relation in the presence of random perturbation to capture the cell mechanism that prevents any damage due to inappropriate signalling. The I/O relation becomes more important when a structure shows bistability (simultaneous existence of two stable equilibrium points) as they play a vital role in cell signalling and functioning. Depending on the initial value of nodes, the output signal can attain any of the two bistable values for the identical parameter set value. It is key for understanding basic phenomena of cellular functioning, such as decision-making processes in cell cycle progression, cellular differentiation [128] and apoptosis [129]. It also plays an important role in diseases like cancer and prion disease [85]. In cancer, bistability is mainly involved in the loss of cellular homeostasis associated with the beginning of the disease. A positive feedback loop with an ultrasensitive regulatory step can generate bistability. The positive feedback loop is an essential regulatory motif in cellular signal transduction [130]. It is known that positive feedback is necessary for the existence of bistability [131]. In the case of negative feedback, the inactivation can be supplemented with a positive term defining a positive feedback (self) loop [132].

In this chapter, we have considered two frequently observed two-node motif structures (see Fig. 2.1). Schematic diagrams of two-node motifs are given in Fig. (2.1), where node A receives the input signal, which then influences the output of node B. Both structures consist of negative feedback loops. In structure 1, node A is activating node B, and node B is inhibiting node A, while in structure 2, it is the opposite. The difference between the first and second structures is in the self-activation and inhibition for node A and node B. In structure 1, node A is a self-activator and node B is a self-inhibitor, while in structure 2, it is the opposite. These motifs consist of negative feedback loops, and the inhibition of a node by the other node is supplemented by the positive feedback (self) loop, thus satisfying the necessary conditions for the existence of bistability. We have analysed these two motifs for the emergence of bistability and examined the signal-noise relation between them. Here, k_A and k_B are the self-regulating

rate constants for node A and node B, respectively. Parameters k_1 and k_2 are regulatory constants of node A on B and node B on A, respectively. The input signal I affects input node A (representing protein A) at a rate k_I. So, the input signal is ultimately the steady state of node A, denoted by A^*. Finally output signal is the steady state of node B (representing protein B) denoted by B^*.

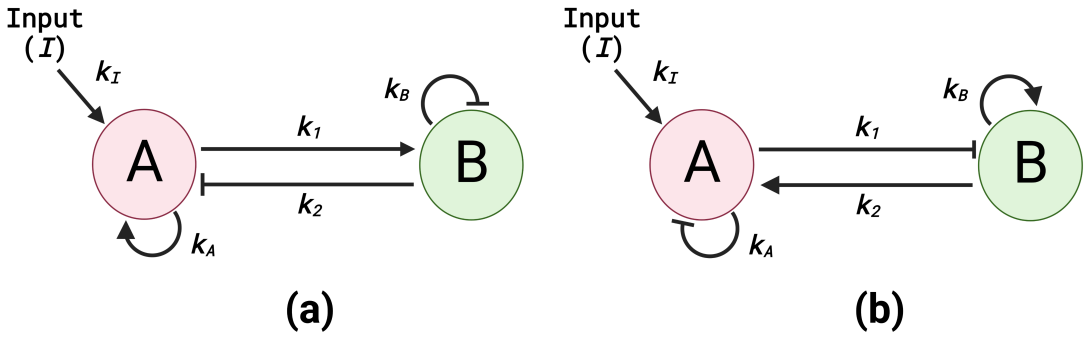

Figure 2.1: **Schematic diagram of two frequently observed two-node motifs.** Fig. (a) depicts structure 1, and Fig. (b) depicts structure 2. Here, node A is the input node, and node B is the output node. The arrows represent activation, while the hammerhead arrows represent inhibition.

2.2 Construction of the deterministic models

An ordinary differential equation (ODE) model is constructed based on the pathway map shown in Fig. 2.1. The first model (for structure 1) consists of coupled-differential equations. The nodes represent the proteins present in a cell. Equations of the model describe the rates of loss and creation of particular labelled forms of proteins (nodes) in the system. Our model is based on ODEs and consists of the activated form of node A (denoted by A) and node B (denoted by B), where node A receives the input signal that affects the output node B and the output of the system is defined by the steady state values achieved by the output node (i.e. node B). Biologically, the total concentration of protein (active and inactive forms) within the system is constant and, for simplicity, assumed to be one as taken in previous models [56]. Thus, the concentrations of the inactivated portions of protein A and B can be given by $(1-A)$ and $(1-B)$, respectively. The rates of loss and creation of node A and B are modelled following the Michaelis-Menten form of kinetics as described in literature [56]. We considered I as the input to node A, which activates the inactive form of node A at a rate k_I. The inactive form of

A lies in the portion $(1-A)$. So the change in the concentration of A due to the input signal I is represented by the enzymatic reaction $\frac{k_I I(1-A)}{k_{mI}+(1-A)}$ following the Michaelis-Menten form. Here k_{mI} is the corresponding half-saturation constant. The self activation of protein A is given by the term $\frac{k_A A(1-A)}{k_{mA}+(1-A)}$, where k_A is the self-activation rate of A and k_{mA} is the half-saturation constant. The last term of the first equation $\frac{k_2 BA}{k_{m2}+A}$ represents the inhibition of protein A due to protein B, where k_2 is the inhibition rate and k_{m2} is the corresponding half-saturation constant. Following similar logic for the second equation, we have added $\frac{k_1 A(1-B)}{k_{m1}+(1-B)}$ to the equation of B when A activates protein B with the rate k_1 and deducted the amount $\frac{k_B B^2}{k_{mB}+B}$ with rate k_B from the equation of B, when B inhibits itself. Here, k_{m1} and k_{mB} are the corresponding half-saturation constants. Based on these assumptions, the proposed model is written as follows:

$$\begin{aligned} \frac{dA}{dt} &= \frac{k_I I(1-A)}{k_{mI}+(1-A)} + \frac{k_A A(1-A)}{k_{mA}+(1-A)} - \frac{k_2 BA}{k_{m2}+A}, \\ \frac{dB}{dt} &= \frac{k_1 A(1-B)}{k_{m1}+(1-B)} - \frac{k_B B^2}{k_{mB}+B}. \end{aligned} \tag{2.1}$$

By similar assumptions as of structure 1 (with the same parameters), an ordinary differential equation model is constructed for structure 2, which is as follows:

$$\begin{aligned} \frac{dA}{dt} &= \frac{k_I I(1-A)}{k_{mI}+(1-A)} + \frac{k_2 B(1-A)}{k_{m2}+(1-A)} - \frac{k_A A^2}{k_{mA}+A}, \\ \frac{dB}{dt} &= \frac{k_B B(1-B)}{k_{mB}+(1-B)} - \frac{k_1 AB}{k_{m1}+B}. \end{aligned} \tag{2.2}$$

2.2.1 Analytical results

2.2.1.1 Positive invariance and boundedness

Let us put the system of Eq. (2.1) in a vector form by setting $X = \begin{bmatrix} A \\ B \end{bmatrix} \in \mathrm{R}^2$.

$$F(X) = \begin{bmatrix} F_1(X) \\ F_2(X) \end{bmatrix} = \begin{bmatrix} \frac{k_I I(1-A)}{k_{mI}+(1-A)} + \frac{k_A A(1-A)}{k_{mA}+(1-A)} - \frac{k_2 BA}{k_{m2}+A} \\ \\ \frac{k_1 A(1-B)}{k_{m1}+(1-B)} - \frac{k_B B^2}{k_{mB}+B} \end{bmatrix}, \tag{2.3}$$

where $F : C_+ \to \mathrm{R}^2$. Then Eq. (2.1) becomes

$$\dot{X} = F(X), \tag{2.4}$$

with $X(0) = X_0 \in {\mathrm{R}_+}^2$. It is easy to check in Eq. (2.3) that whenever choosing $X(0) \in {\mathrm{R}_+}^2$ such that $X_i = 0$, then $F_i(X)|_{X_i=0} \geq 0$, (i=1,2). Due to lemma [133], any solution of Eq. (2.4) with $X(0) \in {\mathrm{R}_+}^2$, say $X(t) = X(t;X_0)$, is such that $X(t) \in {\mathrm{R}_+}^2$ for all $t > 0$.

Since the total concentration of protein/node within the system is constant and equal to 1, the maximum value that A, B can take is 1. Hence by model assumption, both are bounded.

Similarly, for structure 2, again setting $X = \begin{bmatrix} A \\ B \end{bmatrix} \in \mathrm{R}^2$ and

$$\widehat{F}(X) = \begin{bmatrix} \widehat{F}_1(X) \\ \widehat{F}_2(X) \end{bmatrix} = \begin{bmatrix} \frac{k_I I(1-A)}{k_{mI}+(1-A)} + \frac{k_2 B(1-A)}{k_{m2}+(1-A)} - \frac{k_A A^2}{k_{mA}+A} \\ \\ \frac{k_B B(1-B)}{k_{mB}+(1-B)} - \frac{k_1 AB}{k_{m1}+B} \end{bmatrix}. \tag{2.5}$$

By similar arguments as in the case of structure 1, we can prove the positive invariance and boundedness of structure 2.

2.2.1.2 Equilibrium points of the system (2.1) and their stability properties

Here we are interested in studying the I/O relation, so we look for only the interior equilibrium point. The interior equilibrium point is denoted by $E^* \equiv (A^*, B^*)$, where

$$A^* = \frac{k_B B^{*2}\left[k_{m1} + (1 - B^*)\right]}{k_1(k_{mB} + B^*)(1 - B^*)} \tag{2.6}$$

and B^* satisfies the equation

$$\begin{aligned}
&\frac{k_I I\left(1 - \left(\frac{k_B B^{*2}[k_{m1}+(1-B^*)]}{k_1(k_{mB}+B^*)(1-B^*)}\right)\right)}{k_{mI} + \left(1 - \left(\frac{k_B B^{*2}[k_{m1}+(1-B^*)]}{k_1(k_{mB}+B^*)(1-B^*)}\right)\right)} - \frac{k_2 B^*\left(\frac{k_B B^{*2}[k_{m1}+(1-B^*)]}{k_1(k_{mB}+B^*)(1-B^*)}\right)}{k_{m2} + \left(\frac{k_B B^{*2}[k_{m1}+(1-B^*)]}{k_1(k_{mB}+B^*)(1-B^*)}\right)} \\
&+ \frac{k_A\left(\frac{k_B B^{*2}[k_{m1}+(1-B^*)]}{k_1(k_{mB}+B^*)(1-B^*)}\right)\left(1 - \left(\frac{k_B B^{*2}[k_{m1}+(1-B^*)]}{k_1(k_{mB}+B^*)(1-B^*)}\right)\right)}{k_{mA} + \left(1 - \left(\frac{k_B B^{*2}[k_{m1}+(1-B^*)]}{k_1(k_{mB}+B^*)(1-B^*)}\right)\right)} = 0\,.
\end{aligned} \tag{2.7}$$

The corresponding Jacobian matrix (J) evaluated at $E^* = (A^*, B^*)$ is denoted by $J(A^*, B^*)$ and given by

$$J(A^*, B^*) = \begin{bmatrix} a_{11} & -a_{12} \\ a_{21} & a_{22} \end{bmatrix} \tag{2.8}$$

with

$$\begin{aligned}
a_{11} &= \frac{k_A(1 - A^*)}{k_{mA} + (1 - A^*)} - \frac{k_I k_{mI} I}{(k_{mI} + (1 - A^*))^2} - \frac{k_A k_{mA} A^*}{(k_{mA} + (1 - A^*))^2} - \frac{k_2 k_{m2} B^*}{(k_{m2} + A^*)^2}\,, \\
a_{12} &= \frac{k_2 A^*}{k_{m2} + A^*}\,, \\
a_{21} &= \frac{k_1(1 - B^*)}{k_{m1} + (1 - B^*)}\,, \\
a_{22} &= -\frac{k_1 k_{m1} A^*}{(k_{m1} + (1 - B^*))^2} - \frac{k_B B^*(2k_{mB} + B^*)}{(k_{mB} + B^*)^2}\,.
\end{aligned}$$

The characteristic equation is given by

$$\lambda^2 - \text{trace}(J)\lambda + \text{determinant}(J) = 0\,. \tag{2.9}$$

The interior equilibrium point is stable if

$$\begin{aligned} \text{trace}(J) &< 0 \\ \text{determinant}(J) &> 0. \end{aligned} \tag{2.10}$$

So, the interior equilibrium point is stable if

$$a_{11} + a_{22} < 0\,, \tag{2.11}$$

$$a_{11}a_{22} + a_{12}a_{21} > 0\,. \tag{2.12}$$

2.2.1.3 Equilibrium points of the system (2.2) and their stability properties

The system (2.2) has an axial equilibrium point $\widehat{E} \equiv (\widehat{A}, 0)$,where $\widehat{A}$ satisfies the following equation

$$k_A\widehat{A}^3 - \{k_I I + k_A(k_{mI}+1)\}\widehat{A}^2 + (1-k_{mA})k_I I\widehat{A} + k_I I k_{mA} = 0\,. \tag{2.13}$$

It has also an interior equilibrium $E^* \equiv (A^*, B^*)$, where

$$A^* = \frac{k_B B^*(1-B^*)(k_{m1}+B^*)}{[k_{mB}+(1-B^*)]k_1 B^*} \tag{2.14}$$

and B^* satisfies the equation

$$\begin{aligned} &\frac{k_I I\left(1-\left(\frac{k_B B^*(1-B^*)(k_{m1}+B^*)}{[k_{mB}+(1-B^*)]k_1 B^*}\right)\right)}{k_{mI}+\left(1-\left(\frac{k_B B^*(1-B^*)(k_{m1}+B^*)}{[k_{mB}+(1-B^*)]k_1 B^*}\right)\right)} + \frac{k_2 B^*\left(1-\left(\frac{k_B B^*(1-B^*)(k_{m1}+B^*)}{[k_{mB}+(1-B^*)]k_1 B^*}\right)\right)}{k_{m2}+\left(1-\left(\frac{k_B B^*(1-B^*)(k_{m1}+B^*)}{[k_{mB}+(1-B^*)]k_1 B^*}\right)\right)} \\ &-\frac{k_A\left(\frac{k_B B^*(1-B^*)(k_{m1}+B^*)}{[k_{mB}+(1-B^*)]k_1 B^*}\right)^2}{k_{mA}+\left(\frac{k_B B^*(1-B^*)(k_{m1}+B^*)}{[k_{mB}+(1-B^*)]k_1 B^*}\right)} = 0 \end{aligned} \tag{2.15}$$

Following the Jacobian matrix and stability definition (as given in (2.9) and (2.10)), the interior equilibrium point is stable if

$$b_{11} + b_{22} < 0 \tag{2.16}$$

$$b_{11}b_{22} + b_{12}b_{21} > 0 \tag{2.17}$$

where

$$\begin{aligned}
b_{11} &= -\frac{k_I k_{mI} I}{[k_{mI} + (1-A^*)]^2} - \frac{k_2 k_{m2} B^*}{[k_{m2} + (1-A^*)]^2} - \frac{k_A A^* (2k_{mA} + A^*)}{(k_{mA} + A^*)^2} \\
b_{12} &= \frac{k_2 (1-A^*)}{k_{m2} + (1-A^*)} \\
b_{21} &= \frac{k_1 B^*}{k_{m1} + B^*} \\
b_{22} &= \frac{k_B (1-B^*)}{k_{mB} + (1-B^*)} - \frac{k_B k_{mB} B^*}{[k_{mB} + (1-B^*)]^2} - \frac{k_1 k_{m1} A^*}{(k_{m1} + B^*)^2}
\end{aligned}$$

2.2.2 Simulation results

2.2.2.1 Numerical analysis for the system (2.1)

We solved the system of differential equations (2.1) analytically in MATLAB with parameter values as in Table 2.1 and obtained two stable steady states $E_1 = (0.2728, 0.4443)$ and $E_2 = (0.7187, 0.6855)$. Thus bistability is observed in the system. To verify the observed bistability numerically, we plotted the phase portrait of the system for the same parameter set with different initial conditions. We observed that all the trajectories converged towards either of $E_1 = (0.2728, 0.4443)$ or $E_2 = (0.7187, 0.6855)$, see Figure 2.2. We then varied each parameter ten folds up and down from their base value (given in Table 2.1). The range of each parameter for which bi- or mono-stability was observed has been plotted in Figure 2.3. Bistability was observed around the base value, and mono stability was observed as we moved away from the base value.

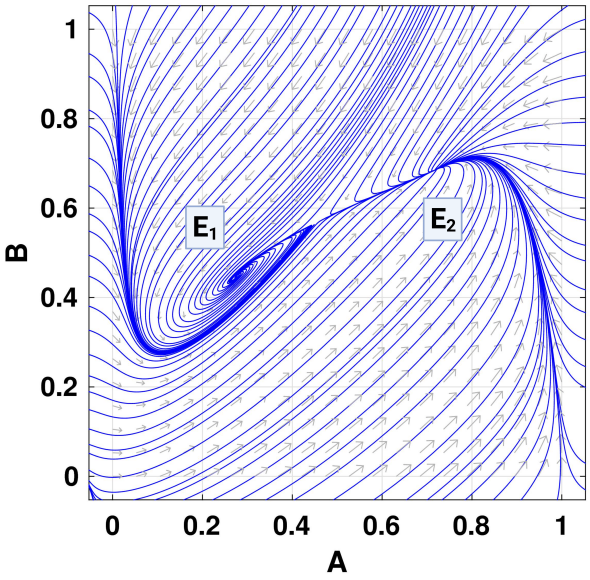

Figure 2.2: **Bistability in structure 1.** Phase portrait showing bistability of the system (2.1). Parameters are as in Table 2.1. Here E_1 and E_2 denote two stable equilibrium points.

Table 2.1: Parameters description and the initial values for structure 1.

Parameters	**Description**	**Default values**
I	Initial input	0.097
k_I	Activation rate of I on node A	1
k_1	Activation rate of node A on node B	1
k_2	Deactivation rate of node B on node A	1
k_A	Self activation rate of node A	1
k_B	Self deactivation rate of node B	1
k_{mI}	Half saturation constant respect to k_I	0.1
k_{m1}	Half saturation constant respect to k_1	0.4
k_{m2}	Half saturation constant respect to k_2	0.1
k_{mA}	Half saturation constant respect to k_A	0.1
k_{mB}	Half saturation constant respect to k_B	0.8

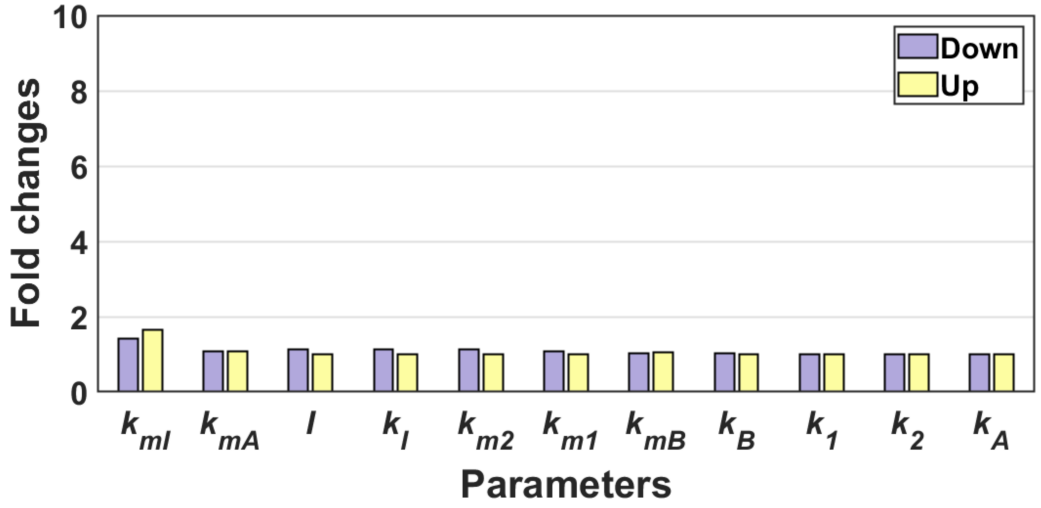

Figure 2.3: **Robustness analysis for structure 1.** The figure shows the robustness of the parameters towards the maintenance of bistability. Each bar in this diagram indicates a parameter range in fold change from its basal values where the system is bistable. Beyond this bistable range, the system is monostable or unstable. The basal values of the parameters are given in Table 2.1.

Global sensitivity analysis

The global sensitivity analysis (GSA) helps to identify model parameters that could be particularly important. We used the Partially Ranked Correlation Coefficients (PRCC) [115] technique for the GSA and their associated p-values to identify the most sensitive parameters. To calculate PRCCs, we used Latin Hypercube Sampling (LHS) method to randomly select vectors of parameter values used for each run of PRCCs calculations. Over 1,000 simulations were performed to calculate PRCCs. In each simulation, the system was solved up to hundred-time steps, as it was observed from the time series solutions that the system behaves uniformly much before the hundred-time steps. Figure 2.4 depicts the sensitivity of each parameter for the variable B. We used a cut-off of ± 0.4 to define the sensitive parameters, i.e. if the PRCC value of a particular parameter lies beyond ± 0.4, then that parameter will be called a sensitive parameter. The GSA analysis suggests that the most sensitive parameters in structure 1 are k_1, k_B, k_{m1} and k_{mB}. These parameters primarily affect the output signal of Node B and are associated with node B.

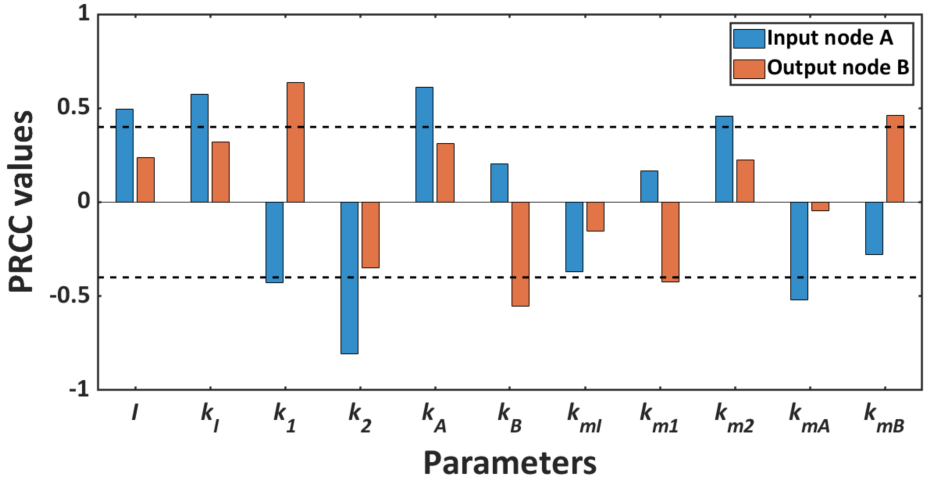

Figure 2.4: **Global sensitivity analysis for structure 1.** In this figure, corresponding to every parameter, two different colour bars represent two state variables (node A and B). And the sensitivity of each parameter is measured by the length of the bars.

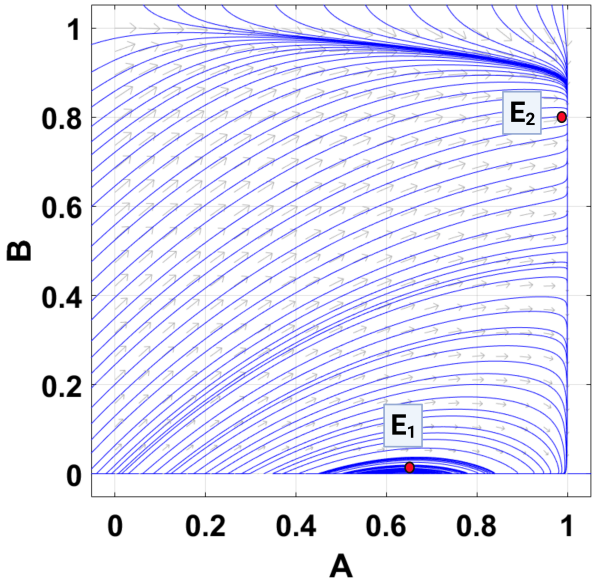

Figure 2.5: **Bistability in structure 2.** Phase portrait showing bistability of the system (2.2). Parameters as in Table 2.2. Here E_1 and E_2 denote two stable equilibrium points.

2.2.2.2 Numerical analysis for the system (2.2)

We solved the system of differential equations (2.2) analytically in MATLAB with parameter values as in Table 2.2 and obtained two stable steady states $E_1 = (0.6367, 0.0041)$ and $E_2 = (0.9998, 0.8001)$. Thus bistability is also observed in this system. To verify the observed bistability numerically, we plotted the phase portrait of the system for the same parameter set with different initial conditions. We observed that all the trajectories converged towards

either of $E_1 = (0.6367, 0.0041)$ or $E_2 = (0.9998, 0.8001)$, see Figure 2.5. We then varied each parameter ten folds up and down from their base value (given in Table 2.2), divided them into equal partitions, and calculated the number of stable equilibrium points. We observed that structure 2 shows bistability for a wider range compared to structure 1 (see Figure 2.6). In the case of structure 2, we also observed a region for the non-existence of a stable equilibrium point, which was not there in structure 1.

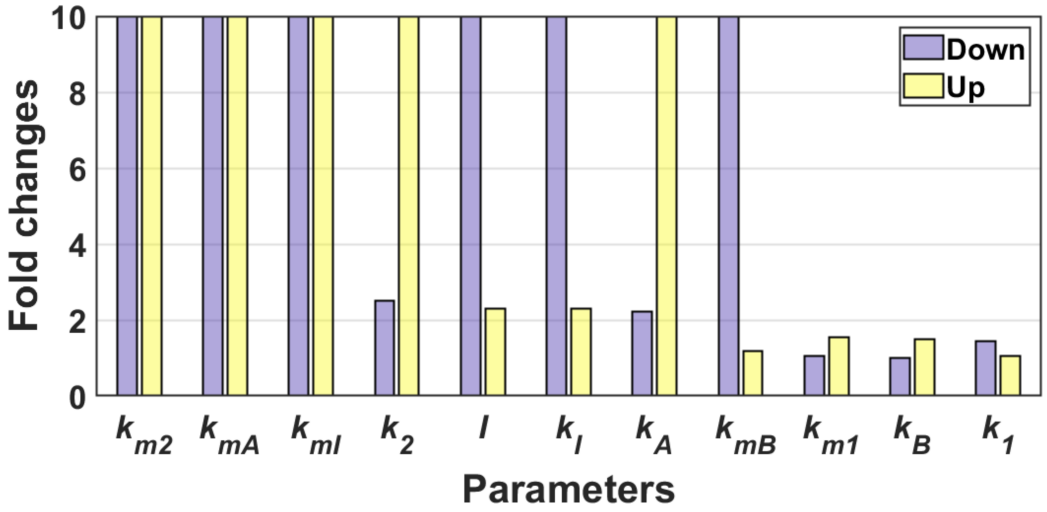

Figure 2.6: **Robustness analysis for structure 2.** The figure shows the robustness of the parameters towards the maintenance of bistability. Each bar in this diagram indicates a parameter range in fold change from its basal values where the system is bistable. Beyond this bistable range, the system is monostable or unstable. The basal values of the parameters are given in Table 2.2.

Table 2.2: Parameters description and the initial values for structure 2.

Parameters	**Description**	**Default values**
I	Initial input	0.3
k_I	Activation rate of I on node A	0.001
k_1	Deactivation rate of node A on node B	1
k_2	Activation rate of node B on node A	1
k_A	Self deactivation rate of node A	0.001
k_B	Self activation rate of node B	1
k_{mI}	Half saturation constant respect to k_I	0.1
k_{m1}	Half saturation constant respect to k_1	0.7
k_{m2}	Half saturation constant respect to k_2	0.1
k_{mA}	Half saturation constant respect to k_A	0.1
k_{mB}	Half saturation constant respect to k_B	0.1

Global sensitivity analysis

The global sensitivity analysis (GSA) of the system (2.2) was done using Partially Ranked Correlation Coefficients (PRCC) [115] technique similar to the system (2.1). Figure 2.7 depicts the sensitivity of each parameter for each variable. We used a cut-off of ± 0.4 to define the sensitive parameters, i.e., if the PRCC value of a particular parameter lies beyond ± 0.4, then that parameter will be called a sensitive parameter. The GSA analysis suggests that the most sensitive parameters in structure 2 are k_1, k_B, k_{m1} and k_{mB}. So, here also, most of the sensitive parameters affecting the output signal are of Node B.

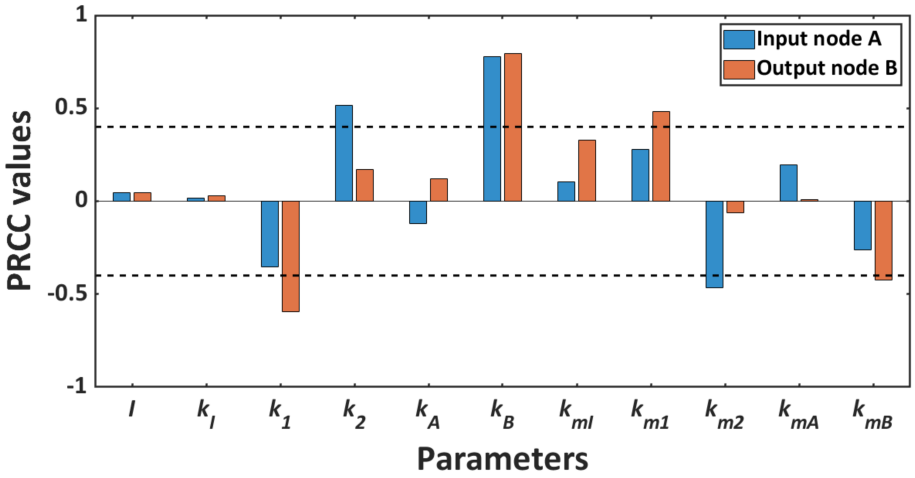

Figure 2.7: **Global sensitivity analysis for structure 2.** In this figure, corresponding to every parameter, two different colour bars represent two state variables (nodes A and B). And the sensitivity of each parameter is measured by the length of the bars.

2.3 Construction of the stochastic models

In previous sections, we observed that depending on the motif structure and the parameter value, the nature of the output signal may vary from mono-stability to bi-stability. Next, we want to see how these rich dynamics behave under random perturbation, which will help us to understand the I/O relationship for the two motifs in the presence of noise. These random perturbations may arise through mutations and alterations in turnover rates. Random perturbation may also appear due to improper network signalling. To explore this, we incorporated a dispersed stochastic perturbation in our model that could influence any of the components of the motif independent of the signal input. The use of dispersed perturbation was justified by the existence of numerous intrinsic and extrinsic factors, including cytokines, growth factors, nutrients, environmental stresses, protein stability modulation, and many others, that may potentially affect any of the signalling components through a wide variety of mechanisms [37, 135, 136]. The cumulative effects of such perturbations would exert a heterogeneous influence on the basal state of the signalling network. We considered such random influences as systemic perturbations and incorporated these effects into the model as multiplicative Gaussian white noise [36, 130]. Thus we introduce the stochastic perturbation terms into the equations of nodes A and B. The stochastic perturbations of the state variables around their steady-state

values E^* are Gaussian white noise proportional to the distances of A, B from their steady-state values A^*, B^* respectively. So, the deterministic model system (2.1) results in the following stochastic model system

$$\begin{aligned} dA &= F_1(A,B)dt + \sigma_1(A-A^*)d\xi_t^1 \,, \\ dB &= F_2(A,B)dt + \sigma_2(B-B^*)d\xi_t^2 \,. \end{aligned} \tag{2.18}$$

where σ_1 and σ_2 are real constants and known as the intensity of the fluctuations, $\xi_t^i = \xi_i(t)$, $i = 1,2$ are standard Wiener processes, independent of each other, and F_1, F_2 are defined in the Eq. (2.3). We consider Eq. (2.18) as an Ito stochastic differential system of the type

$$dX_t = F(t,X_t)dt + G(t,X_t)d\xi_t \tag{2.19}$$

where the solution (X_t,$t > 0$) is an Ito process, 'F' is the drift coefficient, 'G' is the diffusion coefficient, and ξ_t is a two-dimensional stochastic process having scaler Wiener process components with increments $\triangle\xi_t^j = \xi_j(t+\triangle t) - \xi_j(t)$ are independent Gaussian random variables $\mathrm{N}(0, \triangle t)$. In the case of system (2.18),

$$X_t = \begin{bmatrix} A \\ B \end{bmatrix}, \xi_t = \begin{bmatrix} \xi_t^1 \\ \xi_t^2 \end{bmatrix}, \tag{2.20}$$

$$F = \begin{bmatrix} F_1(A,B) \\ F_2(A,B) \end{bmatrix}, G = \begin{bmatrix} \sigma_1(A-A^*) & 0 \\ 0 & \sigma_2(B-B^*) \end{bmatrix} \tag{2.21}$$

Since the diffusion matrix 'G' depends upon the solution of X_t, the system (2.18) is said to have multiplicative noise.

Following above, the deterministic model system (2.2) results in the following stochastic

model system

$$dA = \widehat{F}_1(A,B)dt + \sigma_1(A-A^*)d\xi_t^1 \ ,$$
$$dB = \widehat{F}_2(A,B)dt + \sigma_2(B-B^*)d\xi_t^2 \ . \tag{2.22}$$

where σ_1 and σ_2 are real constants and known as the intensity of the fluctuations, $\xi_t^i = \xi_i(t)$, $i = 1,2$ are standard Wiener processes, independent of each other, and $\widehat{F}_1$, $\widehat{F}_2$ are defined in Eq. (2.5). We consider Eq. (2.18) as an Ito stochastic differential system of the type

$$dX_t = \widehat{F}(t,X_t)dt + G(t,X_t)d\xi_t \tag{2.23}$$

with

$$X_t = \begin{bmatrix} A \\ B \end{bmatrix}, \xi_t = \begin{bmatrix} \xi_t^1 \\ \xi_t^2 \end{bmatrix}, \tag{2.24}$$

$$\widehat{F} = \begin{bmatrix} \widehat{F}_1(A,B) \\ \widehat{F}_2(A,B) \end{bmatrix}, G = \begin{bmatrix} \sigma_1(A-A^*) & 0 \\ 0 & \sigma_2(B-B^*) \end{bmatrix} \tag{2.25}$$

Since the diffusion matrix 'G' depends upon the solution of X_t, the system (2.22) is said to have multiplicative noise.

2.3.1 Stochastic stability of interior equilibrium

The stochastic differential system (2.18) can be centred at its positive equilibrium points $E^*(A^*, B^*)$ by introducing the variables $U_1 = A - A^*, U_2 = B - B^*$. It seems difficult to derive asymptotic stability in the mean square sense by the Lyapunov functions method working on the complete non-linear equation (2.18). For simplicity of mathematical calculations, we deal with the stochastic differential equation obtained by linearising the vector function 'F' in (2.21) about the positive equilibrium point E^*. The linearized version of (2.19) around E^* is given by

$$dU(t) = f(U(t))dt + G(U(t))d\xi(t) \ , \tag{2.26}$$

where

$$U(t) = \begin{bmatrix} U_1(t) \\ U_2(t) \end{bmatrix}, \tag{2.27}$$

$$f(U(t)) = \begin{bmatrix} -P_{11}U_1 - P_{12}U_2 \\ P_{21}U_1 - P_{22}U_2 \end{bmatrix}, \tag{2.28}$$

$$G(U(t)) = \begin{bmatrix} \sigma_1 U_1 & 0 \\ 0 & \sigma_2 U_2 \end{bmatrix} \tag{2.29}$$

with

$$\begin{aligned} P_{11} &= \frac{k_I k_{mI} I}{(k_{mI} + (1-A^*))^2} + \frac{k_2 k_{m2} B^*}{(k_{m2} + A^*)^2}, \\ &\quad + \frac{k_A k_{mA} A^* - k_A (1-A^*)(k_{mA} + (1-A^*))}{(k_{mA} + (1-A^*))^2} \end{aligned} \tag{2.30}$$

$$P_{12} = \frac{k_2 A^*}{k_{m2} + A^*}, \tag{2.31}$$

$$P_{13} = \frac{k_1 (1-B^*)}{k_{m1} + (1-B^*)}, \tag{2.32}$$

$$P_{14} = \frac{k_1 k_{m1} A^*}{(k_{m1} + (1-B^*))^2} + \frac{k_B B^* (2k_{mB} + B^*)}{(k_{mB} + B^*)^2} \tag{2.33}$$

Note that, in (2.26) the positive equilibrium E^* corresponds to the trivial solution $(U_1, U_2) = (0,0)$. Let Ω be the set defined by $\Omega = \left[(t \geqslant t_0) \times \mathrm{R}^2, t_0 \in \mathrm{R}^+\right]$. We define the following theorem [111]

Theorem 2.3.1. *Suppose there exist a differentiable function $V(U,t) \in \mathrm{C}^2(\Omega)$ satisfying the inequalities*

$$K_1 |U|^\alpha \leq V(U,t) \leq K_2 |U|^\alpha \tag{2.34}$$

$$LV(U,t) \leq -K_3 |U|^\alpha, \quad K_i > 0, \quad i = 1,2,3, \quad \alpha > 0\,. \tag{2.35}$$

Then the trivial solution of (2.26) is exponentially α stable for all time $t \geq 0$.

Note that, if in (2.34), (2.35), $\alpha = 2$, then the trivial solution of (2.26) is exponentially mean square stable. Furthermore, the trivial solution of (2.26) is globally asymptotically stable

in probability.

Here, following (2.26),

$$\begin{aligned} LV(t,U) = \frac{\partial V(t,U(t))}{\partial t} + f^T(U(t))\frac{\partial V(t,U)}{\partial U} \\ +\frac{1}{2}Tr\left[G^T(U(t))\frac{\partial^2 V(t,U)}{\partial U^2}G(U(t))\right] \end{aligned} \tag{2.36}$$

where

$$\frac{\partial V}{\partial U} = \begin{pmatrix} \frac{\partial V}{\partial U_1} & \frac{\partial V}{\partial U_2} \end{pmatrix}^T, \quad \frac{\partial^2 V(t,U)}{\partial U^2} = \left(\frac{\partial^2 V}{\partial U_j \partial U_i}\right)_{i,j=1,2}$$

and T means transposition.

We can prove the following theorem:

Theorem 2.3.2. *When the inequality*

$$\frac{k_I k_{mI} I}{(k_{mI}+(1-A^*))^2} + \frac{k_A k_{mA} A^*}{(k_{mA}+(1-A^*))^2} + \frac{k_2 k_{m2} B^*}{(k_{m2}+A^*)^2} > \frac{k_A(1-A^*)}{k_{mA}+(1-A^*)} \tag{2.37}$$

holds true then the zero solutions of the system (2.18) will be exponentially 2-stable if

$$\begin{aligned} {\sigma_1}^2 < 2\left[\frac{k_I k_{mI} I}{(k_{mI}+(1-A^*))^2} + \frac{k_A k_{mA} A^*}{(k_{mA}+(1-A^*))^2}\right] \\ +2\left[\frac{k_2 k_{m2} B^*}{(k_{m2}+A^*)^2} - \frac{k_A(1-A^*)}{k_{mA}+(1-A^*)}\right], \\ {\sigma_2}^2 < 2\left[\frac{k_1 k_{m1} A^*}{(k_{m1}+(1-B^*))^2} + \frac{k_B B^*(2k_{mB}+B^*)}{(k_{mB}+B^*)^2}\right]. \end{aligned}$$

with the positive constants ω_1 *and* ω_2*, where* $\omega_1 = \frac{k_{m2}+A^*}{k_2 A^*}$ *and* $\omega_2 = \frac{k_{m1}+(1-B^*)}{k_1(1-B^*)}$.

Proof. Let us consider the Lyapunov function

$$V(U(t)) = \frac{1}{2}\left[\omega_1 {U_1}^2 + \omega_2 {U_2}^2\right] \tag{2.38}$$

where ω_i are real positive constants to be chosen later. It is easy to check the inequalities in (2.34) are true for $\alpha = 2$.

Next, using (2.29) and (2.36),

$$LV(U(t)) = \left(-P_{11} + \frac{1}{2}{\sigma_1}^2\right)\omega_1 {U_1}^2 + \left(-P_{22} + \frac{1}{2}{\sigma_2}^2\right)\omega_2 {U_2}^2 + (P_{21}\omega_2 - P_{12}\omega_1)U_1U_2 \tag{2.39}$$

Assuming

$$\omega_1 = \frac{k_{m2} + A^*}{k_2 A^*},\ and\ \omega_2 = \frac{k_{m1} + (1 - B^*)}{k_1(1 - B^*)},$$

(2.39) becomes

$$\begin{aligned} LV(U(t)) &= \left(-P_{11} + \frac{1}{2}{\sigma_1}^2\right)\omega_1 {U_1}^2 + \left(-P_{22} + \frac{1}{2}{\sigma_2}^2\right)\omega_2 {U_2}^2 \\ &= -U^T QU \end{aligned} \tag{2.40}$$

where

$$Q = \begin{bmatrix} \left(P_{11} - \frac{1}{2}{\sigma_1}^2\right)\omega_1 & 0 \\ 0 & \left(P_{22} - \frac{1}{2}{\sigma_2}^2\right)\omega_2 \end{bmatrix}.$$

The relations (2.37) and (2.3.2) imply that Q is a real symmetric positive definite matrix and therefore all its eigenvalues $\lambda_i(Q)$, $i = 1,2$ are positive real numbers. Let $\lambda_m = min\{\lambda_i(Q),\ i = 1,2\},\ \lambda_m > 0$. From (2.40), we get

$$LV(U(t)) \leq -\lambda_m |U(t)|^2.$$

If the conditions in Theorem 2.3.2 hold true then the zero solutions of the system (2.18) are exponentially mean square stable.

Hence the proof. □

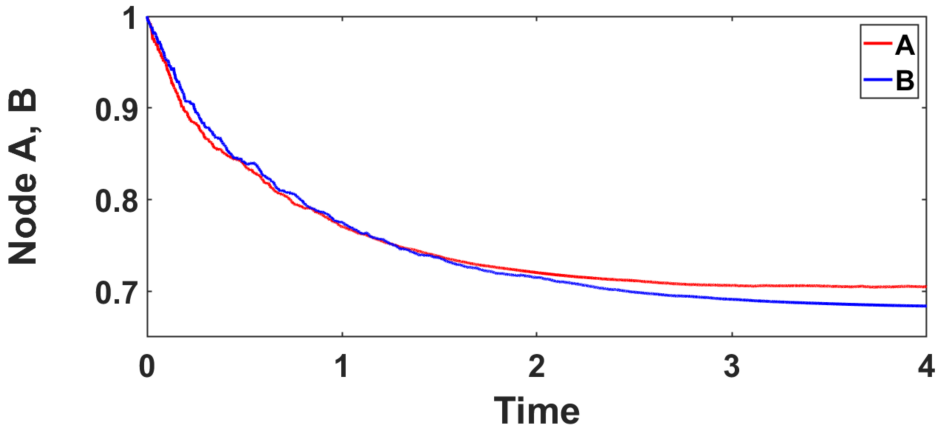

Figure 2.8: **Time series analysis.** The figure showing stability of the system (2.18) under stochastic perturbation for $\sigma_{1,2} = 0.1$.

Thus we observed analytically that under a certain threshold on σ_i's, the deterministic stable system remains stable under stochastic perturbation, which also agrees with our numerical result, see Fig. 2.8. But when σ becomes greater than the threshold value given in Theorem 2.3.2, we observed that the bi-stable points obtained for the system (2.1) with Table 2.1 show scattered dots. Fig. 2.9 confirms that the system (2.1) loses its bi-stability under stochastic perturbation for high noise intensity.

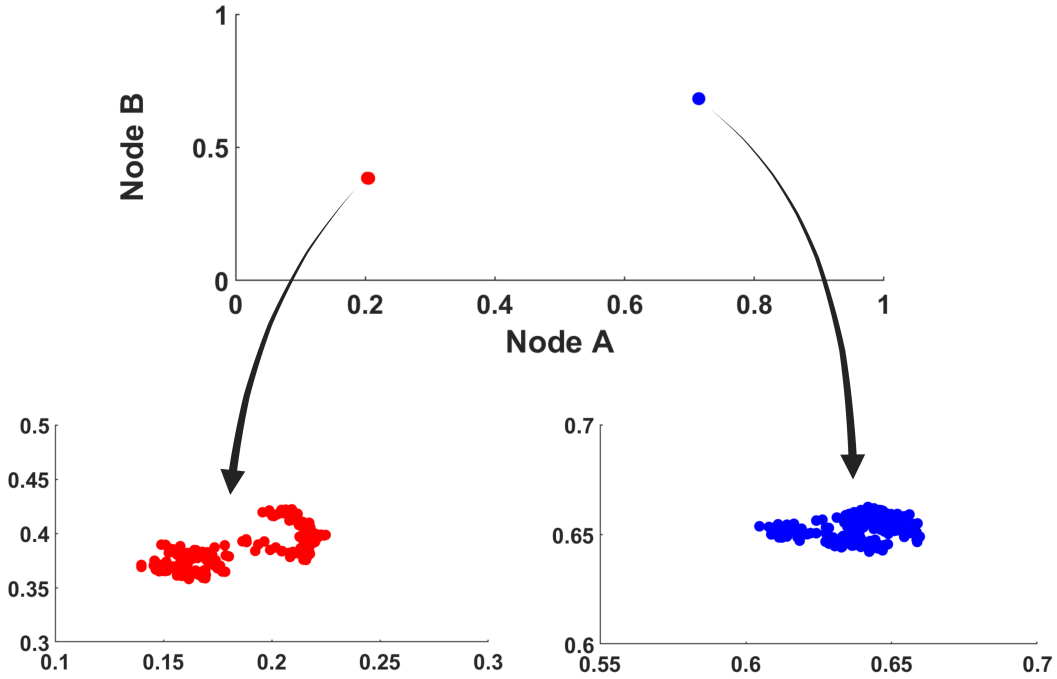

Figure 2.9: **Phase plane of structure 1.** Phase plane diagram for the system (2.18). The top figure shows the stable nature of E^* for a low value of $\sigma_{1,2} = 0.1$, and the bottom figures show the probability clouds for $\sigma_{1,2} = 1.3$, above the threshold value.

Following similar arguments, one can prove the following theorem for the stochastic differential system (2.22).

Theorem 2.3.3. *When the following inequality holds true*

$$\frac{k_B k_{mB} B^*}{(k_{mB} + (1 - B^*))^2} + \frac{k_1 k_{m1} A^*}{(k_{m1} + B^*)^2} > \frac{k_B (1 - B^*)}{k_{mB} + (1 - B^*)} \tag{2.41}$$

then the zero solutions of the system (2.22) will be exponentially 2-stable if

$$\begin{aligned} {\sigma_1}^2 &< 2\left[\frac{k_I k_{mI} I}{(k_{mI} + (1 - A^*))^2} + \frac{k_2 k_{m2} B^*}{(k_{m2} + (1 - A^*))^2} + \frac{k_A A^* (2k_{ma} + A^*)}{(k_{mA} + A^*)^2}\right] \\ {\sigma_2}^2 &< 2\left[\frac{k_B k_{mB} B^*}{(k_{mB} + (1 - B^*))^2} + \frac{k_1 k_{m1} A^*}{(k_{m1} + B^*)^2} - \frac{k_B (1 - B^*)}{k_{mB} + (1 - B^*)}\right] \end{aligned}$$

with positive constants ω_1 *and* ω_2 *are* $\omega_1 = \frac{k_{m2} + (1 - A^*)}{k_2 (1 - A^*)}$, $\omega_2 = \frac{k_{m1} + B^*}{k_1 B^*}$.

The behaviour of the system (2.22) for lower and higher values of sigma than its threshold value (given in Theorem 2.3.3) are presented in Figure 2.10. It shows that two clouds replace

the two stable equilibrium points for higher noise intensity.

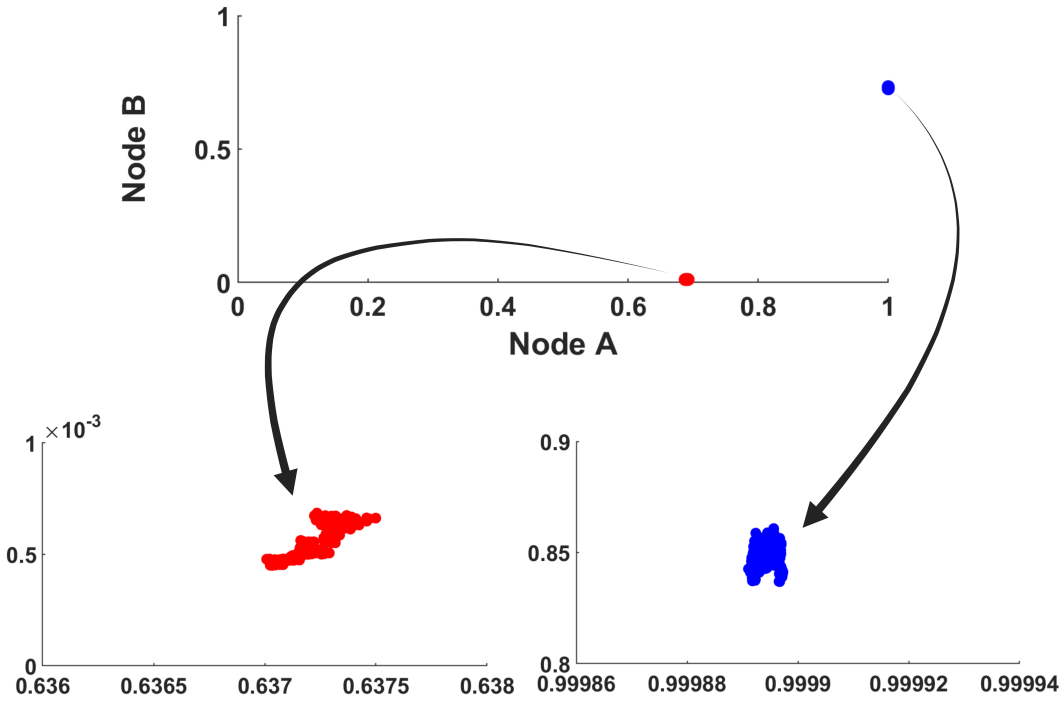

Figure 2.10: **Phase plane of structure 2.** Phase plane diagram for the system (2.22). The top figure shows the stable nature of E^* for a low value of $\sigma_{1,2} = 0.1$, and the bottom figures show the probability clouds for $\sigma_{1,2} = 1.2$, above the threshold value.

2.3.2 Stochasticity induces loss of bistability

It is well known that cellular signalling memory can be affected by an increase in the stochastic perturbations in the system. In other words, it can switch the system from one steady state to another steady state [99, 105]. So, we wanted to examine the change in the system's qualitative behaviour due to the introduction of random perturbation. We have considered one motif structure, structure 1, to demonstrate the changes caused by stochasticity on the observed bistability. The system shows bistability in the deterministic system (Fig. 2.11 (a)) and remains bistable for very small noise intensity ($\sigma_{1,2} = 0.1$) (see Fig. 2.11 (b)). When we increase one of the noise intensities $\sigma_1 = 1.3$ keeping $\sigma_2 = 0.1$, the left cloud (red) moves to the right (blue), making the system monostable (Fig. 2.11 (c)). The result is reversed when σs are switched (Fig. 2.11 (d)). So an increase in the noise intensity disrupts the bistability, and the system converges into a monostable system.

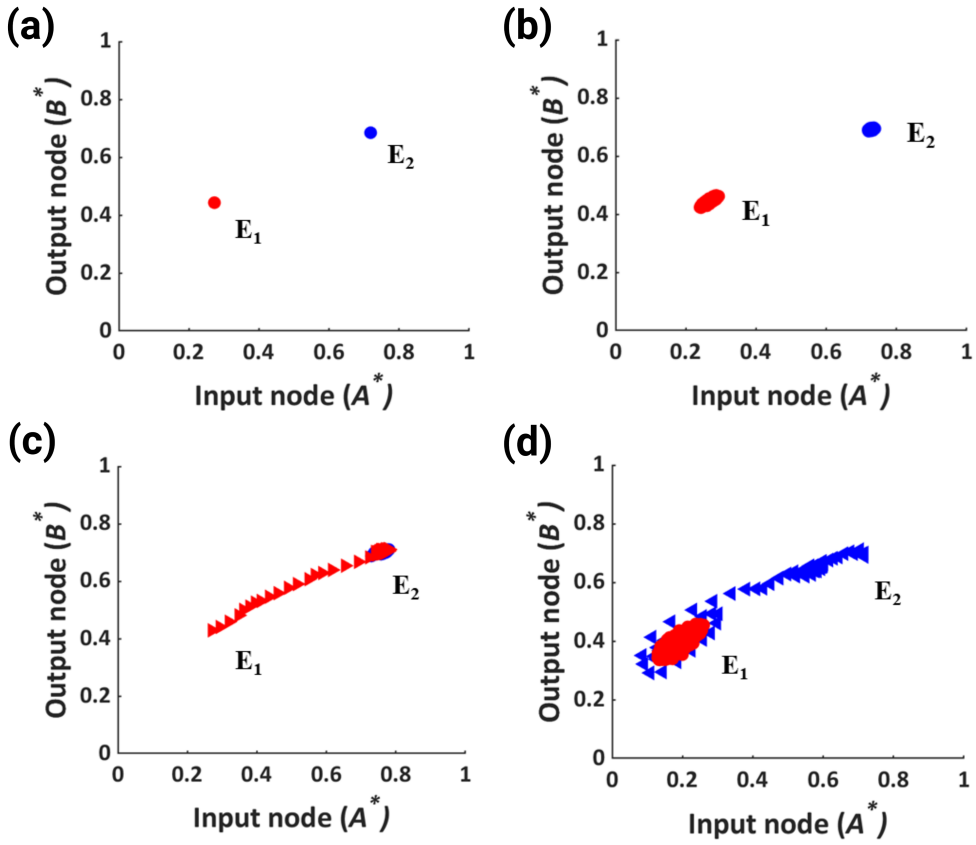

Figure 2.11: **Effect of randomness on bistability.** (a) Here, the red and the blue dots represent deterministic stable points of structure 1. (b) Figure showing the existence of bistability for structure 1 for the low intensity of noise ($\sigma_{1,2} = 0.1$). (c)-(d) The figures illustrate the distortion of the bistable cloud into a monostable cloud with the increase in the noise intensity.

2.4 Discussion

The biological system displays remarkable robustness in the stochastic environment of diverse physical and physiological stimuli. Some attributes that impart robustness to external and internal perturbations include topological features of the signalling network [137]. The topological features can further be weighted in their magnitude of influence depending on the net concentration of the constituent nodes as well as stochastic variations in their level owing to various intrinsic mechanisms [138]. However, the contribution of these features towards the overall robustness and sensitivity of the biological networks still needs to be understood.

In the present study, we studied two well-observed motif structures which show bistability, i.e., depending upon the initial conditions, the outputs can take any of the two steady-state

values. We observed that the range of the output signal depends on the structure, but the parameter's sensitivity is independent of the structure. In both structures, the downstream node is more sensitive to the outcome of the output signal. We also observed that under random perturbation with high noise intensity, the system loses its stability, and the bistable points are scattered, leading to an undesirable output signal. More precisely, we have seen that the system loses its bistability and converges to a monostable system due to an increase in the noise intensity beyond some threshold value. In conclusion, we have observed the emergence of very complex behaviour like bistability in two frequently observed two-node network motifs. We also observed that the bistability might be lost due to the presence of noise in the system.

This pilot study on two specific structures showed the importance of the structure and the noise in the signalling mechanism. This study encourages a deeper investigation of the association between motif structures and noise signalling networks. So, we have considered all possible two-node network motifs in the next chapter to get a global view of the signal-noise relationship of the network motifs. The knowledge obtained from our study could be explored further in screening potential candidates for drug targets. The results will be especially useful in diseases such as cancer, diabetes, and obesity that cause complex perturbations in cellular signalling networks.

3

Understanding noise in cell signalling in the prospect of drug-targets[1]

3.1 Introduction

Cell signalling networks have been studied under the influence of noise to understand noise-motif relations. Chatterjee and Kumar [31] attempted to understand such relations; however, it was restricted to three-node FFLs. Kittisopikul and Suel [139] did a detailed study on different feed-forward loop (FFL) motifs. They observed that the FFL could be categorised depending on whether their ON (stimulated) or OFF (unstimulated) steady states exhibit noise. The role of coherent and incoherent FFL on noise tolerance was also studied by Guantes et al. [124]. They

[1]The bulk of this chapter has been published in *Journal of Theoretical Biology*, 2022, 555, p.111298.

observed that coherent FFLs act as suitable noise tolerance detectors. In another study by Osella et al. [140], the incoherent FFL was observed to couple the fine-tuning of a target protein label with efficient noise control, thus maintaining stability to the overall gene expression program in the presence of noise. Hornung and Barkai [28] have studied the significance of positive feedback in maintaining sensitivity towards the input signal in the presence of noise. In a study by Simpson et al. [141], the negative feedback loop was observed to reduce the effect of noise on protein concentration. The negative feedback loop can suppress internal and external noise [103].

Developing efficient treatment methods necessitates a system-level knowledge of the molecules affected by disease and their complicated relationships. However, the studies discussed above were limited to some groups of network motifs, and more work needs to be done to capture the global understanding of the noise-motif relationships. The whole network must be explored for a concrete understanding of such relations. In the previous chapter, we considered only two frequently observed two-node network motifs and studied them under the influence of noise. This chapter incorporates all possible two-node network motifs to understand the whole network globally, as any network can be constructed by considering two-node motifs.

The current study aims to understand the importance of motif structures in determining cellular function in the presence of noise to filter noise from the network. To achieve this, a detailed study on the sensitivity of motifs in the network is required. The amount of change in the output steady state due to the change in the input signal defines sensitivity. However, stochastic systems also add noise in measuring sensitivity. Sensitivity could be defined as the measure of behavioural change of steady states due to changes in input stimuli and noise intensity. The vulnerability of a node to noise could be a significant factor in causing signalling error and need to be controlled. To capture the noise tolerance of network motifs, in this chapter, we developed a SDE-based mathematical model for different two-node motif structures and studied the association between motif structure and input-noise relation. We classified and ranked these motifs according to their sensitivity toward noise and signal. The ranks of the motifs were used to develop a tool that identifies sensitive nodes in a network, which we hypothesised as potential targets. The significance of the tool was validated through cancer

networks [142] and drug bank database [143].

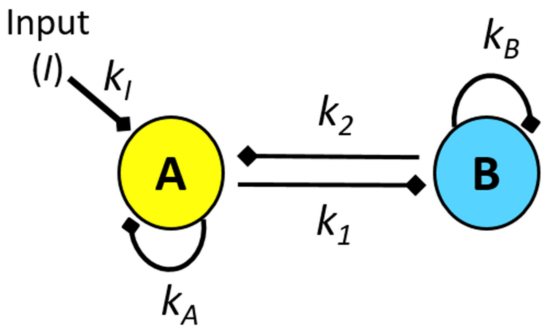

Figure 3.1: **Schematic diagram of the general two-node motif.** The figure shows all possible interactions between two nodes (input node A & output node B). Here the arrows represent regulations (activation or inhibition). Here k_I denotes the input node's activation rate by stimulus I. The parameters k_1 denote the regulation rate of node B by node A. The reverse rate is denoted by k_2. k_A and k_B denote the self-regulation rates of node A and B, respectively.

3.2 Model formulation

3.2.1 Two-node motifs and their nomenclature

A two-node network motif consists of two nodes, node A and node B. Node A receives the input signal (I), which influences output node B (see Fig. 3.1). The total number of possible topologies with two-node motifs is 81 (given by 3^{n^2}, n is the number of node(s)). Among them, there are two kinds of positive and negative feedback loops, which can be termed as positive feedback type I (PF_1), positive feedback type II (PF_2), negative feedback type I (NF_1), and negative feedback type II (NF_2). In PF_1, node A (input node) activates node B (output node) in return node B also activates node A. In PF_2, node A inhibits node B in return node B also inhibits node A. In NF_1, node A activates node B, but node B inhibits node A, and the reverse scenario of NF_1 is given by NF_2. When self-loops are added to these four topologies, we get eight new combinations for each topology. Here self-loop is denoted by S followed by the node with self-loop, and the sign +/- denotes activation/inhibition. So, if PF_1 has a self-activating loop on node A, then it is denoted by PF_1S_{A+}. Also, if both the self-loops are present, i.e. node A with self-activating loop and node B with self-inhibiting loop, then it is denoted by $PF_1S^{B-}_{A+}$. Similarly, all the other topologies can be named. The rest of the topologies consist of linear

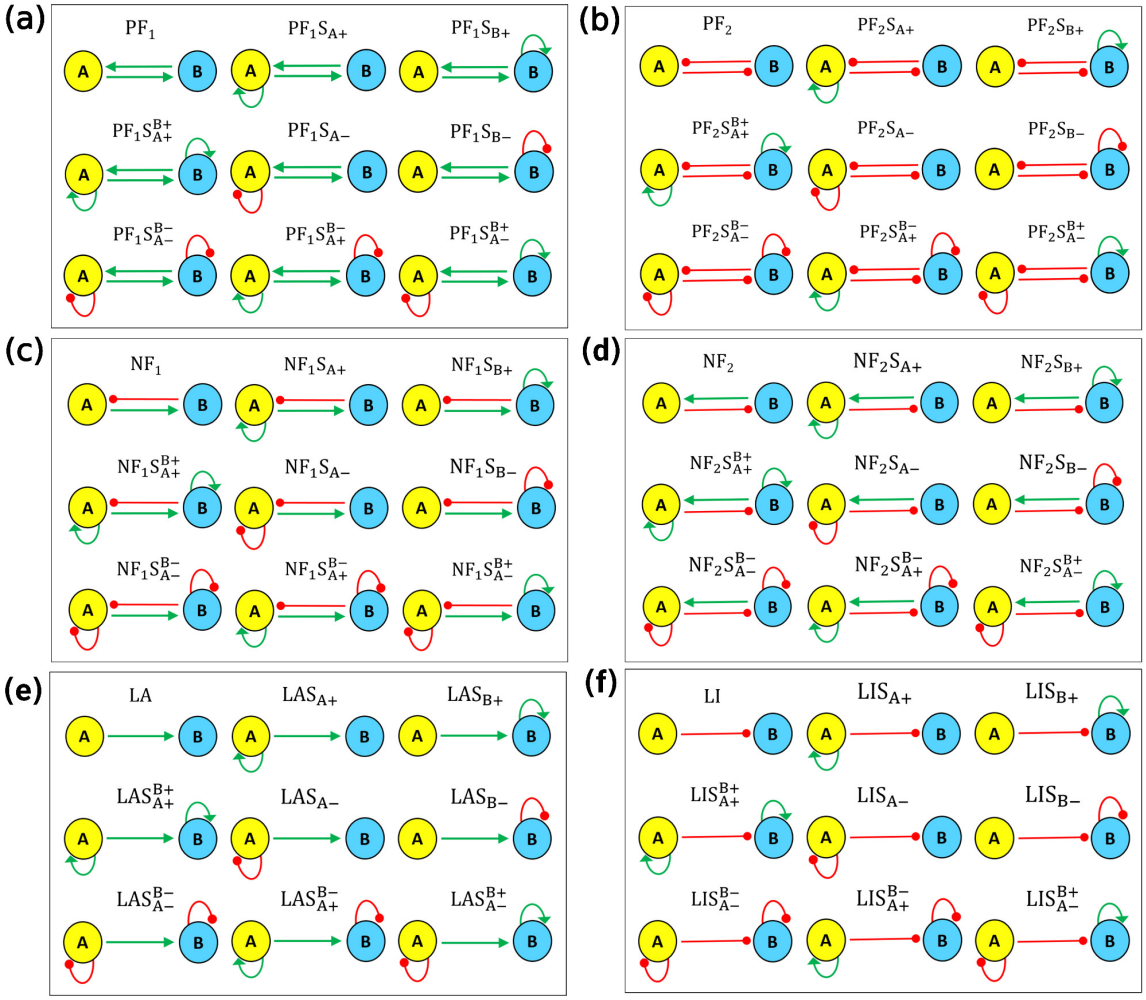

Figure 3.2: **All biologically feasible two-node topologies and their nomenclature.** Here, the motifs are grouped into six possible groups (a-f) according to the feedback. The green and red arrows represent activation and inhibition, respectively. (a) Positive feedback type I (PF_1) with self-loops. (b) Positive feedback type II (PF_2) with self-loops. (c) Negative feedback type I (NF_1) with self-loops. (d) Negative feedback type II (NF_2) with self-loops. (e) Linear activation (LA) with self loops. (f) Linear inhibition (LI) with self loops.

regulations or no regulation between node A and node B. We are interested in studying the I/O relation, so we have not considered the topologies with no regulation from input node A to output node B. The topologies with linear regulations, where node A activates or inhibits node B, are linear activation (LA) and linear inhibition (LI). Including self-loops in these linear topologies gives us sixteen new motifs in addition to LA and LI. Here self-loop is denoted by S, followed by the node with the self-loop, and the sign +/- denotes activation/inhibition. For example, the network motif structure LA with a self-activating loop on the node A is denoted by LAS_{A+}. The node A with the self-activating loop and node B with the self-inhibiting loop

are denoted by LAS^{B-}_{A+}, and so on. So, we get six groups of topologies, namely, PF_1, PF_2, NF_1, NF_2, LA and LI, where each group contains nine motifs, including self-loops. Thus, we obtain a total of 54 motif structures. So, we considered all feasible topologies with two-node motif structures for the study, which are given in Fig. 3.2.

3.2.2 The general model for two-node topology

The two-node network motif system given in Fig. 3.1 was modelled based on ordinary differential equations (ODEs). Each node can activate or inhibit itself and/ or other nodes. The model consists of activated forms of protein A (denoted by A) and protein B (denoted by B). Each protein's inactive form was calculated by deducting the activated form from the unity, thereby maintaining the overall amount of a given molecule constant [56, 122]. Each node has a basal synthesis rate [144]. A general model is given in the equation (3.1), which can be reduced to different individual topologies.

$$\begin{aligned} \frac{dA}{dt} &= b_1 + \frac{k_I I(1-A)}{k_{mI}+(1-A)} + f_A + f_{BA} - \delta_1 A = F_1(A,B), \\ \frac{dB}{dt} &= b_2 + f_B + f_{AB} - \delta_2 B = F_2(A,B). \end{aligned} \tag{3.1}$$

where f_A, f_B, f_{AB} and f_{BA} take the following forms depending upon the motif structure.

$$f_A = \begin{cases} \frac{k_A A(1-A)}{k_{mA}+(1-A)}, & \text{for self-activation on } A \\ -\frac{k_A A^2}{k_{mA}+A}, & \text{for self-inhibition on } A \end{cases}$$

$$f_B = \begin{cases} \frac{k_B B(1-B)}{k_{mB}+(1-B)}, & \text{for self-activation on } B \\ -\frac{k_B B^2}{k_{mB}+B}, & \text{for self-inhibition on } B \end{cases}$$

$$f_{AB} = \begin{cases} \frac{k_1 A(1-B)}{k_{m1}+(1-B)}, & \text{when A activates B} \\ -\frac{k_1 AB}{k_{m1}+B}, & \text{when A inhibits B} \end{cases}$$

$$f_{BA} = \begin{cases} \frac{k_2 B(1-A)}{k_{m2}+(1-A)}, & \text{when B activates A} \\ -\frac{k_2 BA}{k_{m2}+A}, & \text{when B inhibits A} \end{cases}$$

The system of equations (3.1) describes the rates of loss and creation of particular labelled forms of proteins (nodes). I is the input to the first node (i.e. protein A) at a rate k_I, and the enzymatic reaction was modelled following the Michaelis-Menten form of the equation. The output is defined by the steady state values achieved by the second node (i.e. protein B). Here b_1 and b_2 are the basal values of node A and node B, respectively. k_A, k_B are the self activating or self inhibiting rates and k_1, k_2 are the activating or inhibiting rates of A on B and B on A respectively. $k_{mI}, k_{mA}, k_{mB}, k_{m1}, k_{m2}$ are the half saturation constants. δ_1 and δ_2 are the degradation rates of node A and node B respectively. We obtained all possible topologies by considering different combinations in Fig. 3.1. The rate and degradation constants have one unit over time, and the half-max constants have a unit of concentration.

3.2.3 Stochastic model of two-node topology

To account for the network's intrinsic unpredictability, we created stochastic differential equations (SDEs). Mutations and changes in protein turnover rates might cause random perturbations. They may also emerge as a result of faulty network signalling. The I/O interaction in various motif structures in the presence of noise was investigated using these SDE models. The noise under investigation was mainly driven by the fact that a variety of intrinsic and extrinsic factors, including cytokines, growth factors, nutrients, environmental stresses, protein stability modulation, and many others, can potentially influence any of the signalling components through a variety of mechanisms [37, 135, 136]. So, we include a dispersed stochastic perturbation in our model that can affect any network motif's components regardless of the signal input. The cumulative consequences of such perturbations would have a diverse effect on the signalling network's basal state. We treated random impacts such as systemic disturbances as multiplicative Gaussian white noise and included them in the model [36, 130]. Thus, we introduce the stochastic perturbation terms into node A and node B equations. The stochastic perturbations of the state variables around their steady-state values E^* are Gaussian white noise

proportional to the distances of A, B from A^*, B^*, which are the steady-state values of the system in the absence of the noise. So, the deterministic model system (3.1) results in the following stochastic model system.

$$\begin{aligned} dA &= F_1(A,B)dt + \sigma_1(A-A^*)d\xi_t^1 \,, \\ dB &= F_2(A,B)dt + \sigma_2(B-B^*)d\xi_t^2 \,. \end{aligned} \tag{3.2}$$

where σ_1 and σ_2 are real constants and known as the intensity of the noise, $\xi_t^i = \xi_i(t)$, $i = 1,2$ are standard Wiener processes, independent of each other, and F_1, F_2 are defined in the Eq. (3.1). We consider Eq. (3.2) as an Ito stochastic differential system of the type

$$dX_t = F(t,X_t)dt + G(t,X_t)d\xi_t \tag{3.3}$$

where the solution (X_t,$t > 0$) is an Ito process, 'F' is the drift coefficient, 'G' is the diffusion coefficient, and ξ_t is a two-dimensional stochastic process having scaler Wiener process components with increments $\triangle\xi_t^j = \xi_j(t+\triangle t) - \xi_j(t)$ are independent Gaussian random variables $\mathrm{N}(0, \triangle t)$. In the case of system (3.3),

$$X_t = \begin{bmatrix} A \\ B \end{bmatrix}, \xi_t = \begin{bmatrix} \xi_t^1 \\ \xi_t^2 \end{bmatrix}, F = \begin{bmatrix} F_1(A,B) \\ F_2(A,B) \end{bmatrix}, G = \begin{bmatrix} \sigma_1(A-A^*) & 0 \\ 0 & \sigma_2(B-B^*) \end{bmatrix} \tag{3.4}$$

Since the diffusion matrix 'G' depends upon the solution of X_t, the system (3.2) is said to have multiplicative noise.

3.3 Analytical results

3.3.1 Stochastic stability around interior equilibrium point

The stochastic differential system (3.2) can be centred at its positive equilibrium points $E^*(A^*, B^*)$ by introducing the variables $H_1 = A - A^*, H_2 = B - B^*$. For simplicity of mathematical

calculations, we deal with the stochastic differential equation obtained by linearising the vector function 'F' in (3.4) about the positive equilibrium point E^*. The linearised version of (3.3) around E^* is given by

$$dH(t) = f(H(t))dt + G(H(t))d\xi(t)\,, \tag{3.5}$$

where

$$H(t) = \begin{bmatrix} H_1(t) \\ H_2(t) \end{bmatrix}, f(H(t)) = \begin{bmatrix} \left(\frac{\partial F_1}{\partial A}\right) H_1 + \left(\frac{\partial F_1}{\partial B}\right) H_2 \\ \left(\frac{\partial F_2}{\partial A}\right) H_1 + \left(\frac{\partial F_2}{\partial B}\right) H_2 \end{bmatrix}, G(H(t)) = \begin{bmatrix} \sigma_1 H_1 & 0 \\ 0 & \sigma_2 H_2 \end{bmatrix} \tag{3.6}$$

Note that, in (3.5) the positive equilibrium E^* corresponds to the trivial solution $(H_1, H_2) = (0,0)$. Let Ω be the set defined by $\Omega = \left[(t \geqslant t_0) \times \mathrm{R}^2, t_0 \in \mathrm{R}^+\right]$. To define stability following theorem [111] can be used,

Theorem 3.3.1. *Suppose there exist a differentiable function $V(H,t) \in \mathrm{C}^2(\Omega)$ satisfying the inequalities*

$$K_1|H|^\alpha \leq V(H,t) \leq K_2|H|^\alpha \tag{3.7}$$

$$LV(H,t) \leq -K_3|H|^\alpha, \quad K_i > 0, \quad i = 1,2,3, \quad \alpha > 0\,. \tag{3.8}$$

Then the trivial solution of (3.5) is exponentially α stable for all time $t \geq 0$.

Note that, if in (3.7), (3.8), $\alpha = 2$, then the trivial solution of (3.5) is exponentially mean-square stable. Furthermore, the trivial solution of (3.5) is globally asymptotically stable in probability.

Here, following (3.5),

$$LV(t,H) = \frac{\partial V(t,H(t))}{\partial t} + f^T(H(t))\frac{\partial V(t,H)}{\partial H} + \frac{1}{2}Tr\left[G^T(H(t))\frac{\partial^2 V(t,H)}{\partial H^2}G(H(t))\right] \tag{3.9}$$

where

$$\frac{\partial V}{\partial H} = \begin{pmatrix} \frac{\partial V}{\partial H_1} & \frac{\partial V}{\partial H_2} \end{pmatrix}^T, \quad \frac{\partial^2 V(t,H)}{\partial H^2} = \left(\frac{\partial^2 V}{\partial H_j \partial H_i} \right)_{i,j=1,2}$$

and T means transposition.

Using the above Theorem 3.3.1 we can calculate the critical value of noise (σ_c) analytically for a motif structure, such that the deterministic steady state is stochastically stable if the noise intensity is less than the critical value ($\sigma < \sigma_c$). To demonstrate with an example, we have calculated the threshold values of the $\sigma's$ for the motif PF_2.

3.3.2 Analysis for the motif PF_2

The deterministic model for the motif PF_2 takes the following form,

$$\begin{aligned} \frac{dA}{dt} &= b_1 + \frac{k_I I(1-A)}{k_{mI} + (1-A)} - \frac{k_2 BA}{k_{m2} + A} - \delta_1 A = \widehat{F}_1(A,B), \\ \frac{dB}{dt} &= b_2 - \frac{k_1 AB}{k_{m1} + B} - \delta_2 B = \widehat{F}_2(A,B). \end{aligned} \tag{3.10}$$

Considering Gaussian white noise around their steady-state values $E^* = (A^*, B^*)$, the deterministic model system (3.10) results in the following stochastic model system,

$$\begin{aligned} dA &= \widehat{F}_1(A,B)dt + \sigma_1(A - A^*)d\xi_t^1 \,, \\ dB &= \widehat{F}_2(A,B)dt + \sigma_2(B - B^*)d\xi_t^2 \,. \end{aligned} \tag{3.11}$$

where σ_1 and σ_2 are real constants and known as the intensity of the fluctuations, $\xi_t^i = \xi_i(t)$, $i = 1,2$ are standard Wiener processes, independent of each other, and $\widehat{F}_1$, $\widehat{F}_2$ are defined in Eq. (3.10). We consider Eq. (3.11) as an Ito stochastic differential system of the type

$$dX_t = \widehat{F}(t, X_t)dt + G(t, X_t)d\xi_t \tag{3.12}$$

where the solution (X_t,$t > 0$) is an Ito process, '$\widehat{F}$' is the drift coefficient, 'G' is the diffusion

coefficient, and ξ_t is a two-dimensional stochastic process having scaler Wiener process components with increments $\triangle\xi_t^j = \xi_j(t+\triangle t) - \xi_j(t)$ are independent Gaussian random variables $\mathrm{N}(0,\triangle t)$. In the case of system (3.11), with

$$X_t = \begin{bmatrix} A \\ B \end{bmatrix}, \xi_t = \begin{bmatrix} \xi_t^1 \\ \xi_t^2 \end{bmatrix}, \widehat{F} = \begin{bmatrix} \widehat{F_1}(A,B) \\ \widehat{F_2}(A,B) \end{bmatrix}, G = \begin{bmatrix} \sigma_1(A-A^*) & 0 \\ 0 & \sigma_2(B-B^*) \end{bmatrix} \tag{3.13}$$

Since the diffusion matrix 'G' depends upon the solution of X_t, the system (3.11) is said to have multiplicative noise.

The stochastic differential system (3.11) can be centred at its positive equilibrium points $E^*(A^*,B^*)$ by introducing the variables $U_1 = A - A^*, U_2 = B - B^*$. The linearised version of (3.12) around E^* is given by

$$dU(t) = f(U(t))dt + G(U(t))d\xi(t)\,, \tag{3.14}$$

where

$$U(t) = \begin{bmatrix} U_1(t) \\ U_2(t) \end{bmatrix}, f(U(t)) = \begin{bmatrix} -P_{11}U_1 - P_{12}U_2 \\ -P_{21}U_1 - P_{22}U_2 \end{bmatrix}, G(U(t)) = \begin{bmatrix} \sigma_1 U_1 & 0 \\ 0 & \sigma_2 U_2 \end{bmatrix} \tag{3.15}$$

with

$$P_{11} = \frac{k_I k_{mI} I}{(k_{mI} + (1-A^*))^2} + \frac{k_2 k_{m2} B^*}{(k_{m2}+A^*)^2} + \delta_1,\ P_{12} = \frac{k_2 A^*}{k_{m2}+A^*},$$
$$P_{21} = \frac{k_1 B^*}{k_{m1}+B^*},\ P_{22} = \frac{k_1 k_{m1} A^*}{(k_{m1}+B^*)^2} + \delta_2\,. \tag{3.16}$$

Note that, in (3.14) the positive equilibrium E^* corresponds to the trivial solution $(U_1,U_2) = (0,0)$. Let Ω be the set defined by $\Omega = \left[(t \geqslant t_0) \times \mathrm{R}^2, t_0 \in \mathrm{R}^+\right]$. We can define the Theorem 3.3.1 and prove the following theorem.

Theorem 3.3.2. *Assuming the inequality holds true:*

$$\left(2P_{11} - \sigma_1^2\right)\left(2P_{22} - \sigma_2^2\right) > \left(p_{12} + P_{21}\right)^2 \tag{3.17}$$

where P_{11}, P_{12}, P_{21} and P_{22} are given in (3.16), then the zero solutions of the system (3.11) will be exponentially 2-stable if

$$\sigma_1{}^2 < 2\left[\frac{k_I k_{mI} I}{(k_{mI}+(1-A^*))^2} + \frac{k_2 k_{m2} B^*}{(k_{m2}+A^*)^2} + \delta_1\right],\ \sigma_2{}^2 < 2\left[\frac{k_1 k_{m1} A^*}{(k_{m1}+B^*)^2} + \delta_2\right]. \tag{3.18}$$

Proof. Let us consider the Lyapunov function

$$V(U(t)) = \frac{1}{2}\left[U_1{}^2 + U_2{}^2\right] \tag{3.19}$$

It is easy to check the inequalities in (3.7) are true for $\alpha = 2$.

Next, using (3.15) and (3.9),

$$\begin{aligned} LV(U(t)) &= \left(-P_{11} + \frac{1}{2}\sigma_1{}^2\right) U_1{}^2 + \left(-P_{22} + \frac{1}{2}\sigma_2{}^2\right) U_2{}^2 - (P_{12}+P_{21})\, U_1 U_2 \\ &= -U^T Q U \end{aligned} \tag{3.20}$$

where

$$Q = \begin{bmatrix} \left(P_{11} - \frac{1}{2}\sigma_1{}^2\right) & \frac{1}{2}(P_{12}+P_{21}) \\ \frac{1}{2}(P_{12}+P_{21}) & \left(P_{22} - \frac{1}{2}\sigma_2{}^2\right) \end{bmatrix}.$$

The relation (3.17) and (3.18) imply that Q is a real symmetric positive definite matrix and therefore all its eigenvalues $\lambda_i(Q)$, $i = 1,2$ are positive real numbers. Let $\lambda_m = min\{\lambda_i(Q),\ i = 1,2\},\ \lambda_m > 0$. From (3.20), we get

$$LV(U(t)) \leq -\lambda_m |U(t)|^2 .$$

If the conditions in Theorem 3.3.2 hold true then the zero solutions of the system (3.11) are exponentially mean square stable.

Hence the proof. □

3.4 Numerical results

3.4.1 Vulnerability of two-node network motifs under systemic noise

In random perturbation, the output value deviates from its steady-state B^* depending on the value of noise intensity. The output value appears as a range, instead of a single point, with values close to the B^* (see Fig. 3.3 (a)). This range can be observed if the noise intensities are below the critical value (σ_c), which can be calculated mathematically. The detailed calculation to find σ_c for the motif PF_2 is given in section 3.3.2. Similar calculations were also done to

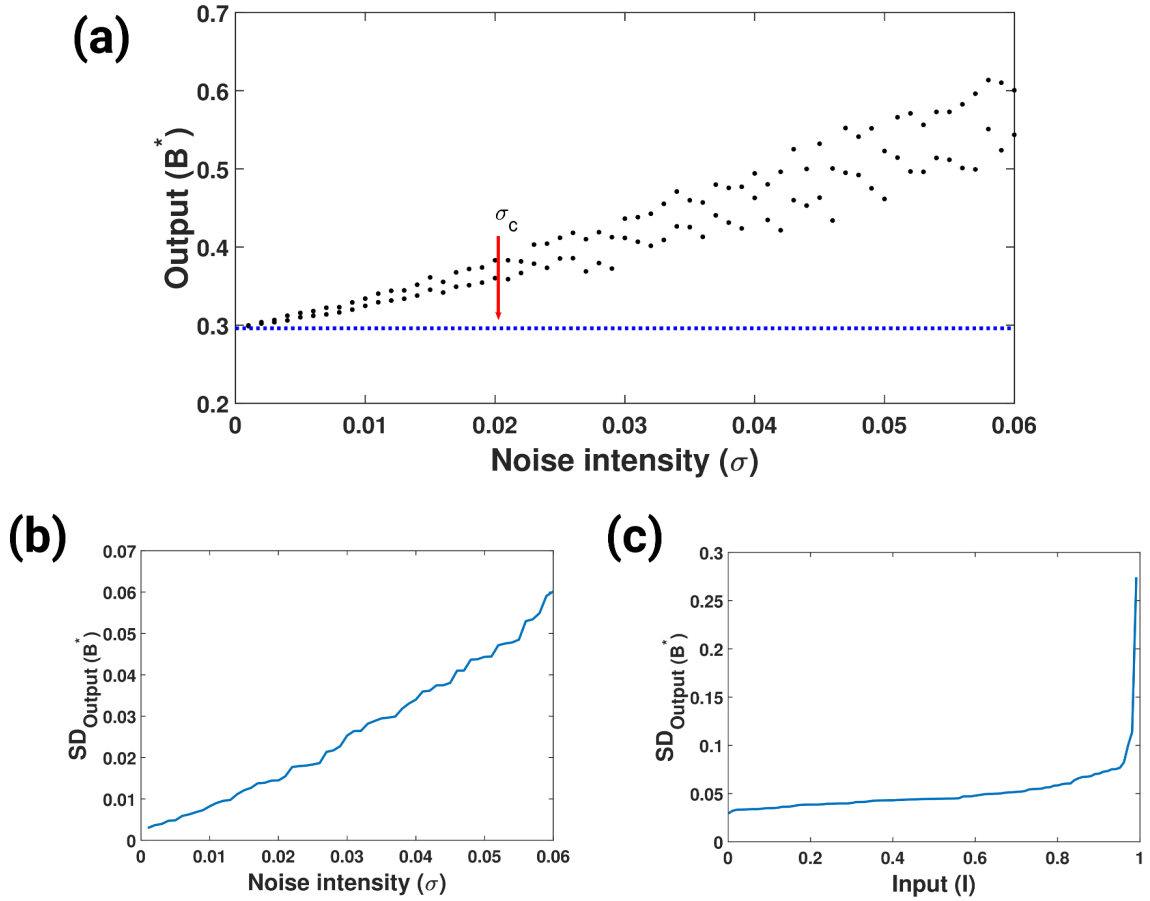

Figure 3.3: **Association of noise and input stimulus with stochastic stability.** Figure (a) depicts output B^* at a given signal as a function of systemic noise (given by black dots). Corresponding output B^* in the absence of noise is also shown by blue dots. The red arrow indicates the threshold noise level (σ_c) at which output becomes divergent. The value of σ_c is obtained mathematically using the Theorem 3.3.2. As an alternate measure of specific input-output (I/O) relationship in the presence of systemic noise, standard deviations (SD) for the B^* are plotted as a function of σ (b) or I (c). Data used to plot (a), (b) and (c) were generated for the motif PF_2.

calculate σ_c for the remaining motifs. The system is stochastically stable when the output values remain close to the deterministic steady state B^*. However, when the noise intensity crosses the threshold value, a precise I/O relationship cannot be determined because the output value range increases and deviates from the steady state, see Fig. 3.3 (b). A similar phenomenon is observed when the input signal varies (Fig. 3.3 (c)). So the vulnerability threshold is governed by noise and input level, beyond which output becomes unstable. Thus, this $\sigma - I$ relation of motifs can be used to calculate the stochastic stability of the network motifs.

Next, to evaluate the stochastic stability of the individual motif structures under the influence of noise and input fluctuation, we have calculated the stochastic stability of the steady-state for the noise-input ($\sigma - I$) region for all the particular topologies. The exercise was done for numerous parameter sets to avoid any parameter-based biases. First, we have generated 1000 random parameter sets (excluding $\sigma\&I$) using the Halton sequences method to pick values from the space (0,1). The unit interval in each dimension is evenly partitioned with equiprobable sub-intervals using this quasi-random sampling approach. As a result, it eliminates potential spatial biases and investigates the whole parameter space between them (0,1). Next, to calculate the stochastic stable region area in the space created by varying input(I) and the strength of noise intensity (σ), we generated another 1000 parameter sets with different σ & I for each previously generated parameter sets. So we get a total of 10^6 parameter sets for the study. Then we filtered out 214 parameter sets out of the first 1000 sets, which yielded stable steady-states in the deterministic system for all the motif structures, as the deterministic equilibrium points are required for the calculations of stochastic stability. Moreover, for each of the 214 parameter sets, we have calculated the stochastic stable $\sigma - I$ region for each motif structure. Then to eliminate data variability due to the choice of parameter sets, we have normalised the data. Normalisation was done by dividing the individual $\sigma - I$ areas by the maximum $\sigma - I$ area for a particular parameter set. So we get a 214×54 matrix with 214 rows of parameters and 54 topologies in columns, where each element denotes a fraction of the stochastic stable area for a particular motif corresponding to a parameter set. Finally, we took each column's mean to calculate the individual motifs' vulnerability. The topology with a larger mean $\sigma - I$ area is said to be stochastically robust, whereas the topology with less mean $\sigma - I$ area will be called

sensitive. The whole method is explained in Fig. 3.4 through a schematic flowchart.

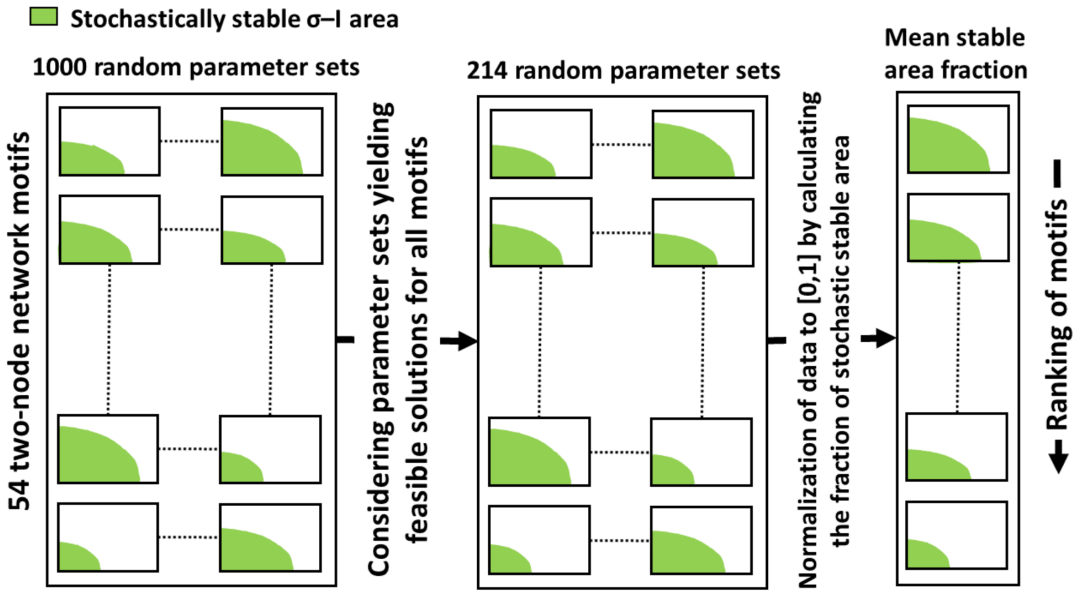

Figure 3.4: **Methodology to calculate stochastic stability.** The figure depicts the flowchart of the method used to calculate the stochastic stability of the motifs. Each small rectangle represents the 2D parameter $\sigma - I$ region, and the green colour shows the stochastically stable area. The X-axis of the big rectangle represent the parameter sets, and the Y-axis represents the 54 motifs. Left box: we have generated 1000 random parameter sets and calculated each motif's stochastically stable $\sigma - I$ region. Middlebox: we have considered only the 214 parameter sets yielding feasible solutions. Right box: we have normalised the data to [0,1] by dividing by the maximum for each parameter set. Ultimately, we have taken the mean of the stochastically stable area and arranged it in decreasing order. This information is used to rank the motifs according to their vulnerability to noise.

After quantifying the vulnerability of the motifs under systemic noise, we have categorised the topologies by calculating their modified z-score and termed them as sensitive (z-score < -1) and robust (z-score > 1) motifs. Z-scores were calculated to significantly distinguish the sensitive and robust motifs from the rest. We found eight motifs in the robust category (denoted by blue bars in Fig. 3.5) and nine motifs in the sensitive category (indicated by red bars in Fig. 3.5). Then a score of 1 to 8 was assigned to the robust motifs, with eight being the most robust and one being the least robust. Similarly, -1 to -9 were assigned to the sensitive motifs, with -9 the most sensitive and -1 the least sensitive. The remaining motifs (denoted by green bars in Fig. 3.5) were given 0. Different motif groups also showed distinctive characteristics under systemic noise. Consistent with previous observations [28], the double-positive feedback loops, i.e., the positive feedback type I, have a larger stable area and are robust under systemic noise

(see Fig. 3.6). In contrast, the double negative feedback, i.e., the positive feedback type II motifs, have the least stable area referring to their vulnerability to the systemic noise (see Fig. 3.6).

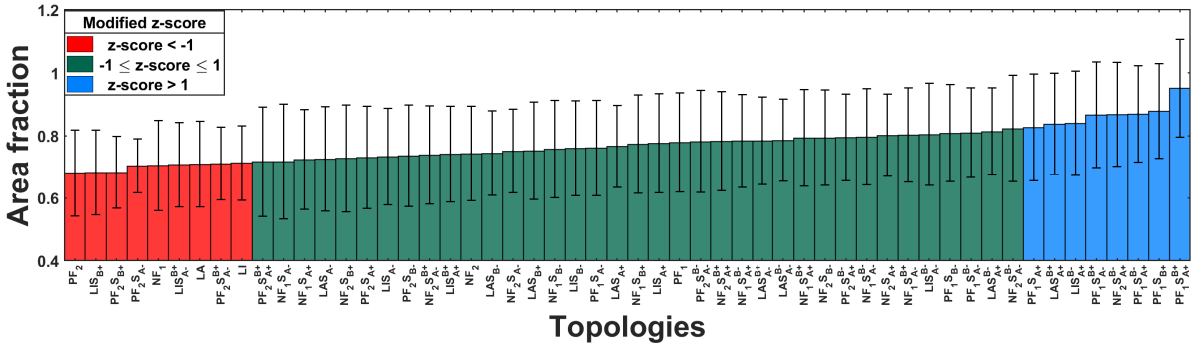

Figure 3.5: **Ranking of the two-node motifs.** The figure depicts the mean stochastically stable region of all 54 topologies in increasing order. Each bar represents the mean stochastic stable $\sigma - I$ area fraction of the motifs calculated for all random parameter sets, and the error bar represents their standard deviations. Motifs were categorised into sensitive (red bars) and robust (blue bars) based on their modified z-score.

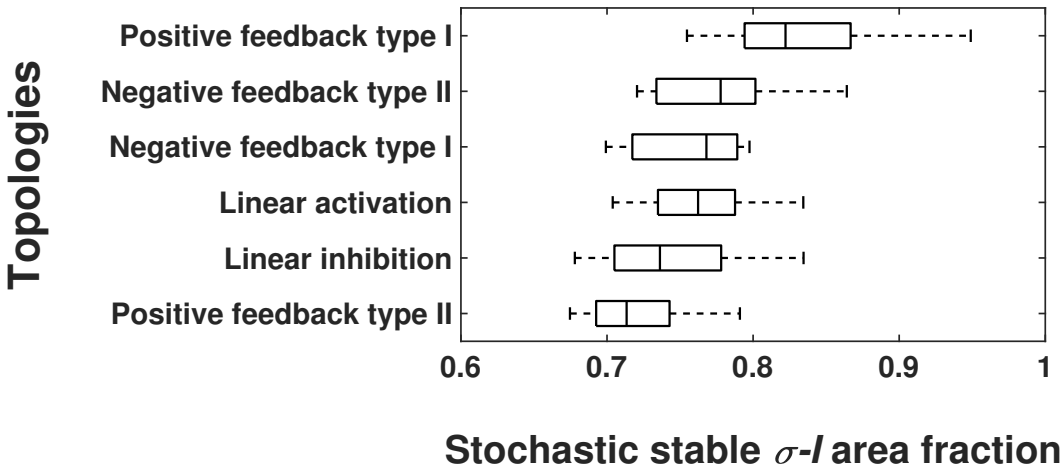

Figure 3.6: **Collective behaviour of the motif groups under systemic noise.** The box plot displays the stochastic stable $\sigma - I$ area distribution for each category mentioned in Fig. 3.2. Here, along Y-axis (top to bottom), the motif groups are arranged in descending order of their median area fraction. The X-axis represents the area fraction of the stochastic stable region.

3.4.2 Significance of sensitive motifs

The cellular signalling system is inherently noisy. With the increase in the fluctuation of the input stimulus or the increase in the noise intensity in the system, the sensitive motifs would

quickly go to the stochastically unstable steady state. So the possibility of getting an undesirable output is maximum for sensitive motifs. The significance of the sensitive motifs could be better understood through the druggability test [145]. We simulated the output node B as the drug target to investigate the druggability of the network motifs. A drug was simulated by an input that inhibited node B and was changed from 0.1 (I_1) to 1.0 (I_2). Two states of the system ($B1$ and $B2$) that corresponded to I_1 and I_2 were used to evaluate the druggability of each network motif as $D = log_{10}\left(\frac{B1-B2}{B1}\right)$ [145]. This metric D represents the fractional reduction of the target B in the logarithm scale. The simulation was conducted on each motif with the random parameter sets described in section 3.4.1 to get a set of values of D. Taking the average of this set gives us the druggability of each motif (see Fig. 3.7). The lower negative value of the druggability metric D indicates a higher reduction of B. We compared the druggability results with the motif categories. We observed that the sensitive motifs showed the highest druggability (red bars in Fig. 3.7), whereas the robust motifs showed the least druggability (blue bars in Fig. 3.7). So, the sudden changes in the concentration of the output node of the sensitive motifs that need to be controlled to maintain the desirable I/O signal in a network are also better druggable than the robust motifs.

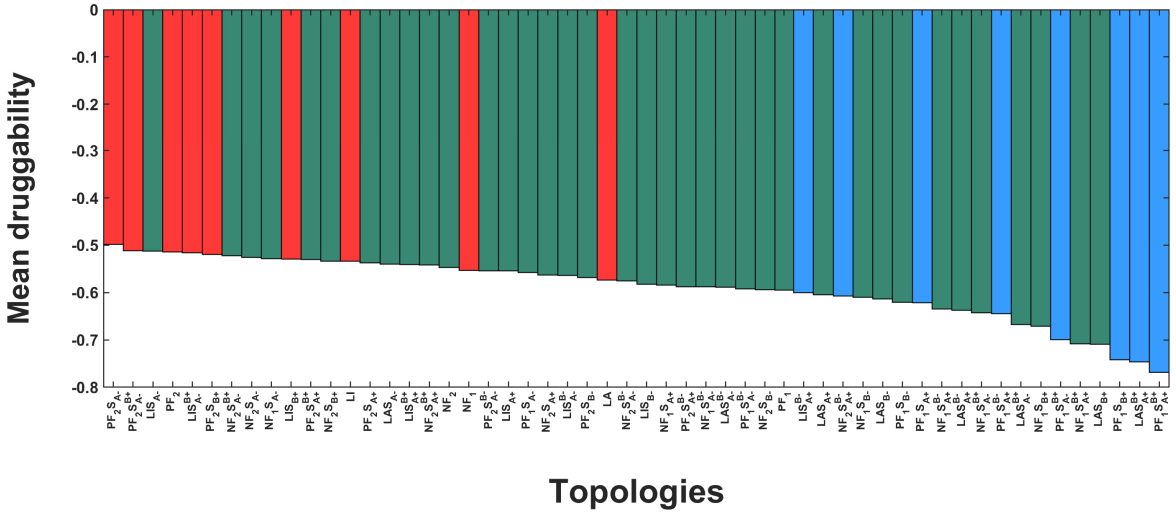

Figure 3.7: **Druggability test.** The bar represents the mean druggability of different motifs calculated following [145]. The red bars represent the sensitive motifs, the blue bars represent the robust ones, and the rest of the motifs are given by green bars (as given in Fig. 3.5).

3.4.3 Identification of sensitive nodes

The proper maintenance of the I/O signalling between two nodes becomes significant in a large protein-protein interaction (PPI) network. This maintenance can be done by targeting particular types of motifs in the network. We found that the sensitive motifs are better druggable than robust ones from the druggability test. That means we get a more significant reduction of the output in the sensitive motif than the robust one for an equal amount of inhibition. Thus, the sensitive motifs can be a better drug target. However, in a PPI network, a particular protein may appear in different motifs, and multiple proteins can appear in a particular motif type. So, to identify the target explicitly, we need to consider the overall sensitivity of a protein in the network. To determine the overall sensitivity, we design a formula to calculate the cumulative score (CS) of the protein in the network. Suppose P denotes the node, which appears in n unique motifs in the network, and K_i denotes the number of times the node P occurs in i^{th} motif with score S_i. Then the CS for node P is given by

$$P_{CS} = \sum_{i=1}^{n} K_i S_i.$$

The proteins frequently appearing in the sensitive motifs will have a higher negative score than the other proteins. Thus, the nodes with high negative CS are considered sensitive nodes and could be considered potential drug targets.

3.4.4 Sensitive nodes and drug targets

We considered three cancer networks, namely breast, ovarian and pancreatic cancers, from literature [142]. We considered all the proteins involved in those cancer networks. To get a directed PPI (signalling) network, we used SIGNOR (SIGnaling Network Open Resource) database [146]. Using the database, we created directed graphs among the signalling proteins. We obtained directed PPI networks with 5241 interactions from 1415 nodes for breast cancer, 3934 interactions from 1045 for ovarian cancer, and 3839 interactions from 990 for pancreatic cancer. The sensitive and robust proteins were extracted from the networks by calculating their CS. We searched the number of approved drugs against each node. We extract drug-target pro-

tein data from the open-source Drugbank database [143]. Extensive information about drugs and their targets is given in the Drugbank database, which includes chemical, pharmacological, and pharmaceutical-specific drugs integrated with structures, pathways, and sequence drug targets. We have considered the information of approved drugs only for our analysis.

Next, we calculated the CS of all the nodes in the three cancer networks. We also find the number of approved drugs against the nodes from the Drugbank database [143]. It is observed that the sensitive nodes have the most approved drugs against them compared to the robust nodes in all three cancer networks. For example, in breast cancer, the highest number of drugs against a single protein is 92, which belongs to the sensitive category, while the highest number of drugs associated with a robust protein is only 3. A similar distribution of drugs was also observed for ovarian and pancreatic cancers (see Fig. 3.8). We also observed that the average number of approved drugs for a sensitive node is three times higher than the robust nodes (see Fig. 3.8). Thus, a relation between sensitive nodes and drug targets is observed in all three cancer networks. The relation shows that nodes from the sensitive category are associated with the most number of drugs.

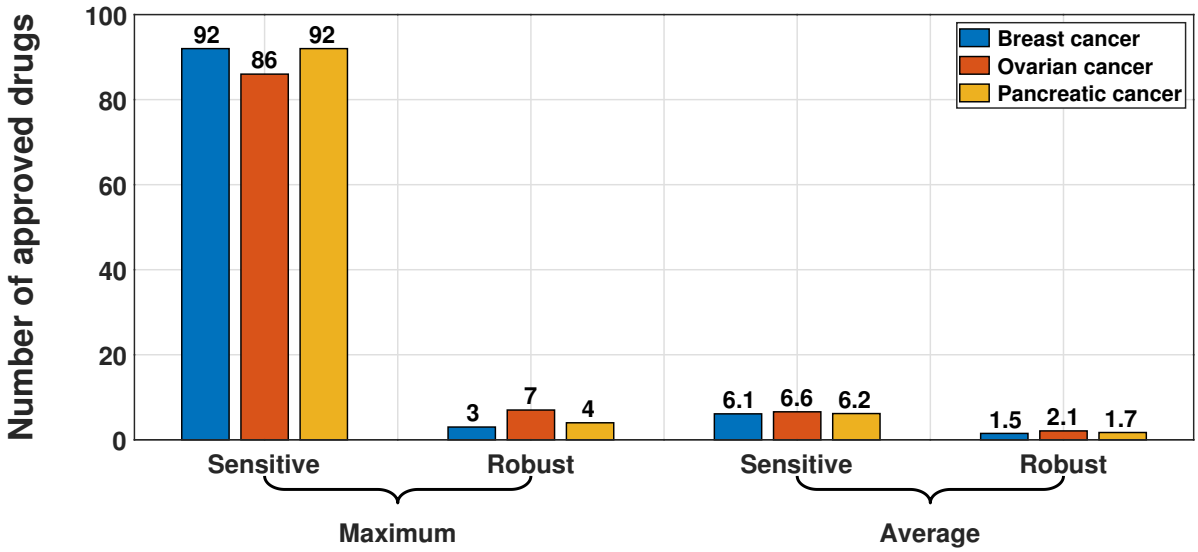

Figure 3.8: **Sensitive and robust nodes vs drugs.** The figure depicts the number of approved drugs against the sensitive and robust nodes across three cancer types. The first two groups of bars show the highest number of drugs observed against a single sensitive and a single robust node. The last two groups of bars show the average number of drugs per node. The bar colours represent different cancers, as mentioned in the figure legend.

To further confirm this relation, we performed a reverse analysis to see the sensitivity of

established drug targets. We used the proposed drug targets from Kanhaiya et al. [142] and calculated their CS for all three cancer networks. Most high-impact drug-target proteins have negative CS for all three cancer networks (see Table 3.1). Only two proteins, PDPK1 and PRKDC, across three cancer types have positive CS (last two rows in Table 3.1).

Table 3.1: Table showing the cumulative score (CS) and total frequency of the highly impact drug-targets of pancreatic, ovarian and breast cancers from Kanhaiya et al. [142]. All the highly impact drug targets except PDPK1 and PRKDC have negative CS.

Drug-target	**Pancreatic cancer**		**Ovarian cancer**		**Breast cancer**	
	CS	**Frequency**	**CS**	**Frequency**	**CS**	**Frequency**
GSK3B	-71	26				
INSR	-70	16				
RAC1	-45	19				
ABL1	-44	23				
RAF1	-39	33				
AKT1	-39	33	-54	47		
HDAC3	-12	4			-12	4
IGF1R	-9	7				
ERBB2	-5	18			-12	20
GRB2			-36	20		
CDK2			-29	11	-22	13
MTOR			-22	12	-22	12
JAK3			-21	18		
RET			-13	4		
SMO			-4	3		
JAK2					-13	36
SRC					-11	46
PDPK1	6	10			6	12
PRKDC			2	4	2	4

Thus our analysis establishes a strong relationship between sensitive nodes and drug targets. We also checked the influence of abundance biasses and observed that the drug targets are independent of their abundance in the networks. Like in the case of pancreatic cancer, AKT1 and RAF1 are more abundant than GSK3B and INSR, but their sensitivity is much more than AKT1 and RAF1. So, the potential drug targets depend not on the network's abundance but their abundance in the sensitive motifs. Thus, the above results support our hypothesis that the nodes with highly negative CS could be considered potential drug targets.

3.4.5 Biological significance of sensitive nodes as drug targets

We applied our mathematical formalism to find natural drug targets from the cancer networks. The CS for each protein in the network were calculated using the scoring formula described in section 3.4.3. The number of proteins having negative CS decreases exponentially as we decrease the CS (see Fig. 3.9 (a)). So the proteins with higher negative cumulative scores significantly differ from the rest of the proteins in the network. The CS curves for all the three cancer networks in Fig. 3.9 (a) tend to be asymptotic after it crosses the -50 CS value, which means the number of proteins decreases very slowly as we decrease the CS value after -50. Thus, we considered the proteins with CS ≤ -50 as the highly sensitive proteins from all cancer networks to determine the natural drug targets. We collected their available approved drugs from the drug bank database. Out of 24 proteins from breast cancer, 14 proteins have approved drugs against them. In the case of ovarian and pancreatic cancers, 11 out of 13 proteins and 7 out of 13 proteins have approved drugs against them, respectively (see Fig. 3.9 (b)).

We also performed gene ontology (GO) and pathway enrichment analysis to see the biological significance of these highly sensitive nodes. We analysed them using the available bioinformatics tools on the list of sensitive proteins. The GO analysis was performed using the publicly available Enrichr database [147]. For the enrichment analysis of biological processes, we used Enrichr [147], and for disease, we used DisGeNet [148], and for pathway analysis, we used Kyoto Encyclopedia of Genes and Genomes (KEGG) pathways [149]. From the GO analysis, the genes were found to be enriched in the different biological processes involved in

the cancer progression, like negative regulations of apoptotic processes [150], response to reactive oxygen species (ROS) [151], response to oxidative stress [152], cell proliferation [153] (see Fig. 3.10). All the top 10 enriched diseases are also related to cancers (Fig. 3.10). The enriched pathways are also majorly cancer-related (Fig. 3.10). Moreover, the number of genes enriched in all these cases is also significant. Thus, the analysis revealed that the highly sensitive nodes are also closely associated with different cancer-related biological events, and targeting them will influence cancer progression.

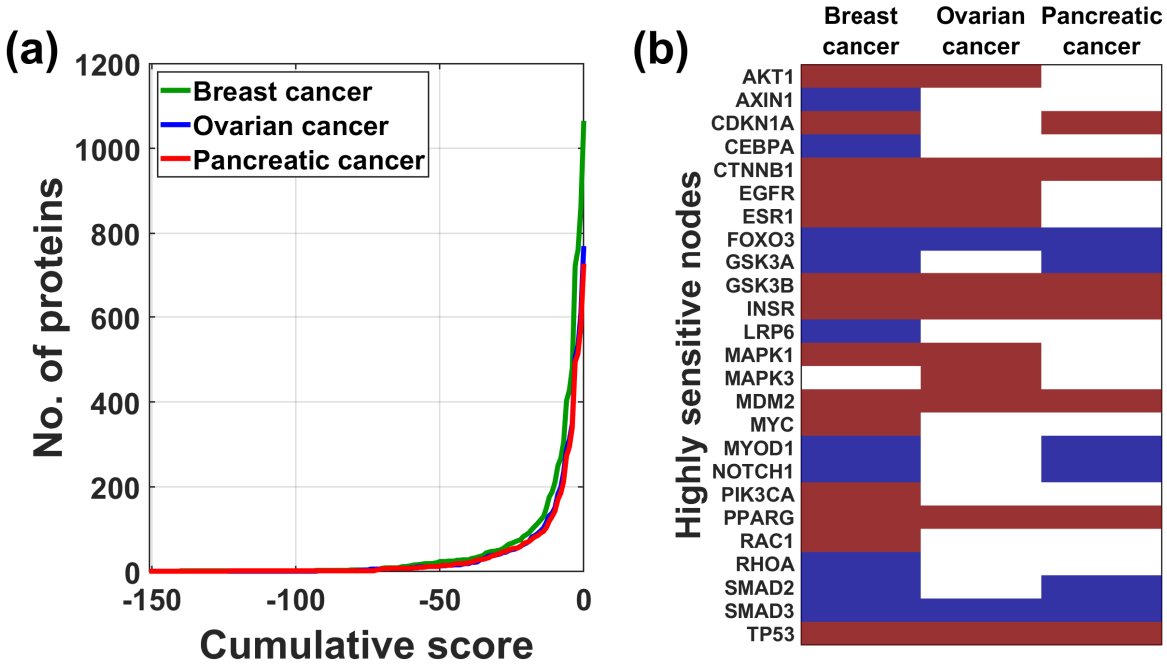

Figure 3.9: **Significance and application of cumulative score.** (a) Graph portrays the abundance of proteins as a function of CS in all three cancer networks. The number of nodes decreases exponentially as we decrease the CS value. (b) The Y-axis shows the highly sensitive nodes (CS ≤ -50) from three cancer networks. Here, the brown colour represents the nodes with approved drugs against them, whereas the blue-coloured nodes do not have approved drugs against them. The white blank shows that the node is not highly sensitive in that particular cancer network.

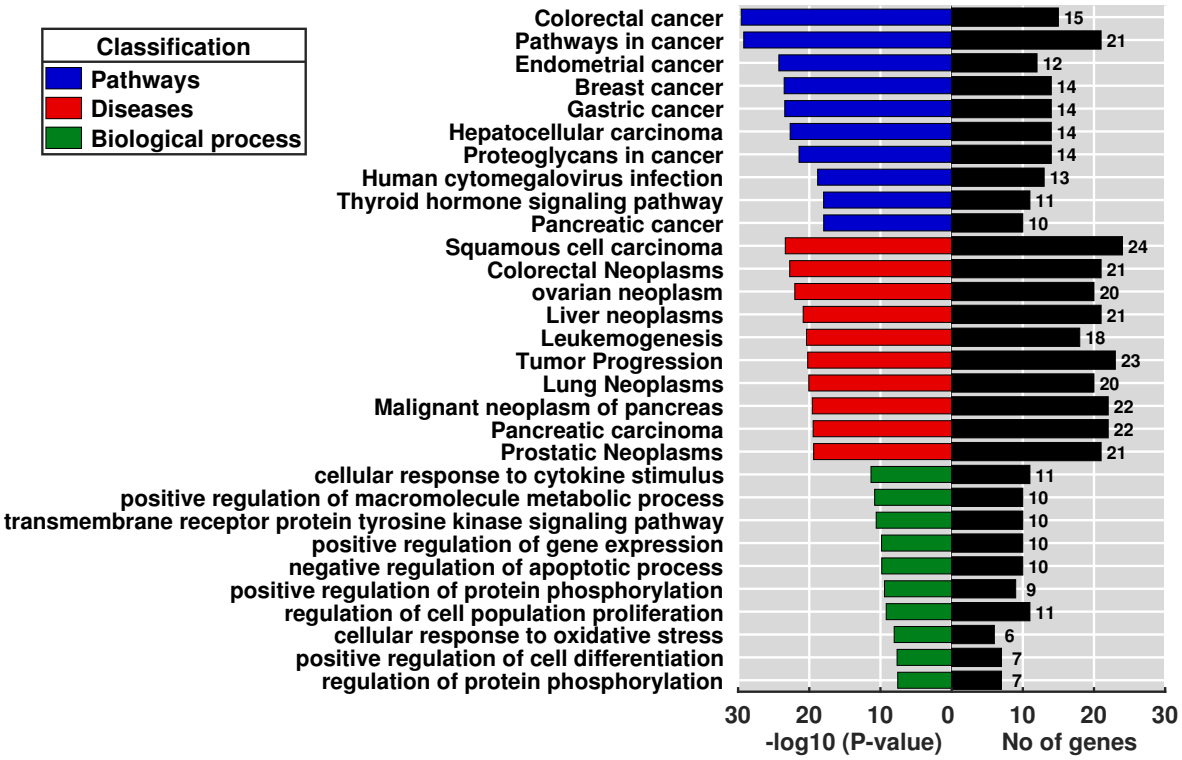

Figure 3.10: **GO annotation and KEGG pathway enrichment analysis of the highly sensitive nodes.** The figure displays the number of genes enriched (black bars) and -log10 (P-value) for the top 10 GO terms in biological processes (green), diseases (red), and KEGG pathways (blue). The classifications are sorted by -log10 (P-value). GO, Gene Ontology; KEGG, Kyoto Encyclopedia of Genes and Genomes.

3.5 Discussion

Protein-protein interactions (PPIs) are crucial for efficient internal or external signals, but this connectivity also amplifies stochastic fluctuations by propagating noise between components [28]. We searched for biological circuits that can maintain proper signalling by minimising noise propagation, focusing on cases where rapid fluctuations characterise the noise. The system's output misbehaves when the noise intensity exceeds the critical value or with an increase in the input stimuli. Moreover, this alteration in the output steady-state is undesirable as up-regulation of an oncogene and down-regulation of a tumour suppressor; in both cases, the system will lead to cancer [154]. We studied such a phenomenon by considering the smallest network motif of a two-node structure and systematically analysed two-component circuits for sensitivity in the presence of noise. The variation in noise tolerance was observed for different

motif structures. We ranked all the motifs according to their vulnerability to systematic noise. Moreover, motif ranking was used to calculate the CS of all nodes in a PPI network to identify potential drug-target candidates. The analysis revealed that the positive feedbacks are mostly robust than the other motif structures with exposure to ample parameter space [28]. In comparison, the double negative feedbacks are the most sensitive one. The motifs without self-loops have also shown vulnerability to intrinsic noise.

We identified some motif structures that are sensitive under systemic perturbations. These sensitive motifs are more likely to go to stochastic instability with the introduction of noise above the critical value or an increase in the input stimuli. Thus, the sensitive motifs play a significant role in maintaining cell signalling through proper I/O relationships. We need to monitor sensitive motifs in case of any unwanted network signal. The druggability [145] of these sensitive motifs was studied, and they were found most likely druggable, whereas the robust motifs are most undesirable for drug targets. So, these sensitive motifs require careful monitoring and are druggable and thus could be used to identify potential drug targets.

In a large protein-protein interaction (PPI) network, maintaining adequate I/O relations between two nodes becomes critical. This could be accomplished by targeting the output node *B*, which appears more frequently in sensitive motifs. We devised a methodology for calculating the CS to identify those nodes, and nodes with a strongly negative CS are regarded as the network's sensitive nodes. We hypothesised that sensitive nodes are prospective drug targets. Our hypothesis was validated by considering three cancer networks from literature [142]. Most approved drugs against all three cancers targeted the sensitive nodes. So, a strong association between the sensitive nodes and the approved drug target was observed. A reverse analysis of the established drug targets by Kanhaiya *et al.* [142] further confirms our proposition.

The biological relevance of the highly sensitive nodes revealed natural drug targets from the cancer networks. It was observed that more than 55% of sensitive proteins from each network already had approved drugs against them (Fig. 3.9(b)). Enrichment analysis of the highly sensitive nodes reveals that the top ten enriched diseases are cancer-related. Also, they are highly enriched in pathways related to cancers. In the case of biological processes, they are enriched in cancer-related processes like negative regulation of apoptotic process [150], regulation of

reactive oxygen species [151], cell proliferation [153] etc. This enrichment analysis reveals that highly sensitive nodes are linked with various cancer-related biological events and that targeting them will affect the disease. Thus, further cementing the possibility of considering sensitive nodes of the cancer networks for the potential drug-target candidates.

The current chapter describes the significance of network motifs in maintaining cell signalling in a noisy environment and provides a methodology for finding potential drug targets. However, the study ignores the importance of bistability in the context of input-output relations. We have observed in Chapter 2 that bistability plays an important role in maintaining proper input-output relation in the presence of noise. So, in the next chapter, we explored all the structures to seek for the existence of bistability and then studied its importance in cell signalling.

4

Bistability in cell signalling and its significance in identifying potential drug targets[1]

4.1 Introduction

The aberration to the complex signalling interactome of cell signalling could lead to various diseases as it governs most of the cellular responses in our body. The complexity of the process further increases in the presence of bistability, where two different output signals coexist for an input signal. The importance of bistability in a biological system is well known, especially in

[1]The bulk of this chapter has been published in *Bioinformatics*, 2021, 37(22), pp.4156-4163.

cell signalling and functioning [71, 76–80], differentiation [71, 76, 77] and cell cycle progression [79–81]. It can enrich the adaptation in organisms extending from bacteria to mammals by storing the cellular memory of the past stimuli [82, 83]. Ferrell and co-workers illustrated that bistability might be led by ultra-sensitivity in positive feedback networks, where the input to the MAPK cascade is positively regulated by the activated MAPK [71, 77, 78]. The possibility of bistability at the level of a single stage of the MAPK cascade is established by Kholodenko *et al.* [84]. The necessary condition for the oscillatory behaviour at the cascade level is single-stage bistability was studied computationally by Qiao *et al.* [94]. The self-perpetuated activation of a signalling circuit is a declaration of its bistability. Alam *et al.* [86] have demonstrated the existence of self-perpetuated activation mechanisms for ERK1/2 in bronchial epithelial cells. As a result, ERK1/2 bistability arises from repetitive stimulation of the cell. They have hypothesised that this self-perpetuated ERK1/2 signal plays an important role in the pathogenesis of asthma.

Inherent stochasticity of the signalling network may influence the emergence of bistability. In recent years, many interesting consequences of random fluctuations have been elucidated theoretically and observed in experiments [25, 97–99]. It has been observed that the deterministic system has a single steady state for all parameter values, but the stochastic response is bimodal [100]. Arkun *et al.* [101] investigate how the positive and negative feedback loops affect the dynamic characteristics that determine the cellular outcome. Positive and negative feedback regulation in the presence of stochastic fluctuation was also observed in other studies [104]. Despite numerous studies, not much work is done on motif structures in deciding input-output (I/O) signal relation in the presence of noise, especially when bistability emerges. In Chapter 2, we have seen the effect of the random perturbation on the observed bistability for two frequently observed motif structures, which demands a more detailed study to understand the global view of the emergence of bistability. So, in this chapter, we have considered all possible two-node network motifs and elucidated the association between the motif structures in the emergence of bistability in a signalling network. Here, we are interested to see how the choice of motif structure influences the I/O relation between two nodes focusing on the existence of bistability. We systematically explore parameter space for different motifs to cap-

ture their role in maintaining bistability. We also studied bistable switching through hysteresis. The findings were then used to design a method that can be applied to any disease network to identify potential drug targets and validate them with the existing data. We also studied the system under random perturbation through stochastic differential equations to probe the issue of maintenance of bistability.

4.2 Mathematical model of general topology with two-node motif structure

To understand a global idea about noise-motif relationship and bistability, in this study, we have considered all the 54 biologically feasible two-node network motifs as discussed in the previous chapter (Chapter 3). Following similar arguments from Chapter 3, we then proposed a model based on a system of ordinary differential equations (ODEs) that consists of activated forms of protein A (denoted by A) and protein B (denoted by B). Here, we have not considered the basal synthesis rate of the individual nodes [56]. Thus a general model can be given by the system of equations (4.1), which then can be reduced to different individual topologies.

$$\begin{aligned} \frac{dA}{dt} &= \frac{k_I I(1-A)}{k_{mI}+(1-A)} + f_A + f_{BA} - \delta_1 A = F_1(A,B), \\ \frac{dB}{dt} &= f_B + f_{AB} - \delta_2 B = F_2(A,B). \end{aligned} \tag{4.1}$$

where f_A, f_B, f_{AB} and f_{BA} take the following forms depending upon the motif structure.

$$f_A = \begin{cases} \frac{k_A A(1-A)}{k_{mA}+(1-A)}, & \text{for self-activation on } A \\ -\frac{k_A A^2}{k_{mA}+A}, & \text{for self-inhibition on } A \end{cases}$$

$$f_B = \begin{cases} \frac{k_B B(1-B)}{k_{mB}+(1-B)}, & \text{for self-activation on } B \\ -\frac{k_B B^2}{k_{mB}+B}, & \text{for self-inhibition on } B \end{cases}$$

$$f_{AB} = \begin{cases} \frac{k_1 A(1-B)}{k_{m1}+(1-B)}, & \text{when A activates B} \\ -\frac{k_1 AB}{k_{m1}+B}, & \text{when A inhibits B} \end{cases}$$

$$f_{BA} = \begin{cases} \frac{k_2 B(1-A)}{k_{m2}+(1-A)}, & \text{when B activates A} \\ -\frac{k_2 BA}{k_{m2}+A}, & \text{when B inhibits A} \end{cases}$$

The system of equations (4.1) describes the rates of loss and creation of particular labelled forms of proteins (nodes). The parameters are described in the previous chapter, Chapter 3. Considering different combinations, we can obtain all the feasible two-node topologies.

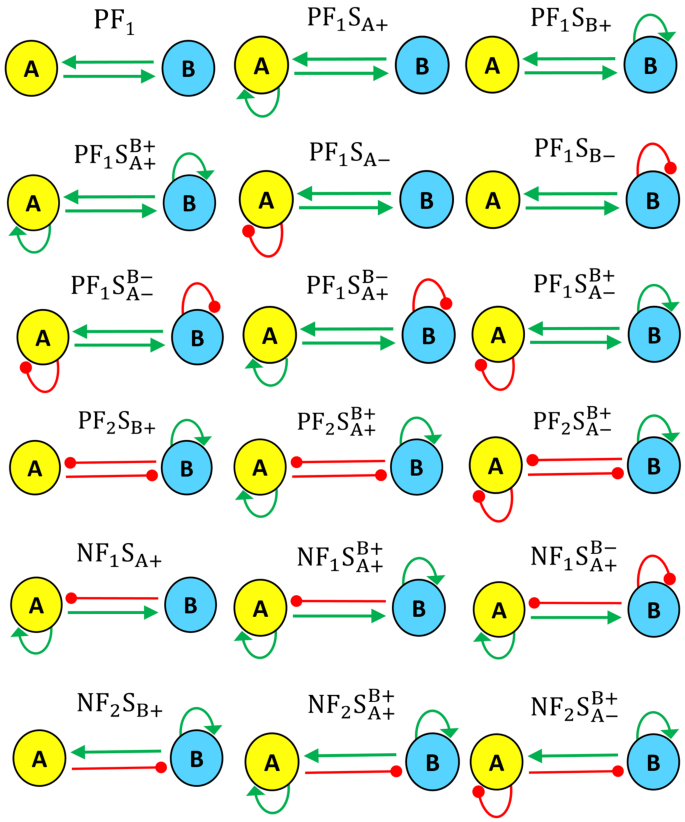

Figure 4.1: **All possible bistable two-node motifs.** The figure illustrates all possible bistable two-node motifs considered in this study. Here arrowed lines (green) represent activation, and lines ending with a circle (red) represent inhibition.

4.3 Existence of possible two-node bistable structures in a signalling network

To address the aim of the study, we look for the existence of bistability in the motif structures. It is known that positive feedback is necessary for the existence of bistability [131]. In the case of negative feedback, the inactivation can be supplemented with a positive term defining a positive feedback (self) loop [132]. We have a total of 12 positive feedback topologies and 6 negative feedback topologies with positive self-loops in the inactivated node that can be considered for the possible bistable topologies. So, for the existence of bistability, further study is done on these 18 topologies depicted in Fig. 4.1.

Next, the steady states were calculated for these 18 topologies to find the bistable motifs. To solve numerically, we choose our model parameter sets from (0,1). We generate 10^5 random parameter sets using the Halton sequences method to pick values uniformly from the space. This quasi-random sampling method uniformly partitions the unit interval in each dimension with equiprobable sub-intervals. So, it removes possible space biases, explores the whole parameter space between (0,1), and looks for a possible parameter set for which the system shows bistability. Then for every motif structure, we calculated the number of feasible (numerical value between 0-1) stable steady states corresponding to each parameter set. So we get a matrix of 10^5 rows (each row is a parameter set) and 18 columns (each column is a motif structure) containing the number of feasible stable steady states. Out of these 10^5 rows, 161 rows contain at least one element greater or equal to 2, i.e. 161 parameter sets have at least one motif showing bistability for that particular parameter set. The topologies that were showing bistability with these 161 parameter sets were $(PF_2S_{A+}^{B+})$, (NF_1S_{A+}), $(NF_1S_{A+}^{B+})$, $(NF_1S_{A+}^{B-})$, (NF_2S_{B+}), $(NF_2S_{A+}^{B+})$ and $(NF_2S_{A-}^{B+})$, see Fig. 4.2. Some of these seven motifs are identified in the literature to be associated with real bistable circuits. The motifs identified are (NF_1S_{A+}), $(NF_1S_{A+}^{B+})$, (NF_2S_{B+}), which is present in the real network as bistable motifs through the proteins given in [132]. The motif structures and the corresponding proteins are known to show bistability are given in Table 4.1.

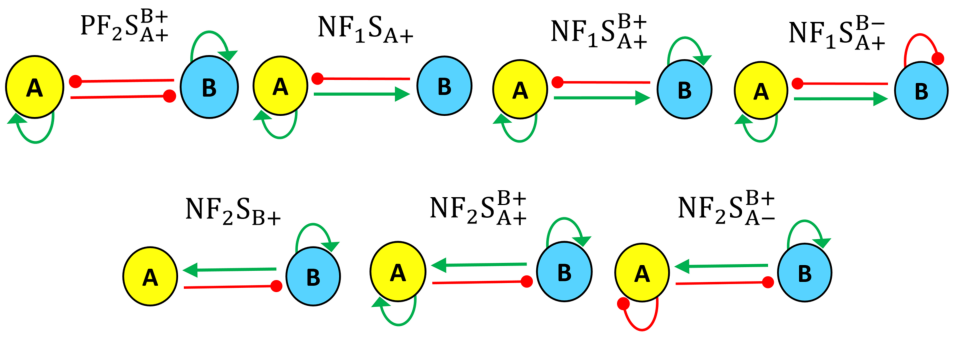

Figure 4.2: **Bistable two-node motifs.** The structures of the seven frequently observed bistable topologies. Here arrowed lines (green) represent activation, and lines ending with a circle (red) represent inhibition.

Table 4.1: The table contains the motifs and the corresponding proteins as a real example from Pfeuty *et al.* [132].

Motif	Protein as input node	Protein as output node
NF_1S_{A+}	CycB	APC
	HetR	PatC
	MEF2	Hdac9
	p53	mdm2
	FOXL2	SIRT1
	Notch	Hes
$NF_1S^{B+}_{A+}$	CycE	CycA
	Ime1	Ime2
NF_2S_{B+}	Ptc	Gli

4.4 Sensitivity of parameters towards the occurrence of bistability

It is known in the literature that the sensitivity of a circuit depends on parameters like positive feedback [28, 155]. Next, we want to see the effect of parameters on the occurrence of bistability. The sensitivity of the parameters for each topology was identified with respect to output by performing the global sensitivity analysis. The global sensitivity analysis (GSA) is used to

determine the important parameters of the model. In GSA, the Partially Ranked Correlation Coefficients (PRCC) [115] technique is used to calculate the associated p-values to determine the most sensitive parameters. For each run of PRCC calculations, the randomly selected vectors of parameter values were generated by Latin Hypercube Sampling (LHS) method. Over 1,000 simulations were performed to calculate PRCCs. For each simulation, the system was solved up to 100 time steps, as it was observed from the time series solutions that the system behaves uniformly much before 100 time steps. We used a cut-off of ± 0.3 [156, 157] to define the sensitive parameters, i.e. if the PRCC value of a particular parameter lies beyond ± 0.3, then that parameter will be called a sensitive parameter. The global sensitivity analysis (GSA) result is given in Fig. 4.3. The GSA analysis suggests that the most sensitive parameters are k_I, k_1, δ_2, I, δ_1, k_B and k_{m1}. Explicitly it can be seen that δ_2, the degradation rate of node B, is negatively correlated with the output node B for all the motif structures. The rate of activation of input node A by input stimuli I (k_I), rate of activation or inhibition of output node B by node A (k_1) and input stimuli I (I) are positively correlated with the output node B for the motif structures where node A activates node B and they are negatively correlated in those motifs with node A inhibiting node B.

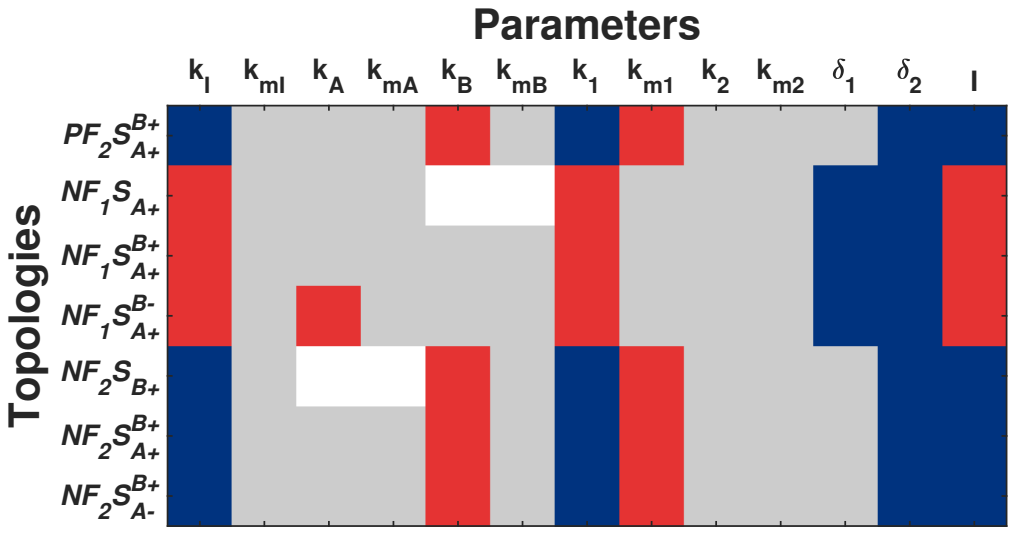

Figure 4.3: **Global sensitivity analysis.** Figure depicts the sensitivity of system parameters for all seven bistable motifs. Here red and blue colours represent sensitive parameters with respect to output node B. The correlation of parameters with respect to output node B are as follows: Red: PRCCs ≥ 0.3, Blue: PRCCs ≤ -0.3, Grey: $0.3 >$ PRCCS > -0.3, White: parameter is not present in the motif.

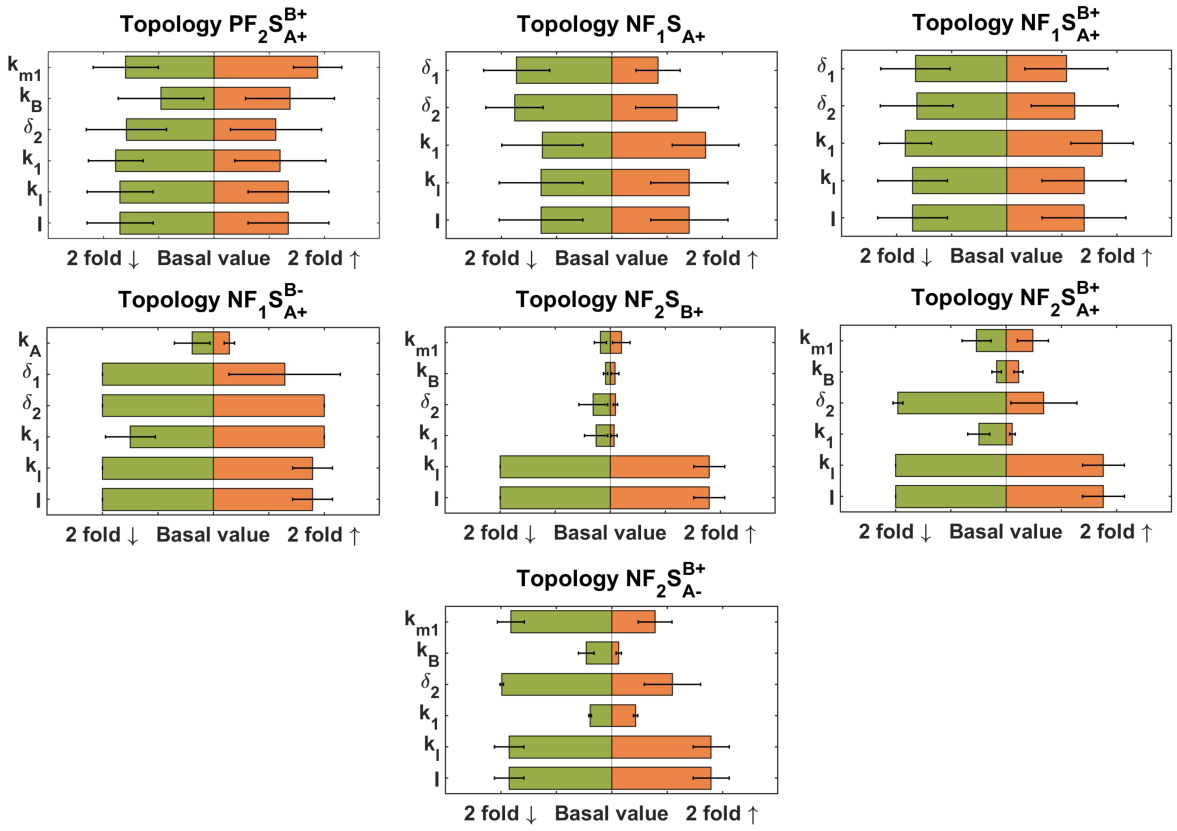

Figure 4.4: **Robustness analysis.** Here, each bar represents the mean fold change of a particular sensitive parameter from its basal value for which the topology shows bistability, and the error bar represents the standard deviation. Green bars on the left-hand side of the basal value portray the range of parameters when it is reduced from the basal values, while the orange bars on the right are the ranges when they are increased from the basal values.

4.5 Robustness of sensitive parameters towards the maintenance of bistability

We varied each sensitive parameter two-fold up and down from the basal values to study their effect on the existence of bistability. Here the basal values are defined by the parameter values for which we obtained the bistability of the motif structures. The same exercise is repeated for all the bistable parameter sets of each motif structure and plotted their mean and standard deviation (Fig. 4.4). We observed that the input stimulus (I) and its rate (k_I) are robust in all motif structures with respect to the bistability of the system. That is, the input parameter maintains bistability for a wider variation compared to the other sensitive parameters of the systems. Since bistability is crucial in cell signalling and functioning, the robustness shown by

the input parameter in maintaining the bistability of the system motivates us to explore further the role of this parameter in the existence of bistability.

4.6 Bistable property of a motif structure can be applied to identify potential drug targets through hysteresis

Bistable systems often exhibit a kind of memory known as hysteresis [72]. Hysteresis is the phenomenon where bistable switching is observed for different stimulus-response [73, 74]. The two response curves form two loops, known as the hysteresis loop [75], that represent two discrete stable steady states for a single value of the stimulus. Thus the input-output (I/O) relation becomes a loop rather than a curve. This hysteretic switching can be categorised into two types, reversible and irreversible [75]. If it comes back, it is reversible hysteresis; otherwise, it is irreversible. Whether a system will have reversible or irreversible hysteresis depends on the strength of the feedback parameter [71]. A reversible hysteresis can be changed to an irreversible hysteresis by increasing the strength of the feedback parameter. Here we varied the input parameter I between 0 to 1, showing the strength of the input signal. The input signal is weak when close to zero and is highest at 1. A similar range is also available in literature [132]. To understand the reversible and irreversible hysteresis in our bistable motifs, let us take the example of the topology NF_1S_{A+}. It was observed that one steady state (say OFF) goes to another steady state (say ON) with the increase in the input stimulus (I). The system may or may not return to its initial OFF state when the input parameter is reversed (Fig. 4.5). Both types of hysteresis were also observed in other bistable structures.

As the feedback strength of the bistable system defines the nature of hysteresis, it is important to study each motif structure for the separate ranges of feedback strengths. So we calculated the fold change of the feedback parameter for every bistable parameter set and its mean and standard deviations (Fig. 4.6). We could use this information to rank the motifs according to their ability to reverse back. The topology $NF_1S^{B+}_{A+}$ has the largest feedback parameter range, while $NF_2S^{B+}_{A+}$ with the smallest. Since in reversible hysteresis, we can bring back the initial steady state by reversing the input parameter value. We hypothesize that the motif with a larger

reversible hysteretic feedback parameter range might be a better consideration for a potential drug target candidate.

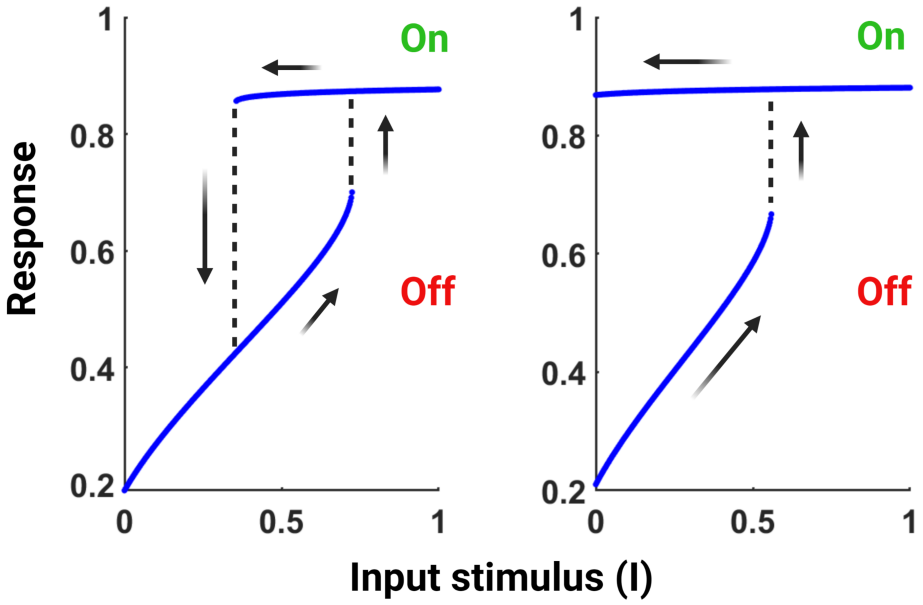

Figure 4.5: **Bistable properties through hysteresis.** The figure illustrates reversible and irreversible hysteresis. The left and the right panels show reversible and irreversible hysteresis in NF_1S_{A+} for feedback parameter $k_2 = 0.28$ and 0.2652, respectively.

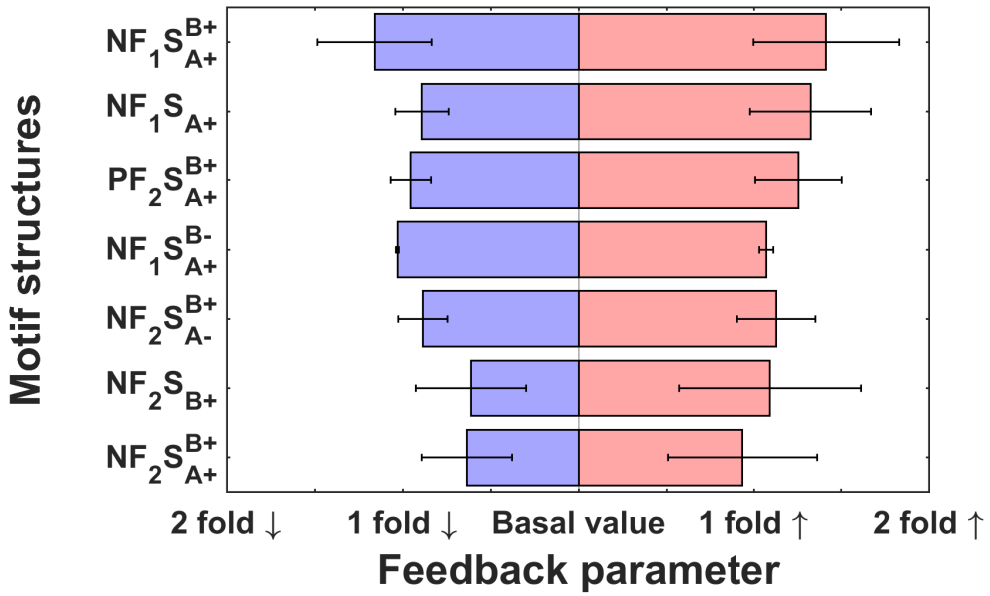

Figure 4.6: **Feedback and reversible hysteresis.** The figure depicts the mean range of feedback parameter (k_2) fold change for which different structures show reversible hysteresis, and the error bar represents its standard deviation. The motifs are arranged in the decreasing order of their reversible hysteretic feedback parameter range.

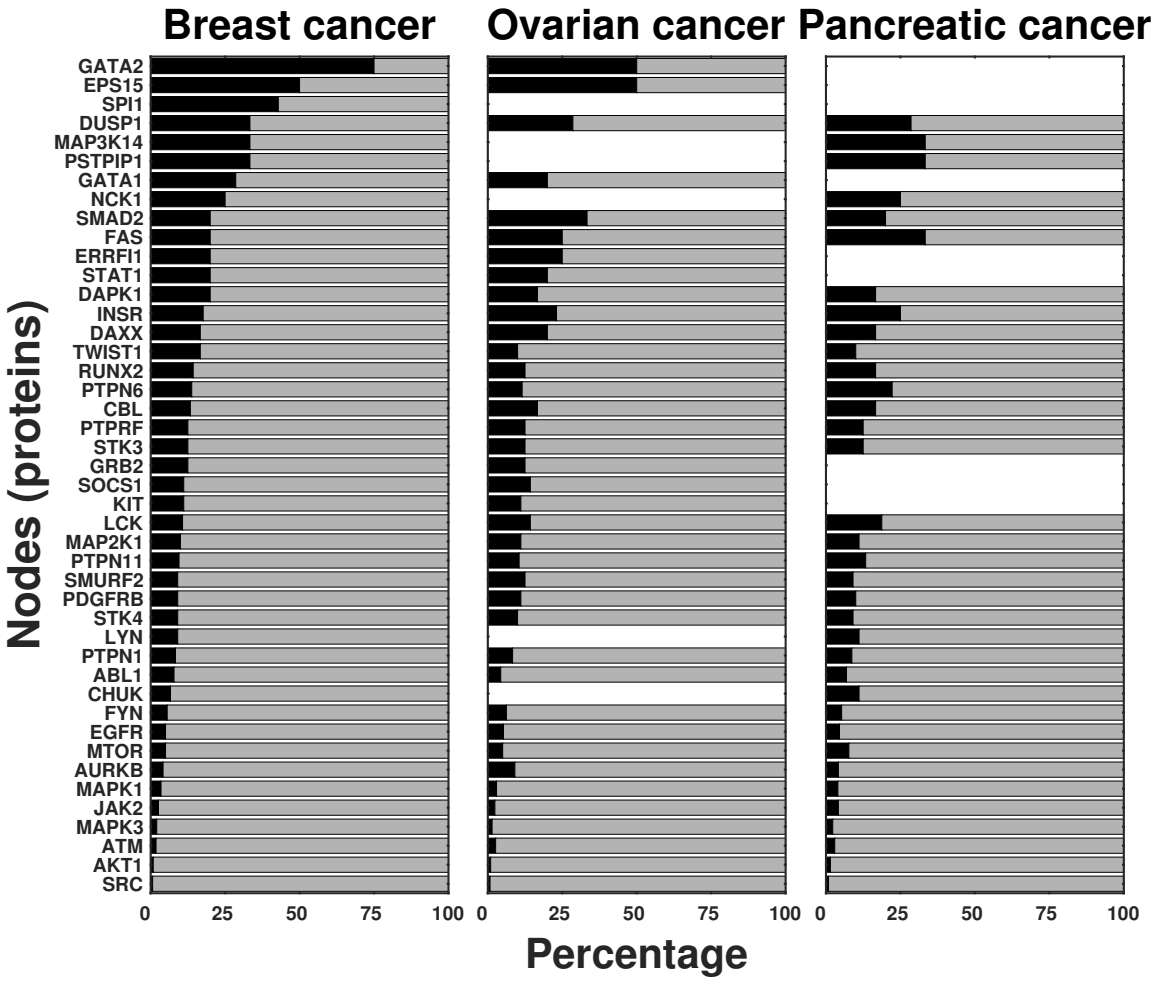

Figure 4.7: **Abundance of bistable nodes (proteins) in PPI networks.** Here Y-axis represents the list of proteins from the cancer networks that are present in bistable motifs as input nodes. The black bar in the X-axis represents the percentage of those proteins present in the network as a part of the seven bistable motifs. The grey bar shows the percentage when they are present in other motifs. White blanks show the absence of the protein as either of the two.

4.7 Validation of the model predictions using existing drug information

Bistability exists in networks, and we establish that its occurrence depends on the motif structure. We also hypothesize that the structure with a larger reversible hysteretic range could be a better drug target. So, we now look to validate our hypothesis in a real biological network, which will also establish the significance of the present study. We considered three disease networks and studied them in the context of bistability. The three diseases considered for our

study are breast, ovarian and pancreatic cancer. We built directed protein-protein interaction (PPI) networks using the data available in the literature [142]. To get a directed PPI (signalling) network, we used SIGNOR (SIGnaling Network Open Resource) database [146], which outputs binary matrix representations of the user-provided protein lists. Using the database, we created directed graphs among the signalling proteins. We obtained directed PPI networks of 5092 interactions from 1415 nodes for breast cancer, 4134 interactions from 1045 nodes for ovarian cancer, and 4030 interactions from 990 nodes for pancreatic cancer.

Next, we wanted to find the distribution of proteins associated with the bistable motifs in these networks. 44 out of 1415 nodes in the breast cancer network, 38 out of 1045 nodes in ovarian cancer and 35 out of 990 in pancreatic cancer are present as input nodes of bistable motifs. The distribution of those proteins in respective networks is given in Fig. 4.7. It was observed that the sets of 38 nodes from the ovarian cancer network and 35 from the pancreatic cancer network are subsets of the 44 nodes from the breast cancer network. So, some proteins are missing from the ovarian and pancreatic cancer list in the distribution of bistable nodes.

We then compared our results with available drug target information to see how many of these proteins are known as drug targets. Reversible hysteresis reverses the system back to the non-disease state from the disease state by reducing the input parameter, which can be done with the help of a drug. So in our study, we will use input nodes as the drug target. Firstly, we extract drug-target protein data from the open-source Drugbank database [158]. Extensive information about drugs and their targets is given in the Drugbank database, which includes information of chemical, pharmacological and pharmaceutical-specific drugs integrated with structures, pathways and sequence drug targets. We first draw out only the proteins that have been used as a drug target. Next, we find the available drugs targeting only those bistable proteins obtained from our study. We considered those proteins in the networks present as the input node of the bistable motifs and used as drug targets at least once in the open-source Drugbank database [158]. We arranged the motif structures in the descending order of their feedback parameter range of reversible hysteresis and plotted their frequency in those motifs. We observe that the proteins which are present in the motifs with higher reversible feedback range tend to be associated with higher numbers of drugs (Fig. 4.8), thus, validating our hypothesis that the

structure with larger reversible hysteretic range can be a better drug target.

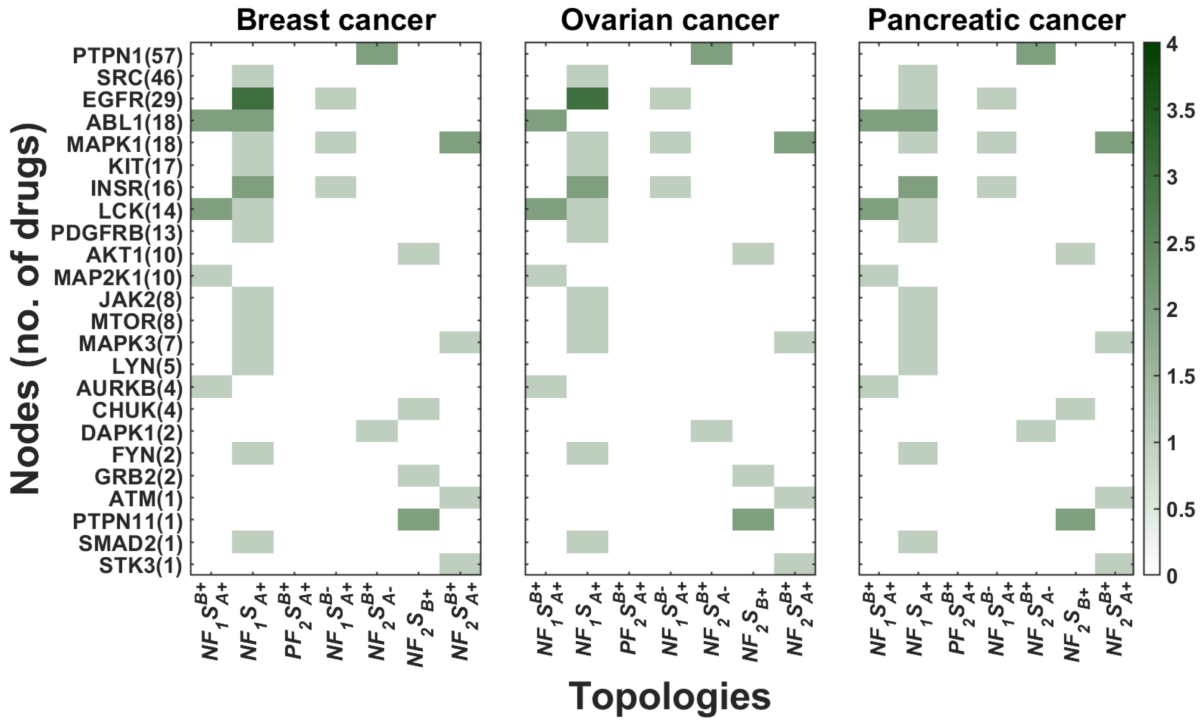

Figure 4.8: **Drug targets and reversible hysteresis.** In this figure, the Y-axis represents proteins that are present in bistable motifs as input nodes in cancer networks and also used as drug targets. The X-axis represents the topologies in descending order of the reversible hysteresis feedback parameter range. The colour bar represents the frequency of a particular protein as an input node in that particular motif.

We want to verify that the observed result is not because the higher-ranked motifs are more abundant than the others. In other words, the claim that the proteins associated with motifs with larger reversible hysteretic ranges are better drug targets is unrelated to their abundance. The frequency distribution of bistable motifs in three cancer networks is given in Table 4.2. We calculated the Spearman's rank correlation [159] between the motif's rank according to the hysteretic property and its rank according to its abundance in all three cancer networks. No correlation was observed between the two motif ranks in the three cancer networks. The rank correlation coefficients are -0.171 for the breast cancer network and -0.2143 for the ovarian and pancreatic cancer networks. Hence, the motifs with larger reversible hysteretic ranges may not be abundantly present in the cancer networks, but still, the associated proteins are targets of numerous drugs.

Finally, we looked for the drug targets in the network associated with the list of drugs

Table 4.2: Frequency distribution of bistable motifs in three cancer networks.

Motif	Breast cancer	Ovarian cancer	Pancreatic cancer
$NF_1S_{A+}^{B+}$	8	7	6
NF_1S_{A+}	22	18	18
$PF_2S_{A+}^{B+}$	4	0	0
$NF_1S_{A+}^{B-}$	3	3	3
$NF_2S_{A-}^{B+}$	3	3	3
NF_2S_{B+}	22	18	18
$NF_2S_{A+}^{B+}$	8	7	6

mentioned by Kanhaiya *et al.* [142] (Table 4.3) and found that they belong to the motifs with larger reversible hysteretic range. For example, one of the two targets of the drug Lapatinib is EGFR which belongs to the bistable motif with a higher reversible range. In another example, the drug Dasatinib has 23 targets, of which seven are from bistable motifs and that too from the top two ranks. We will see our formalism on these real targets through an illustrative example. Let's consider the ABL1 as a target to understand how hysteresis might play a role in switching the system's behaviour. ABL1 interacts with NCK1 through the NF_1S_{A+} motif. Dasatinib, bosutinib and ponatinib inhibit ABL1 causing a reduction in NCK1 as they are present in NF_1S_{A+} motif (see Table 4.4). The decrease in NCK1 reduces cell proliferation that controls the breast cancer [160], similar to what was observed in the reversible hysteresis (left panel Fig. 4.5), where reduction in the input signal causing a switch in the output node state leading to a change in the system behaviour. To further validate this theory, it was observed that the output nodes associated with the other drug target proteins through the bistable motifs are also linked with breast cancer. The input and output proteins corresponding to each drug target are given in Table 4.4. The downregulation of these proteins or reduction in their concentration leads to a reduction of cell proliferation [161–163].

Table 4.3: Table showing drugs from Kanhaiya *et al.* [142] with their targets present as bistable motifs

Drugs	**Total number of targets**	**Targets present as bistable motifs**	**Bistable motif where the targets are present**
Lapatinib	2	EGFR	NF_1S_{A+}, $NF_1S^{B-}_{A+}$
Dasatinib	23	ABL1, SRC, LCK, KIT LYN, FYN, PDGFRB	NF_1S_{A+}, $NF_1S^{B+}_{A+}$
Bosutinib	10	ABL1, SRC, LYN, MAP2K1	NF_1S_{A+}, $NF_1S^{B+}_{A+}$
Ponatinib	15	ABL1, KIT, LCK, SRC, LYN	NF_1S_{A+}, $NF_1S^{B+}_{A+}$
Temsirolimus	1	MTOR	NF_1S_{A+}
Ruxolitinib	4	JAK2	NF_1S_{A+}
Erlotinib	2	EGFR	NF_1S_{A+}, $NF_1S^{B-}_{A+}$

Table 4.4: Distribution of the output nodes of the drug targets mentioned in the Table 4.3.

Drug targets	NF_1S_{A+} **(output node)**	$NF_1S^{B+}_{A+}$ **(output node)**
KIT	GRB2	-
JAK2	PTPN11	-
PDGFRB	PTPN11	-
MTOR	AKT1	-
MAP2K1	-	MAPK1
FYN	PTPRF	-
EGFR	CBL, EPS15, ERRFI1	-
ABL1	NCK1, PSTPIP1	STK3, STK4
LCK	PTPN6	MAPK1, MAPK3
SRC	PTPN6	-
LYN	PTPN6	-

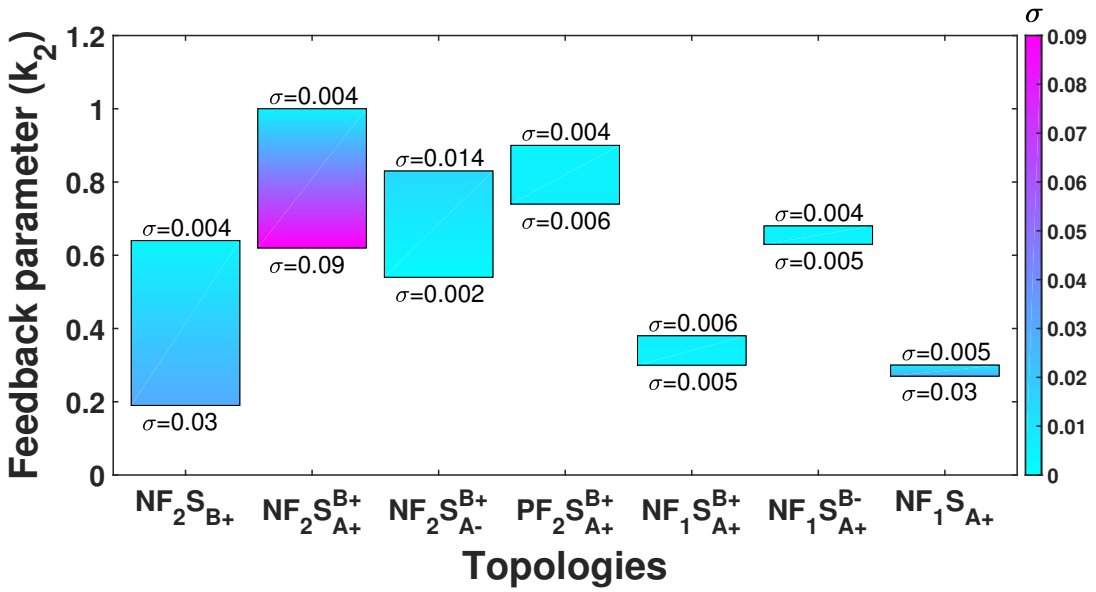

Figure 4.9: **Effect of stochasticity on model prediction.** Figure depicts the reversible hysteretic range of feedback parameter (k_2) and their corresponding minimum strength of noise (σ) required to move one of the steady state clouds to the other for all the bistable topologies. The reversible hysteretic feedback range along with the σ_c value were calculated with the parameters given in Table 4.5.

4.8 Disruption of bistability due to the introduction of random perturbations

It is known that an increase in stochastic perturbation may affect the cellular signalling memory. In other words, it can switch the system from one steady state to another steady state [99, 105], which we have seen in Chapter 2. So, it would be interesting to see the effect of the stochastic perturbation on the bistability of our systems. We build a stochastic differential equation (SDE) based model by adding noise to the deterministic system, following similar arguments in Chapter 3. We calculated the steady states keeping the intensity of the fluctuations σ_1, σ_2 below a certain threshold value σ_c determined by solving the SDE models. We observed a similar loss of bistability for topology $NF_1S^{B-}_{A+}$ as of structure 1 in Chapter 2. We observed that the system remained bistable for small noise intensity less than σ_c. When one of the σ's was increased, movement of stochastic clouds was observed. Thus an increase in the noise intensity distorts the bistable system into a monostable system. In such a condition, the system can not be reversed back to the previous steady state, making it irreversible, though the corresponding

deterministic system shows reversible hysteresis. The influence of the stochasticity on the reversibility depends on the strength of the noise intensity, which again depends on the feedback parameter values. So, we have calculated the minimum noise strength required to change the bistable system to a monostable system for all the bistable motifs for the parameter set given in Table 4.5, see Fig. 4.9. This analysis was performed for one parameter set to demonstrate the effect of the random perturbation on the model hypothesis. That is, even though deterministic systems experience reversible hysteresis, reversibility may be lost due to noise above some threshold value.

Table 4.5: Table contains one parameter set for each topology from 161 sets that give bistable steady state.

Parameters	**Topologies**						
	$PF_2S_{A+}^{B+}$	NF_1S_{A+}	$NF_1S_{A+}^{B+}$	$NF_1S_{A+}^{B-}$	NF_2S_{B+}	$NF_2S_{A+}^{B+}$	$NF_2S_{A-}^{B+}$
I	0.3671	0.2904	0.4348	0.2161	0.2204	0.1616	0.0286
k_I	0.2823	0.1155	0.1867	0.1263	0.1360	0.4012	0.1580
k_{mI}	0.5802	0.7652	0.7801	0.3401	0.4375	0.6755	0.4596
k_A	0.9336	0.3448	0.9833	0.4998	-	0.7117	0.3104
k_{mA}	0.1014	0.0565	0.4083	0.0203	-	0.7927	0.9311
k_B	0.6998	-	0.8252	0.2573	0.4370	0.5659	0.7611
k_{mB}	0.1833	-	0.5157	0.8689	0.1815	0.0532	0.1517
k_1	0.4267	0.6000	0.3132	0.8099	0.4440	0.5460	0.2076
k_{m1}	0.8511	0.2887	0.5770	0.6115	0.9046	0.1709	0.0288
k_2	0.6279	0.2625	0.2636	0.6280	0.5688	0.8600	0.7021
k_{m2}	0.3624	0.0936	0.1090	0.4531	0.9936	0.6307	0.9699
δ_1	0.0832	0.0107	0.0697	0.0443	0.0252	0.8200	0.1001
δ_2	0.0930	0.1755	0.0226	0.0567	0.0256	0.1473	0.3314

4.9 Discussion

Bistability is a crucial feature of dynamical systems and is used in various all-or-none kinds of decision-making processes [14, 164]. It is a phenomenon where two distinct stable steady states coexist in a given set of experimental conditions [70]. It has been observed in a number of biochemical systems [165, 166]. The occurrence of bistability in biological systems has attracted a lot of attention in recent years [167–170]. The presence of bistability in a signalling network plays a crucial role in the input-output (I/O) relation. It is also known that stochastic fluctuations or randomness are inherently present in the signalling network [96]. So, we were interested in studying the effect of stochastic fluctuations or randomness on the occurrence of bistability. Here, by means of a theoretical model, we have also analysed the conditions for which bistability occurs. We looked for a relation between network motif structures and the occurrence of bistability in a signalling network.

We considered the smallest network motif of a two-node structure and analysed for the existence of bistability. Our analysis revealed that 7 out of 18 two-node possible bistable structures were showing bistability with exposure to ample parameter space. We observed six of them have negative feedback supplemented by positive self-loops. Some of the identified motifs are reported in the literature to show bistability. After establishing the link between the motif structure and the occurrence of bistability, we wanted to identify parameters driving the motif structures towards bistability. Our sensitivity analysis revealed that the parameters, like the output node's degradation rate, are sensitive in most of the motif structures. We take forward eight such sensitive parameters to study their effect on the existence of bistability for each structure. The effect of parameter variation leads to different outcomes for different motif structures. In some structures, these parameters showed little effects like $PF_2S_{A+}^{B+}$, NF_1S_{A+} and $NF_1S_{A+}^{B+}$, while in others, the effect was immediately observed with parameter variation like NF_2S_{B+} and $NF_2S_{A+}^{B+}$.

One of the most sensitive parameters obtained from our study is the input signal I. It is known that the bistability switching phenomenon, referred to as hysteresis, is observed for different stimulus-response [73, 74]. So, we studied the effect of the input signal on bistability through hysteresis. It better captures the importance of input signals in maintaining and switch-

ing states in a bistable system. We studied the hysteresis in all seven bistable motif structures. Up-regulation of a particular protein is a common phenomenon in many cancers [154]. So we referred to the higher steady state of the hysteresis loop as the disease state (or ON state) and the lower disease-free state (or OFF state). However, in some cases, the higher state could be disease-free, like in the case of tumour suppressor proteins [154]. In both these cases, the absence of input stimulus is referred to disease-free (OFF) state, which will change if the absence of stimulus is referred to disease state. By this consideration, we can explain all the possibilities. We are not specifying the disease and disease-free state as it is beyond the scope of the current study. However, our method can be applied to a specific motif in a network to extract relevant information. For simplicity, we refer to one state as disease free (OFF) and the other as disease state (ON). A protein in any state (ON or OFF) remains robust for certain levels of perturbation [171]. So a certain increase in the input signal does not affect the steady state, and if it is in a disease-free state, it remains there until the input signal crosses a certain value, and the system migrates to the disease state.

The bistable system can reverse back to its previous state if it shows reversible hysteresis, which is impossible for irreversible hysteresis. So reversible hysteresis can make the system disease-free (OFF) state from a disease (ON) state by reversing the input parameter, which is difficult for irreversible hysteresis. The transition of reversible and irreversible hysteresis depends on the feedback parameter of the system. We obtained ranges of feedback parameters for reversible and irreversible hysteresis for each bistable motif structure. We hypothesise that the nodes following motifs with a larger feedback range of reversible hysteresis can be better or easier drug targets. Based on the hypothesis, we ranked the motifs, and the obtained rank is independent of the chosen parameter set.

The hypothesis was validated using three directed protein-protein interaction networks associated with breast, ovarian and pancreatic cancer. 50% of the nodes were only present as the input node of bistable motif structures and not featured in the other motifs. We also searched for the nodes already used as drug targets from the open-source Drugbank database. The nodes in the motifs with larger reversible hysteretic feedback range are associated with a higher number of drugs. Thus reversible hysteresis might be a good indicator for identifying drug targets.

We further observed that the known drugs tended to target the bistable motifs and are associated with those with larger feedback effects. However, the challenge involves the existence of such reversible hysteresis in the presence of a noisy environment. It has been observed that stochastic effects can change the reversible and irreversible hysteresis [172]. When a cell goes to ON state from OFF state due to stochastic perturbation, it does not reverse back [60]. We also observed in Chapter 2 that when the noise intensity crosses the critical value, the system loses its bistability and becomes monostable. The existence of bistability is important in many biological processes, so the loss of bistability in the presence of random perturbation may cause cellular dysfunction, which needs further investigation. We also observed that the effect of stochasticity on reversibility depends on the strength of the feedback and noise intensity.

In this chapter, we explored the emergence of bistability and used it to identify the potential drug targets from the cancer networks. After establishing the significance of bistability in cell signalling networks, we want to explore it further to understand how bistability works in making decisions in real biological processes. So in the next chapter, we have considered the tumour necrosis factor (TNF) signalling network to understand the complex mechanism of cell survival and death in regulatory T cells.

5

Bistability regulates TNFR2-mediated survival and death of T-regulatory cells[1]

5.1 Introduction

A particular subpopulation of T cells known as T-regulatory cells (Tregs) suppresses immunological response to preserve homeostasis and self-tolerance. It has been demonstrated that Tregs can limit T cell expansion and cytokine production and are essential for avoiding autoimmunity [173]. On the other hand, in the case of cancer, Tregs infiltrate into several tumour tissues to suppress the effector functions of tumour-specific T cells [174]. Through direct and bystander inhibition, Tregs influence immunological tolerance. In direct suppression, Tregs act

[1]The bulk of this chapter has been published in *Journal of Biological Physics*, 2023, https://doi.org/10.1007/s10867-023-09625-3

to specifically inhibit the target cell in response to an antigen. Whereas in bystander suppression, Tregs specific for one antigen might inhibit immunological responses to other antigens in close proximity. Thus, immunological tolerance is restored, and these anti-inflammatory responses maintain immune homeostasis [175].

Conventionally, a decrease in the functional Treg number is often correlated with the disease severity in autoimmune diseases [176]. However, a diverse pattern related to Treg frequency can be seen in the case of autoimmune diseases. A consistent decrease in Tregs number is observed in systemic lupus erythematosus (SLE) subjects [176], in the case of multiple sclerosis (MS), both an increase [177], and a decrease [178] in Tregs numbers were observed. Contrastingly, an increase in Tregs number was observed in rheumatoid arthritis (RA) and type-1 diabetes (T1D) patients [179, 180]. Although the number of Tregs in peripheral blood increases in the case of T1D but they have diminished functionality [181], a similar functional deficiency was also observed in the case of RA patients [182].

The contributing inflammatory responses that mark the pathogenesis of many autoimmune diseases begin with the up-regulation of tumour necrosis factor (TNF), which can bind to its two receptors, tumour necrosis factor receptor 1 (TNFR1) and tumour necrosis factor receptor 2 (TNFR2). Nearly every cell in the body expresses TNFR1. TNFR2 is expressed in more limited cells, which include T-regulatory cells (Tregs). Thus, TNFR2 becomes a more attractive molecular target than TNFR1 [183]. Exogenous TNF alone has a systemic harmful effect when TNFR1 is activated. TNFR2 offers better protective behaviour in diseases like autoimmunity, cardiac diseases, demyelinating, neurodegenerative disorders, and infectious diseases [183]. Several defects, including TNFR2 gene polymorphisms and TNFR2 receptor shedding, are present in many autoimmune disorders. These include graft versus host disease, Crohn's disease, ulcerative colitis, and familial rheumatoid arthritis [183]. TNFR2 agonism has been a common strategy to destroy autoreactive T cells in various autoimmune diseases [183–187].

A highly complicated signalling network like TNF signalling frequently exhibits intricate dynamic regulation in response to perturbations. It has been established that mathematical modelling is a crucial method in the study of complex networks and dynamic systems in TNF signalling. Since mathematical modelling is important in molecular biology, it has been used

to construct testable hypotheses and guide experimental design to maximise the information obtained [188–193]. These mathematical models can unravel complex mechanisms like bistability, demonstrating the all-or-none decision-making processes to determine the fate of cells [194, 195]. The mathematical model on bistability was also used to understand evolutionary reversibility by Kheir Gouda *et al.* [87]. These extremely complex signalling systems could be further influenced by the inherent noise present in the signalling network [96]. Low copy numbers of the chemical reactants and their diverse distribution inside the cell are the root causes of randomisation at the intracellular level [196]. Numerous intriguing effects of random fluctuations have recently been theorised and experimentally verified [25, 95, 97–99]. In Chapter 2, we have seen that the bistability can be lost due to the presence of randomness in the system. Therefore, it is important to examine noise in these complicated systems.

The commonality of TNFR2 signalling abnormalities and the diverse patterns related to Treg frequency observed in autoimmune diseases motivated us to study the TNFR2 signalling pathway in Treg cells. TNF-mediated apoptosis is one of the intricate and carefully controlled cellular processes brought on by activating both pro- and anti-apoptotic signalling pathways. So, we are curious to understand the mechanism governing Treg cell survival and death that could facilitate targeted treatment for the disease. To capture the process of cell survival and death in Treg cells via TNFR2 signalling, an ordinary differential equation (ODE) based model was developed and analysed. The model reveals the existence of bistability in the system. The system strives to adapt to changing stimuli through hysteretic switching. We compute bifurcation diagrams and create cell fate maps to analyse how stimulus strength and feedback strength affect cell survival and death. Our findings suggest that the main causes of the death of Tregs are an elevated level of TNF and enhanced JNK phosphorylation. Finally, the system was studied in the presence of random perturbations to capture the influence of noise in the observed bistability.

5.2 Construction of the deterministic model

We proposed a simplified mathematical model of TNFR2 signalling in Treg cells to understand the underlying mechanism of TNF-mediated survival and death. To construct the mathematical model, we adopted the TNFR2 signalling pathway described in Fig. 5.1 from Kyoto Encyclopedia of Genes and Genomes (KEGG) pathways [149, 197] and literature [183, 198]. The model consists of the input stimuli TNF (I), which binds to its receptor TNFR2, forming the TNF-TNFR2 complex ($TR2$). After the initial trigger, we suppose that the signal moves towards the end irreversibly. The complex $TR2$ activates TNF receptor-associated factors 1, 2, 3 (TRAF1/2/3), which further activates the downstream signalling pathways. TRAF1/2/3 activates the IkB kinase (IKKs) via multiple signalling pathways through successive phosphorylation of the intermediate molecules like phosphoinositide 3 kinase (PI3K), protein kinase B (Akt), nuclear factor kappa B inducing kinase (NIK), cellular inhibitors of apoptosis proteins 1 and 2 (cIAP1/2) and receptor-interacting protein (RIP). Finally, IKKs activate nuclear factor kappa B (NF-κB) by phosphorylating the inhibitor of NF-κB (IκBα). The transcription factor NF-κB ensures cell viability by dissociating from its cytoplasmic inhibitor protein IkBα and moving to the nucleus, where it activates target genes that are involved in cell survival [183]. So, we have considered the concentration of activated NF-κB as the survival complex (S). $TR2$ also activates disabled homolog 2-interacting protein (AIP1), which further activates its downstream protein c-Jun N-terminal kinase (JNK (J)), which can promote cell survival by activating transcription factor Jun (c-Jun). Moreover, c-Jun promotes cell survival by activating the Akt survival pathway [199], which eventually activates NF-kB. Thus, we can consider the activation of the survival complex by JNK via an indirect link. Also, c-Jun can prevent apoptosis by cooperating with NF-κB [200]. Apoptosis is triggered and carried out by caspase activation [198]. Thus, we have taken the concentration of caspase as the apoptotic complex (A), which is also the system's output. Long-term JNK activation "breaks the brake" on apoptosis by inactivating suppressors of the mitochondrial-dependent death cascade [198]. TNF activates NF-κB, which prevents caspase activation and prevents TNF-induced apoptosis [198]. The additional downstream linkages and the cross-talks were not included to keep the mathematical model simple for analysis.

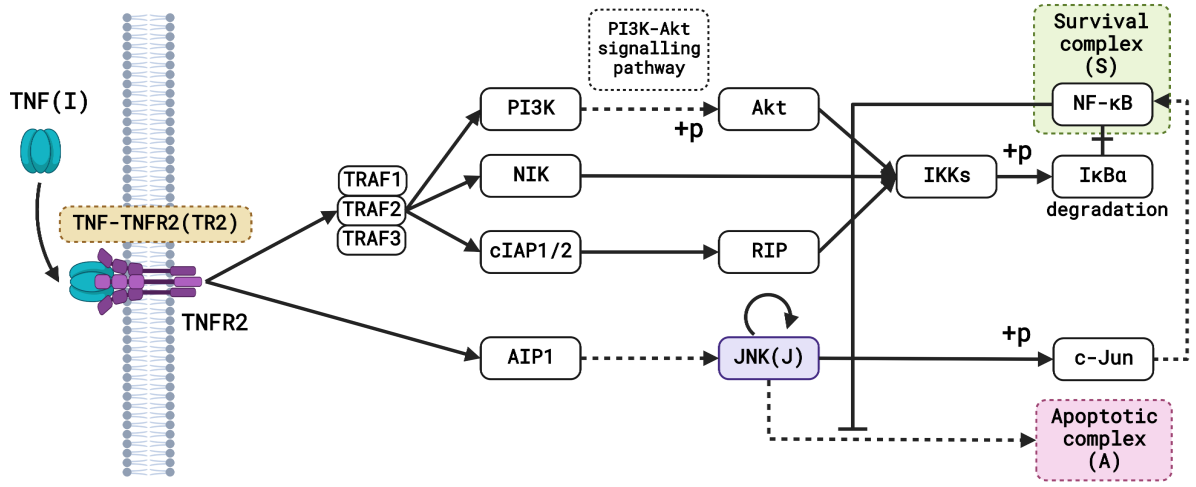

Figure 5.1: **Map of the TNFR2 pathway.** The figure depicts the schematic representation of the TNFR2 signalling pathway. The solid lines represent molecular interactions or relations, and the dashed lines represent indirect links. Furthermore, the arrow represents activation, and the line with the hammerhead denotes inhibition. The input TNF (I) and all the state variables used in the model system are written inside parentheses.

The model's equations describe the rates of loss and formation of the TNF-TNFR2 complex ($TR2(t)$), survival complex ($S(t)$), JNK ($J(t)$), and the apoptotic complex $A(t)$ at time t. Here the input stimulus TNF, I, binds to the free TNFR2. Grell et al. [201] have shown that the formation of TNF-TNFR2 ($TR2$) has a saturation, so to replicate this behaviour, we have considered the Michaelis-Menten form of kinetics for TR2 formation. Similar enzymatic kinetics has been used to describe the interaction of TNF with its receptor [202]. The total number of TNFR2 in different cell types remains constant. For example, the number of TNFR2 in KYM-1 cells is approximately 30,000 per cell [201], and HeLa cells contain about 50,000 TNFR2 per cell [203]. Wang et al. [204] showed that the number of TNFR2 on the Treg cell surface is three times higher than the other T cell types, but their actual number is unknown. So, we have considered the total concentration of TNFR2 to be a constant and normalized to 1 [56]. So the concentration of free TNFR2 at the membrane is (1-TR2). Thus, the formation of TR2 can be given by $\frac{k_1 I(1-TR2)}{k_{m1}+(1-TR2)}$, where k_1 is the maximum rate of TR2 formation and k_{m1} is the half-saturation constant. The production of S depends on the number TR2 of TNF-TNFR2 complexes on the cell membrane, with a rate constant k_2 [193]. Also, the production of J depends on the number of TR2, with a rate constant of k_4. Similarly, the production of S and A depends on the number of J, with rate constant k_3 and k_7, respectively. So, a linear positive growth term

is added to the respective equations. The cell survival pathway inhibits the apoptotic reactions in A with a rate k_8S [193]. Thus, a negative term is added to the apoptosis equation. Bagowski et al. [69] experimentally found that the steady-state response of the JNK cascade is highly ultrasensitive and exhibits switch-like responses to various stimuli. This ultra-sensitivity is due to strong positive feedback, which is given by the autocatalysis of the JNK activation [12]. The Hill equation can model this switch-like ultrasensitive response with a Hill coefficient greater than one [67]. Hence, we have added the term $\frac{k_5 J^2}{k_6^2+J^2}$ for the autocatalysis to the equation of J considering the Hill coefficient to be equal to two. The ligand/receptor complexes $TR2$ can be degraded with a rate constant d_1. The activated JNK has a degradation with a rate constant of d_3. The processes described by the rate constants d_2 and d_4, respectively, represent the degradation of S and A by ubiquitination and proteasome cleavage and/or irreversibly inhibited by other molecular species [193]. All these assumptions lead to the following model:

$$\begin{aligned}
\frac{dTR2}{dt} &= \frac{k_1 I(1-TR2)}{k_{m1}+(1-TR2)} - d_1 TR2 = F_1(TR2,S,J,A),\\
\frac{dS}{dt} &= k_2 TR2 + k_3 J - d_2 S = F_2(TR2,S,J,A),\\
\frac{dJ}{dt} &= k_4 TR2 + \frac{k_5 J^2}{k_6^2+J^2} - d_3 J = F_3(TR2,S,J,A),\\
\frac{dA}{dt} &= k_7 J - k_8 SA - d_4 A = F_4(TR2,S,J,A).
\end{aligned} \tag{5.1}$$

with initial conditions

$$TR2(0) = TR2_0 > 0, S(0) = S_0 > 0, J(0) = J_0 > 0, A(0) = A_0 > 0. \tag{5.2}$$

5.3 Analytical results

5.3.1 Positive invariance and boundedness of the solutions

Theorem 5.3.1. *All solutions of (5.1) satisfying the initial condition (5.2) are positively invariant.*

Proof. From the first equation of (5.1), we have

$$TR2(t) = TR2_0 e^{-d_1 t} + \frac{k_1 I}{d_1}\left[1 - e^{-d_1 t}\right] - k_1 k_{m1} I e^{-d_1 t} \int_0^t \left\{ \frac{e^{d_1 s}}{k_{m1} + 1 - TR2(s)} \right\} ds$$

It implies that $TR2(t) \geq 0$ for all $t > 0$ as $TR2_0 > 0$.

Similarly, from the third equation of (5.1)

$$J(t) = J_0 e^{-d_3 t} + \frac{k_5}{d_3}\left[1 - e^{-d_3 t}\right] + e^{-d_3 t} \int_0^t \left\{ k_4 TR2(s) - \frac{k_5 k_6^2}{k_6^2 + J(s)^2} \right\} e^{d_3 s}\, ds$$

Since $TR2(t)$ is positive, then $J(t)$ remains non-negative for all $t > 0$ provided $J_0 > 0$.

Also, we have

$$S(t) = S_0 e^{-d_2 t} + e^{-d_2 t} \int_0^t \left\{ k_2 TR2(s) + k_3 J(s) \right\} e^{d_2 s}\, ds$$

Since $TR2(t)$ and $J(t)$ both are positive, then $S(t)$ remains non-negative for all $t > 0$ provided $S_0 > 0$.

Following similar arguments, we have

$$A(t) = A_0 e^{-d_4 t} + e^{-d_4 t} \int_0^t \left\{ k_7 J(s) - k_8 S(s) A(s) \right\} e^{d_4 s}\, ds$$

Since $J(t)$ and $S(t)$ both are positive, then $A(t)$ remains non-negative for all $t > 0$ provided $A_0 > 0$. Thus, all solutions of (5.1) satisfying the initial condition (5.2) are positively invariant. This completes the proof. □

Theorem 5.3.2. *All solutions of system (5.1) with initial condition (5.2) are bounded within a region* Γ*, where*

$$\Gamma = \left\{ (TR2, S, J, A) \varepsilon R_+^4 : 0 < TR2(t) \leq \frac{k_1 I}{d_1}, 0 < S(t) \leq \Omega_1, \right.$$
$$\left. 0 < J(t) \leq \frac{1}{d_3}\left(k_4 \frac{k_1 I}{d_1} + k_5 \right), 0 < A(t) \leq \frac{k_7 \left(k_4 \frac{k_1 I}{d_1} + k_5 \right)}{d_3 (d_4 + k_8 \alpha)} \right\},$$

$\Omega_1 = \frac{1}{d_2}\left\{ k_2 \frac{k_1 I}{d_1} + \frac{k_3}{d_3}\left(k_4 \frac{k_1 I}{d_1} + k_5 \right) \right\}$ *and* α *is the minimum of S(t).*

Proof. From the first equation of system (5.1), we can write

$$\frac{dTR2}{dt} + d_1 TR2 \leq k_1 I$$

where $k_1 I$ is the maximum of $\frac{k_1 I(1-TR2)}{k_{m1}+(1-TR2)}$. Thus, following [205], we have $TR2(t) \leq \frac{k_1 I}{d_1}$ as $t \to \infty$.

From the third equation of system (5.1), we can write

$$\frac{dJ}{dt} + d_3 J \leq k_4 \frac{k_1 I}{d_1} + k_5$$

where $\frac{k_1 I}{d_1}$ is the maximum of $TR2(t)$ and k_5 is the maximum of $\frac{k_5 J^2}{k_6^2+J^2}$. Thus, following [205], we have $J(t) \leq \frac{1}{d_3}\left(k_4 \frac{k_1 I}{d_1} + k_5\right)$ as $t \to \infty$.

Using the second equation, we have

$$\frac{dS}{dt} + d_2 S \leq k_2 \frac{k_1 I}{d_1} + \frac{k_3}{d_3}\left(k_4 \frac{k_1 I}{d_1} + k_5\right)$$

giving $S(t) \leq \frac{1}{d_2}\left\{k_2 \frac{k_1 I}{d_1} + \frac{k_3}{d_3}\left(k_4 \frac{k_1 I}{d_1} + k_5\right)\right\}$ as $t \to \infty$.

From the fourth equation, we get

$$\frac{dA}{dt} + (d_4 + k_8 \alpha)A \leq \frac{k_7}{d_3}\left(k_4 \frac{k_1 I}{d_1} + k_5\right)$$

where α is the minimum of S(t). Thus, following [205], we have $A(t) \leq \frac{k_7}{d_3(d_4+k_8\alpha)}\left(k_4 \frac{k_1 I}{d_1} + k_5\right)$ as $t \to \infty$.

Hence all solutions of system (5.1) with initial condition (5.2) are ultimately bounded within the region Γ, where

$$\Gamma = \left\{ (TR2, S, J, A) \varepsilon R_+^4 : 0 < TR2(t) \leq \frac{k_1 I}{d_1}, 0 < S(t) \leq \Omega_1, \right.$$
$$\left. 0 < J(t) \leq \frac{1}{d_3}\left(k_4 \frac{k_1 I}{d_1} + k_5\right), 0 < A(t) \leq \frac{k_7\left(k_4 \frac{k_1 I}{d_1} + k_5\right)}{d_3(d_4 + k_8\alpha)} \right\},$$

$\Omega_1 = \frac{1}{d_2}\left\{k_2 \frac{k_1 I}{d_1} + \frac{k_3}{d_3}\left(k_4 \frac{k_1 I}{d_1} + k_5\right)\right\}$ and α is the minimum of S(t). This completes the proof.

□

5.3.2 Equilibrium point and stability analysis

The system has no axial equilibrium points. The interior equilibrium point $E^*(TR2^*, S^*, J^*, A^*)$ of the system is obtained by solving the following algebraic equations:

$$\begin{aligned} \frac{k_1 I(1-TR2^*)}{k_{m1}+(1-TR2^*)} - d_1 TR2^* &= 0, \\ k_2 TR2^* + k_3 J^* - d_2 S^* &= 0, \\ k_4 TR2^* + \frac{k_5 (J^*)^2}{k_6^2 + (J^*)^2} - d_3 J^* &= 0, \\ k_7 J^* - k_8 S^* A^* - d_4 A^* &= 0. \end{aligned} \tag{5.3}$$

Solving the first equation we get a quadratic equation of $TR2^*$, given by

$$d_1 (TR2^*)^2 - [d_1(k_{m1}+1) + k_1 I] TR2^* + k_1 I = 0.$$

The discriminant (D) of this quadratic equation is given by $D = (d_1(k_{m1}-1)+k_1 I)^2 + 4d_1^2 k_{m1} > 0$. Thus, we get two distinct positive real roots $TR2^*$. So, $TR2^*$ is feasible when $0 \leq TR2^* \leq 1$.

From the third equation of (5.3), we get J^* in terms of $TR2^*$ which satisfies the cubic equation

$$d_3 J^{*3} - (k_4 TR2^* + k_5) J^{*2} + d_3 k_6^2 J^* - k_4 k_6^2 TR2^* = 0.$$

From Descartes' rule of sign, we can easily find that the J^* have either one or three positive roots.

Next, by solving the second equation of (5.3) we get $S^* = \frac{1}{d_2}(k_2 TR2^* + k_3 J^*)$ and from fourth equation we get $A^* = \frac{k_7 J^*}{k_8 S^* + d_4}$.

The Jacobian matrix evaluated at the interior equilibrium E^* is given by

$$V(TR2^*, S^*, J^*, A^*) =$$
$$\begin{pmatrix} -d_1 - \frac{k_1 k_{m1} I}{(k_{m1}+1-TR2^*)^2} & 0 & 0 & 0 \\ k_2 & -d_2 & k_3 & 0 \\ k_4 J^* & 0 & -d_3 + \frac{2k_5 k_6^2 J^*}{(k_6^2+J^{*2})^2} & 0 \\ 0 & -k_8 A^* & k_7 & -k_8 S^* - d_4 \end{pmatrix}$$

The eigenvalues $\lambda_i (i = 1,2,3,4)$ are the roots of the characteristics equation

$$\left(-d_1 - \frac{k_1 k_{m1} I}{(k_{m1}+1-TR2^*)^2} - \lambda_1\right)(-d_2 - \lambda_2)$$
$$\left(-d_3 + \frac{2k_5 k_6^2 J^*}{(k_6^2+J^{*2})^2} - \lambda_3\right)(-k_8 S^* - d_4 - \lambda_4) = 0. \tag{5.4}$$

Note that the three eigenvalues $\lambda_i (i = 1,2,4)$ of (5.4) are always negative and the fourth eigenvalue λ_3 is negative iff $\frac{2k_5 k_6^2 J^*}{(k_6^2+J^{*2})^2} < d_3$. Hence, the interior equilibrium point E^* is locally asymptotically stable (LAS) iff $\frac{2k_5 k_6^2 J^*}{(k_6^2+J^{*2})^2} < d_3$.

5.4 Construction of the stochastic model

Signalling systems are inherently noisy [206], so to study the effect of noise in the system, we built the stochastic differential equations (SDE) model by incorporating random perturbation in the system (5.1). The random influences were viewed as systemic disturbances, and their effects were included in the model as multiplicative Gaussian white noise [36, 130]. Consequently, we added the stochastic perturbation terms to the equations relating to each state variable. The random fluctuations of the state variables around their steady-state values $E^*(TR2^*, S^*, J^*, A^*)$ are Gaussian white noise, and they are proportional to the distances of $TR2$, S, J and A from their steady-state values, respectively. In light of this, the stochastic model system that follows the deterministic model system (5.1) is as follows:

$$\begin{aligned} dTR2 &= F_1(TR2,S,J,A)dt + \sigma_1(TR2-TR2^*)d\xi_t^1 \,, \\ dS &= F_2(TR2,S,J,A)dt + \sigma_2(S-S^*)d\xi_t^2 \,, \\ dJ &= F_3(TR2,S,J,A)dt + \sigma_3(J-J^*)d\xi_t^3 \,, \\ dA &= F_4(TR2,S,J,A)dt + \sigma_4(A-A^*)d\xi_t^4 \,. \end{aligned} \tag{5.5}$$

where σ_i $(i = 1,2,3,4)$ are real constants and known as the intensity of the fluctuations, $\xi_t^i = \xi_i(t)$ $(i = 1,2,3,4)$ are standard Wiener processes, independent of each other, and F_i $(i = 1,2,3,4)$ are defined in the Eq. (5.1). We consider Eq. (5.5) as an Ito stochastic differential system of the type

$$dX_t = F(t,X_t)dt + G(t,X_t)d\xi_t \tag{5.6}$$

where the solution $(X_t, t > 0)$ is an Ito process, 'F' is the drift coefficient, 'G' is the diffusion coefficient, and ξ_t is a four-dimensional stochastic process having scaler Wiener process components with increments $\triangle\xi_t^j = \xi_j(t+\triangle t) - \xi_j(t)$ are independent Gaussian random variables $\mathrm{N}(0,\triangle t)$. In the case of the system (5.5),

$$X_t = \begin{bmatrix} TR2 \\ S \\ J \\ A \end{bmatrix}, \xi_t = \begin{bmatrix} \xi_t^1 \\ \xi_t^2 \\ \xi_t^3 \\ \xi_t^4 \end{bmatrix}, F = \begin{bmatrix} F_1(TR2,S,J,A) \\ F_2(TR2,S,J,A) \\ F_3(TR2,S,J,A) \\ F_4(TR2,S,J,A) \end{bmatrix},$$

$$G = \begin{bmatrix} \sigma_1(TR2-TR2^*) & 0 & 0 & 0 \\ 0 & \sigma_2(S-S^*) & 0 & 0 \\ 0 & 0 & \sigma_3(J-J^*) & 0 \\ 0 & 0 & 0 & \sigma_4(A-A^*) \end{bmatrix}. \tag{5.7}$$

Since the diffusion matrix 'G' depends upon the solution of X_t, the system (5.5) is said to have multiplicative noise.

5.4.1 Stochastic stability of the interior equilibrium point

The variables $U_1 = TR2 - TR2^*, U_2 = S - S^*, U_3 = J - J^*, U_4 = A - A^*$ were introduced to centre the stochastic differential system (5.5) at its positive equilibrium points $E^*(TR2^*, S^*, J^*, A^*)$. To keep mathematical computations simple, we work with the stochastic differential equation created by linearising the vector function 'F' (5.7) about the positive equilibrium point E^*. The linearised system of (5.6) around E^* is given by

$$dU(t) = f(U(t))dt + G(U(t))d\xi(t)\,, \tag{5.8}$$

where

$$U(t) = \begin{bmatrix} U_1(t) \\ U_2(t) \\ U_3(t) \\ U_4(t) \end{bmatrix}, f(U(t)) = \begin{bmatrix} -a_{11}U_1 \\ k_2U_1 - d_2U_2 + k_3U_3 \\ k_4J^*U_1 - a_{33}U_3 \\ -k_8A^*U_2 + k_7U_3 - a_{44}U_4 \end{bmatrix},$$

$$G(U(t)) = \begin{bmatrix} \sigma_1U_1 & 0 & 0 & 0 \\ 0 & \sigma_2U_2 & 0 & 0 \\ 0 & 0 & \sigma_3U_3 & 0 \\ 0 & 0 & 0 & \sigma_4U_4 \end{bmatrix}, \tag{5.9}$$

$$a_{11} = d_1 + \frac{k_1k_{m1}I}{(k_{m1} + 1 - TR2^*)^2}, \quad a_{33} = d_3 - \frac{2k_5k_6^2J^*}{(k_6^2 + J^{*2})^2}, \quad a_{44} = d_4 + k_8S^*.$$

Note that, in (5.8) the positive equilibrium E^* corresponds to the trivial solution $(U_1, U_2, U_3, U_4) = (0,0,0,0)$. Let Ω be the set defined by $\Omega = \left[(t \geqslant t_0) \times \mathrm{R}^4, t_0 \in \mathrm{R}^+\right]$. To define stability following theorem [111] can be used,

Theorem 5.4.1. *Suppose there exist a differentiable function $V(U,t) \in \mathrm{C}^4(\Omega)$ satisfying the inequalities*

$$K_1|U|^\alpha \leq V(U,t) \leq K_2|U|^\alpha \tag{5.10}$$

$$LV(U,t) \leq -K_3|U|^\alpha, \quad K_i > 0, \quad i = 1,2,3, \quad \alpha > 0\,. \tag{5.11}$$

Then the trivial solution of (5.8) is exponentially α stable for all time $t \geq 0$.

Note that, if in (5.10), (5.11), $\alpha = 2$, then the trivial solution of (5.8) is exponentially mean-square stable. Furthermore, the trivial solution of (5.8) is globally asymptotically stable in probability.

Here, following (5.8),

$$\begin{aligned} LV(t,U) = \frac{\partial V(t,U(t))}{\partial t} + f^T(U(t))\frac{\partial V(t,U)}{\partial U} \\ + \frac{1}{2}Tr\left[G^T(U(t))\frac{\partial^2 V(t,U)}{\partial U^2}G(U(t))\right] \end{aligned} \tag{5.12}$$

where

$$\frac{\partial V}{\partial U} = \begin{pmatrix} \frac{\partial V}{\partial U_1} & \frac{\partial V}{\partial U_2} \end{pmatrix}^T, \quad \frac{\partial^2 V(t,U)}{\partial U^2} = \left(\frac{\partial^2 V}{\partial U_j \partial U_i}\right)_{i,j=1,2}$$

and T means transposition.

Using the above Theorem 5.4.1, we have calculated the critical value of noise (σ_c), below which the system is stochastically stable. We can define and prove the following Theorem 5.4.2.

Theorem 5.4.2. *Assume that for some positive real value ω_1, ω_2, ω_3, ω_4 and ω_5 the following inequality holds:*

$$\left(2a_{33} - {\sigma_3}^2\right)\left(2a_{44} - {\sigma_4}^2\right) > \frac{k_7^2}{\omega_2}(\omega_3 + \omega_4 + \omega_5) \tag{5.13}$$

then the zero solutions of the system (5.8) will be exponentially 2-stable if

$${\sigma_1}^2 < \frac{2P_{11}}{(\omega_1 + \omega_2 + \omega_4)}, \ {\sigma_2}^2 < \frac{2P_{22}}{(\omega_1 + 1)}, \ {\sigma_3}^2 < 2a_{33}, \ {\sigma_4}^2 < 2a_{44}, \tag{5.14}$$

where $\omega_1 = \frac{P}{a_{11}+d_2-P}$, $\omega_2 = \frac{k_3\omega_1 + k_7\omega_4}{a_{11}-k_4J^*}$, $\omega_3 = \frac{k_3}{k_7}(1+\omega_1)$, $\omega_4 = \frac{a_{11}\omega_3}{a_{11}+a_{44}}$, $\omega_5 = \left(\frac{a_{44}}{k_8A^*} - 1\right)\omega_3 - \omega_4$, $P = k_2 - \frac{a_{11}k_3}{k_7}\left[1 + \frac{k_8A^*}{a_{11}+a_{44}}\right]$, $P_{11} = a_{11}(\omega_1 + \omega_2 + \omega_4) - k_2\omega_1 - k_4J^*\omega_2$ *and* $P_{22} = d_2(\omega_1 + 1) - k_8A^*\omega_3$.

Proof. Let us consider the Lyapunov function

$$V(U(t)) = \frac{1}{2}\left[\omega_1(U_1+U_2)^2 + {U_2}^2 + \omega_2(U_1+U_3)^2 + \omega_3(U_2-U_4)^2 + \omega_4(U_1+U_4)^2\right] \tag{5.15}$$

It is easy to check the inequalities in (5.10) are true for $\alpha = 2$.

Next, using (5.9) and (5.12),

$$\begin{aligned} LV(U(t)) &= \left(-P_{11} + \frac{1}{2}(\omega_1+\omega_2+\omega_4){\sigma_1}^2\right){U_1}^2 + \left(-P_{22} + \frac{1}{2}(\omega_1+1){\sigma_2}^2\right){U_2}^2 \\ &+ \left(-a_{33} + \frac{1}{2}{\sigma_3}^2\right)\omega_2{U_3}^2 + \left(-a_{44} + \frac{1}{2}{\sigma_4}^2\right)(\omega_3+\omega_4+\omega_5){U_4}^2 \\ &+ k_7\,(\omega_3+\omega_4+\omega_5)\,U_3U_4 \\ &= -U^T QU \end{aligned} \tag{5.16}$$

where

$$Q = \begin{bmatrix} H_{11} & 0 & 0 & 0 \\ 0 & H_{22} & 0 & 0 \\ 0 & 0 & H_{33} & \frac{1}{2}k_7(\omega_3+\omega_4+\omega_5) \\ 0 & 0 & \frac{1}{2}k_7(\omega_3+\omega_4+\omega_5) & H_{44} \end{bmatrix},$$

and

$$H_{11} = P_{11} - \frac{1}{2}(\omega_1+\omega_2+\omega_4){\sigma_1}^2,\ H_{22} = P_{22} - \frac{1}{2}(\omega_1+1){\sigma_2}^2,$$
$$H_{33} = \left(a_{33} - \frac{1}{2}{\sigma_3}^2\right)\omega_2,\ H_{44} = \left(a_{44} - \frac{1}{2}{\sigma_4}^2\right)(\omega_3+\omega_4+\omega_5).$$

The relation (5.13) and (5.14) imply that Q is a real symmetric positive definite matrix and, therefore, all its eigenvalues $\lambda_i(Q)$, $i = 1,2,3,4$ are positive real numbers. Let $\lambda_m = min\{\lambda_i(Q),\ i = 1,2,3,4\}$, $\lambda_m > 0$. From (5.16), we get

$$LV(U(t)) \leq -\lambda_m |U(t)|^2 .$$

If the conditions in Theorem 5.4.2 hold, then the zero solutions of the system (5.8) are exponentially mean-square stable.

Hence the proof. □

Table 5.1: Kinetic parameters involved in the system.

Parameter	Description	Value	Reference
I	Concentration of free TNF acting as input stimulus	0.59 μM	Estimated
k_1	Association rate constant of TNF and TNFR2 giving TNF-TNFR2	1.49 min^{-1}	[201]
k_{m1}	Half saturation constant of TNF-TNFR2 formation	0.42×10^{-3} μM	[207]
k_2	Activation rate of survival complex by TNF-TNFR2 complex	0.016 min^{-1}	[193]
k_3	Activation rate of survival complex by JNK	0.02 min^{-1}	Estimated
k_4	Activation rate of JNK by TNF-TNFR2 complex	0.01 min^{-1}	Estimated
k_5	Maximum expression level of JNK	0.9 $\mu M min^{-1}$	Estimated
k_6	Half saturation constant of JNK	0.5 μM	Estimated
k_7	Activation rate of death complex by JNK	0.9 min^{-1}	Estimated
k_8	Caspase inhibition rate	2.2×10^3 $\mu M^{-1} min^{-1}$	[193]
d_1	Rate of degradation of TNF-TNFR2 complex	0.829 min^{-1}	Estimated
d_2	Rate of degradation of survival complex	0.003 min^{-1}	[193]
d_3	Rate of degradation of JNK	0.059 $\mu M min^{-1}$	Estimated
d_4	Rate of degradation of death complex	0.003 min^{-1}	[193]

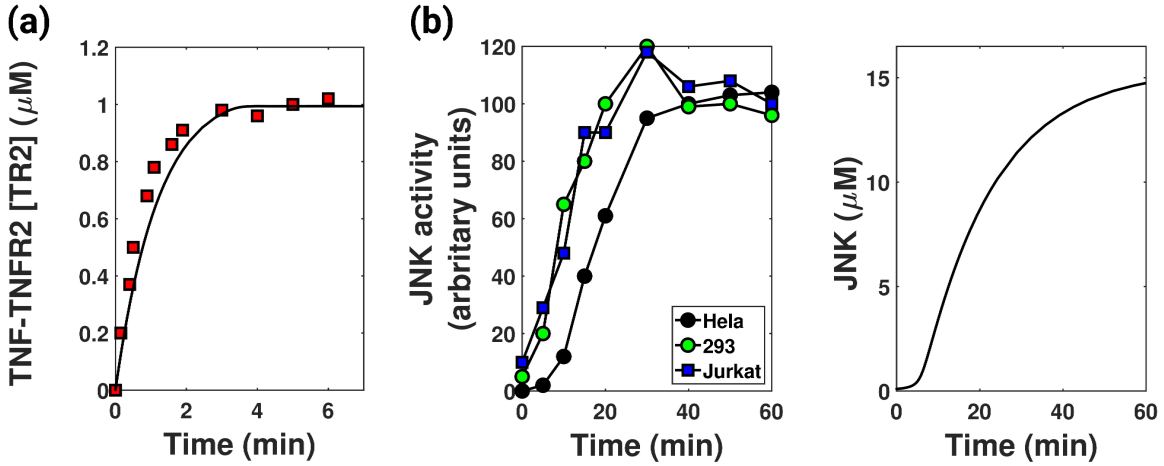

Figure 5.2: **Model validation with experimental data.** (a) The figure depicts the time series of TNF-TNFR2 formation with parameters given in Table 5.1. Inconsistent with existing literature [201], the black curve shows saturation kinetics of TNF-TNFR2 formation. Here, the red boxes represent experimental data from Grell et al. [201]. (b) Left panel: Sigmoidal curve of JNK activity when HeLa, HEK 293 and Jurkat T cells were treated with sorbitol (data taken from literature [69]). Right panel: The figure shows the sigmoidal response of JNK, similar to the curves in the left panel. The parameters used are given in Table 5.1.

5.5 Numerical results

5.5.1 Model validation with experimental data

The model is first established by demonstrating certain key facets of the biological system. The model is observed to generate saturated TNF-TNFR2 formation [201], and sigmoidal JNK response [12, 69]. It is observed that the association of TNF with TNFR2 is very rapid [201]. Our model successfully depicts the saturation kinetics of TNF-TNFR2 formation (represented by the black line in Fig. 5.2 (a)) incongruent with the experimental data (red dots in Fig. 5.2 (a)) from Grell et al. [201]. The model also showed a sigmoidal JNK response (right panel Fig. 5.2 (b)) as reported by Bagowski et al. [12, 69] (left panel Fig. 5.2 (b)). Some parameter values were collected from the literature, and the rest were estimated to generate these curves. Grell et al. [201] conducted their experiment using 4×10^5 KYM-1 cells in a volume of 150 μl. The average number of TNFR2 is approximately 30,000 per cell. Thus, we have considered the initial concentration of TNFR2 to be $13.2 \times 10^{-5} \mu M$. Also, from Grell et al. [201], the

association rate of TNF-TNFR2 (k_1) is 1.49 min^{-1}. From Lang et al. [207], the half saturation constant of TNF-TNFR2 formation (k_{m1}) is 0.42 $\times$ 10^{-3} μM. From Chignola et al. [193], the activation rate of survival complex by TNF-TNFR2 complex (k_2) is between [0.016, 0.3] min^{-1}, the caspase inhibition rate (k_8) is between [2.2 $\times$ 10^3, 4.5 $\times$ 10^4] $\mu M^{-1} min^{-1}$, the degradation rate of survival complex (d_2) and death complex (d_4) lie in the interval [0.0014, 0.003] min^{-1}. All these parameters from the literature and the other parameters estimated to validate the model are mentioned in Table 5.1. The output response (caspase concentration (A)) generated by this parameter set is in the scale of $10^{-5}\mu M$, in agreement with the literature [195].

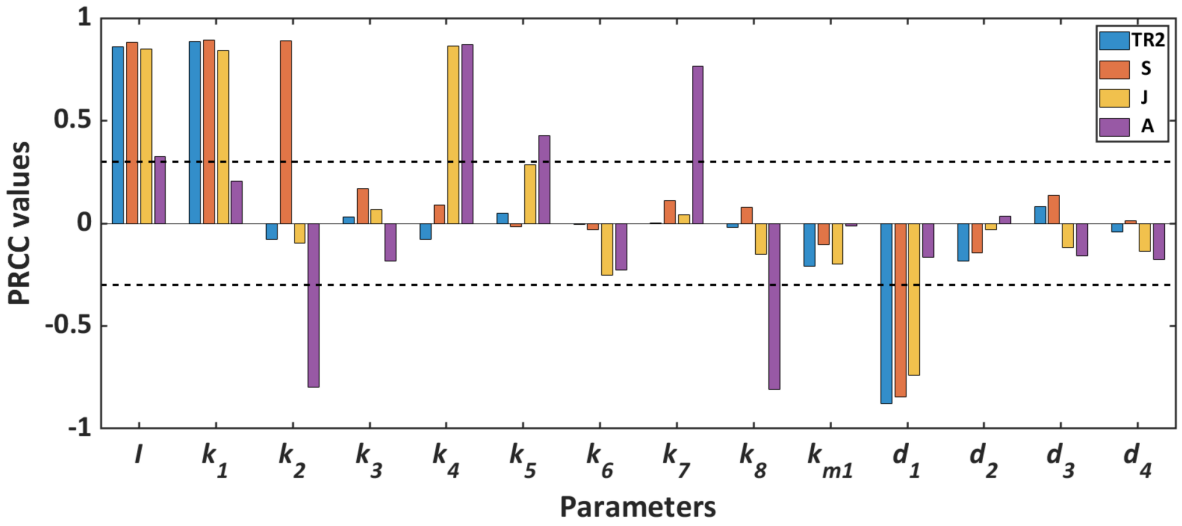

Figure 5.3: **Global sensitivity of the system parameters.** Here, corresponding to every parameter, four different colour bars represent four state variables. And the sensitivity of each parameter is measured by the length of the bars.

5.5.2 Global sensitivity analysis

We conducted global sensitivity analysis (GSA) using Latin Hypercube Sampling (LHS) and Partial Ranked Correlation Coefficient (PRCC) to evaluate the sensitivity of each parameter [115]. A parameter is considered sensitive if its PRCC value is equal to or larger than the predetermined threshold value of ± 0.3 [206, 208]. The GSA reveals that the input parameter (I) is sensitive to all the state variables of the system. It is further observed that the output of the system (A) is sensitive to the parameters k_2, k_4, k_5, k_7 and k_8 (see Fig. 5.3).

5.5.3 Existence of bistability

The presence of positive feedback on JNK production satisfies the necessary condition for the existence of bistability in the system [206]. In addition, Bagowski et al. [12, 69] reported that the JNK response is ultrasensitive, i.e., it can show abrupt responses when subjected to different stimuli. These shreds of evidence suggest that with the change in feedback strength and the variation of input stimulus, the system may attain different characteristics of bistability [71]. Initially, the system exhibits bistability when we decrease the input concentration to 0.026 μM, and the rest of the parameter values are as in Table 5.1. We lower the feedback strength of the system to $k_5 = 0.075\ \mu M min^{-1}$ to examine different stability patterns of the system. For three different values of the input stimuli, viz. $I = 0.2\ \mu M$, $I = 0.3\ \mu M$ and $I = 0.4\ \mu M$, the J vs $\dot{J}$ or $\frac{dJ}{dt}$ phase portrait display monostability, bistability and monostability respectively (see Fig. 5.4 (a)). The system's output response also shows saddle-node bifurcation at L_1 and L_2 (see Fig. 5.4 (b)) in the process displaying bistability for a range of input stimuli.

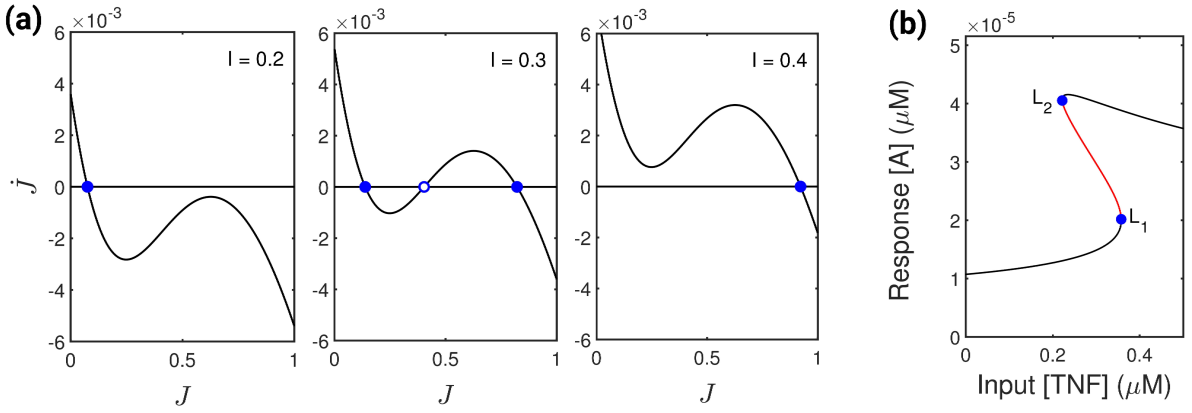

Figure 5.4: **Existence of bistability.** (a) The figure depicts the phase portrait of $\dot{J}$ vs J (solid black line) for three distinct levels of the input stimulus, I. Blue dots with full and open centres denote stable and unstable fixed points. The units of J and I are in μM. (b) Single parameter saddle-node bifurcation diagram of response A showing stable (black line) and unstable (red lines) steady states. Bifurcations occurs at points L_1 and L_2. The feedback strength (k_5) used to generate figures (a) and (b) is 0.075 $\mu M min^{-1}$, and the other parameters are given in Table 5.1.

5.5.4 Robustness of bistability

The observed bistability is robust if the sensitive parameters are varied and maintained bistability. So, to calculate the robustness of the bistability, we varied each sensitive parameter ten

folds up and down from their basal values and evaluated their bistable region. The basal parameter values correspond to the parameters given in Table 5.1 with $I = 0.026\ \mu M$. We can see from Fig. 5.5 that the parameters k_2, k_7, k_8 can maintain bistability for the entire range of their variations. The other parameters k_4, k_5, and I retain bistability for the entire range when they are decreased. Thus, we could conclude that the bistability of the system is robust.

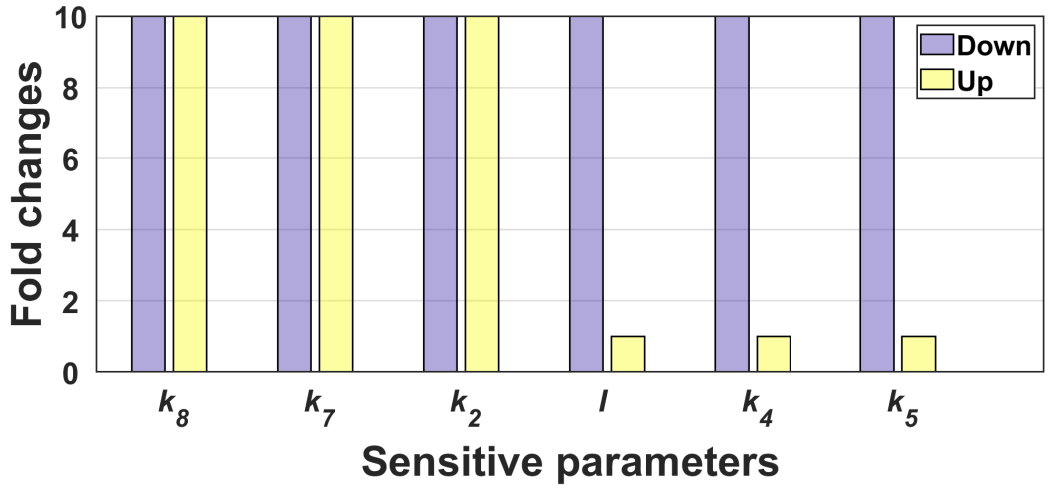

Figure 5.5: **Robustness analysis.** The figure shows the robustness of the sensitive parameters towards the maintenance of bistability. Each bar in this diagram indicates a parameter range in fold change from its basal values where the system is bistable. The basal value for I is 0.026 μM, and the rest of the parameters are given in Table 5.1.

5.5.5 Bistability determines cell's fate: survival or death

The robustness analysis of the sensitive parameters shows that the system exhibits bistability for a wide range of parameters. This motivates us to look for the significance of bistability. In the bistable region (shaded region in Fig. 5.6), the two stable steady states attained by the output of the system are termed as the lower steady state (LSS) for the low value of A and an upper steady state (USS) for the high value of A. That means in LSS, the apoptotic complex concentration or the caspase concentration is low, and the cell goes to survival. In USS, the caspase concentration is high, and the cell goes to apoptosis. Hence, LSS signifies cell survivability, and USS represents cell death (see Fig. 5.6). Similar considerations were also made by Bagci et al. [195]. Beyond this bistable range, the system is monostable, i.e., only one stable, steady state exists. In this monostable range, the caspase concentration is either high or low. So, the cell can go only in one direction: survival or death.

One of the hallmarks of bistability is the existence of hysteresis, i.e., the system's output becomes a loop rather than a curve [206]. This hysteresis can be of two types: reversible (see Fig. 5.6 (a)) and irreversible hysteresis (see Fig. 5.6 (b)). In reversible hysteresis, the system can come back to its previous steady state only by changing the input stimulus (Fig. 5.6 (a)), whereas in irreversible hysteresis, it can not (Fig. 5.6 (b)) [206]. The nature of hysteresis depends on the strength of the feedback parameter [14, 206]. The change of qualitative behaviour of the response curve when we change the feedback strength is depicted in Fig. 5.7. With a low feedback strength (k_5 = 0.04 $\mu Mmin^{-1}$) the response is a smooth curve. When k_5 is gradually raised to 0.06 $\mu Mmin - 1$, it becomes sigmoidal (but still monostable). Upon further increasing the feedback strength to 0.07 $\mu Mmin^{-1}$, the response splits into two curves and becomes bistable. And the system shows reversible hysteresis for k_5 = 0.07 $\mu Mmin^{-1}$ & 0.08 $\mu Mmin^{-1}$. Eventually, when the feedback becomes too large (k_5 = 0.09 $\mu Mmin^{-1}$), the response shows irreversible hysteresis. The system can retain its current state through this hysteresis even when the input concentration is varied. Hence, these hystereses make the system robust against fluctuations in the input stimuli.

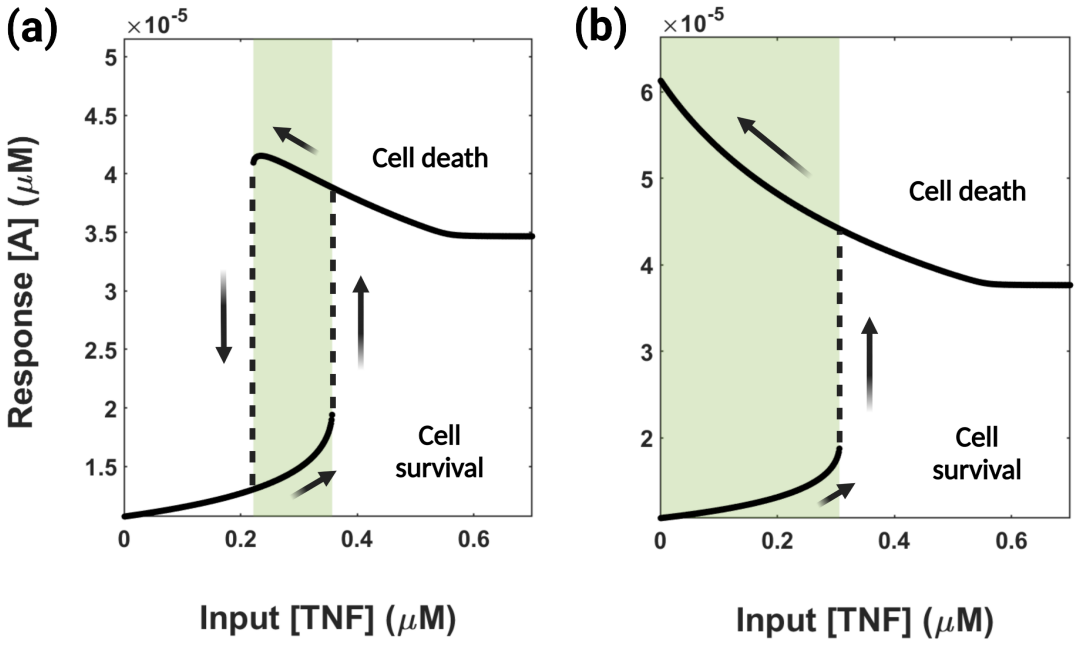

Figure 5.6: **Hysteresis: the hallmark of bistability.** (a) The figure depicts the reversible hysteresis in the system. (b) Here the figure shows the irreversible hysteresis in the system. In both figures, the shaded region refers to the bistable region. The feedback parameter strength for reversible hysteresis (a) is k_5 = 0.075 $\mu Mmin^{-1}$ and for irreversible hysteresis (b) is k_5 = 0.085 $\mu Mmin^{-1}$. Table 5.1 gives all the other parameters.

5.5.6 TNF concentration regulates cell death

The diverse pattern of Treg frequency observed in various autoimmune diseases may result from bistable caspase concentrations in the Treg system. That is, two systems with similar parametric conditions can attain opposite outputs. That means for equal concentrations of TNF, one system can achieve the survival state, whereas in the other case, it can go to apoptosis. To fully comprehend the mechanism, we have considered three different autoimmune diseases: inflammatory bowel disease (IBD), rheumatoid arthritis (RA) and systemic lupus erythematosus (SLE). In the case of IBD and SLE subjects, a decrease in Tregs number is observed in peripheral blood [176, 209]. However, in the case of RA, contradictory observations are reported that the number of Tregs in the peripheral blood increase, unchanged, or decreases [182]. However, a more precise analysis shows that the number of Tregs in peripheral blood decreases [182]. It suggests that the death of Tregs can mark the onset of the disease. Thus, the USS in Fig. 5.6 could be defined as the disease state which marks the death of Tregs due to higher caspase concentrations. In the case of reversible hysteresis Fig. 5.6 (a), the system will attain the USS when the TNF concentration is high, which means higher TNF concentration implies a high apoptosis rate of Tregs and can be reversed by reducing the TNF concentration. Similar observations are also reported in the literature that the serum TNF concentration is elevated in IBD [210], RA [211, 212] and SLE [213, 214] patients. The viability of the hypothesis can be examined by comparing the mathematical results with the existing literature. Through our model, we observe that the system could be reversed, i.e., it can change the stable steady states by reducing the TNF concentrations in the system. Veltkamp et al. [215] demonstrated that patients with active IBD showed more local CD4(+)Foxp3(+) Treg cell apoptosis in the inflamed mucosa than non-inflamed control colon tissue. In addition, there was a decrease in the frequency of Treg cells and an increase in their apoptosis, accompanied by increased caspase activity in the serum. They observed that anti-TNF therapy reduced Treg cell death with increased peripheral Treg cell numbers in tandem with a decrease in caspase activation and disease activity. These data suggest that the onset of IBD is marked by increased apoptosis of the Tregs and can be reversed by anti-TNF treatment, i.e., by reducing the TNF concentration, thus, validating our hypothesis. Similar kinds of narratives are reported in the literature for RA

and SLE. When TNF antagonists were used to treat RA patients, they showed marked improvement in the disease symptoms [216]. In the case of SLE, an open-label reported that anti-TNF therapy suppresses local tissue destruction [217]. These findings suggest that we can explain the complex mechanism of cell survival and death in Treg cells through bistable switching. Furthermore, by reducing TNF concentration, the system can be reversed.

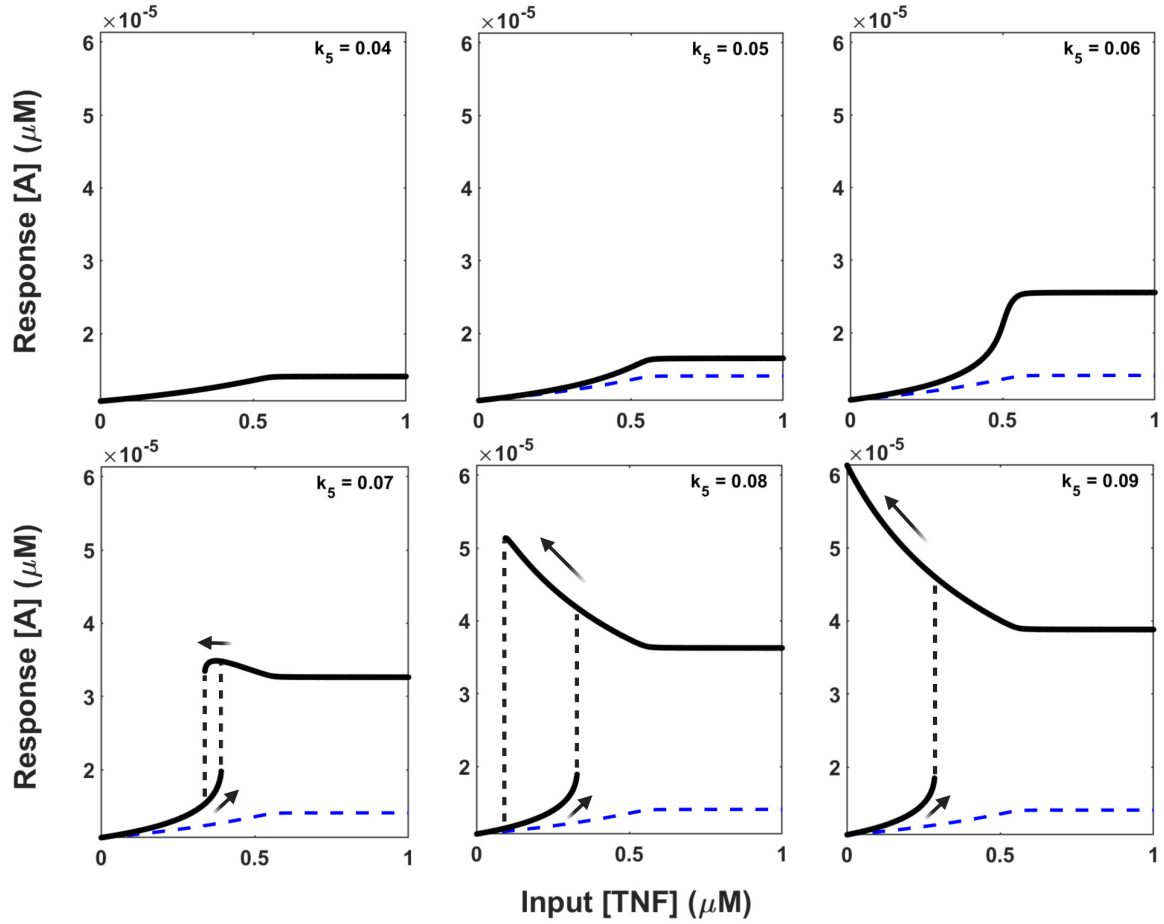

Figure 5.7: **Response and feedback strength.** Figure depicts the change of the response curve upon changing the feedback strength (k_5). The response is a smooth curve when the feedback strength is low ($k_5 = 0.04\ \mu Mmin^{-1}$). It becomes sigmoidal when k_5 is increased slowly to 0.06 $\mu Mmin^{-1}$ (but still monostable). Upon further increasing, the response curve splits into two curves and becomes bistable at $k_5 = 0.07\ \mu Mmin^{-1}$, and it shows reversible hysteresis for $k_5 = 0.07\ \mu Mmin^{-1}$ & $0.08\ \mu Mmin^{-1}$. Eventually, the curve shows irreversible hysteresis when k_5 is $0.09\ \mu Mmin^{-1}$. In this figure, the blue line curves (with $k_5 = 0.04\ \mu Mmin^{-1}$) are included for comparison. The rest of the parameter values are given in Table 5.1.

A major factor that controls the nature of hysteresis is the feedback strength of the system. We can revert the system to its previous steady state if it is in reversible hysteresis. So, along with TNF concentration, we need to control the autoregulation of the JNK production to revert

the system to the survival state. On the contrary, the increase in the feedback strength will make the system go to irreversible hysteresis. Then, even with a decrease in the TNF concentration, the disease state will persist. Thus, increased JNK activation will be associated with autoimmune patients. Related results have been reported that the increased JNK activation was associated with organ damage in SLE patients [218]. Similarly, increased phosphorylation of JNK was detected in inflamed joints of different animal models of RA and patients with autoimmune arthritis [219]. As JNK is autoregulated by its production [220]. Thus the inhibition of its activation can limit its rate. Administration of JNK specific inhibitors like SP600125 (anthra[1,9-cd]pyrazol-6(2H)-one), CC-930 improved symptoms related to autoimmune arthritis [219]. In our model, JNK is a function of TNF-TNFR2 concentration, which means a decrease in TNF indicates a decrease in TNF-TNFR2 formation, hence inferring a reduction in JNK production. Similar results were reported that in synovial samples from RA patients, immunological staining for JNK is reduced after anti-TNF therapy [219]. This evidence strongly suggests that the bistable mechanism of cell survival and apoptosis could be controlled. The system can be reverted to a survival state by reducing the TNF concentration.

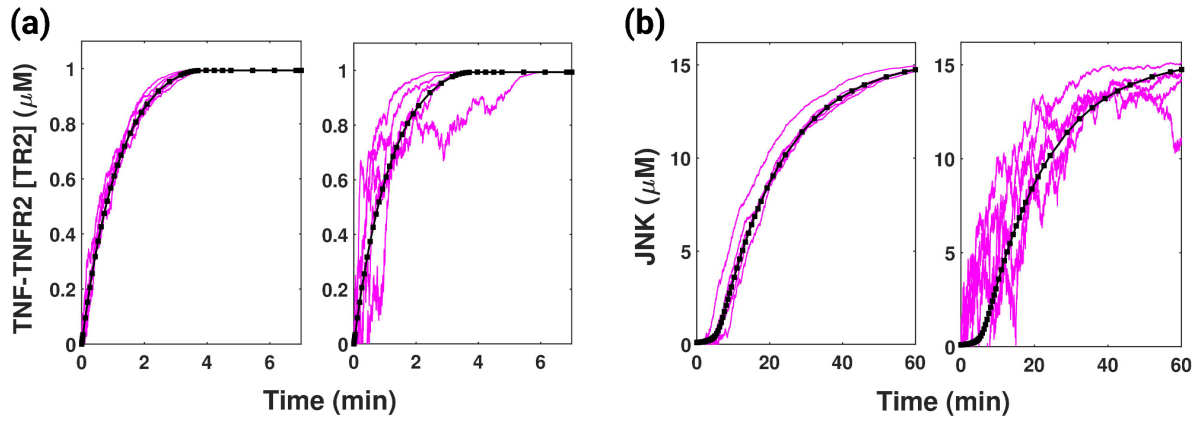

Figure 5.8: **Time evolution of TNF-TNFR2 and JNK in the presence of noise.** At low noise intensity (σ = 0.02), the time series of TR2 and JNK (see left panel of (a) and (b)) experience a little deviation from its deterministic curve (plotted in black). However, in case of high noise (σ = 0.1), the system becomes stochastically unstable (see right panel of (a) and (b)). The parameters used are given in Table 5.1.

5.5.7 Addition of randomness triggers loss of bistability

The effect of the inherent noise on the system's bistability was studied through the stochastic model constructed on the deterministic system (5.1). The effect of stochasticity on the model system's dynamics is depicted in Fig. 5.8. For a low value of noise, i.e., with the noise intensity (σ) below the critical value (σ_c), the system shows slight deviation from its deterministic values, which means the system is stochastically stable (see left panel of Fig. 5.8 (a) and 5.8 (b)). With the noise intensity above the critical value, the time series shows significant deviations from its deterministic values, i.e., the system becomes stochastically unstable (see right panel of Fig. 5.8 (a) and 5.8 (b)).

In Chapter 2, it has been observed that the system may lose bistability in the presence of noise. Thus, the system converges to one of the two stable steady states when noise intensity increases beyond the critical value [206]. In addition, the bistable properties of the model depend on the input parameter and the system's feedback. So, to observe the effect of noise on the bistability of the system, we have calculated different stochastic stability regions when input is varied for different values of feedback strengths. In Fig. 5.9, the coloured regions of $\sigma - I$ plane depicts the stochastically bistable (green), monostable (magenta) and unstable (yellow) regions. The system is stochastically bistable when the TNF concentration and noise intensity are low (the green region near the origin). However, with an increase in the noise value, the system becomes stochastically monostable (magenta). So, a deterministically bistable system may become monostable for high noise intensity. The system becomes stochastically unstable (yellow) with a further increase in the noise intensity, exceeding its critical value. When we gradually increase the value of TNF, the system shows a gradual decrease in σ values for the stochastic bistable region. Beyond the bistable TNF concentration, the system attains stochastic monostability up to a certain σ value, exceeding which, the system becomes stochastically unstable. These stochastic bistable region decreases as we gradually increase the feedback strength (k_5) of the system from 0.2 $\mu Mmin^{-1}$ to 1 $\mu Mmin^{-1}$. Thus, the bistable range of the input stimuli and the feedback parameter decreases when randomness is introduced to the system; hence the reversibility of the system is reduced.

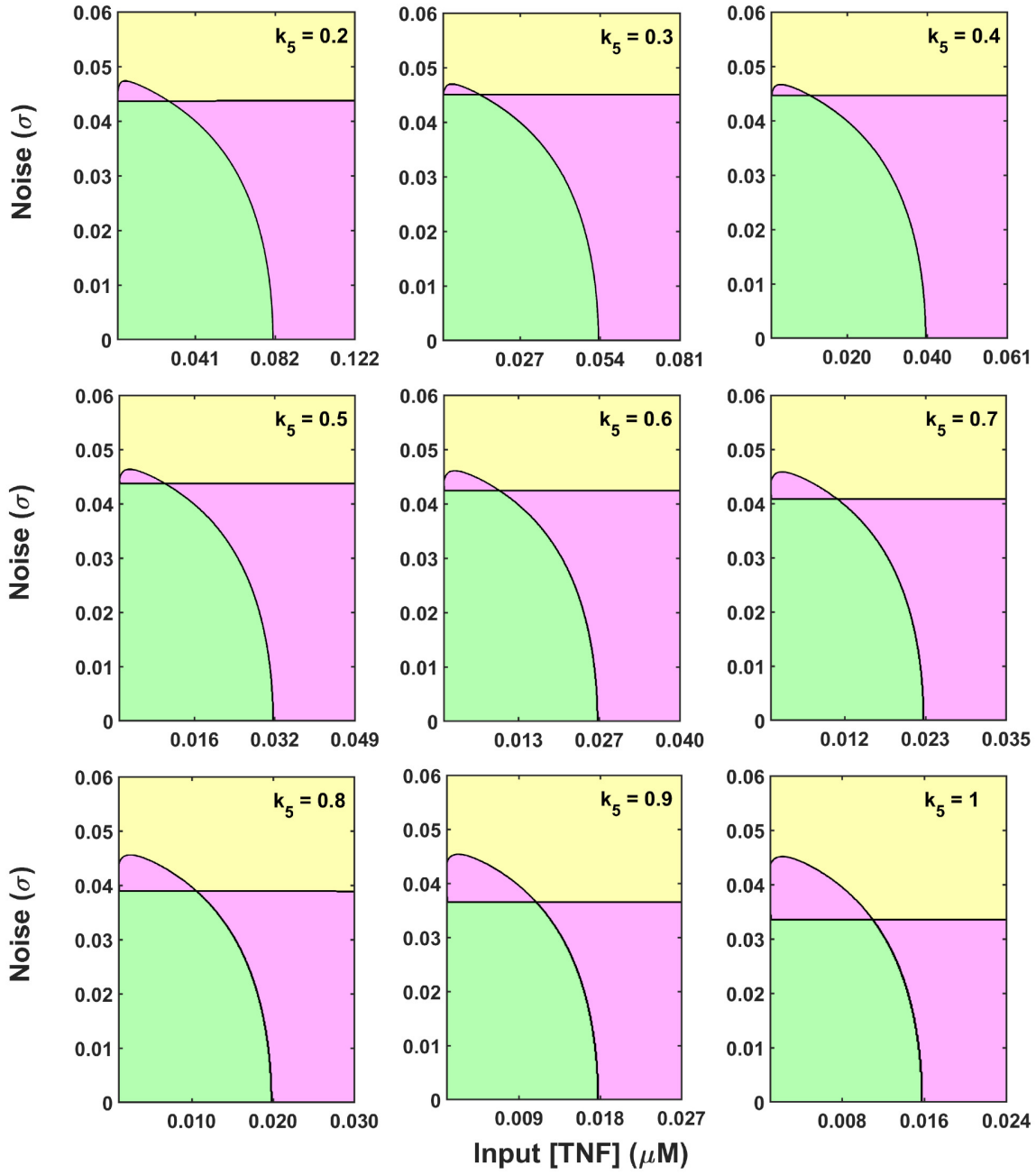

Figure 5.9: **Change of stochastic stability with variation in feedback strength.** The figure depicts the change of stochastic stability of the equilibrium points with the variation of input stimulus (I) and the noise intensity (σ) for different values of feedback strength (k_5), as indicated in the plots. The unit of k_5 is $\mu M min^{-1}$. The green, magenta and yellow coloured regions depict the stochastically bistable, monostable and unstable regions, respectively. The length of the X-axis in each figure refers to the deterministic bistability range of the input parameter for the feedback strength mentioned inside the figure. The rest of the calculation parameters are given in Table 5.1.

5.5.8 Effect of saturated synthesis of S, J and A on model results

Although we have constructed a minimal model of the complex signalling system, which was further validated with experimental data and showed the emergence of complex behaviour like bistability, it would be interesting to check the change in the results with the introduction of additional non-linearity in the system. The mathematical model (5.1) was modified by considering the non-linear synthesis of three state variables S, J, and A. In place of linear synthesis of S, J, and A in model (5.1), we have considered saturated synthesis of S, J, and A as we used for the formation of $TR2$. The modified mathematical model is given below:

$$\begin{aligned}
\frac{dTR2}{dt} &= \frac{k_1 I(1-TR2)}{k_{m1}+(1-TR2)} - d_1 TR2, \\
\frac{dS}{dt} &= \frac{k_2 TR2(1-S)}{k_{m2}+(1-S)} + k_3 J - d_2 S, \\
\frac{dJ}{dt} &= \frac{k_4 TR2(1-J)}{k_{m4}+(1-J)} + \frac{k_5 J^2}{k_6^2+J^2} - d_3 J, \\
\frac{dA}{dt} &= \frac{k_7 J(1-A)}{k_{m7}+(1-A)} - k_8 SA - d_4 A.
\end{aligned} \tag{5.17}$$

with initial conditions

$$TR2(0) = TR2_0 > 0, S(0) = S_0 > 0, J(0) = J_0 > 0, A(0) = A_0 > 0. \tag{5.18}$$

We performed a numerical analysis with the parameters from Table 5.1 and sought bistability. The new model also showed the existence of bistability. Bistability was obtained for the parameters $T = 0.026$, $k_5 = 0.075$, $k_{m2} = 0.04$, $k_{m4} = 0.6940$ and $k_{m7} = 0.0053$ and the other parameters are mentioned in Table 5.1. The units of k_{m2}, k_{m4} and k_{m7} are in μM. GSA reveals similar results for the new and the old systems, see Fig. 5.10 (a). All the sensitive parameters of the system (5.1) were also sensitive for the system (5.17). In system (5.17) we obtained four additional sensitive parameters namely k_6, d_1, k_{m2} and k_{m4}. The robustness of the sensitive parameters (see Fig. 5.10 (b)) also remains the same as observed for system (5.1), with the highly robust parameters remaining highly robust and least robust parameters remaining least robust. Thus, the addition of non-linearity to the system does not significantly affect the qualitative

outcome of the study.

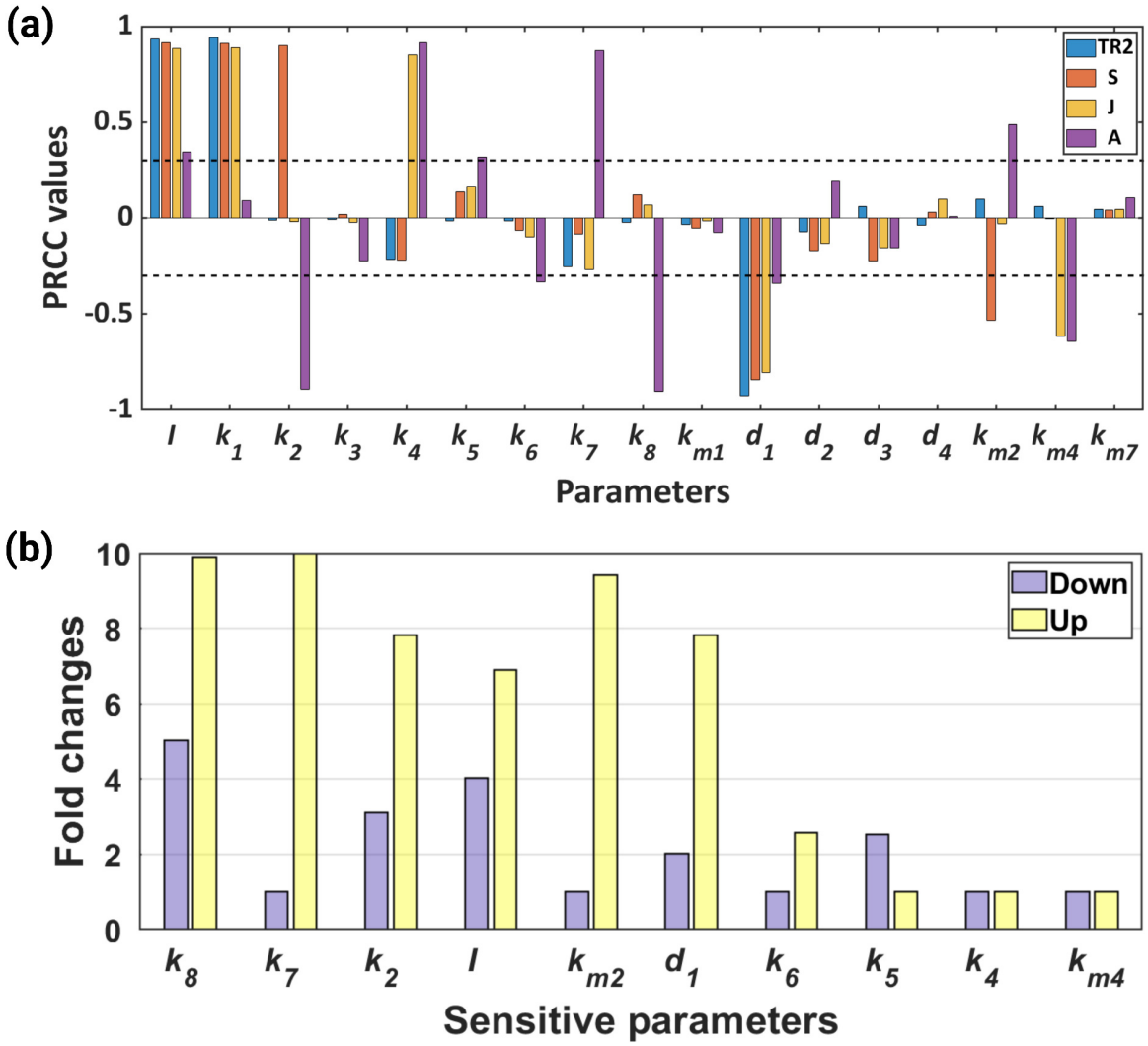

Figure 5.10: **Global sensitivity analysis and robustness analysis.** (a) The figure depicts the GSA of model parameters of the model (5.17). Here, corresponding to every parameter, four different colour bars represent four state variables. And the sensitivity of each parameter is measured by the length of the bars. (b) The figure shows the robustness of the sensitive parameters towards the maintenance of bistability. Each bar in this diagram indicates a parameter range in fold change from its basal value where the system is bistable. The basal values for the parameters are $T = 0.026$, $k_5 = 0.075$, $k_{m2} = 0.04$, $k_{m4} = 0.6940$ and $k_{m7} = 0.0053$ and the other parameters are mentioned in Table 5.1.

5.6 Discussion

Immunological homeostasis of the body is maintained by a special subset of T cells known as Treg cells. They can influence immunological tolerance in an antigen-specific manner or

by bystander suppression [175]. In bystander suppression of Tregs, TNF plays an important role, initiating the signalling by binding to its two receptors, TNFR1 and TNFR2. Generally, TNFR1 sends the signal for apoptosis, whereas TNFR2 signalling can lead to both survival and apoptosis [183]. Defects in TNFR2 signalling are prominent in many autoimmune diseases [183]. The contrasting patterns of Treg cell frequency have also been observed in different autoimmune diseases [176–180]. Thus, the similarity of TNFR2 signalling defects and abnormalities in Treg cell frequency in autoimmune diseases motivates us to study the mechanism of cell survival and cell death through TNFR2 signalling. To unravel the underlying mechanism of Treg cell survivability, we have constructed a theoretical model of TNFR2 signalling. We have formulated an ODE-based model to study the mechanism of cell survival and cell death in Treg cells. The proposed ODE model successfully reproduces the saturation kinetics for the TNF-TNFR2 formation as described by Grell et al. [201]. It also reproduces the sigmoidal JNK curve as reported by Bagowski et al. [12, 69]. It generates a response of apoptosis concentration in the 10^{-5} μM range as reported by Bagci et al. [195]. Thus, the model is validated by generating these important biological facets of the system.

The global sensitivity analysis reveals that six of fourteen model parameters are sensitive to the system's output. Out of these six parameters, only the input parameter (I) is sensitive to all the state variables. The presence of feedback in the system satisfies the necessary condition for the existence of bistability [206]. JNK also exhibits graded responses for various stimuli [12, 69]. These pieces of evidence inspire us to study the present system for the existence of bistability. Initially, bistability is observed when we decrease the input TNF concentration. The robustness analysis of the sensitive parameters showed that the model could maintain this bistability for a wide range of parameter variations. Thus, the deterministic model can generate a graded response for significant variations of parameters. However, the system can exhibit different bistable behaviour when we alter the feedback strength of the system [71]. When the system's feedback is modulated, the bistable curve becomes a loop called hysteresis [206]. Depending on the feedback strength, the system can have two types of hysteresis, reversible and irreversible [71]. In reversible hysteresis, the system can be reverted by reducing the input stimulus of the system, but not in the case of irreversible hysteresis [206]. Through this

bistability, we can explain the complex behaviour of cell survival and cell death in Treg cells. Thus, the observed bistability can explain the diverse patterns related to Treg cell survivability observed in autoimmune diseases.

We have considered three different autoimmune diseases to understand the mechanism clearly: IBD, RA and SLE. These diseases are marked by the decrease in the number of Tregs in the peripheral blood [176, 182, 209]. The death of Treg is characterized by high caspase concentration [195]. This evidence suggests that the increase of caspase is high in the autoimmune state. Our model reveals that the system can be reverted by reducing the TNF concentration in the system. This hypothesis is validated by the fact that the patients with these diseases have shown marked improvement with the anti-TNF therapy [215–217]. Thus, when the TNF concentration is reduced, the caspase concentration of the system can be decreased. Another factor that determines the output of the system is the feedback strength of the system. This feedback strength decides the type of hysteresis the system will show [71]. In reversible hysteresis, we can revert the system to its previous state [206]. Here, the feedback is defined by the autoregulation of the JNK; that is, it can enhance its production [220]. Thus, inhibition of JNK would limit its production. Similar observations were made when inhibitors of JNK were used to treat RA patients, and they showed marked improvements in the symptoms related to RA [219]. As JNK is a function of TNF-TNFR2, a reduction in the TNF would reduce the production of JNK. Similar stories were reported that anti-TNF therapy showed a decrease of JNK in synovial samples of RA patients [219]. This evidence cements our hypothesis that the bistability in the system regulates cell survival and apoptosis in Treg cells and can be controlled by reducing the TNF concentration. Finally, our study incorporated inherent noise through a SDE-based model. We have shown that the presence of noise in the system can reduce the bistable parameter region of the system. Thus, the reversibility of the output is reduced due to the presence of randomness in the system, which may hinder normal functioning.

In this chapter, we have observed the existence of bistability in TNF signalling in T regulatory cells. Through bistable switching, we could explain the complex behaviour of cell survival and death. The model reveals that the elevated TNF concentration and increased c-Jun N-terminal kinase (JNK) phosphorylation are the major contributors to the death of T-regulatory

cells and can be controlled by reducing the TNF concentration. It also explained how inherent stochasticity could reduce a system's bistability and affect its normal functioning. In the next chapter we have selected another real biological system to examine the effect of randomness. We have considered the calcium signalling pathway in cardiomyocytes to understand the complex aetiology of diabetic cardiomyopathy and study calcium oscillation under a stochastic environment.

6

Studying the role of random translocation of GLUT4 in cardiomyocytes on calcium oscillations[1]

6.1 Introduction

The International Diabetes Federation predicts that by 2030, 643 million people worldwide will be diagnosed with diabetes between the ages of 20 and 79. The number is projected to rise to 783 million by 2045 [221]. Diabetes is frequently associated with cardiovascular diseases, including heart failure [222, 223]. The emergence of a cardiac injury, known as "diabetic

[1]The bulk of this chapter has been communicated for possible publication.

cardiomyopathy", is a factor that develops heart failure in persons with diabetes [224]. Diabetic cardiomyopathy is an aberrant myocardial structure, and it functions in the absence of other cardiac risks factors such as coronary artery disease or hypertension [225, 226]. DCM's pathophysiology is intricate and complicated. Predisposition to ventricular dysfunction, which affects myocardial energetics and contractile function, is one of its functional characteristics [227–230]. Diabetes has a pathologic impact on cardiomyocyte function due to altered calcium ion regulation and insulin signalling [223, 231]. The primary function of cardiomyocytes is to contract synchronously to meet the heart's pumping function. The heart's four chambers must contract and relax in a highly synchronized manner to optimize circulation and ensure a supply of nutrients and signals throughout the body. These heart contractions are caused by the periodic increase and decrease in the intracellular Ca^{2+} concentration. Electrical depolarization of the cardiomyocyte sarcolemma coordinates the intracellular Ca^{2+} exchanges. For an effective cardiac pump, individual myocytes are synchronized throughout the heart by the electric signal originating from the sinoatrial node [232, 233]. The altered Ca^{2+} homeostasis establishes these fundamental roles of Ca^{2+} in the heart. Faulty hemodynamics and rhythmic disturbances are marked by altered Ca^{2+} signalling [232, 233].

One of the main reasons for contractile dysfunction connected to DCM is defective excitation-contraction coupling (ECC). During ECC, the sarcoplasmic reticulum (SR) is a significant source of Ca^{2+} influx into the cytosol. SR Ca^{2+} concentration is maintained via ryanodine receptor (RyR2) channels, L-type Ca^{2+} channels (LTCCs), SR Ca^{2+} ATPase (SERCA2a) pumps, and/or a coordinated action of all three. ECC is started by extracellular Ca^{2+} entering the cell through LTCCs, which then causes the release of SR Ca^{2+} into the cytosol by RyR2, completing the trigger [134]. At the same time, the other ATP-driven pumps, exchangers, and channels mediate the calcium fluxes between sub-cellular compartments and across the plasma membrane. The core calcium dynamics in cardiomyocytes are primarily governed by the membrane's electrical activity that drives voltage-gated channels, allowing calcium to enter the cell [234]. The level of intracellular calcium oscillates due to electrical bursting. Any disturbance in calcium homeostasis may significantly contribute to the development of common cardiovascular diseases, such as heart failure and cardiac arrhythmias [235]. For typical cardiac cells, Ca^{2+}

oscillates in a dynamic range of 40 to 180 beats per minute (bpm). Any deviation implies an unhealthy state [236]. Significant amounts of cellular energy are used via EC coupling, mainly offset by mitochondrial oxidative phosphorylation [237]. Glucose metabolism makes up to 20% of the total energy needed by a healthy heart. In mature cardiomyocytes, GLUT4 is the primary glucose transporter that carries extracellular glucose into the cell [238]. The primary glucose transporter in adult cardiomyocytes, GLUT4, is translocated to the sarcolemmal membrane in response to elevated intracellular Ca^{2+} concentration. An instantaneous 10- to 20-fold increase in glucose absorption happens when GLUT4 is translocated to the sarcolemmal membrane [238]. In adult rat cardiomyocytes, GLUT4 expression is down-regulated in myocardial insulin resistance and is linked to momentary insulin resistance [239]. This insulin resistance can promote the development of diabetic cardiomyopathy [240, 241]. In animal and in vitro models of type 1 and type 2 diabetes, impaired SERCA2a function is correlated with myocyte insulin resistance [242, 243]. Additionally, starting insulin therapy in diabetic mice returns SERCA2a levels to normal [244] and boosts intracellular Ca^{2+} oscillations [245], leading to a restoration of cardiac function. GLUT4 is randomly recruited to the sarcolemmal membrane upon insulin stimulation [246].

The severity of the insulin resistance is associated with the degree of defect in GLUT4 mRNA regulation [247]. Significant insulin resistance and glucose intolerance are caused by the targeted disruption of GLUT4 in muscle [248]. On the other hand, type 2 diabetes treatment may benefit from the enhanced insulin- or contraction-stimulated glucose transfer and was seen in skeletal muscle after GLUT4 overexpression [249, 250]. Cardioprotection is linked to the up-regulation of GLUT4 [251]. According to evidence from Yamaguchi *et al.* [252], 5' adenosine monophosphate-activated protein kinase (AMPK) regulates GLUT4's translocation to the plasma membrane in 3T3-L1 adipocytes. In cardiomyocytes, long-term (18 h) metformin treatment increased glucose transport capacity 3- to 5-fold through a decrease in GLUT4 endocytosis [253]. In a different study, metformin administration for four weeks lowered insulin resistance and dramatically raised GLUT4 expression in cardiac tissues in mice [254]. These studies indicate that glucose absorption mediated by GLUT4 is essential for maintaining glucose homeostasis.

The complex aetiology of DCM is further complicated by the oscillatory participation of LTCC, SERCA2a, RyR2, and NCX in the regulation of Ca^{2+} homeostasis. To better understand this, it would be prudent to divide the whole picture into more manageable sections. Dupont *et al.* [255] reviewed the new developments in understanding the underlying mechanism of calcium oscillations by using the power of mathematical modelling. First, they demonstrated how computational simulations of Ca^{2+} oscillations could help us draw several crucial inferences regarding the mechanics behind oscillation formation. Models help us conceptualize and quantify our intuition, especially for oscillatory events. Additionally, they provided an overview of the research on the mechanisms by which calcium oscillations couple to downstream effectors and the significance of calcium entry through store-operated channels in maintaining calcium oscillations. More recently, many mathematical models have been constructed to unravel this complex signalling [134, 236]. However, only a few studies included the effect of randomness involved in the system [109]. Firstly, the recruitment of GLUT4 to the sarcolemmal membrane happens at random [246]. The opening and closing of the RyR channels are also stochastic [93]. As a whole, this calcium oscillation is stochastic in nature [256, 257]. Recent research has hypothesized and experimentally confirmed various fascinating random fluctuations effects on the system behaviour [25, 95, 97–99]. Therefore, this study aims to comprehend how stochasticity affects calcium dynamics in cardiomyocytes. More specifically, we wish to assess the impact of GLUT4's random translocation on the Ca^{2+} dynamics. In an earlier study [236], we observed that the time delay involved in GLUT4 translocation to the plasma membrane plays a vital role in maintaining normal physiological oscillations in cardiomyocytes. However, the study does not include the cell membrane GLUT4 concentration and its random translocation, which plays an essential role in glucose-calcium dynamics. So, the present study aims to capture the relationship between glucose uptake by cardiomyocytes and calcium oscillation essential for normal cardiac functioning. This will help us to explore the possible factors related to DCM. To capture glucose uptake by cardiomyocytes and how it changes in diabetic conditions, we examine the dynamics of GLUT4. Since randomness plays a vital role in the translocation of GLUT4 to the membrane that controls the glucose uptake, we focused our study on exploring the dynamics of GLUT4 with other players like glucose and calcium under a stochastically

perturbed environment.

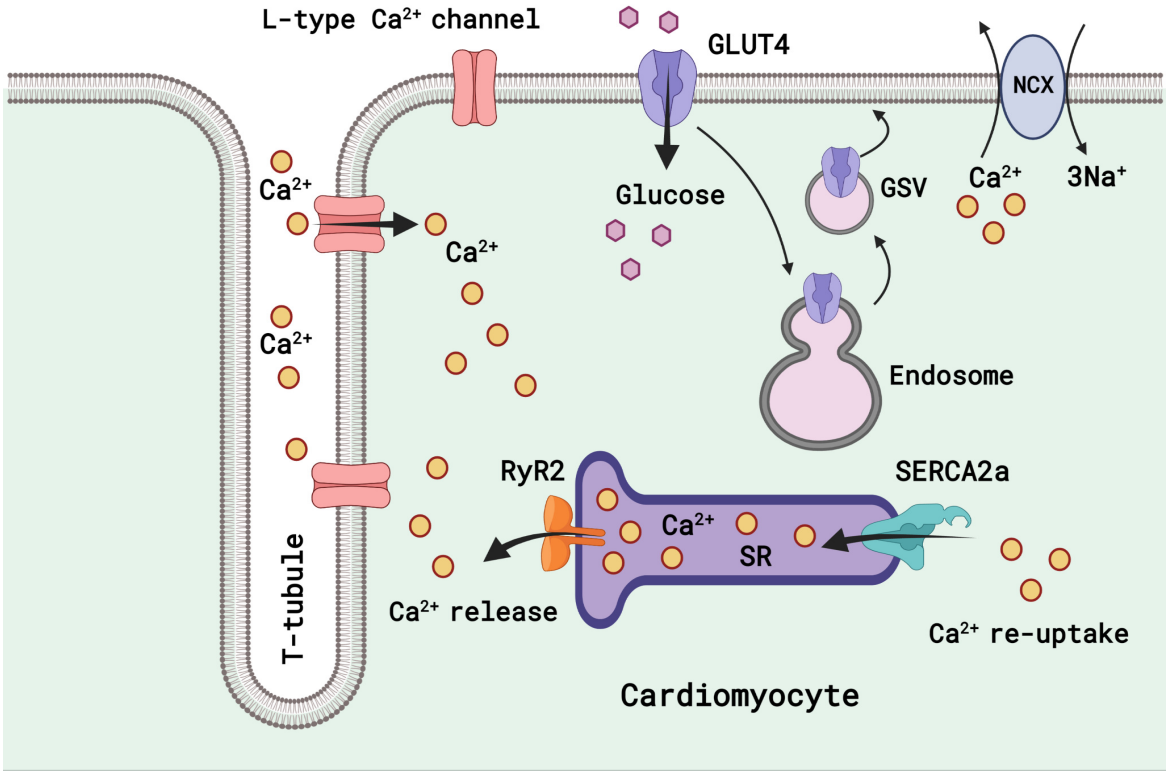

Figure 6.1: **Calcium signaling in cardiomyocytes.** The figure depicts the schematic representation of the calcium dynamics in cardiomyocytes. The arrows represent the direction of movement of the specific molecules. A detailed description of the interactions is given in the text. SR: sarcoplasmic reticulum; SERCA2a: SR Ca^{2+} ATPase 2a; RyR2: ryanodine receptor 2; NCX: Na^{+}/Ca^{2+} exchanger; GLUT4: glucose transporter type 4; GSV: GLUT4 storage vesicles.

6.2 Construction of deterministic model

To decipher the complex mechanism of calcium (Ca^{2+}) oscillation in cardiomyocytes, we proposed a simplified mathematical model of calcium signalling. The model system comprises the interactions between the insulin-regulated glucose transporter type 4 (GLUT4), glucose and calcium molecules in cardiomyocytes illustrated in the schematic diagram, Fig. 6.1. Let T_i and T_p represent the intracellular and plasma membrane GLUT4 concentrations, respectively. Since T_p is recruited from T_i, we always assume $T_p \subseteq T_i$. Assume that G_i represents the intracellular glucose level, while C_c and C_s represent the cytoplasmic and sarcoplasmic reticulum (SR) calcium levels. The rate equations of the two GLUT4 variables are adopted from Sedaghat *et al.*

[258] with some simplifications. Constant inclusion of intracellular GLUT4 from its sources is considered with the term k_1, while a self-degradation is included by the term $-k_2T_i$ in its rate equation. GLUT4 is found in specialized vesicles called GLUT4 storage vesicles (GSV) before the translocation to the plasma membrane. In the translocation of GLUT4 from intracellular space to the plasma membrane, the term $-k_4T_i$ is considered, where k_4 is the translocation rate. Insulin is the most extensively studied stimulus that triggers this translocation of GLUT4 from intracellular stores to the cell surface [259]. Note that this translocated GLUT4 is now the membrane GLUT4 which allows the cell to intake extracellular glucose inside cardiomyocytes. Once the glucose transportation is completed, some of the membrane GLUT4 goes back to the intracellular space and organelles. We consider this phenomenon with the term k_3T_p in the rate equation of T_i, where k_3 is the relocation rate of membrane GLUT4. In the rate equation of membrane GLUT4, we have only considered the translocation and relocation of GLUT4. Hence two terms, k_3T_p and k_4T_i, are included here with the opposite signs, as in the rate equation of intracellular GLUT4. Although the amount of recycling GLUT4 molecules and the cell surface GLUT4 level gradually increase as insulin concentrations increase, the kinetics of the increase in time is independent of insulin concentration [246]. Also, the internalization of GLUT4 is independent of the stimulus [260], and therefore, we have not explicitly considered any insulin-related parameters in the equations of the GLUT4. Now, in the rate equation of intracellular glucose, the term $\frac{rT_pG_i}{k_5+G_i}$ stands for glucose intake due to the opening of transporters on the plasma membrane. This intake is assumed to be proportional to membrane GLUT4 and saturated by glucose concentration. To describe this phenomenon, we considered a Holling type II function. Here r is the maximum intake rate, and k_5 is the corresponding half-saturation constant. The degradation of intracellular glucose is taken from Das *et al.* [134] and is represented by $-k_6G_i$ with the degradation rate constant k_6. The rate equations of cytoplasmic and SR calcium are adopted from the proposed model of Das *et al.* [134]. In the rate equation of cytoplasmic calcium concentrations, we include a constant input rate L to represent calcium input by L-type channels from extracellular space into the cytoplasm [261, 262]. Calcium efflux via NCX (Na^+/Ca^{2+} exchanger) channels is assumed to be linear [261, 262] and is represented by the term d_1C_c with d_1 as the rate constant. For calcium release from SR via ryanodine receptor

2 (RyR2), we used the term $\frac{pC_cC_s}{k_7^2+C_c^2}$, where p is the maximum release rate and k_7 is a positive constant [263, 264]. The calcium restoration in SR from the cytoplasm is sarcoplasmic reticulum Ca^{2+}-ATPase (SERCA2a) dependent, which is defined by the term $\frac{nC_c^2G_i}{k_8^2+C_c^2}$ [264], where n is the maximum restoration rate and k_8 is the corresponding half-saturation constant. These two terms are considered in the SR calcium rate equation with opposite signs. There is always an additional calcium ions leakage from SR into intracellular space [261, 262] and we use the term $-d_2C_s$ to represent it, where d_2 is the corresponding rate constant. Moreover, this leakage amount of calcium comes into the cytoplasmic space. Thus d_2C_s is added to the cytoplasmic calcium rate equation. Based on all these assumptions, the proposed model can be written as follows:

$$\begin{aligned}
\frac{dT_i}{dt} &= k_1 - k_2T_i + k_3T_p - k_4T_i,\\
\frac{dT_p}{dt} &= -k_3T_p + k_4T_i,\\
\frac{dG_i}{dt} &= \frac{rT_pG_i}{k_5+G_i} - k_6G_i,\\
\frac{dC_c}{dt} &= L + d_2C_s + \frac{pC_cC_s}{k_7^2+C_c^2} - \frac{nC_c^2G_i}{k_8^2+C_c^2} - d_1C_c,\\
\frac{dC_s}{dt} &= \frac{nC_c^2G_i}{k_8^2+C_c^2} - \frac{pC_cC_s}{k_7^2+C_c^2} - d_2C_s.
\end{aligned} \tag{6.1}$$

with the initial conditions $T_i(0) = T_{i0} > 0$, $T_p(0) = T_{p0} > 0$, $G_i(0) = G_{i0} > 0$, $C_c(0) = C_{c0} > 0$ and $C_s(0) = C_{s0} > 0$. All parameters are non-negative from a physiological viewpoint. The descriptions and default values of the parameters are presented in Table 6.1.

Table 6.1: Description of system parameters with their default values and references.

Parameters	Description	Values & unit	Source
k_1	Intracellular GLUT4 recruitment rate constant	5 $mML^{-1}s^{-1}$	Estimated
k_2	Self-degradation rate of intracellular GLUT4	1 mML^{-1}	Estimated
k_3	Relocation rate of membrane GLUT4	1.2 s^{-1}	Estimated
k_4	Translocation rate of intracellular GLUT4 to membrane	5.1 s^{-1}	Estimated
r	Maximum glucose input rate constant via GLUT4	0.278 μMs^{-1}	Estimated
k_5	Half-saturation constant for glucose input	0.5 μM	Estimated
k_6	Glucose degradation rate constant	0.5 s^{-1}	Estimated
L	Ca^{2+} input constant via L-type channels	3.02 μMs^{-1}	[261]
d_1	Ca^{2+} efflux rate constant through NCX	10 s^{-1}	[261, 262]
d_2	Sarcoplasmic Ca^{2+} leakage rate constant	1 s^{-1}	[261, 262]
p	Maximum activity rate constant of RyR2	20 μMs^{-1}	[262]
k_7	Positive constant related to RyR2	0.5 μM	[262]
n	Ca^{2+} flux constant through SERCA2a pump	6 s^{-1}	[262]
k_8	SERCA2a pump half-saturation constant	0.1 μM	[261]

6.3 Analysis of the deterministic model

6.3.1 Positivity and boundedness

Theorem 6.3.1. *For the system* (6.1)*, the interior* $\mathbb{R}^5_+$ *is invariant, and solutions with positive initial conditions are uniformly bounded within a region* Ω*, where*

$$\Omega = \left\{ (T_i, T_p, G_i, C_c, C_s) \in \mathbb{R}^5_+ : \; 0 < T_i(t) < \alpha, \; 0 < T_p(t) < \frac{\alpha k_4}{k_3}, \; 0 < G_i(t) < \frac{r\alpha k_4}{k_3 k_6}, \right.$$
$$\left. 0 < C_c(t) \leq \frac{\beta}{d_1}, \; 0 < C_s(t) \leq \frac{nr\alpha k_4}{d_2 k_3 k_6} \right\}$$

with $k_2 + k_4 > k_3$, $\alpha = \frac{k_1}{k_2 + k_4 - k_3}$ *and* $\beta = L + \left(d_2 + \frac{p}{k_7} \right) \frac{nr\alpha k_4}{d_2 k_3 k_6}$.

Proof. To prove the positive invariance, we express the system (6.1) in the vector form

$$\dot{v} = f(v) \tag{6.2}$$

with $v(0) = v_0 \in \mathbb{R}^5_+$, where $v = (T_i, T_p, G_i, C_c, C_s)^T \in \mathbb{R}^5_+$, $f = (f_1, f_2, f_3, f_4, f_5)^T$, $f_i(v) = f_i(T_i, T_p, G_i, C_c, C_s)$, $i = 1, 2, \cdots, 5$. Here $f : C_+ \to \mathbb{R}^5$ and $f \in C^\infty(\mathbb{R}^5)$. One can check that the functions f_i are continues and Lipschitzian on $\mathbb{R}^5_+ = \{(T_i, T_p, G_i, C_c, C_s) : T_i \geq 0, T_p \geq 0, G_i \geq 0, C_c \geq 0, C_s \geq 0\}$. Hence a solution of (6.1) with a non-negative initial condition exists and is unique. Due to the lemma of Nagumo [133], any solution of equation (6.2) with $v_0 \in \mathbb{R}^5_+$, say $v(t) = v(t; v_0)$, is such that $v(t) \in \mathbb{R}^5_+$ for all $t > 0$. Hence, the interior $\mathbb{R}^5_+$ is invariant for the system (6.2), and hence for (6.1).

Since T_p is recruited from T_i, so without loss of generality, we can assume that $T_p \leq T_i$. Using this assumption, the first equation of (6.1) gives

$$\frac{dT_i}{dt} + (k_2 + k_4 - k_3)T_i \leq k_1$$

Form the theory of differential inequalities [205], and assuming $k_2 + k_4 > k_3$, we have

$$0 < T_i(t) < \frac{k_1}{k_2 + k_4 - k_3}\left(1 - e^{-(k_2+k_4-k_3)t}\right) + T_{i0}e^{-(k_2+k_4-k_3)t}.$$

As $t \to \infty$, we then have $0 < T_i(t) < \alpha$, where $\alpha = \frac{k_1}{k_2+k_4-k_3}$.

Since $T_i(t) < \alpha$, the second equation of (6.1) gives

$$\frac{dT_p}{dt} + k_3 T_p \leq \alpha k_4.$$

Accordingly, when $t \to \infty$, we have $0 < T_p(t) < \frac{\alpha k_4}{k_3}$.

The third equation of (6.1) gives

$$\frac{dG_i}{dt} + k_6 G_i \leq \frac{r\alpha k_4}{k_3}.$$

Taking $t \to \infty$, we have $0 < G_i(t) < \frac{r\alpha k_4}{k_3 k_6}$.

Using the last equation of (6.1), one can write

$$\frac{dC_s}{dt} + d_2 C_s \leq \frac{nr\alpha k_4}{k_3 k_6}.$$

Following the same arguments, we have $0 < C_s(t) < \frac{nr\alpha k_4}{d_2 k_3 k_6}$.

Finally, from the fourth equation of (6.1), we have

$$\frac{dC_c}{dt} + d_1 C_c \leq \beta,$$

where $\beta = L + \left(d_2 + \frac{p}{k_7}\right)\frac{nr\alpha k_4}{d_2 k_3 k_6}$. Hence, one obtains $0 < C_c(t) < \frac{\beta}{d_1}$, when $t \to \infty$.

This shows the existence of a compact neighbourhood Ω, which is a proper subset of $\mathbb{R}^5_+$, such that, for sufficiently large initial conditions $(T_{i0}, T_{p0}, G_{i0}, C_{c0}, C_{s0})$, the solutions of system (6.1) will always be within the set Ω. This completes the proof. □

6.3.2 Equilibrium point and its stability

The equilibrium points of the system (6.1) are the solutions of the following equations:

$$\begin{aligned}
k_1 - k_2 T_i + k_3 T_p - k_4 T_i &= 0, \\
-k_3 T_p + k_4 T_i &= 0, \\
\frac{r T_p G_i}{k_5 + G_i} - k_6 G_i &= 0, \\
L + d_2 C_s + \frac{p C_c C_s}{k_7^2 + C_c^2} - \frac{n C_c^2 G_i}{k_8^2 + C_c^2} - d_1 C_c &= 0, \\
\frac{n C_c^2 G_i}{k_8^2 + C_c^2} - \frac{p C_c C_s}{k_7^2 + C_c^2} - d_2 C_s &= 0.
\end{aligned} \tag{6.3}$$

Its first two equations give $T_i = \frac{k_1}{k_2}$ and $T_p = \frac{k_1 k_4}{k_2 k_3}$. Form Eq. (6.3c), either $G_i = 0$ or $G_i = \frac{r k_1 k_4}{k_2 k_3 k_6} - k_5$. From the last two equations, one obtains $C_c = \frac{L}{d_1}$. One can then easily obtain from the last equation either $C_s = 0$ or $C_s = \frac{nL^2}{d_1^2 k_8^2 + L^2}\left(\frac{p d_1 L}{d_1^2 k_7^2 + L^2} + d_2\right)^{-1}\left(\frac{r k_1 k_4}{k_2 k_3 k_6} - k_5\right)$.

Thus, the system (6.1) has two equilibrium points $E_0 = \left(\frac{k_1}{k_2}, \frac{k_1 k_4}{k_2 k_3}, 0, \frac{L}{d_1}, 0\right)$ and $E^* = (T_i^*, T_p^*, G_i^*, C_c^*, C_s^*)$, where $T_i^* = \frac{k_1}{k_2}$, $T_p^* = \frac{k_1 k_4}{k_2 k_3}$, $G_i^* = \frac{r k_1 k_4}{k_2 k_3 k_6} - k_5$, $C_c^* = \frac{L}{d_1}$ and $C_s^* = \frac{nL^2}{d_1^2 k_8^2 + L^2}\left(\frac{p d_1 L}{d_1^2 k_7^2 + L^2} + d_2\right)^{-1}\left(\frac{r k_1 k_4}{k_2 k_3 k_6} - k_5\right)$. The feasibility of E^* is ensured by the condition $r > \frac{k_2 k_3 k_5 k_6}{k_1 k_4}$. We are interested in the interior equilibrium point E^* and its stability hence, and analyze the system around that point.

Theorem 6.3.2. *If $r > \frac{k_2 k_3 k_5 k_6}{k_1 k_4}$, then the unique interior equilibrium point $E^* = (T_i^*, T_p^*, G_i^*, C_c^*, C_s^*)$ of the system* (6.1) *is locally asymptotically stable if $a_{44} + a_{55} > 0$, where $a_{44} = d_1 - \frac{p C_s^* (k_7^2 - C_c^{*2})}{(k_7^2 + C_c^{*2})^2} + \frac{2 n k_8^2 G_i^* C_c^*}{(k_8^2 + C_c^{*2})^2}$ and $a_{55} = d_2 + \frac{p C_c^*}{k_7^2 + C_c^{*2}}$.*

Proof. The Jacobian matrix of the system (6.1) at the interior equilibrium point is given by

$$J(E^*) = \begin{bmatrix} -(k_2 + k_4) & k_3 & 0 & 0 & 0 \\ k_4 & -k_3 & 0 & 0 & 0 \\ 0 & a_{32} & -a_{33} & 0 & 0 \\ 0 & 0 & -a_{43} & -a_{44} & a_{45} \\ 0 & 0 & a_{53} & a_{54} & -a_{55} \end{bmatrix}, \tag{6.4}$$

where

$$\begin{aligned} a_{32} &= \frac{r G_i^*}{k_5 + G_i^*}, \\ a_{33} &= \frac{r T_p^* G_i^*}{(k_5 + G_i^*)^2}, \\ a_{43} &= \frac{n C_c^{*2}}{k_8^2 + C_c^{*2}} \; = \; a_{53}, \\ a_{44} &= d_1 - \frac{p C_s^* (k_7^2 - C_c^{*2})}{(k_7^2 + C_c^{*2})^2} + \frac{2 n k_8^2 G_i^* C_c^*}{(k_8^2 + C_c^{*2})^2}, \\ a_{45} &= d_2 + \frac{p C_c^*}{k_7^2 + C_c^{*2}} \; = \; a_{55}, \\ a_{54} &= a_{44} - d_1. \end{aligned} \tag{6.5}$$

The characteristic equation then reads

$$(\lambda + a_{33})\left[\lambda^2 + (k_2 + k_3 + k_4)\lambda + k_2 k_3\right]\left[\lambda^2 + (a_{44} + a_{55})\lambda + d_1 a_{55}\right] = 0. \tag{6.6}$$

Clearly, Eq. (6.6) has five eigenvalues. Of which, one is $\lambda_1 = -a_{33} < 0$. Note that both roots of the equation

$$\lambda^2 + (k_2 + k_3 + k_4)\lambda + k_2 k_3 = 0$$

are real negative. The roots of the equation

$$\lambda^2 + (a_{44} + a_{55})\lambda + d_1 a_{55} = 0 \tag{6.7}$$

will have negative real parts if $a_{44} + a_{55} > 0$. Thus, all the roots of the characteristic equation (6.6) will have negative real parts if $a_{44} + a_{55} > 0$, and the equilibrium will be locally asymptotically stable. Thus, the theorem is proven. □

Analysis of calcium subsystem

We have already demonstrated the stability of the system (6.1) through Theorem 6.3.2. However, the Ca^{2+} oscillation plays an important role in the functioning of cardiomyocytes. To study the existence of oscillation for calcium, we consider the following two-dimensional system (6.8) with C_c and C_s as variables. The glucose G_i in this subsystem is considered at the equilibrium value G_i^*. The calcium subsystem reads

$$\begin{aligned} \frac{dC_c}{dt} &= L + d_2 C_s + \frac{pC_c C_s}{k_7^2 + C_c^2} - \frac{nC_c^2 G_i^*}{k_8^2 + C_c^2} - d_1 C_c, \\ \frac{dC_s}{dt} &= \frac{nC_c^2 G_i^*}{k_8^2 + C_c^2} - \frac{pC_c C_s}{k_7^2 + C_c^2} - d_2 C_s. \end{aligned} \tag{6.8}$$

The equilibrium point of the calcium subsystem (6.8) is given by $E^p = (C_c^p, C_s^p)$, where $C_c^p = \frac{L}{d_1}$ and $C_s^p = \frac{nL^2}{d_1^2 k_8^2 + L^2}\left(\frac{pd_1 L}{d_1^2 k_7^2 + L^2} + d_2\right)^{-1}\left(\frac{rk_1 k_4}{k_2 k_3 k_6} - k_5\right)$. We can see that C_c^p and C_s^p are equal to the C_c^* and C_s^*, respectively. The Jacobian matrix of (6.8) is $J^p(C_c^p, C_s^p) = \begin{bmatrix} -a_{44} & a_{45} \\ a_{54} & -a_{55} \end{bmatrix}$ and the characteristic equation is given by

$$\lambda^2 + (a_{44} + a_{55})\lambda + d_1 a_{55} = 0,$$

which is identical with equation (6.7). It is mentionable that the roots of this equation may be real or complex. Therefore, Hopf bifurcation may occur in this subsystem.

6.3.3 Hopf bifurcation analysis

Our stability analysis shows that a pair of complex conjugate roots can only be obtained from the third factor of the equation (6.6). The third factor of equation (6.6) gives

$$\lambda^2 + A\lambda + B = 0, \tag{6.9}$$

where, $A = a_{44} + a_{55}$ and $B = d_1 a_{55}$. In diabetic conditions, the glucose uptake rate (r) by cardiomyocytes decreases. Therefore, we consider r as the Hopf bifurcation parameter. One can also choose another parameter of interest for such a study.

Theorem 6.3.3. *The system* (6.1) *experiences a Hopf bifurcation around E^* when the glucose intake rate through GLUT4 crosses a critical value r^* such that $A = a_{44} + a_{55} = 0$ at $r = r^*$ along with the transversality condition $\frac{dA}{dr} \neq 0$ at $r = r^*$.*

Proof. The necessary and sufficient conditions for Hopf bifurcation to occur at some critical value $r = r^*$ are

(i) $A(r^*) = 0$,

(ii) $\frac{dA}{dr}\big|_{r=r^*} \neq 0$.

Let us assume, at $r = r^*$, $A = 0$. Then from (6.9), we have

$$\lambda^2 + B = 0. \tag{6.10}$$

which has two roots, namely $\lambda_{4,5} = \pm i\sqrt{B}$.

Now note that $A = d_1 + d_2 + \frac{pC_c^*}{k_7^2 + C_c^{*2}} + \frac{2nk_8^2 G_i^* C_c^*}{(k_8^2 + C_c^{*2})^2} - \frac{pC_s^*(k_7^2 - C_c^{*2})}{(k_7^2 + C_c^{*2})^2}$. Substituting the values of G_i^*

and C_s^*, one can write

$$A = d_1 + d_2 + \frac{pC_c^*}{k_7^2 + C_c^{*2}} + \left[\frac{2nk_8^2 C_c^*}{(k_8^2 + C_c^{*2})^2} - \frac{p(k_7^2 - C_c^{*2})}{(k_7^2 + C_c^{*2})^2} \times \frac{nL^2}{d_1^2 k_8^2 + L^2}\left(\frac{pd_1 L}{d_1^2 k_7^2 + L^2} + d_2\right)^{-1}\right] \left(\frac{k_1 k_4}{k_2 k_3 k_6} r - k_5\right).$$

Differentiating A with respect to r, we get

$$\frac{dA}{dr} = \left[\frac{2nk_8^2 C_c^*}{(k_8^2 + C_c^{*2})^2} - \frac{p(k_7^2 - C_c^{*2})}{(k_7^2 + C_c^{*2})^2} \times \frac{nL^2}{d_1^2 k_8^2 + L^2}\left(\frac{pd_1 L}{d_1^2 k_7^2 + L^2} + d_2\right)^{-1}\right] \frac{k_1 k_4}{k_2 k_3 k_6}. \tag{6.11}$$

Note that the right-hand side of (6.11) is independent of r. Thus, $\frac{dA}{dr} \neq 0$ at $r = r^*$, and the transversality condition holds. Therefore, there exists a Hopf bifurcation around E^* when r crosses the critical value r^*. This completes the proof. □

Remark: It is to be noted that the Hopf bifurcation occurs in the calcium subsystem only when the other system variables attain their equilibrium values. Thus, oscillations in the concentrations of C_c and C_s will be observed even when the other three concentrations of E^* maintain their steady-state levels.

6.4 Analysis of the stochastic model

6.4.1 Construction of the stochastic model

In a natural system, the translocation of the GLUT4 molecule is a random process [246]. Also, inherent stochastic dynamics are displayed by the opening and closing of the RyR2 channels [109]. Stochastic effects could significantly impact [265] the characteristics of oscillations [266, 267]. Thus, we have explored the effects of randomness on the Ca^{2+} oscillations in the deterministic model (6.1). The stochastic perturbations of the state variables around their steady-state values E*, which are Gaussian white noise, and are proportional to the distances of T_i, T_p, G_i, C_c, C_s from their steady-state values T_i^*, T_p^*, G_i^*, C_c^*, C_s^*. So, the deterministic model

system (6.1) results in the following stochastic system:

$$\begin{aligned} dT_i &= F_1(T_i,T_p,G_i,C_c,C_s)dt + \sigma_1(T_i - T_i^*)d\xi_t^1 \,, \\ dT_p &= F_2(T_i,T_p,G_i,C_c,C_s)dt + \sigma_2(T_p - T_p^*)d\xi_t^2 \,, \\ dG_i &= F_3(T_i,T_p,G_i,C_c,C_s)dt + \sigma_3(G_i - G_i^*)d\xi_t^3 \,, \\ dC_c &= F_4(T_i,T_p,G_i,C_c,C_s)dt + \sigma_4(C_c - C_c^*)d\xi_t^4 \,, \\ dC_s &= F_5(T_i,T_p,G_i,C_c,C_s)dt + \sigma_5(C_s - C_s^*)d\xi_t^5 \,, \end{aligned} \tag{6.12}$$

where σ_i $(i = 1,2,3,4,5)$ are real constants, called the intensity of the fluctuations, $\xi_t^i = \xi_i(t)$ $(i = 1,2,3,4,5)$ are standard Wiener processes, independent of each other, and F_i $(i = 1,2,3,4,5)$ are defined in the Eq. (6.1). We consider Eq. (6.12) as an Ito stochastic differential system of the type

$$dX_t = F(t,X_t)dt + G(t,X_t)d\xi_t \tag{6.13}$$

where the solution $(X_t,\, t > 0)$ is an Ito process, 'F' is the drift coefficient, 'G' is the diffusion coefficient, and ξ_t is a five-dimensional stochastic process having scaler Wiener process components with increments $\triangle\xi_t^j = \xi_j(t+\triangle t) - \xi_j(t)$ are independent Gaussian random variables $\mathrm{N}(0,\triangle t)$. In the case of system (6.12),

$$X_t = \begin{bmatrix} T_i \\ T_p \\ G_i \\ C_c \\ C_s \end{bmatrix}, \xi_t = \begin{bmatrix} \xi_t^1 \\ \xi_t^2 \\ \xi_t^3 \\ \xi_t^4 \\ \xi_t^5 \end{bmatrix}, F = \begin{bmatrix} F_1(T_i,T_p,G_i,C_c,C_s) \\ F_2(T_i,T_p,G_i,C_c,C_s) \\ F_3(T_i,T_p,G_i,C_c,C_s) \\ F_4(T_i,T_p,G_i,C_c,C_s) \\ F_5(T_i,T_p,G_i,C_c,C_s) \end{bmatrix},$$

$$G = \begin{bmatrix} \sigma_1(T_i - T_i^*) & 0 & 0 & 0 & 0 \\ 0 & \sigma_2(T_p - T_p^*) & 0 & 0 & 0 \\ 0 & 0 & \sigma_3(G_i - G_i^*) & 0 & 0 \\ 0 & 0 & 0 & \sigma_4(C_c - C_c^*) & 0 \\ 0 & 0 & 0 & 0 & \sigma_5(C_s - C_s^*) \end{bmatrix}. \tag{6.14}$$

6.4.2 Stochastic stability of interior equilibrium

The stochastic differential system (6.12) can be centred at its positive equilibrium point $E^*(T_i^*, T_p^*, G_i^*, C_c^*, C_s^*)$ by introducing the variables $U_1 = T_i - T_i^*, U_2 = T_p - T_p^*, U_3 = G_i - G_i^*, U_4 = C_c - C_c^*, U_5 = C_s - C_s^*$. It seems difficult to derive asymptotic stability in the mean square sense by the Lyapunov functions method working on the complete non-linear equation (6.12). For simplicity of mathematical calculations, we deal with the stochastic differential equation obtained by linearising the vector function 'F' in (6.14) about the positive equilibrium point E^*. The linearised version of (6.13) around E^* is given by

$$dU(t) = f(U(t))dt + G(U(t))d\xi(t)\,, \tag{6.15}$$

where

$$U(t) = \begin{bmatrix} U_1(t) \\ U_2(t) \\ U_3(t) \\ U_4(t) \\ U_5(t) \end{bmatrix}, f(U(t)) = \begin{bmatrix} -(k_2+k_4)U_1 + k_3U_2 \\ k_4U_1 - k_3U_2 \\ a_{32}U_2 - a_{33}U_3 \\ -a_{43}U_3 - a_{44}U_4 + a_{45}U_5 \\ a_{53}U_3 + a_{54}U_4 - a_{55}U_5 \end{bmatrix},$$

$$G(U(t)) = \begin{bmatrix} \sigma_1 U_1 & 0 & 0 & 0 & 0 \\ 0 & \sigma_2 U_2 & 0 & 0 & 0 \\ 0 & 0 & \sigma_3 U_3 & 0 & 0 \\ 0 & 0 & 0 & \sigma_4 U_4 & 0 \\ 0 & 0 & 0 & 0 & \sigma_5 U_5 \end{bmatrix} \tag{6.16}$$

Note that, in (6.15) the positive equilibrium E^* corresponds to the trivial solution $(U_1, U_2, U_3, U_4, U_5) = (0,0,0,0,0)$. Let Ω be the set defined by $\Omega = \left[(t \geqslant t_0) \times \mathrm{R}^5, t_0 \in \mathrm{R}^+\right]$. To define stability, the following theorem from Carletti [111] can be used.

Theorem 6.4.1. *Suppose there exist a differentiable function $V(U,t) \in \mathrm{C}^5(\Omega)$ satisfying the*

inequalities

$$K_1|U|^{\alpha} \leq V(U,t) \leq K_2|U|^{\alpha}, \tag{6.17}$$

$$LV(U,t) \leq -K_3|U|^{\alpha}, \quad K_i > 0, \quad i = 1,2,3, \quad \alpha > 0\,. \tag{6.18}$$

Then the trivial solution of (6.15) is exponentially α-stable for all time $t \geq 0$.

Note that, if $\alpha = 2$ in (6.17), (6.18), then the trivial solution of (6.15) is exponentially mean square stable. Furthermore, the trivial solution of (6.15) is globally asymptotically stable in probability.

From (6.15),

$$LV(t,U) = \frac{\partial V(t,U(t))}{\partial t} + f^T(U(t))\frac{\partial V(t,U)}{\partial U} + \frac{1}{2}Tr\left[G^T(U(t))\frac{\partial^2 V(t,U)}{\partial U^2}G(U(t))\right], \tag{6.19}$$

where

$$\frac{\partial V}{\partial U} = \begin{pmatrix} \frac{\partial V}{\partial U_1} & \frac{\partial V}{\partial U_2} \end{pmatrix}^T, \quad \frac{\partial^2 V(t,U)}{\partial U^2} = \left(\frac{\partial^2 V}{\partial U_j \partial U_i}\right)_{i,j=1,2}$$

and T means transposition.

The critical noise level (σ_c), below which the system is stochastically stable, has been determined using the aforementioned Theorem 6.4.1. Thus, we can define and prove the following Theorem.

Theorem 6.4.2. *For some positive real values of $\omega_1, \omega_2, \omega_3, \omega_4$ and ω_5 if the following inequalities hold true*

$$\begin{aligned} &\left[k_3\omega_2 - \frac{1}{2}(1+\omega_2)\sigma_2^2\right]\left[\left(a_{33} - a_{43} - \frac{1}{2}{\sigma_3}^2\right)\omega_3\right] > \left(\frac{1}{2}a_{32}\omega_3\right)^2, \\ &\left[\left(a_{33} - a_{43} - \frac{1}{2}{\sigma_3}^2\right)\omega_3\right]\left[-a_{54} + (1+\omega_3+\omega_4)\left(a_{44} - \frac{1}{2}{\sigma_4}^2\right)\right] \\ &\qquad\qquad \left[k_3\omega_2 - \frac{1}{2}(1+\omega_2)\sigma_2^2\right] \\ &> \left[\left(a_{33} - a_{43} - \frac{1}{2}{\sigma_3}^2\right)\omega_3 - a_{54} + (1+\omega_3+\omega_4)\left(a_{44} - \frac{1}{2}{\sigma_4}^2\right)\right] \\ &\qquad\qquad \left(\frac{1}{2}a_{32}\omega_3\right)^2, \end{aligned} \tag{6.20}$$

then the zero solution of the system (6.15) will be exponentially 2-stable if

$$\begin{gathered}\sigma_1{}^2 < 2\left[\frac{k_4\omega_1+(1+\omega_1)k_2}{(1+\omega_1)}\right],\ \sigma_2{}^2 < 2\left[\frac{k_3\omega_2}{(1+\omega_2)}\right],\ \sigma_3{}^2 < 2\left[a_{33}-a_{44}\right],\\ \sigma_4{}^2 < 2\left[\frac{a_{44}(1+\omega_3+\omega_4)-a_{54}}{(1+\omega_3+\omega_4)}\right],\ \sigma_5{}^2 < 2\left[\frac{a_{45}\omega_5}{(1+\omega_5)}\right],\end{gathered} \tag{6.21}$$

where $\omega_1 = \frac{k_2-k_4\omega_2}{k_3}$, $\omega_2 = \frac{1}{10}$, $\omega_3 = \frac{d_1 a_{43}}{a_{45}(a_{33}+a_{44}+a_{54})}$, $\omega_4 = \left(\frac{a_{33}+a_{44}}{a_{43}}-1\right)\omega_3$, $\omega_5 = \frac{a_{45}}{a_{43}}\omega_3$ *and* $a_{32}, a_{33}, a_{43}, a_{44}$, a_{45}, a_{53}, a_{54}, a_{55} *are given in* (6.5).

Proof. Let us consider the Lyapunov function

$$V(U(t)) = \frac{1}{2}\left[(U_1+U_2)^2+\omega_1 U_1^2+\omega_2 U_2^2+\omega_3(U_3-U_4)^2+(U_4+U_5)^2+\omega_4 U_4^2+\omega_5 U_5^2\right], \tag{6.22}$$

where ω_i are real positive constants to be chosen later.

It is easy to check the inequalities in (6.17) are true for $\alpha = 2$. So, we have

$$\frac{\partial V}{\partial U} = \begin{bmatrix}(1+\omega_1)U_1+U_2\\ U_1+(1+\omega_2)U_2\\ \omega_3(U_3-U_4)\\ -\omega_3 U_3+(1+\omega_3+\omega_4)U_4+U_5\\ U_4+(1+\omega_5)U_5\end{bmatrix},$$

$$\frac{\partial^2 V}{\partial U^2} = \begin{bmatrix}1+\omega_1 & 1 & 0 & 0 & 0\\ 1 & 1+\omega_2 & 0 & 0 & 0\\ 0 & 0 & \omega_3 & -\omega_3 & 0\\ 0 & 0 & -\omega_3 & 1+\omega_3+\omega_4 & 1\\ 0 & 0 & 0 & 1 & 1+\omega_5\end{bmatrix}. \tag{6.23}$$

Using (6.16) and (6.19), we have

$$
\begin{aligned}
LV(U(t)) = & \left(-[k_2+\omega_1(k_2+k_4)]+\frac{1}{2}(1+\omega_1)\sigma_1^2\right){U_1}^2+\left(-k_3\omega_2+\frac{1}{2}(1+\omega_2)\sigma_2^2\right){U_2}^2 \\
& +\left(-a_{33}+a_{43}+\frac{1}{2}{\sigma_3}^2\right)\omega_3{U_3}^2+\left(-a_{45}\omega_5+\frac{1}{2}(1+\omega_5){\sigma_5}^2\right){U_5}^2 \\
& +\left(-a_{44}(1+\omega_3+\omega_4)+a_{54}+\frac{1}{2}(1+\omega_3+\omega_4){\sigma_4}^2\right){U_4}^2 \\
& +[-k_2+\omega_1k_3+\omega_2k_4]U_1U_2+a_{32}\omega_3U_2U_3-a_{32}\omega_3U_2U_4 \\
& +[(a_{33}+a_{44}-a_{43})\omega_3-a_{43}\omega_4]U_3U_4+[-a_{45}\omega_3+a_{43}\omega_5]U_3U_5 \\
& +[-d_1+a_{45}(\omega_3+\omega_4)+a_{54}\omega_5]U_4U_5.
\end{aligned}
$$

Choosing $\omega_1=\frac{k_2-k_4\omega_2}{k_3}$, $\omega_3=\frac{d_1a_{43}}{a_{45}(a_{33}+a_{44}+a_{54})}$, $\omega_4=\left(\frac{a_{33}+a_{44}}{a_{43}}-1\right)\omega_3$ and $\omega_5=\frac{a_{45}}{a_{43}}\omega_3$, the above equation reduces to

$$
\begin{aligned}
LV(U(t)) = & \left(-[k_2+\omega_1(k_2+k_4)]+\frac{1}{2}(1+\omega_1)\sigma_1^2\right){U_1}^2+\left(-k_3\omega_2+\frac{1}{2}(1+\omega_2)\sigma_2^2\right){U_2}^2 \\
& +\left(-a_{33}+a_{43}+\frac{1}{2}{\sigma_3}^2\right)\omega_3{U_3}^2+\left(-a_{45}\omega_5+\frac{1}{2}(1+\omega_5){\sigma_5}^2\right){U_5}^2 \\
& +\left(-a_{44}(1+\omega_3+\omega_4)+a_{54}+\frac{1}{2}(1+\omega_3+\omega_4){\sigma_4}^2\right){U_4}^2 \\
& +a_{32}\omega_3U_2U_3-a_{32}\omega_3U_2U_4 \\
& =-U^TQU,
\end{aligned}
\tag{6.24}
$$

where

$$Q = \begin{bmatrix} A_{11} & 0 & 0 & 0 & 0 \\ 0 & A_{22} & -\frac{1}{2}a_{32}\omega_3 & \frac{1}{2}a_{32}\omega_3 & 0 \\ 0 & -\frac{1}{2}a_{32}\omega_3 & A_{33} & 0 & 0 \\ 0 & \frac{1}{2}a_{32}\omega_3 & 0 & A_{44} & 0 \\ 0 & 0 & 0 & 0 & A_{55} \end{bmatrix},$$

and

$$\begin{aligned} A_{11} &= \omega_1 k_4 + (1+\omega_1)\left[k_2 - \frac{1}{2}\sigma_1^2\right], \\ A_{22} &= k_3\omega_2 - \frac{1}{2}(1+\omega_2)\sigma_2^2, \\ A_{33} &= \left(a_{33} - a_{43} - \frac{1}{2}{\sigma_3}^2\right)\omega_3, \\ A_{44} &= -a_{54} + (1+\omega_3+\omega_4)\left[a_{44} - \frac{1}{2}{\sigma_4}^2\right], \\ A_{55} &= a_{45}\omega_5 - \frac{1}{2}(1+\omega_5){\sigma_5}^2. \end{aligned}$$

The relation (6.20) and (6.21) imply that Q is a real symmetric positive definite matrix, and therefore, all its eigenvalues $\lambda_i(Q)$, $i = 1,2,3,4,5$ are positive real numbers. Let $\lambda_m = min\{\lambda_i(Q), i = 1,2,3,4,5\}$, $\lambda_m > 0$. From (6.24), we then have

$$LV(U(t)) \leq -\lambda_m |U(t)|^2 .$$

If the conditions in Theorem 6.4.2 hold, then the zero solutions of the system (6.15) are exponentially mean-square stable. This completes the proof. □

6.5 Numerical analysis

6.5.1 Parameter choice and model validation

The parameter values were collected from the literature to build the primary parameter set for the numerical analysis (see Table 6.1). The remaining parameters were calculated to fit the calcium kinetics observed through experiment [268]. The frequency of cytosolic calcium ($[Ca^{2+}]_c$) oscillations determines whether or not the reported dynamics represent physiologically healthy conditions. In this study, we have considered the level of cytosolic calcium ($[Ca^{2+}]_c$) as the output of the system. We assumed that physiological oscillations of $[Ca^{2+}]_c$ occur at a frequency of 40 to 180 bpm (beats per minute) [269, 270] with an amplitude of $\geq$0.4 μM [271]. It was observed that the cytosolic calcium ($[Ca^{2+}]_c$) in Fig. 6.2 oscillate in the PO range (with frequency 78 bpm and amplitude $\geq$ 0.4 μM) for the parameter set mentioned in Table 6.1. The outcomes shown in Fig. 6.2 further confirm our analytical findings that calcium concentration will fluctuate due to Hopf-bifurcation. Non-physiological oscillations (NPO) represent calcium oscillations outside the PO range. In Fig. 6.3, we have depicted the PO and NPO patterns for easier comprehension.

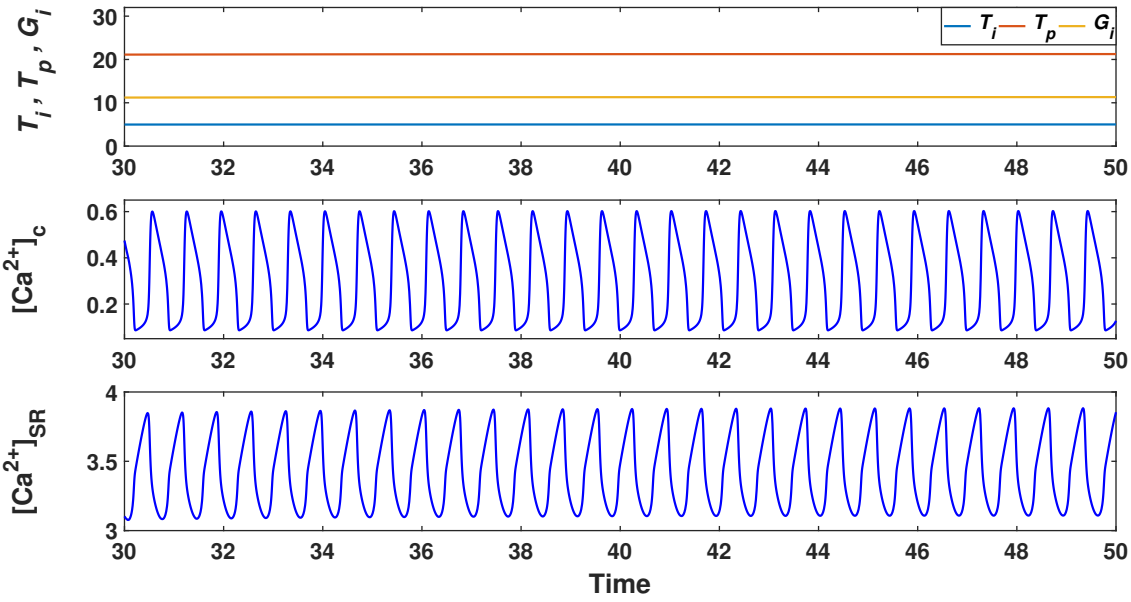

Figure 6.2: **Time series analysis of the deterministic system (6.1).** The figure depicts Ca^{2+} oscillation when GLUT4 and glucose maintain a steady state. Time course simulation recreating experimentally reported [268] calcium oscillations for the parameter set presented in Table 6.1. The time scale on this x-axis is measured in seconds. The time scale begins at thirty to eliminate the transient dynamics.

6.5.2 Effect of parameter variations on the Ca^{2+} oscillation

We performed a single-parameter variation study to find the variational effect of individual parameters on the system. We perturbed the parameters up and down from their basal values and recorded their PO, NPO, and stable ranges, see Table 6.2. The component-wise descriptions are given below.

(i) Effect of GLUT4 related parameters (k_1, k_2, k_3, k_4)**.** All the GLUT4-related parameters show an extensive PO range, especially k_1 and k_4 have shown vast PO ranges. The large range of the translocation rate (k_4) of GLUT4 to the plasma membrane indicates that the system is very robust in maintaining the PO of cytosolic calcium. When insulin stimulation exceeds some threshold value, GLUT4 translocates to the membrane and facilitates glucose entry into the cardiomyocytes. This glucose helps to maintain healthy physiological calcium oscillations.

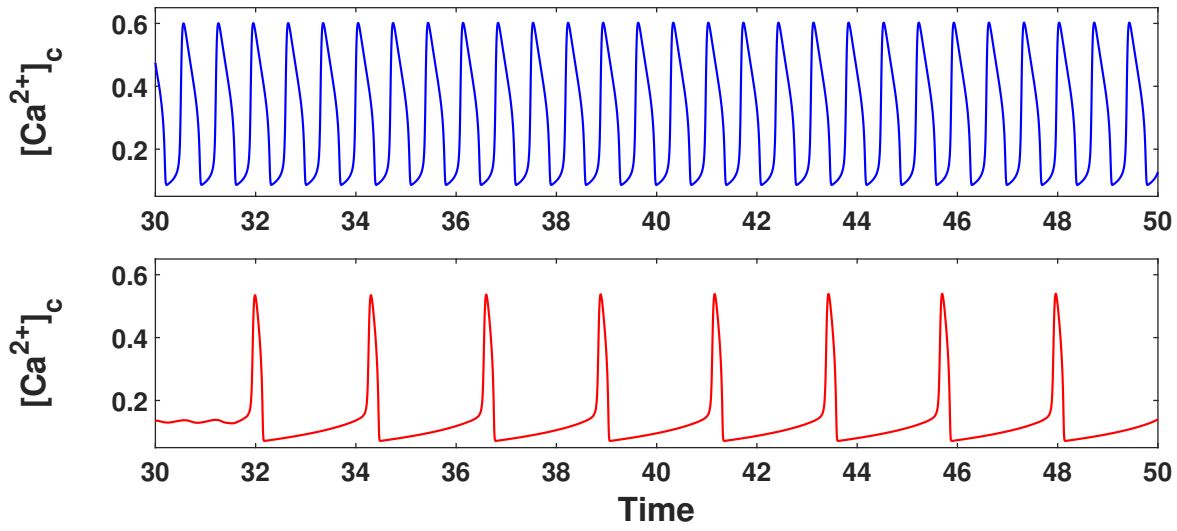

Figure 6.3: **PO and NPO patterns of the deterministic system (6.1).** The top panel shows cytosolic calcium's physiological oscillation (PO) with a frequency equal to 80 bpm and amplitude $> 40.4\ \mu M$. The bottom panel depicts the non-physiological oscillation (NPO) of cytosolic calcium with a frequency equal to 24 bpm (much below the normal range of 40 to 180 bpm). The parameters used to generate these curves are given in Table 6.1, with $L = 3.02$ for PO and $L = 1.338$ for NPO.

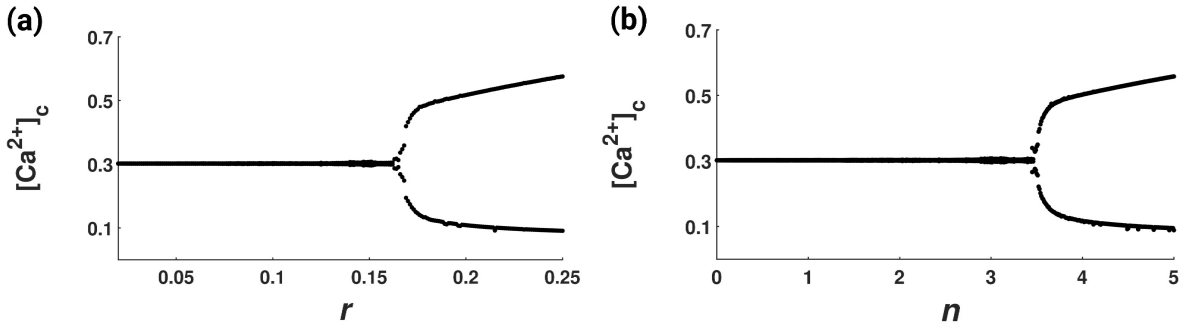

Figure 6.4: **Existence of periodic solution through Hopf bifurcation.** The figure shows the bifurcation of cytoplasmic calcium $[Ca^{2+}]_c$ when the bifurcating parameter r, the maximum glucose input rate constant via GLUT4, is varied smoothly (Fig. (a)). Fig. (b) shows a similar bifurcation for the Ca^{2+} flux parameter through the SERCA2a pump, n. The rest of the parameters are mentioned in Table 6.1. Here, we plotted the maximum and minimum values of $[Ca^{2+}]_c$ for each parameter value. Both values are the same when the system is stable but differ when the system is unstable (oscillatory). Stability switching occurs at the Hopf bifurcation points $r = 0.168$ and $n = 3.49$ in the left and right figures, respectively.

(ii) Role of glucose related parameters (r, k_5, k_6). When the maximum rate of glucose absorption (r) through GLUT4 was changed from its predetermined value of 0.278, we saw that the system maintained PO within the range of $0.2 \leq r \leq 0.68$, but it showed NPO outside of

this range. As r was decreased below 0.168, the system displayed stability toward the interior equilibrium point E^*. The Hopf bifurcation (following Theorem 6.3.3) occurred at $r = 0.168$ (see Fig. 6.4 (a)). The system (6.1) may also experience Hopf bifurcation for other sensitive parameters. For example, when we vary the parameter n, representing the Ca^{2+} flux constant through the SERCA2a pump, the system loses its stability through Hopf bifurcation at $n = 3.49$ (see Fig. 6.4 (b)). Similar PO, NPO, and stability patterns were observed for the glucose degradation rate (k_6) and the half-saturation constant of glucose input (k_5).

(iii) Parameters associated with calcium fluxes through cell membrane (L, d_1): For a brief interval of $1.34 \leq L \leq 3.5$, the calcium influx rate constant (L) of L-type channels displays PO. To keep the system in PO, L must be tightly regulated because it is quite sensitive. The PO range for the NCX-dependent calcium efflux rate via the cell membrane was $8.5 \leq d_1 \leq 18.1$. To sustain proper calcium oscillations, a delicate balance must exist between the LTCC input rate (L) and NCX-dependent calcium outflow rate (d_1).

Table 6.2: Impact of individual parameters on the overall performance of the system. Each parameter was altered independently, and the results were recorded along with their ranges.

Parameters	**Dynamics**	**Parameter ranges**	**Parameters**	**Dynamics**	**Parameter ranges**
k_1	Stable	$0.3 \leq k_1 \leq 3$	k_8	Stable	$k_8 > 0.124$
	NPO	$3 < k_1 \leq 3.5$ and $k_1 > 11.7$		NPO	$0.111 \leq k_8 \leq 0.124$
	PO	$3.5 < k_1 \leq 11.7$		PO	$0 < k_8 < 0.111$
k_2	Stable	$k_2 > 1.66$	d_1	Stable	$0 < d_1 \leq 8.4$ and $d_1 \geq 21.7$
	NPO	$1.43 \leq k_2 \leq 1.66$		NPO	$18.2 \leq d_1 \leq 21.6$
	PO	$0 < k_2 < 1.43$		PO	$8.5 \leq d_1 \leq 18.1$
k_3	Stable	$k_3 > 1.99$	d_2	Stable	$d_2 \geq 5.2$
	NPO	$1.72 \leq k_3 \leq 1.99$		NPO	$2.8 < d_2 < 5.2$
	PO	$0 < k_3 < 1.72$		PO	$0 < d_2 \leq 2.8$
k_4	Stable	$0 < k_4 < 3.07$	p	Stable	$0 < p \leq 1.4$
	NPO	$3.07 \leq k_4 \leq 3.57$		NPO	$1.5 \leq p \leq 2.9$ and $p \geq 41.8$
	PO	$k_4 > 3.57$		PO	$3 \leq p \leq 41.7$
k_5	Stable	$k_5 > 5.21$	r	Stable	$0 < r \leq 0.16$
	NPO	$4.01 \leq k_5 \leq 5.21$		NPO	$0.16 < r < 0.2$ and $r > 0.68$
	PO	$0 < k_5 < 4.01$		PO	$0.2 \leq r \leq 0.68$
k_6	Stable	$k_6 > 0.83$	L	Stable	$0 < L \leq 1.32$ and $L \geq 3.6$
	NPO	$0.72 \leq k_6 \leq 0.83$		NPO	$1.32 < L < 1.34$
	PO	$0 < k_6 < 0.72$		PO	$1.34 \leq L \leq 3.5$
k_7	Stable	$0 < k_7 < 0.45$ and $k_7 > 4.13$	n	Stable	$0 < n \leq 3.4$
	NPO	$1.19 < k_7 < 4.13$		NPO	$3.5 \leq n \leq 4.1$
	PO	$0.45 \leq k_7 \leq 1.19$		PO	$4.2 \leq n \leq 10.9$

(iv) Aspects of RyR2 channel parameters (p, k_7): We found a wide range of interval ($3 \leq p \leq 41.7$) for p and a thin range of interval $0.45 \leq k_7 \leq 1.19$ for k_7 in which the system maintains PO. Beyond this, the system either displayed NPO or became stable.

(v) Kinetic input of the SERCA2a pump (n, k_8): When we changed the SERCA2a pump-related parameters, namely the maximal calcium removal rate through the pump (n) and its half saturation constant (k_8), we found that the system could sustain PO over a wide range ($4.2 \leq n \leq 10.9$) for the parameter n and a relatively narrow range for k_8 ($0 \leq k_8 \leq 0.111$).

(vi) Impact of calcium leakage rate from SR (d_2): We looked at the calcium leakage parameter d_2's variational influence. We saw that the system switches from a PO to an NPO state when d_2 crosses 2.8, stabilizing after 5.2.

6.5.3 Global sensitivity analysis

Global Sensitivity Analysis (GSA) was performed based on Latin Hypercube Sampling (LHS) and Partial Ranked Correlation Coefficient (PRCC) [115] to evaluate the sensitivity of the parameters. A cut-off value of $\pm$ 0.3 on PRCC values [206, 208] was taken to identify the sensitive parameters. The GSA reveals that the parameters related to intracellular GLUT4 recruitment rate constant (k_1), self-degradation rate of intracellular GLUT4 (k_2), translocation rate of intracellular GLUT4 to the membrane (k_4), maximum glucose input rate constant via GLUT4 (r), Ca^{2+} input constant via L-type channels (L) and Ca^{2+} flux constant through SERCA2a pump (n) were most sensitive to the output of the system (see Fig. 6.5). All these parameters are essential for the energy requirements of the cardiomyocytes. The GLUT4-related parameters are sensitive to all the system's state variables. Parameters L and n are Ca^{2+} related parameters and are essential in maintaining calcium homeostasis in the cell.

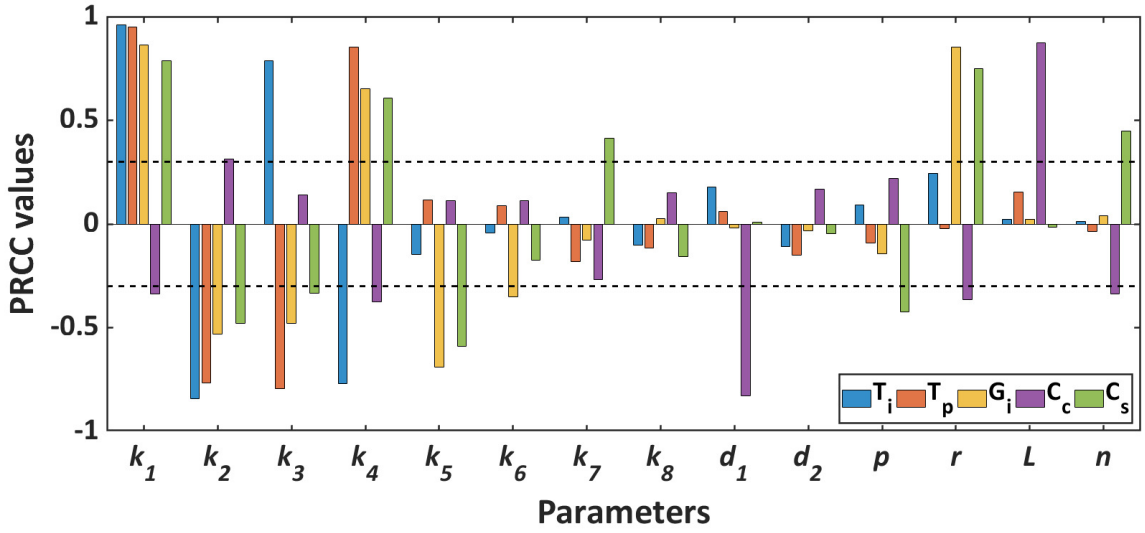

Figure 6.5: **Global sensitivity analysis.** Here, five different colour bars represent five state variables of the system. The sensitivity of each parameter is measured by the length of the bars corresponding to the state variables. Parameters with PRCC values beyond ± 0.3 are considered sensitive in this study [206, 208]. It is evident from the figure that the parameters k_1, k_2 and k_4 are sensitive to all the state variables of the system, whereas the parameters k_1, k_2, k_4, d_1, r, L and n are sensitive for the cytosolic calcium (C_c).

6.5.4 Robustness analysis of the sensitive parameters

To determine the robustness of the sensitive parameters in maintaining cytosolic Ca^{2+} oscillation in the PO range, we have perturbed each of the sensitive parameters individually, keeping the other parameters at their basal values given in Table 6.1. The strength of the parameter in maintaining the PO of cytoplasmic calcium is indicated by the length of the bars in Fig. 6.6. The shorter bars suggest that the PO is disrupted with smaller perturbations to the parameters, whereas for longer bars, the parameter can hold PO for larger perturbations. We observed that the parameters d_1 (Ca^{2+} efflux rate constant through NCX) and r (maximum glucose input rate constant via GLUT4) were the top robust parameters in maintaining PO when perturbed up or down. In contrast, parameters k_2 (self-degradation rate of intracellular GLUT4) were the least robust. Other parameters k_1, k_4, n, and L could maintain PO for a sizeable downward perturbation from their basal values but could not preserve PO when perturbed upward.

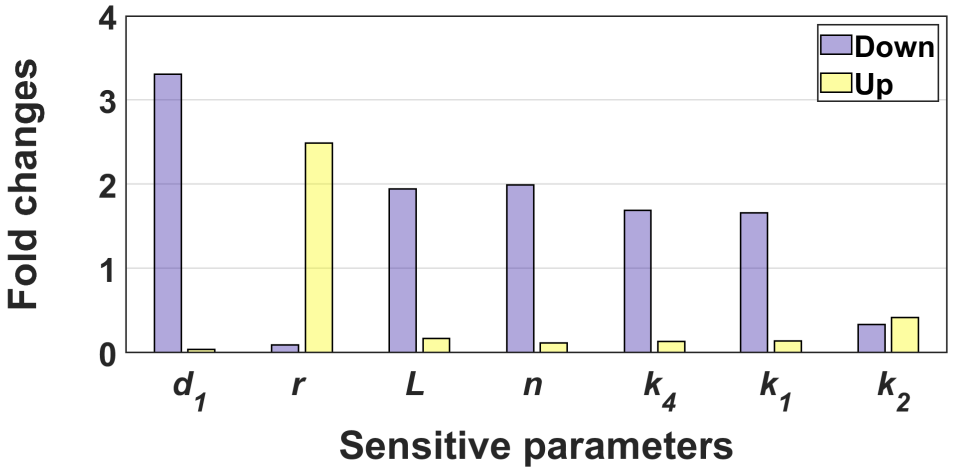

Figure 6.6: **Robustness analysis.** The figure describes the robustness of the sensitive parameters toward maintaining the PO of cytosolic calcium. Each sensitive parameter was perturbed individually from its basal values given in Table 6.1, keeping the other parameters at their basal levels. Here, each bar indicates a parameter range in fold change from its basal values up to which it can maintain the PO of cytosolic calcium. The blue bar represents the downward perturbation, and the yellow represents the upward perturbation.

6.5.5 Effect of randomness on Hopf bifurcation

The translocation of the GLUT4 molecule is a random process [246]. Similarly, the opening and closing of the RyR2 channels have inherent stochastic dynamics [109]. Stochasticity with minimal intensity is observed to impact the properties of oscillation significantly [265–267]. To observe the effect of noise on the system behaviour, we first calculated the critical value of the noise intensity (σ_c) using Theorem 6.4.2. The zero solution of the system (6.15) will be exponentially 2-stable for any noise intensity below this critical level. As the theorem is based on the stable equilibrium point, we considered $n = 0.5$, keeping all the parameters as mentioned in Table 6.1 so that the deterministic system remains stable. Theorem 6.4.2 allows us to estimate the critical sigma value as $\sigma_c = 0.2377$. The population densities will remain concentrated around the deterministic equilibrium value $E^* = (5, 21.25, 11.315, 0.302, 0.272)$ if the noise strength is lower than the critical σ_c (see Fig. 6.7a). For a higher noise intensity, the population densities diffuse more around the deterministic equilibrium value (see Fig. 6.7b).

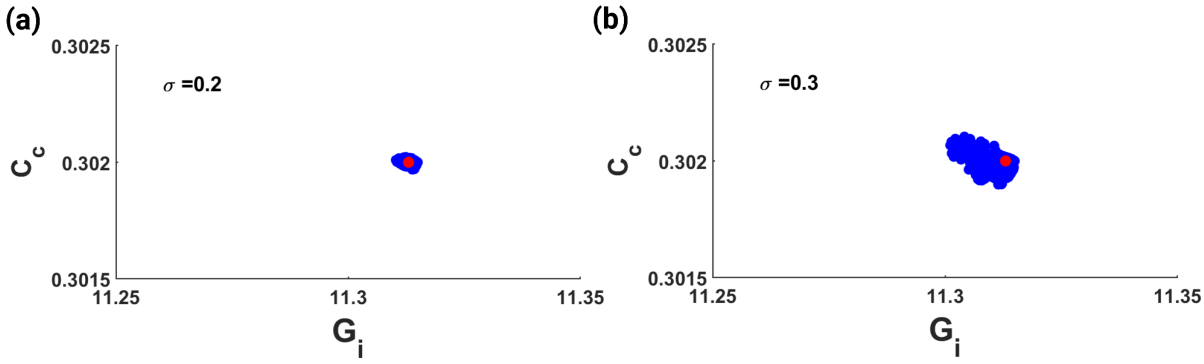

Figure 6.7: **Population distribution for low and high noise intensities.** (a) This figure shows populations (indicated by blue dots) are concentrated near the deterministic steady state value (denoted by red dot) when noise intensity is below the critical value $\sigma_c = 0.2377$. (b) This figure shows populations (indicated by blue dots) are dispersed around the deterministic steady state (denoted by red dot) when noise intensity is above the critical value $\sigma_c = 0.2377$.

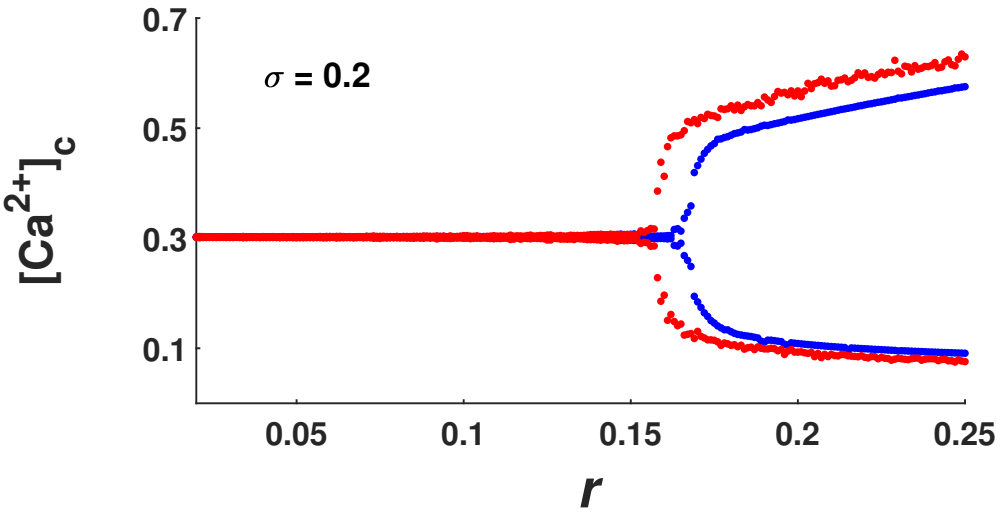

Figure 6.8: **Comparison of Hopf bifurcation results for the deterministic and stochastic systems.** The figure compares the bifurcation results of cytoplasmic calcium $[Ca^{2+}]_c$ for the deterministic system (represented by blue dots) and stochastic system (indicated by red dots) for the variation in r. An early bifurcation occurs in the stochastic system due to a small noise ($\sigma = 0.2 < \sigma_c = 0.2377$). The amplitude of oscillations is also increased for this noise. The parameters remain as in Table 6.1.

To observe how noise affects the bifurcation, we compared the bifurcation results of the deterministic and stochastic systems in Fig. 6.8. It reveals that the stochastic system displayed early bifurcation than the deterministic system as the parameter r is gradually increased. The bifurcation occurs at $r = 0.156$ (red dots in Fig. 6.8) whereas the Hopf-bifurcation occurred at $r = 0.168$ for the deterministic system (blue dots in Fig. 6.8). In addition, noise increases the amplitude of oscillations, which helps to attain the PO range. It has been seen that biological

oscillators can utilize stochastic noise by channelling it into oscillatory power [102]. Marchena *et al.* [109] observed that adding a small amount of noise to the RyR behaviour increases the oscillatory regime of calcium oscillations. Thus, randomness may enhance the PO range as the amplitude of the oscillations measures the PO and NPO.

Table 6.3: Restoration of cytosolic Ca^{2+} PO by adjusting the sensitive parameters after perturbing parameter r up and down by 2, 3, 4, and 5 folds. Here each entry represents the fold changes of the sensitive parameters required to restore the PO of cytosolic Ca^{2+}. The abbreviation NR means variation not required. The ↑ and ↓ represent fold increase and decrease, respectively.

Parameters	σ	$r/5$	$r/4$	$r/3$	$r/2$	$2r$	$3r$	$4r$	$5r$
k_1	0	3.52 ↑	2.82 ↑	2.12 ↑	1.42 ↑	NR	4.16 ↓	5.55 ↓	6.25 ↓
	0.1	3.28 ↑	2.60 ↑	1.98 ↑	1.34 ↑	NR	1.56 ↓	2.08 ↓	2.50 ↓
k_2	0	4.00 ↓	3.03 ↓	2.17 ↓	1.42 ↓	NR	1.24 ↑	1.65 ↑	2.07 ↑
	0.1	4.00 ↓	2.70 ↓	2.00 ↓	1.31 ↓	NR	1.54 ↑	1.99 ↑	2.16 ↑
k_4	0	3.80 ↑	2.92 ↑	2.14 ↑	1.41 ↑	NR	1.24 ↓	1.65 ↓	2.06 ↓
	0.1	3.35 ↑	2.60 ↑	1.97 ↑	1.29 ↑	NR	1.52 ↓	2.00 ↓	2.53 ↓
d_1	0	-	-	-	-	NR	-	-	-
	0.1	-	-	-	-	NR	-	-	-
L	0	-	-	-	-	NR	-	-	-
	0.1	-	-	-	-	NR	-	-	-
n	0	4.2 ↑	3.19 ↑	2.27 ↑	1.44 ↑	NR	1.24 ↓	1.65 ↓	2.08 ↓
	0.1	3.83 ↑	2.89 ↑	2.07 ↑	1.32 ↑	NR	1.50 ↓	1.74 ↓	2.56 ↓

6.5.6 Restoration strategies and potential drug-targets

The robustness analysis determines that one of the most robust parameters for preserving the physiological oscillations of cytosolic Ca^{2+} is the maximal glucose input rate constant (r) via GLUT4. In essence, it relies on insulin stimulation, which could significantly affect the development of diabetic cardiomyocytes. The transfer of plasma glucose into cardiomyocytes is impeded in the event of insulin-resistant diabetes, which mainly affects the parameter r. With further exploration, we found that the suppression and over-expression of r result in altered

calcium oscillations. It is demonstrated that the system operates normally for a 2-fold increase in r and that no parameters need recalibration. However, a more significant fold change in r causes cardiomyocyte malfunction. Although parameters d_1 and L individually could maintain PO with two folds reduction, they cannot restore PO of $[Ca^{2+}]_c$ due to a perturbation in r (see Table 6.3). By controlling the rest of the sensitive parameters, one might preserve normalcy even for a 5-fold increase or decrease of r. The analysis was performed both for the deterministic ($\sigma = 0$) and stochastic systems ($\sigma = 0.1$). A comprehensive result outlining the contribution of several sensitive parameters to the restoration of PO of $[Ca^{2+}]_c$ with the change in r is tabulated in Table 6.3. For both the deterministic and stochastic systems, the parameters k_2, k_4, and n need about a maximum of 3 fold perturbations for restoring PO even when r is perturbed five times its basal value. However, it is different in the case of parameter k_1. The deterministic system requires a six-fold decrease of k_1 to restore PO when r is perturbed five times its basal value (see Fig. 6.9). Interestingly, this change is significantly reduced (less than three folds) when a small amount of randomness (less than the critical value σ_c) is added to the system. The stochastic system only requires a three-fold decrease in the k_1 value to restore PO (see Fig. 6.9).

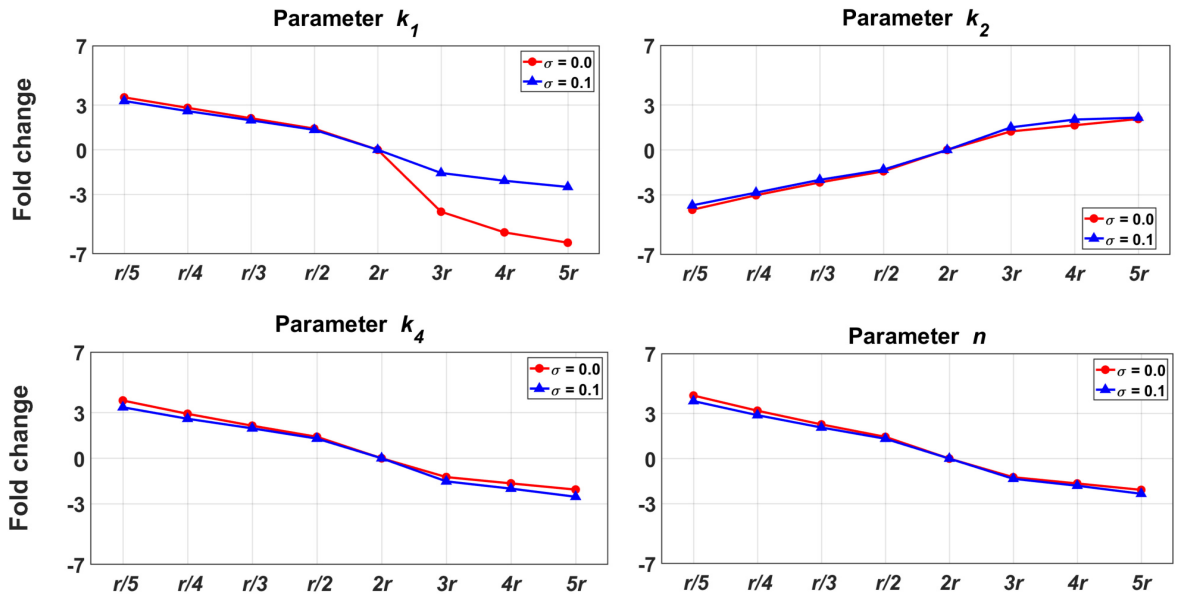

Figure 6.9: **Parameter recalibration.** The figure depicts the perturbation of sensitive parameters required to restore PO of $[Ca^{2+}]_c$ after up and down regulations of r by 2, 3, 4, and 5 times. Parameter recalibration was done for the deterministic system (represented by red colour) and the stochastic system (represented by blue colour). The positive and negative fold change represents the up and down-regulation of the sensitive parameters.

Insulin resistance (IR) plays a central role in the progression of cardiovascular diseases related to diabetes, including diabetic cardiomyopathy [272, 273]. In models of insulin resistance, there has been evidence of a decrease in GLUT4 expression [273]. As insulin signalling causes GLUT4 to move to the plasma membrane and boosts glucose absorption, so in insulin resistance conditions, a reduction of GLUT4 implies a reduction of glucose uptake [273, 274]. Thus, in our model system, we have used this strategy of reduction of glucose uptake to mimic insulin resistance. Therefore in case of insulin resistance, when the maximum glucose input rate constant via GLUT4 (r) decreases, PO of $[Ca^{2+}]_c$ could be restored by increasing the GLUT4 related parameters, namely, intracellular GLUT4 recruitment rate constant (k_1) and translocation rate of intracellular GLUT4 to the membrane (k_4) and also by increasing Ca^{2+} flux constant through SERCA2a pump (n). A decrease in the self-degradation rate of intracellular GLUT4 (k_2) is also capable of restoring the PO of $[Ca^{2+}]_c$ in the IR heart. Thus by controlling GLUT4 related parameters (k_1, k_2 and k_4) and the Ca^{2+} flux constant through SERCA2a pump (n) we could restore the PO of $[Ca^{2+}]_c$ in IR cardiomyocytes.

6.6 Discussion

According to the International Diabetes Federation, 643 million people aged between 20 to 79 worldwide will be diagnosed with diabetes by 2030. That number will rise to 783 million by 2045 [221]. Cardiovascular disorders, particularly heart failure and diabetes, are frequently linked [222, 223]. Diabetes-related heart failure is influenced by the onset of cardiac damage known as "diabetic cardiomyopathy" [224]. One of its functional characteristics is a propensity for ventricular dysfunction, which influences the myocardial energy and contractile function [227–230]. Systematic plasma glucose delivery into cardiomyocytes and other cells is necessary to preserve a healthy cardiac function. The primary function of cardiomyocytes is to contract, which creates the pressure required to pump blood through the circulatory system [275]. Calcium oscillation in cardiomyocytes facilitates this contractile function. From controlling proliferation in human cardiac progenitor cells to controlling pacemaker rhythm in both early embryonic heart cells and sinoatrial nodal pacemaker cells, calcium oscillations play a

significant function [109]. Calcium is essential for preserving physiological oscillations (PO), whereas glucose transporters like GLUT4 are responsible for maintaining glucose uptake. Any deviations from its normal range will affect the normal functioning of the cardiomyocytes. Understanding how these aberrations affect cardiomyocytes at the molecular level can help predict how diabetes will affect the structural and functional changes in the heart.

The present study demonstrated the emergence of periodic calcium oscillation using a precise subcellular calcium model of cardiomyocytes. It analyzed the critical facets of the system using ODE and SDE-based mathematical models and studied the importance of calcium oscillations in the normal functioning of cardiomyocytes. The parameter set satisfying the existence of physiological oscillation (PO) of cytosolic calcium is considered the basal parameter set. Then by altering these parameters, we induced non-physiological oscillations (NPO) to mimic the diseased conditions. The emergence of Hopf bifurcation around the interior equilibrium point established the existence of periodic solutions. Randomness is crucial for GLUT4 translocation to the membrane, which regulates glucose absorption. So, the present study focused on GLUT4 dynamics related to other players like glucose and calcium in a stochastically perturbed environment.

Single parameter variation analysis explored the relation of different parameters on the system's output in terms of PO, NPO, and stability. The sensitive parameters were identified through Global sensitivity analysis (GSA). We identified the range for every sensitive parameter for the existence of PO. Outside of the PO range, the system either exhibits stability or non-physiological oscillations (NPO). An interesting phenomenon of early bifurcation was observed when minimal noise was introduced to the deterministic system. With early bifurcation, the oscillation amplitude also gets enlarged in the stochastic case. In our case, we are not only interested in the oscillatory behaviour of the system but also in the physiological and the non-physiological oscillations, which mark healthy and unhealthy cardiac functions.

The primary goal of this work was to simulate the diabetic condition that can alter physiological calcium oscillations, causing heart dysfunction. Our model could mimic this diabetic condition by inducing insulin resistance (IR) in cardiomyocytes by perturbing the maximum glucose input rate constant via GLUT4 (r). Plasma glucose enters the cell with the help of

insulin-stimulated GLUT4 to supply the cell's energy needs. The plasma glucose entry is impeded in IR cardiomyocytes. In such a condition, we tried to restore the PO of the cytosolic Ca^{2+} by changing the other sensitive parameters. The parameter recalibration was performed for both systems with respect to the sensitive parameters. Parameters L and d_1 are linearly related to the amount of cytosolic calcium $[Ca^{2+}]_c$, so any alteration in those parameters would directly affect the concentrations of $[Ca^{2+}]_c$. However, here we observed that if parameter r is perturbed to mimic the IR condition, L and d_1 cannot restore the PO of $[Ca^{2+}]_c$. The only Ca^{2+} related parameter that could restore the PO of $[Ca^{2+}]_c$ is n, which represents the Ca^{2+} flux rate through SERCA2a pump. The GLUT4-related parameters, like intracellular GLUT4 recruitment rate (k_1), self-degradation rate of intracellular GLUT4 (k_2), and translocation rate of intracellular GLUT4 to the membrane (k_4), can restore PO. Thus, restoration of PO is possible by altering three GLUT4-related parameters and one Ca^{2+} related parameter. The stochasticity in the system tends to ease this restoration process.

Cardioprotection has been linked to GLUT4 up-regulation [251]. Recent studies also emphasized the regulation of the GLUT4 transporter for the prevention of type 2 diabetes [276]. Thus, the drugs that target enhancing GLUT4 expression and GLUT4 translocation are the most suitable to restore the PO of $[Ca^{2+}]_c$. An earlier study [277] reports that chloroquine improves insulin resistance by boosting GLUT4 translocation and fusion with the plasma membrane in L6 muscle cells. Neferine also stimulates the expression of GLUT4 and its fusion with the plasma membrane to trigger glucose uptake in L6 muscle cells [278]. This neferine-induced GLUT4 fusion with the plasma membrane and glucose uptake are Ca^{2+}-dependent [278]. In the case of cardiomyocytes, recent articles report the protective effects of neferine in cardiac dysfunctions [279–281], and many other pathologies [282, 283]. Many efforts have been made, including targetting insulin signalling, especially GLUT4, in treating diabetes and cardiovascular diseases [284]. Up-regulation of GLUT4 has been related to cardioprotection [251]. Ormazabal *et al.* [272] opined that making overexpression of GLUT4 might be the potential strategy for creating a new class of medications in treating diabetic cardiomyopathy. It has been demonstrated that in 3T3-L1 adipocytes, AMPK controls the translocation of GLUT4 to the plasma membrane [252]. According to Yang *et al.* [253], long-term (18

h) metformin administration of cardiomyocytes boosted glucose transport activity 3- to 5-fold through a reduction in GLUT4 endocytosis that was dependent on AMP-activated protein kinase. In another study, metformin treatment for four weeks in metabolic syndrome-induced mice significantly reduced insulin resistance and significantly increased GLUT4 expression in heart tissues [254]. Through the stimulation of AMPK activity, berberine also reduces insulin resistance in H9c2 cardiomyocytes [285]. By restoring PI3K/AKT signalling-mediated GLUT4 membrane translocation, carvacrol is a possible therapeutic drug for DCM [286]. Therefore, in a state resembling diabetes, an increase in the GLUT4 expression and GLUT4 translocation to the plasma membrane might be crucial in sustaining PO and might be utilized as therapeutic targets. An increase in GLUT4 expression and its translocation to the plasma membrane may be essential for maintaining PO in a diabetic condition and may be used as therapeutic targets. We have demonstrated here that the PO of $[Ca^{2+}]_c$ in IR cardiomyocytes could be restored by increasing the intracellular GLUT4 recruitment rate (k_1) and GLUT4 translocation rate to the membrane (k_4) and could be used as therapeutic strategies.

In conclusion, this chapter discusses the effect of randomness in calcium signalling in cardiomyocytes. The current study developed a SDE-based mathematical model to examine the effect of the random movement of GLUT4, which facilitates glucose entry in the cardiomyocytes. Then, by altering system parameters, we induced insulin resistance (IR) in cardiomyocytes to mimic diabetic conditions and proposed potential restoration strategies to recover the physiological oscillations of cytosolic calcium. Early bifurcation was observed when we introduced randomness in the system. Thus, the random translocation of GLUT4 facilitates the restoration mechanisms.

7

Conclusions and future directions

7.1 Conclusions

Cell signalling research has emerged with significant progress in interdisciplinary fields in the era of high throughput techniques. However, therapeutic strategies targeting key molecules have yet to fulfil the expected promises for most common malignancies. Major difficulties include incomplete understanding due to single-pathway targeted approaches. Signalling pathways are not linear, but they have molecular cross-talk. To achieve this, we must consider the system as a complex network of interacting components. Such departure from the traditional paradigm of studying a single pathway to a more global approach will aid the design of novel therapeutics.

The present thesis incorporated a systems biology approach integrated with mathematical

modelling to understand complex mechanisms of cell signalling systems in a global manner. The complexity in signalling networks arises due to the presence of highly connected modules that regulate multiple functions. This complexity increases even more due to the presence of intrinsic noise. The signalling systems must be robust enough to execute their cellular activities. At the same time, they must be sensitive enough to capture the variations in the input stimuli. To unravel this complexity, we have considered the smaller functional subunits known as network motifs. The motif organisation influences their sensitivity, robustness, and trade-off in a signalling network. We have developed analytical formulas derived by solving mathematical models that classify and rank motifs depending on their sensitivity profile under random perturbation. In the following bullet points, we have summarised different results obtained from different chapters.

- The study on two frequently observed two-node network motifs reveals the emergence of complex qualitative behaviour, like bistability, that can be disrupted due to the presence of randomness in the system. These signal-noise relations are useful in diseases that cause complex perturbations in cellular signalling networks, like cancer, diabetes, and autoimmunity. That encouraged us for a deeper investigation of the association between motif structures and the noise in signalling networks.

- The study considering all possible two-node network motifs provides a global view of the significance of network motifs in maintaining cell signalling in a noisy environment and also provides a methodology for screening potential drug targets. We observed that the double-positive feedback loops have a larger stable area and are robust under systemic noise. In contrast, the double negative feedback has the least stable area referring to their vulnerability to systemic noise. The druggability test reveals that the sensitive motifs have the highest druggability, whereas the robust motifs have the least druggability. So, the sudden changes in the concentration of the output node of the sensitive motifs that need to be controlled to maintain the desirable input-output signal in a network are also better druggable than the robust motifs. We applied the dependency of the input-output relation on motif structure and designed a quantitative scoring formula to identify critical nodes in protein-protein interaction networks. High-impact drug targets like GSK3B,

ERBB2, INSR, RET, SRC etc., were identified from three cancer networks, namely breast, pancreatic and ovarian cancers, using the formula. We observed a strong association between the sensitivity of the proteins towards noise and the proteins approved as drug targets. A reverse analysis of the established drug targets from the literature further confirmed our proposition.

- We explored the emergence of bistability and used it to identify the potential drug targets from the cancer networks. Seven out of the eighteen possible bistable motifs showed bistability in our study. A bistable system often shows hallmark characteristics like hysteresis, a switching phenomenon observed for different stimulus-response. This hysteresis can be of two types: reversible and irreversible hysteresis. In reversible hysteresis, the system can return to its previous steady state only by changing the input stimulus, whereas in irreversible hysteresis, it can not. The nature of hysteresis depends on the strength of the feedback parameter. We obtained ranges of feedback parameters for reversible and irreversible hysteresis for each bistable motif structure. Based on the reversible hysteretic feedback parameter range, we ranked the motifs and found that they are better or easier drug targets. We further observed that the known drugs tended to target the bistable motifs and are associated with those with larger feedback effects.

- Our study introduced methods to identify prospective drug targets independent of the data structure. All currently used network-based techniques rely heavily on centrality and differentia. Differential network analysis identifies drug targets by analysing different networks that are data-dependent. In comparison, the centrality-based approach detects nodes with high-degree, betweenness, closeness centrality etc. Targeting these central positions helps to disintegrate the network. However, employing the disintegration methods to identify the targets has detrimental side effects. The study overcomes these drawbacks by proposing a methodology independent of the data and network structure.

- The significance of bistability in cell signalling networks was explored by studying decision-making processes in the tumour necrosis factor (TNF) signalling network in T regulatory

cells. Through bistable switching, we explained the complex behaviour of cell survival and death. The model reveals that the elevated TNF concentration and increased c-Jun N-terminal kinase (JNK) phosphorylation are the major contributors to the death of T-regulatory cells and can be controlled by reducing the TNF concentration. Inherent stochasticity reduces the system's bistability and affects its normal functioning.

- The significance of randomness on the existence of calcium oscillation in cardiomyocytes was investigated. The calcium signalling pathway in cardiomyocytes reveals the complex aetiology of diabetic cardiomyopathy in terms of calcium oscillations under a stochastic environment. Diabetes develops due to altered calcium signalling in the presence of randomness, which can be utilised to determine targets for diabetic hearts. We induced insulin resistance in cardiomyocytes to mimic diabetic conditions and proposed potential restoration strategies to recover the physiological oscillations (PO) of cytosolic calcium. We observed that in case of insulin resistance when the maximum glucose input rate constant via GLUT4 decreases, PO of cytosolic calcium could be restored by increasing the GLUT4-related parameters, namely, intracellular GLUT4 recruitment rate constant and translocation rate of intracellular GLUT4 to the membrane and also by increasing calcium flux constant through SERCA2a pump. Random translocation of GLUT4 to the plasma membrane that controls glucose uptake unfolds early oscillations in cytosolic calcium, facilitating the restoration mechanisms.

Overall the thesis developed novel methods and tools to identify regulatory points of the complex biological networks by exploring the emergence of bistability and the presence of intrinsic randomness in the system. In the early part of the thesis, the developed methods are independent of data and network structures that can be used to identify potential drug targets. The kinetic models developed in the last two chapters studied the significance of randomness in various biological problems. It captured the significance of bistability in TNF signalling, especially in decision-making processes. It also showed the importance of random translocation of GLUT4 in diabetic cardiomyocytes in facilitating the physiological calcium oscillations restoration.

7.2 Future directions

The current research presents several intriguing theories that merit additional investigation and can be extended through different facets of systems biology and mathematical modelling. In the following bullet points, we have presented the possible future extensions of the current thesis.

- Protein-protein interaction networks include various classes of proteins like kinases, phosphatases, transcription factors, etc. However, in our study, we have considered only the enzymatic reactions based on the Michaelis-Menten form of kinetics. But these protein classes may differ in their functional relationships. This study takes a global approach that may lack mechanistic details displayed by various protein classes. So, an in-depth study considering specific functional relationships of different protein classes needs to be done to get more mechanistic insights.

- This study also does not include the effect of coupling of individual motifs. Reports suggest that coupling two-node feedback motifs increase the safety zone or the hysteretic region, which can be crucial in determining input-output relations, especially under random perturbations. Thus this study can be extended for the coupled motifs.

- Although the study of TNF signalling in T regulatory cells quantitatively captured the realistic mechanism of cell survival and death, it excluded many intermediate molecules and cross-talks. An extensive study of TNF signalling can be done by considering all the intermediate molecules to investigate TNF treatment exclusively.

- We all know the biological system works in unison and is minutely organised and coordinated. But to focus on capturing the effect of random translocation of GLUT4, we have taken a portion of the calcium signalling in cardiomyocytes. So, a detailed study of the whole calcium signalling system can be done to get more mechanistic insights.

- Finally, the study can be extended by performing the experimental validations of the proposed drug targets identified from the cancer networks in the thesis. The proposed therapeutic targets identified by the kinetic model of the TNF signalling and restoration strategies of the diabetic cardiomyocytes also can be verified through experiments.

References

[1] Lisa A Urry, Michael Lee Cain, Steven Alexander Wasserman, Peter V Minorsky, and Jane B Reece. *Campbell Biology*. Pearson Education, Incorporated, 2017.

[2] Matteo Mossio, Maël Montévil, and Giuseppe Longo. Theoretical principles for biology: Organization. *Progress in Biophysics and Molecular Biology*, 122(1):24–35, 2016.

[3] Mikaela Koutrouli, Evangelos Karatzas, David Paez-Espino, and Georgios A Pavlopoulos. A guide to conquer the biological network era using graph theory. *Frontiers in Bioengineering and Biotechnology*, page 34, 2020.

[4] Frank Emmert-Streib and Matthias Dehmer. Biological networks: the microscope of the twenty-first century?, 2015.

[5] Tuba Sevimoglu and Kazim Yalcin Arga. The role of protein interaction networks in systems biomedicine. *Computational and Structural Biotechnology Journal*, 11(18):22–27, 2014.

[6] William JH Kim. Cellular signaling in tissue regeneration. *Yonsei Medical Journal*, 41(6):692–703, 2000.

[7] Julian Downward. The ins and outs of signalling. *Nature*, 411(6839):759–762, 2001.

[8] Boris N Kholodenko. Cell-signalling dynamics in time and space. *Nature Reviews Molecular Cell Biology*, 7(3):165–176, 2006.

[9] G Steven Martin. Cell signaling and cancer. *Cancer Cell*, 4(3):167–174, 2003.

[10] Michael Berridge. Signalling defects and disease. *Cell Signalling Biology*, 2014(1):1–98, 2014.

[11] Narat J Eungdamrong and Ravi Iyengar. Modeling cell signaling networks. *Biology of the Cell*, 96(5):355–362, 2004.

[12] Christoph P Bagowski and James E Ferrell Jr. Bistability in the jnk cascade. *Current Biology*, 11(15):1176–1182, 2001.

[13] Upinder S Bhalla, Prahlad T Ram, and Ravi Iyengar. Map kinase phosphatase as a locus of flexibility in a mitogen-activated protein kinase signaling network. *Science*, 297(5583):1018–1023, 2002.

[14] James E Ferrell Jr. Self-perpetuating states in signal transduction: positive feedback, double-negative feedback and bistability. *Current Opinion in Cell Biology*, 14(2):140–148, 2002.

[15] J Dedrick Jordan, Emmanuel M Landau, and Ravi Iyengar. Signaling networks: the origins of cellular multitasking. *Cell*, 103(2):193–200, 2000.

[16] Olaf Wolkenhauer, Peter Wellstead, Kwang-Hyun Cho, Padmini Rangamani, and Ravi Iyengar. Modelling cellular signalling systems. *Essays in Biochemistry*, 45:83–94, 2008.

[17] Steven M Hill, Yiling Lu, Jennifer Molina, Laura M Heiser, Paul T Spellman, Terence P Speed, Joe W Gray, Gordon B Mills, and Sach Mukherjee. Bayesian inference of signaling network topology in a cancer cell line. *Bioinformatics*, 28(21):2804–2810, 2012.

[18] Dániel Kondor and Gábor Vattay. Dynamics and structure in cell signaling networks: Off-state stability and dynamically positive cycles. *PloS One*, 8(3):e57653, 2013.

[19] Callie Johnson Miller and Lance A Davidson. The interplay between cell signalling and mechanics in developmental processes. *Nature Reviews Genetics*, 14(10):733–744, 2013.

[20] Patrizia Camelliti, Colin R Green, Ian LeGrice, and Peter Kohl. Fibroblast network in rabbit sinoatrial node: structural and functional identification of homogeneous and heterogeneous cell coupling. *Circulation Research*, 94(6):828–835, 2004.

[21] Toshihiko Toyofuku, Masanori Yabuki, Kinya Otsu, Tsunehiko Kuzuya, Masatsugu Hori, and Michihiko Tada. Intercellular calcium signaling via gap junction in connexin-43-transfected cells. *Journal of Biological Chemistry*, 273(3):1519–1528, 1998.

[22] Shinwan Kany, Jan Tilmann Vollrath, and Borna Relja. Cytokines in inflammatory disease. *International Journal of Molecular Sciences*, 20(23):6008, 2019.

[23] Mark D Turner, Belinda Nedjai, Tara Hurst, and Daniel J Pennington. Cytokines and chemokines: At the crossroads of cell signalling and inflammatory disease. *Biochimica et Biophysica Acta (BBA)-Molecular Cell Research*, 1843(11):2563–2582, 2014.

[24] Walter Blum, Thomas Henzi, Beat Schwaller, and László Pecze. Biological noise and positional effects influence cell stemness. *Journal of Biological Chemistry*, 293(14):5247–5258, 2018.

[25] Michael B Elowitz, Arnold J Levine, Eric D Siggia, and Peter S Swain. Stochastic gene expression in a single cell. *Science*, 297(5584):1183–1186, 2002.

[26] Mads Kaern, Timothy C Elston, William J Blake, and James J Collins. Stochasticity in gene expression: from theories to phenotypes. *Nature Reviews Genetics*, 6(6):451–464, 2005.

[27] Narendra Maheshri and Erin K O'Shea. Living with noisy genes: how cells function reliably with inherent variability in gene expression. *Annu. Rev. Biophys. Biomol. Struct.*, 36:413–434, 2007.

[28] Gil Hornung and Naama Barkai. Noise propagation and signaling sensitivity in biological networks: a role for positive feedback. *PLoS Computational Biology*, 4(1):e8, 2008.

[29] Javier De Las Rivas and Celia Fontanillo. Protein–protein interaction networks: unraveling the wiring of molecular machines within the cell. *Briefings in Functional Genomics*, 11(6):489–496, 2012.

[30] John E Ladbury and Stefan T Arold. Noise in cellular signaling pathways: causes and effects. *Trends in Biochemical Sciences*, 37(5):173–178, 2012.

[31] Samrat Chatterjee and Dhiraj Kumar. Unraveling the design principle for motif organization in signaling networks. *PloS One*, 6(12):e28606, 2011.

[32] Donald A McQuarrie. Stochastic approach to chemical kinetics. *Journal of Applied Probability*, 4(3):413–478, 1967.

[33] Shuqiang Wang, Yanyan Shen, Changhong Shi, Tao Wang, Zhiming Wei, and Hanxiong Li. Defining biological networks for noise buffering and signaling sensitivity using approximate bayesian computation. *The Scientific World Journal*, 2014, 2014.

[34] Upinder S Bhalla and Ravi Iyengar. Emergent properties of networks of biological signaling pathways. *Science*, 283(5400):381–387, 1999.

[35] Leland H Hartwell, John J Hopfield, Stanislas Leibler, and Andrew W Murray. From molecular to modular cell biology. *Nature*, 402(6761):C47–C52, 1999.

[36] Tomáš Helikar, John Konvalina, Jack Heidel, and Jim A Rogers. Emergent decision-making in biological signal transduction networks. *Proceedings of the National Academy of Sciences*, 105(6):1913–1918, 2008.

[37] Dhiraj Kumar, Ravichandran Srikanth, Helena Ahlfors, Riitta Lahesmaa, and Kanury VS Rao. Capturing cell-fate decisions from the molecular signatures of a receptor-dependent signaling response. *Molecular Systems Biology*, 3(1):150, 2007.

[38] Steven H Strogatz. Exploring complex networks. *Nature*, 410(6825):268–276, 2001.

[39] Gezhi Weng, Upinder S Bhalla, and Ravi Iyengar. Complexity in biological signaling systems. *Science*, 284(5411):92–96, 1999.

[40] Hui Xu, Jianpei Zhang, Jing Yang, and Lijun Lun. Identifying important nodes in complex networks based on multiattribute evaluation. *Mathematical Problems in Engineering*, 2018, 2018.

[41] Ren Xiaolong and Lv Linyuan. Review of ranking nodes in complex networks. *Chinese Science Bulletin*, 59(13):1175–1197, 2014.

[42] Pei Wang. Statistical identification of important nodes in biological systems. *Journal of Systems Science and Complexity*, 34(4):1454–1470, 2021.

[43] Pei Wang, Jinhu Lü, and Xinghuo Yu. Identification of important nodes in directed biological networks: A network motif approach. *PloS One*, 9(8):e106132, 2014.

[44] Mengyuan Wang, Haiying Wang, and Huiru Zheng. A mini review of node centrality metrics in biological networks. *International Journal of Network Dynamics and Intelligence*, 1(1):99–110, 2022.

[45] Jianguo Liu, Yanzhong Dang, and Zhongtuo Wang. Complex network properties of chinese natural science basic research. *Physica A: Statistical Mechanics and its Applications*, 366:578–586, 2006.

[46] Justin Balthrop, Stephanie Forrest, Mark EJ Newman, and Matthew M Williamson. Technological networks and the spread of computer viruses. *Science*, 304(5670):527–529, 2004.

[47] Yamir Moreno, Maziar Nekovee, and Amalio F Pacheco. Dynamics of rumor spreading in complex networks. *Physical Review E*, 69(6):066130, 2004.

[48] Christopher Herbert. War of no pity. In *War of No Pity*. Princeton University Press, 2021.

[49] Maliackal Poulo Joy, Amy Brock, Donald E Ingber, and Sui Huang. High-betweenness proteins in the yeast protein interaction network. *Journal of Biomedicine and Biotechnology*, 2005(2):96, 2005.

[50] Xiwen Xiong, Rongya Tao, Ronald A DePinho, and X Charlie Dong. Deletion of hepatic foxo1/3/4 genes in mice significantly impacts on glucose metabolism through downregulation of gluconeogenesis and upregulation of glycolysis. *PloS One*, 8(8):e74340, 2013.

[51] JW Black, P Leff, NP Shankley, and J Wood. An operational model of pharmacological agonism: the effect of e/[a] curve shape on agonist dissociation constant estimation. *British Journal of Pharmacology*, 84(2):561, 1985.

[52] ROBERT F Furchgott. Pharmacological characterization of receptors: its relation to radioligand-binding studies. In *Federation Proceedings*, volume 37, pages 115–120, 1978.

[53] BERNHARD O Palsson, ABHAY Joshi, and SADETTIN S Ozturk. Reducing complexity in metabolic networks: making metabolic meshes manageable. In *Federation Proceedings*, volume 46, pages 2485–2489, 1987.

[54] Markus W Covert, Christophe H Schilling, Iman Famili, Jeremy S Edwards, Igor I Goryanin, Evgeni Selkov, and Bernhard O Palsson. Metabolic modeling of microbial strains in silico. *Trends in Biochemical Sciences*, 26(3):179–186, 2001.

[55] Kai Velten. *Mathematical Modeling and Simulation: Introduction for Scientists and Engineers*. John Wiley & Sons, 2009.

[56] Wenzhe Ma, Ala Trusina, Hana El-Samad, Wendell A Lim, and Chao Tang. Defining network topologies that can achieve biochemical adaptation. *Cell*, 138(4):760–773, 2009.

[57] Luis A Martinez, Yian Chen, Susan M Fischer, and Claudio J Conti. Coordinated changes in cell cycle machinery occur during keratinocyte terminal differentiation. *Oncogene*, 18(2):397–406, 1999.

[58] Dieter Walz and S Roy Caplan. Chemical oscillations arise solely from kinetic nonlinearity and hence can occur near equilibrium. *Biophysical Journal*, 69(5):1698–1707, 1995.

[59] Matthew Freeman. Feedback control of intercellular signalling in development. *Nature*, 408(6810):313–319, 2000.

[60] Attila Becskei, Bertrand Séraphin, and Luis Serrano. Positive feedback in eukaryotic gene networks: cell differentiation by graded to binary response conversion. *The EMBO Journal*, 20(10):2528–2535, 2001.

[61] Denis Thieffry, Araceli M Huerta, Ernesto Pérez-Rueda, and Julio Collado-Vides. From specific gene regulation to global regulatory networks: a characterization of escherichia coli transcriptional network. *BioEssays*, 20(5), 1998.

[62] Attila Becskei and Luis Serrano. Engineering stability in gene networks by autoregulation. *Nature*, 405(6786):590–593, 2000.

[63] Erik Bateman. Autoregulation of eukaryotic transcription factors. *Progress in Nucleic Acid Research and Molecular Biology*, 60:133–168, 1998.

[64] Chi-Ying Huang and James E Ferrell Jr. Ultrasensitivity in the mitogen-activated protein kinase cascade. *Proceedings of the National Academy of Sciences*, 93(19):10078–10083, 1996.

[65] Debora Tenenbaum, Juan Ignacio Marrone, Hernán E Grecco, and Alejandra C Ventura. Robustness in spatially driven bistability in signaling systems. *Scientific Reports*, 10(1):1–10, 2020.

[66] Gheorghe Craciun, Yangzhong Tang, and Martin Feinberg. Understanding bistability in complex enzyme-driven reaction networks. *Proceedings of the National Academy of Sciences*, 103(23):8697–8702, 2006.

[67] Nils Blüthgen, Stefan Legewie, Hanspeter Herzel, and Boris Kholodenko. Mechanisms generating ultrasensitivity, bistability, and oscillations in signal transduction. In Sangdun Choi, editor, *Introduction to Systems Biology*, pages 282–299. Springer, Totowa, NJ, 2007.

[68] Paul Smolen, Douglas A Baxter, and John H Byrne. Frequency selectivity, multistability, and oscillations emerge from models of genetic regulatory systems. *American Journal of Physiology-Cell Physiology*, 274(2):C531–C542, 1998.

[69] Christoph P Bagowski, Jaya Besser, Christian R Frey, and James E Ferrell Jr. The jnk cascade as a biochemical switch in mammalian cells: ultrasensitive and all-or-none responses. *Current Biology*, 13(4):315–320, 2003.

[70] Gianluca M Guidi, Marie-France Carlier, and Albert Goldbeter. Bistability in the isocitrate dehydrogenase reaction: an experimentally based theoretical study. *Biophysical Journal*, 74(3):1229–1240, 1998.

[71] Wen Xiong and James E Ferrell. A positive-feedback-based bistable 'memory module'that governs a cell fate decision. *Nature*, 426(6965):460–465, 2003.

[72] Richard Losick and Claude Desplan. Stochasticity and cell fate. *Science*, 320(5872):65–68, 2008.

[73] AS Sedra and KC Smith. Microelectronic circuits. new york: Oxford university press. 1998.

[74] May Lim and Caesar Saloma. Emergence of hysteresis in a network of nonhysteretic agents with continuous responses. *Physical Review Letters*, 88(3):038701, 2002.

[75] Jeong-Rae Kim and Kwang-Hyun Cho. The regulatory circuits for hysteretic switching in cellular signal transduction pathways. *The FEBS Journal*, 279(18):3329–3337, 2012.

[76] Ariane Abrieu, Marcel Dorée, and Daniel Fisher. The interplay between cyclin-b-cdc2 kinase (mpf) and map kinase during maturation of oocytes. *Journal of Cell Science*, 114(2):257–267, 2001.

[77] James E Ferrell Jr and Eric M Machleder. The biochemical basis of an all-or-none cell fate switch in xenopus oocytes. *Science*, 280(5365):895–898, 1998.

[78] James E Ferrell Jr and Wen Xiong. Bistability in cell signaling: How to make continuous processes discontinuous, and reversible processes irreversible. *Chaos: An Interdisciplinary Journal of Nonlinear Science*, 11(1):227–236, 2001.

[79] Roland Wedlich-Soldner, Stephanie C Wai, Thomas Schmidt, and Rong Li. Robust cell polarity is a dynamic state established by coupling transport and gtpase signaling. *The Journal of Cell Biology*, 166(6):889–900, 2004.

[80] Joseph R Pomerening, Eduardo D Sontag, and James E Ferrell. Building a cell cycle oscillator: hysteresis and bistability in the activation of cdc2. *Nature Cell Biology*, 5(4):346–351, 2003.

[81] Albert Goldbeter. Dissipative structures in biological systems: bistability, oscillations, spatial patterns and waves. *Philosophical Transactions of the Royal Society A: Mathematical, Physical and Engineering Sciences*, 376(2124):20170376, 2018.

[82] Markus Arnoldini, Ima Avalos Vizcarra, Rafael Peña-Miller, Nicolas Stocker, Médéric Diard, Viola Vogel, Robert E Beardmore, Wolf-Dietrich Hardt, and Martin Ackermann. Bistable expression of virulence genes in salmonella leads to the formation of an antibiotic-tolerant subpopulation. *PLoS Biology*, 12(8):e1001928, 2014.

[83] Yassine X Bouchoucha, Jürgen Reingruber, Charlotte Labalette, Michel A Wassef, Elodie Thierion, Carole Desmarquet-Trin Dinh, David Holcman, Pascale Gilardi-Hebenstreit, and Patrick Charnay. Dissection of a krox20 positive feedback loop driving cell fate choices in hindbrain patterning. *Molecular Systems Biology*, 9(1):690, 2013.

[84] Nick I Markevich, Jan B Hoek, and Boris N Kholodenko. Signaling switches and bistability arising from multisite phosphorylation in protein kinase cascades. *The Journal of Cell Biology*, 164(3):353–359, 2004.

[85] Thomas Wilhelm. The smallest chemical reaction system with bistability. *BMC Systems Biology*, 3(1):1–9, 2009.

[86] Rafeul Alam and Magdalena M Gorska. Mitogen-activated protein kinase signalling and erk1/2 bistability in asthma. *Clinical & Experimental Allergy*, 41(2):149–159, 2011.

[87] Mirna Kheir Gouda, Michael Manhart, and Gábor Balázsi. Evolutionary regain of lost gene circuit function. *Proceedings of the National Academy of Sciences*, 116(50):25162–25171, 2019.

[88] Paul Smolen, Douglas A Baxter, and John H Byrne. Mathematical modeling of gene networks. *Neuron*, 26(3):567–580, 2000.

[89] JS Hallinan and Paul T Jackway. Network motifs, feedback loops and the dynamics of genetic regulatory networks. In *2005 IEEE Symposium on Computational Intelligence in Bioinformatics and Computational Biology*, pages 1–7. IEEE, 2005.

[90] K Sriram and MS Gopinathan. A two variable delay model for the circadian rhythm of neurospora crassa. *Journal of Theoretical Biology*, 231(1):23–38, 2004.

[91] James CW Locke, Andrew J Millar, and Matthew S Turner. Modelling genetic networks with noisy and varied experimental data: the circadian clock in arabidopsis thaliana. *Journal of Theoretical Biology*, 234(3):383–393, 2005.

[92] Peter Ruoff, Melinda K Christensen, and Vijay K Sharma. Per/tim-mediated amplification, gene dosage effects and temperature compensation in an interlocking-feedback loop model of the drosophila circadian clock. *Journal of Theoretical Biology*, 237(1):41–57, 2005.

[93] Ohad Cohen and Samuel A Safran. Cardiomyocyte calcium ion oscillations—lessons from physics. *Frontiers in Physiology*, 11:164, 2020.

[94] Liang Qiao, Robert B Nachbar, Ioannis G Kevrekidis, and Stanislav Y Shvartsman. Bistability and oscillations in the huang-ferrell model of mapk signaling. *PLoS Computational Biology*, 3(9):e184, 2007.

[95] Suvankar Halder, Sumana Ghosh, Joydev Chattopadhyay, and Samrat Chatterjee. Understanding noise in cell signalling in the prospect of drug-targets. *Journal of Theoretical Biology*, 555:111298, 2022.

[96] Bhaswar Ghosh, Rajesh Karmakar, and Indrani Bose. Noise characteristics of feed forward loops. *Physical Biology*, 2(1):36, 2005.

[97] Harley H McAdams and Adam Arkin. Stochastic mechanisms in gene expression. *Proceedings of the National Academy of Sciences*, 94(3):814–819, 1997.

[98] Leor S Weinberger, John C Burnett, Jared E Toettcher, Adam P Arkin, and David V Schaffer. Stochastic gene expression in a lentiviral positive-feedback loop: Hiv-1 tat fluctuations drive phenotypic diversity. *Cell*, 122(2):169–182, 2005.

[99] Murat Acar, Attila Becskei, and Alexander Van Oudenaarden. Enhancement of cellular memory by reducing stochastic transitions. *Nature*, 435(7039):228–232, 2005.

[100] Maxim N Artyomov, Jayajit Das, Mehran Kardar, and Arup K Chakraborty. Purely stochastic binary decisions in cell signaling models without underlying deterministic bistabilities. *Proceedings of the National Academy of Sciences*, 104(48):18958–18963, 2007.

[101] Yaman Arkun and Mohammadreza Yasemi. Dynamics and control of the erk signaling pathway: Sensitivity, bistability, and oscillations. *PloS One*, 13(4):e0195513, 2018.

[102] David Orrell and Hamid Bolouri. Control of internal and external noise in genetic regulatory networks. *Journal of Theoretical Biology*, 230(3):301–312, 2004.

[103] Yann Dublanche, Konstantinos Michalodimitrakis, Nico Kümmerer, Mathilde Foglierini, and Luis Serrano. Noise in transcription negative feedback loops: simulation and experimental analysis. *Molecular Systems Biology*, 2(1):41, 2006.

[104] Tomasz Lipniacki, Beata Hat, James R Faeder, and William S Hlavacek. Stochastic effects and bistability in t cell receptor signaling. *Journal of Theoretical Biology*, 254(1):110–122, 2008.

[105] Wun-Sin Jhang, Shih-Chiang Lo, Chen-Chao Yeh, and Che-Chi Shu. Inhibitors alter the stochasticity of regulatory proteins to force cells to switch to the other state in the bistable system. *Scientific Reports*, 7(1):1–7, 2017.

[106] Jeff Hasty, Joel Pradines, Milos Dolnik, and James J Collins. Noise-based switches and amplifiers for gene expression. *Proceedings of the National Academy of Sciences*, 97(5):2075–2080, 2000.

[107] Junwei Wang, Jiajun Zhang, Zhanjiang Yuan, and Tianshou Zhou. Noise-induced switches in network systems of the genetic toggle switch. *BMC Systems Biology*, 1(1):1–14, 2007.

[108] Moritz Lang, Steffen Waldherr, and Frank Allgöwer. Amplitude distribution of stochastic oscillations in biochemical networks due to intrinsic noise. *PMC Biophysics*, 2(1):1–28, 2009.

[109] Miquel Marchena, Blas Echebarria, Yohannes Shiferaw, and Enrique Alvarez-Lacalle. Buffering and total calcium levels determine the presence of oscillatory regimes in cardiac cells. *PLoS Computational Biology*, 16(9):e1007728, 2020.

[110] Jingkui Wang, Marc Lefranc, and Quentin Thommen. Stochastic oscillations induced by intrinsic fluctuations in a self-repressing gene. *Biophysical Journal*, 107(10):2403–2416, 2014.

[111] Margherita Carletti. On the stability properties of a stochastic model for phage–bacteria interaction in open marine environment. *Mathematical Biosciences*, 175(2):117–131, 2002.

[112] Andrea Saltelli and Paola Annoni. How to avoid a perfunctory sensitivity analysis. *Environmental Modelling & Software*, 25(12):1508–1517, 2010.

[113] Simeone Marino, Ian B Hogue, Christian J Ray, and Denise E Kirschner. A methodology for performing global uncertainty and sensitivity analysis in systems biology. *Journal of theoretical biology*, 254(1):178–196, 2008.

[114] Michael D McKay, Richard J Beckman, and William J Conover. A comparison of three methods for selecting values of input variables in the analysis of output from a computer code. *Technometrics*, 42(1):55–61, 2000.

[115] Sally M Blower and Hadi Dowlatabadi. Sensitivity and uncertainty analysis of complex models of disease transmission: an hiv model, as an example. *International Statistical Review/Revue Internationale de Statistique*, pages 229–243, 1994.

[116] Ron Milo, Shai Shen-Orr, Shalev Itzkovitz, Nadav Kashtan, Dmitri Chklovskii, and Uri Alon. Network motifs: simple building blocks of complex networks. *Science*, 298(5594):824–827, 2002.

[117] Shmoolik Mangan, Alon Zaslaver, and Uri Alon. The coherent feedforward loop serves as a sign-sensitive delay element in transcription networks. *Journal of Molecular Biology*, 334(2):197–204, 2003.

[118] Onn Brandman and Tobias Meyer. Feedback loops shape cellular signals in space and time. *Science*, 322(5900):390–395, 2008.

[119] Joshua W Williams, Xiaohui Cui, Andre Levchenko, and Ann M Stevens. Robust and sensitive control of a quorum-sensing circuit by two interlocked feedback loops. *Molecular Systems Biology*, 4(1):234, 2008.

[120] Quincey A Justman, Zach Serber, James E Ferrell Jr, Hana El-Samad, and Kevan M Shokat. Tuning the activation threshold of a kinase network by nested feedback loops. *Science*, 324(5926):509–512, 2009.

[121] Uri Alon. Network motifs: theory and experimental approaches. *Nature Reviews Genetics*, 8(6):450–461, 2007.

[122] Shmoolik Mangan and Uri Alon. Structure and function of the feed-forward loop network motif. *Proceedings of the National Academy of Sciences*, 100(21):11980–11985, 2003.

[123] Roby P Bhattacharyya, Attila Reményi, Brian J Yeh, Wendell A Lim, et al. Domains, motifs, and scaffolds: the role of modular interactions in the evolution and wiring of cell signaling circuits. *Annual Review of Biochemistry*, 75(1):655–680, 2006.

[124] Raúl Guantes, Javier Estrada, and Juan F Poyatos. Trade-offs and noise tolerance in signal detection by genetic circuits. *PloS One*, 5(8):e12314, 2010.

[125] Raymond Cheong, Alex Rhee, Chiaochun Joanne Wang, Ilya Nemenman, and Andre Levchenko. Information transduction capacity of noisy biochemical signaling networks. *Science*, 334(6054):354–358, 2011.

[126] Tharmaraj Jesan, Uddipan Sarma, Subhadra Halder, Bhaskar Saha, and Sitabhra Sinha. Branched motifs enable long-range interactions in signaling networks through retrograde propagation. *PloS One*, 8(5):e64409, 2013.

[127] James E Ferrell and Ramesh R Bhatt. Mechanistic studies of the dual phosphorylation of mitogen-activated protein kinase. *Journal of Biological Chemistry*, 272(30):19008–19016, 1997.

[128] Ahmadreza Ghaffarizadeh, Nicholas S Flann, and Gregory J Podgorski. Multistable switches and their role in cellular differentiation networks. *BMC Bioinformatics*, 15(7):1–13, 2014.

[129] Thomas Eissing, Holger Conzelmann, Ernst D Gilles, Frank Allgower, Eric Bullinger, and Peter Scheurich. Bistability analyses of a caspase activation model for receptor-induced apoptosis. *Journal of Biological Chemistry*, 279(35):36892–36897, 2004.

[130] Onn Brandman, James E Ferrell Jr, Rong Li, and Tobias Meyer. Interlinked fast and slow positive feedback loops drive reliable cell decisions. *Science*, 310(5747):496–498, 2005.

[131] Chieh Hsu, Vincent Jaquet, Mumun Gencoglu, and Attila Becskei. Protein dimerization generates bistability in positive feedback loops. *Cell Reports*, 16(5):1204–1210, 2016.

[132] Benjamin Pfeuty and Kunihiko Kaneko. The combination of positive and negative feedback loops confers exquisite flexibility to biochemical switches. *Physical Biology*, 6(4):046013, 2009.

[133] Mitio Nagumo. Über die lage der integralkurven gewöhnlicher differentialgleichungen. *Proceedings of the Physico-Mathematical Society of Japan. 3rd Series*, 24:551–559, 1942.

[134] Phonindra Nath Das, Ajay Kumar, Nandadulal Bairagi, and Samrat Chatterjee. Restoring calcium homeostasis in diabetic cardiomyocytes: an investigation through mathematical modelling. *Molecular BioSystems*, 13(10):2056–2068, 2017.

[135] Hsueh-Chi Sherry Yen, Qikai Xu, Danny M Chou, Zhenming Zhao, and Stephen J Elledge. Global protein stability profiling in mammalian cells. *Science*, 322(5903):918–923, 2008.

[136] Mina J Bissell and Derek Radisky. Putting tumours in context. *Nature Reviews Cancer*, 1(1):46–54, 2001.

[137] Yaneer Bar-Yam and Irving R Epstein. Response of complex networks to stimuli. *Proceedings of the National Academy of Sciences*, 101(13):4341–4345, 2004.

[138] Frank J Bruggeman, Nils Blüthgen, and Hans V Westerhoff. Noise management by molecular networks. *PLoS Computational Biology*, 5(9):e1000506, 2009.

[139] Mark Kittisopikul and Gürol M Süel. Biological role of noise encoded in a genetic network motif. *Proceedings of the National Academy of Sciences*, 107(30):13300–13305, 2010.

[140] Matteo Osella, Carla Bosia, Davide Corá, and Michele Caselle. The role of incoherent microrna-mediated feedforward loops in noise buffering. *PLoS Computational Biology*, 7(3):e1001101, 2011.

[141] Michael L Simpson, Chris D Cox, and Gary S Sayler. Frequency domain analysis of noise in autoregulated gene circuits. *Proceedings of the National Academy of Sciences*, 100(8):4551–4556, 2003.

[142] Krishna Kanhaiya, Eugen Czeizler, Cristian Gratie, and Ion Petre. Controlling directed protein interaction networks in cancer. *Scientific Reports*, 7(1):1–12, 2017.

[143] David S Wishart, Yannick D Feunang, An C Guo, Elvis J Lo, Ana Marcu, Jason R Grant, Tanvir Sajed, Daniel Johnson, Carin Li, Zinat Sayeeda, et al. Drugbank 5.0: a major update to the drugbank database for 2018. *Nucleic Acids Research*, 46(D1):D1074–D1082, 2018.

[144] Jeong-Rae Kim, Yeoin Yoon, and Kwang-Hyun Cho. Coupled feedback loops form dynamic motifs of cellular networks. *Biophysical Journal*, 94(2):359–365, 2008.

[145] Fan Wu, Cong Ma, and Cheemeng Tan. Network motifs modulate druggability of cellular targets. *Scientific Reports*, 6(1):1–11, 2016.

[146] Luana Licata, Prisca Lo Surdo, Marta Iannuccelli, Alessandro Palma, Elisa Micarelli, Livia Perfetto, Daniele Peluso, Alberto Calderone, Luisa Castagnoli, and Gianni Cesareni. Signor 2.0, the signaling network open resource 2.0: 2019 update. *Nucleic Acids Research*, 48(D1):D504–D510, 2020.

[147] Maxim V Kuleshov, Matthew R Jones, Andrew D Rouillard, Nicolas F Fernandez, Qiaonan Duan, Zichen Wang, Simon Koplev, Sherry L Jenkins, Kathleen M Jagodnik, Alexander Lachmann, et al. Enrichr: a comprehensive gene set enrichment analysis web server 2016 update. *Nucleic Acids Research*, 44(W1):W90–W97, 2016.

[148] Janet Piñero, Juan Manuel Ramírez-Anguita, Josep Saüch-Pitarch, Francesco Ronzano, Emilio Centeno, Ferran Sanz, and Laura I Furlong. The disgenet knowledge platform for disease genomics: 2019 update. *Nucleic Acids Research*, 48(D1):D845–D855, 2020.

[149] Minoru Kanehisa and Susumu Goto. Kegg: kyoto encyclopedia of genes and genomes. *Nucleic Acids Research*, 28(1):27–30, 2000.

[150] Kaleigh Fernald and Manabu Kurokawa. Evading apoptosis in cancer. *Trends in Cell Biology*, 23(12):620–633, 2013.

[151] Geou-Yarh Liou and Peter Storz. Reactive oxygen species in cancer. *Free Radical Research*, 44(5):479–496, 2010.

[152] John D Hayes, Albena T Dinkova-Kostova, and Kenneth D Tew. Oxidative stress in cancer. *Cancer Cell*, 38(2):167–197, 2020.

[153] Mark A Feitelson, Alla Arzumanyan, Rob J Kulathinal, Stacy W Blain, Randall F Holcombe, Jamal Mahajna, Maria Marino, Maria L Martinez-Chantar, Roman Nawroth, Isidro Sanchez-Garcia, et al. Sustained proliferation in cancer: Mechanisms and novel therapeutic targets. In *Seminars in Cancer Biology*, volume 35, pages S25–S54. Elsevier, 2015.

[154] Kathleen Schmit and Carine Michiels. Tmem proteins in cancer: a review. *Frontiers in Pharmacology*, 9:1345, 2018.

[155] Rutger Hermsen, Bas Ursem, and Pieter Rein Ten Wolde. Combinatorial gene regulation using auto-regulation. *PLoS Computational Biology*, 6(6):e1000813, 2010.

[156] Gabriele Pedruzzi, Kanury VS Rao, and Samrat Chatterjee. Mathematical model of mycobacterium–host interaction describes physiology of persistence. *Journal of Theoretical Biology*, 376:105–117, 2015.

[157] Simeone Marino and Denise E Kirschner. A multi-compartment hybrid computational model predicts key roles for dendritic cells in tuberculosis infection. *Computation*, 4(4):39, 2016.

[158] David S Wishart, Craig Knox, An Chi Guo, Dean Cheng, Savita Shrivastava, Dan Tzur, Bijaya Gautam, and Murtaza Hassanali. Drugbank: a knowledgebase for drugs, drug actions and drug targets. *Nucleic Acids Research*, 36(suppl_1):D901–D906, 2008.

[159] Ziwei Dai, Shiyu Yang, Liyan Xu, Hongrong Hu, Kun Liao, Jianghuang Wang, Qian Wang, Shuaishi Gao, Bo Li, and Luhua Lai. Identification of cancer–associated metabolic vulnerabilities by modeling multi-objective optimality in metabolism. *Cell Communication and Signaling*, 17(1):1–15, 2019.

[160] N Winston West, Aileen Garcia-Vargas, Charles E Chalfant, and Margaret A Park. Osu-03012 sensitizes breast cancers to lapatinib-induced cell killing: a role for nck1 but not nck2. *BMC Cancer*, 13(1):1–11, 2013.

[161] Ana Maria Tari, Ralph Arlinghaus, and Gabriel Lopez-Berestein. Inhibition of grb2 and crkl proteins results in growth inhibition of philadelphia chromosome positive leukemic cells. *Biochemical and Biophysical Research Communications*, 235(2):383–388, 1997.

[162] Tong Gan, Ashley T Stevens, Xiaopeng Xiong, Yang-An Wen, Trevor N Farmer, Austin T Li, Payton D Stevens, Sanam Golshani, Heidi L Weiss, B Mark Evers, et al. Inhibition of protein tyrosine phosphatase receptor type f suppresses wnt signaling in colorectal cancer. *Oncogene*, 39(44):6789–6801, 2020.

[163] Qi-guang Chen, Wei Zhou, Tao Han, Shu-qi Du, Zhen-hua Li, Zhe Zhang, Guang-yi Shan, and Chui-ze Kong. Mir-378 suppresses prostate cancer cell growth through down-regulation of mapk1 in vitro and in vivo. *Tumor Biology*, 37(2):2095–2103, 2016.

[164] John J Tyson and Béla Novák. Functional motifs in biochemical reaction networks. *Annual Review of Physical Chemistry*, 61:219–240, 2010.

[165] Hans Degn. Bistability caused by substrate inhibition of peroxidase in an open reaction system. *Nature*, 217(5133):1047–1050, 1968.

[166] A Naparstek, JL Romette, JP Kernevez, and D Thomas. Memory in enzyme membranes. *Nature*, 249(5456):490–491, 1974.

[167] Guang Yao, Tae Jun Lee, Seiichi Mori, Joseph R Nevins, and Lingchong You. A bistable rb–e2f switch underlies the restriction point. *Nature Cell Biology*, 10(4):476–482, 2008.

[168] Naren Ramakrishnan and Upinder S Bhalla. Memory switches in chemical reaction space. *PLoS Computational Biology*, 4(7):e1000122, 2008.

[169] Chikara Furusawa and Kunihiko Kaneko. A dynamical-systems view of stem cell biology. *Science*, 338(6104):215–217, 2012.

[170] Kate M Byrne, Naser Monsefi, John C Dawson, Andrea Degasperi, Jimi-Carlo Bukowski-Wills, Natalia Volinsky, Maciej Dobrzyński, Marc R Birtwistle, Mikhail A Tsyganov, Anatoly Kiyatkin, et al. Bistability in the rac1, pak, and rhoa signaling network drives actin cytoskeleton dynamics and cell motility switches. *Cell Systems*, 2(1):38–48, 2016.

[171] Tetsuya Shiraishi, Shinako Matsuyama, and Hiroaki Kitano. Large-scale analysis of network bistability for human cancers. *PLoS Computational Biology*, 6(7):e1000851, 2010.

[172] Timothy S Gardner, Charles R Cantor, and James J Collins. Construction of a genetic toggle switch in escherichia coli. *Nature*, 403(6767):339–342, 2000.

[173] K Kondelkova, Doris Vokurková, Jana Krejsek, Lenka Borská, Zdeněk Fiala, and Andrỳs Ctirad. Regulatory t cells (treg) and their roles in immune system with respect to immunopathological disorders. *Acta Medica (Hradec Kralove)*, 53(2):73–7, 2010.

[174] Jung-Ho Kim, Beom Seok Kim, and Sang-Kyou Lee. Regulatory t cells in tumor microenvironment and approach for anticancer immunotherapy. *Immune Network*, 20(1), 2020.

[175] Peter J Eggenhuizen, Boaz H Ng, and Joshua D Ooi. Treg enhancing therapies to treat autoimmune diseases. *International Journal of Molecular Sciences*, 21(19):7015, 2020.

[176] S Alice Long and Jane H Buckner. Cd4+ foxp3+ t regulatory cells in human autoimmunity: more than a numbers game. *The Journal of Immunology*, 187(5):2061–2066, 2011.

[177] Manoj Kumar, Norman Putzki, Volker Limmroth, Ralph Remus, Monika Lindemann, Dietmar Knop, Norbert Mueller, Cornelia Hardt, Ernst Kreuzfelder, and Hans Grosse-Wilde. Cd4+ cd25+ foxp3+ t lymphocytes fail to suppress myelin basic protein-induced proliferation in patients with multiple sclerosis. *Journal of Neuroimmunology*, 180(1-2):178–184, 2006.

[178] Koen Venken, Niels Hellings, Tom Broekmans, Karen Hensen, Jean-Luc Rummens, and Piet Stinissen. Natural naive cd4+ cd25+ cd127low regulatory t cell (treg) development and function are disturbed in multiple sclerosis patients: recovery of memory treg homeostasis during disease progression. *The Journal of Immunology*, 180(9):6411–6420, 2008.

[179] Guang Ming Han, Nancy J O'Neil-Andersen, Robert B Zurier, and David A Lawrence. Cd4+ cd25high t cell numbers are enriched in the peripheral blood of patients with rheumatoid arthritis. *Cellular Immunology*, 253(1-2):92–101, 2008.

[180] Ashish K Marwaha, Sarah Q Crome, Constadina Panagiotopoulos, Kyra B Berg, Huilian Qin, Qin Ouyang, Lixin Xu, John J Priatel, Megan K Levings, and Rusung Tan. Cutting edge: increased il-17–secreting t cells in children with new-onset type 1 diabetes. *The Journal of Immunology*, 185(7):3814–3818, 2010.

[181] Anabelle Visperas and Dario AA Vignali. Are regulatory t cells defective in type 1 diabetes and can we fix them? *The Journal of Immunology*, 197(10):3762–3770, 2016.

[182] Qi Jiang, Guocan Yang, Qi Liu, Shengjun Wang, and Dawei Cui. Function and role of regulatory t cells in rheumatoid arthritis. *Frontiers in Immunology*, 12:626193, 2021.

[183] Denise L Faustman and Miriam Davis. Tnf receptor 2 and disease: autoimmunity and regenerative medicine. *Frontiers in Immunology*, 4:478, 2013.

[184] Xuehui He and Xinhui Wang. Tnfr2 and regulatory t cells: Potential immune checkpoint target in cancer immunotherapy. In Payam Behzadi, editor, *Cytokines*, chapter 4. IntechOpen, Rijeka, 2019.

[185] Kamar-Sulu N Atretkhany, Ilgiz A Mufazalov, Josefine Dunst, Anna Kuchmiy, Violetta S Gogoleva, David Andruszewski, Marina S Drutskaya, Denise L Faustman, Marius Schwabenland, Marco Prinz, et al. Intrinsic tnfr2 signaling in t regulatory cells provides protection in cns autoimmunity. *Proceedings of the National Academy of Sciences*, 115(51):13051–13056, 2018.

[186] Liqin Ban, Jack Zhang, Limei Wang, Willem Kuhtreiber, Douglas Burger, and Denise L Faustman. Selective death of autoreactive t cells in human diabetes by tnf or tnf receptor 2 agonism. *Proceedings of the National Academy of Sciences*, 105(36):13644–13649, 2008.

[187] José L Cohen and Kathryn J Wood. Tnfr2: The new treg switch? *Oncoimmunology*, 7(1):e1373236, 2018.

[188] Kolja Schleich and Inna N Lavrik. Mathematical modeling of apoptosis. *Cell Communication and Signaling*, 11(1):1–7, 2013.

[189] Leonie K Amstein, Jörg Ackermann, Jennifer Hannig, Ivan Dikić, Simone Fulda, and Ina Koch. Mathematical modeling of the molecular switch of tnfr1-mediated signaling pathways applying petri net formalism and in silico knockout analysis. *PLoS Computational Biology*, 18(8):e1010383, 2022.

[190] Geoffrey Koh and Dong-Yup Lee. Mathematical modeling and sensitivity analysis of the integrated tnfα-mediated apoptotic pathway for identifying key regulators. *Computers in Biology and Medicine*, 41(7):512–528, 2011.

[191] M Jit, B Henderson, M Stevens, and RM Seymour. Tnf-α neutralization in cytokine-driven diseases: a mathematical model to account for therapeutic success in rheumatoid arthritis but therapeutic failure in systemic inflammatory response syndrome. *Rheumatology*, 44(3):323–331, 2005.

[192] Padmini Rangamani and Lawrence Sirovich. Survival and apoptotic pathways initiated by tnf-α: Modeling and predictions. *Biotechnology and Bioengineering*, 97(5):1216–1229, 2007.

[193] Roberto Chignola, Vladislav Vyshemirsky, Marcello Farina, Alessio Del Fabbro, and Edoardo Milotti. Modular model of tnfα cytotoxicity. *Bioinformatics*, 27(13):1754–1757, 2011.

[194] Sol M Fernández Arancibia, Hernán E Grecco, and Luis G Morelli. Effective description of bistability and irreversibility in apoptosis. *Physical Review E*, 104(6):064410, 2021.

[195] EZ Bagci, Y Vodovotz, TR Billiar, GB Ermentrout, and I Bahar. Bistability in apoptosis: roles of bax, bcl-2, and mitochondrial permeability transition pores. *Biophysical Journal*, 90(5):1546–1559, 2006.

[196] Max Delbrück. Statistical fluctuations in autocatalytic reactions. *The Journal of Chemical Physics*, 8(1):120–124, 1940.

[197] Minoru Kanehisa, Miho Furumichi, Yoko Sato, Masayuki Kawashima, and Mari Ishiguro-Watanabe. Kegg for taxonomy-based analysis of pathways and genomes. *Nucleic Acids Research*, 51(D1):D587–D592, 2023.

[198] Jing Liu and Anning Lin. Role of jnk activation in apoptosis: a double-edged sword. *Cell research*, 15(1):36–42, 2005.

[199] K Hettinger, F Vikhanskaya, MK Poh, MK Lee, I De Belle, JT Zhang, SAG Reddy, and K Sabapathy. c-jun promotes cellular survival by suppression of pten. *Cell Death & Differentiation*, 14(2):218–229, 2007.

[200] Ron Wisdom, Randall S Johnson, and Connie Moore. c-jun regulates cell cycle progression and apoptosis by distinct mechanisms. *The EMBO Journal*, 18(1):188–197, 1999.

[201] Matthias Grell, Harald Wajant, Gudrun Zimmermann, and Peter Scheurich. The type 1 receptor (cd120a) is the high-affinity receptor for soluble tumor necrosis factor. *Proceedings of the National Academy of Sciences*, 95(2):570–575, 1998.

[202] Kwang-Hyun Cho, Sung-Young Shin, Hyeon-Woo Lee, and Olaf Wolkenhauer. Investigations into the analysis and modeling of the tnfα-mediated nf-κb-signaling pathway. *Genome Research*, 13(11):2413–2422, 2003.

[203] Kirstin Kucka, Isabell Lang, Tengyu Zhang, Daniela Siegmund, Juliane Medler, and Harald Wajant. Membrane lymphotoxin-$\alpha 2\beta$ is a novel tumor necrosis factor (tnf) receptor 2 (tnfr2) agonist. *Cell Death & Disease*, 12(4):1–9, 2021.

[204] Jun Wang, Ricardo Ferreira, Wanhua Lu, Samatha Farrow, Kate Downes, Lutz Jermutus, Ralph Minter, Rafia S Al-Lamki, Jordan S Pober, and John R Bradley. Tnfr2 ligation in human t regulatory cells enhances il2-induced cell proliferation through the non-canonical nf-κb pathway. *Scientific Reports*, 8(1):1–11, 2018.

[205] Garrett Birkhoff and Gian-Carlo Rota. *Ordinary Differential Equations*. John Wiley & Sons, Boston, 1978.

[206] Suvankar Halder, Sumana Ghosh, Joydev Chattopadhyay, and Samrat Chatterjee. Bistability in cell signalling and its significance in identifying potential drug-targets. *Bioinformatics*, 37(22):4156–4163, 2021.

[207] Isabell Lang, Simone Füllsack, Agnes Wyzgol, Andrea Fick, Johannes Trebing, José Antonio Carmona Arana, Viktoria Schäfer, Daniela Weisenberger, and Harald Wajant. Binding studies of tnf receptor superfamily (tnfrsf) receptors on intact cells. *Journal of Biological Chemistry*, 291(10):5022–5037, 2016.

[208] Phonindra Nath Das, Suvankar Halder, Nandadulal Bairagi, and Samrat Chatterjee. Delay in atp-dependent calcium inflow may affect insulin secretion from pancreatic beta-cell. *Applied Mathematical Modelling*, 84:202–221, 2020.

[209] Megan E Himmel, Yu Yao, Paul C Orban, Theodore S Steiner, and Megan K Levings. Regulatory t-cell therapy for inflammatory bowel disease: more questions than answers. *Immunology*, 136(2):115–122, 2012.

[210] Momoko Komatsu, Daisuke Kobayashi, Kaori Saito, Daisuke Furuya, Atsuhito Yagihashi, Hiroshi Araake, Naoki Tsuji, Sumio Sakamaki, Yoshiro Niitsu, and Naoki Watanabe. Tumor necrosis factor-α in serum of patients with inflammatory bowel disease as measured by a highly sensitive immuno-pcr. *Clinical Chemistry*, 47(7):1297–1301, 2001.

[211] Pallinti Vasanthi, Ganesan Nalini, and G Rajasekhar. Role of tumor necrosis factor-alpha in rheumatoid arthritis: a review. *APLAR Journal of Rheumatology*, 10(4):270–274, 2007.

[212] Sivasankari Thilagar, Uma Sudhakar Ramakrishnan Theyagarajan, Snophia Suresh, Parthiban Saketharaman, and Nizar Ahamed. Comparison of serum tumor necrosis factor-α levels in rheumatoid arthritis individuals with and without chronic periodontitis: A biochemical study. *Journal of Indian Society of Periodontology*, 22(2):116, 2018.

[213] Martin Aringer and Josef S Smolen. The role of tumor necrosis factor-alpha in systemic lupus erythematosus. *Arthritis Research & Therapy*, 10(1):1–8, 2008.

[214] Corinna E Weckerle, Dorothy Mangale, Beverly S Franek, Jennifer A Kelly, Marissa Kumabe, Judith A James, Kathy L Moser, John B Harley, and Timothy B Niewold. Brief report: Large-scale analysis of tumor necrosis factor α levels in systemic lupus erythematosus. *Arthritis & Rheumatism*, 64(9):2947–2952, 2012.

[215] Claudia Veltkamp, Matthias Anstaett, Kristin Wahl, Sarah Möller, Saskia Gangl, Oliver Bachmann, Matthias Hardtke-Wolenski, Florian Länger, Wolfgang Stremmel, Michael P Manns, et al. Apoptosis of regulatory t lymphocytes is increased in chronic inflammatory bowel disease and reversed by anti-tnfα treatment. *Gut*, 60(10):1345–1353, 2011.

[216] Xixi Ma and Shengqian Xu. Tnf inhibitor therapy for rheumatoid arthritis. *Biomedical Reports*, 1(2):177–184, 2013.

[217] Lang-Jing Zhu, Xiao Yang, and Xue-Qing Yu. Anti-tnf-α therapies in systemic lupus erythematosus. *Journal of Biomedicine and Biotechnology*, 2010, 2010.

[218] Olga Bloch, Mirit Amit-Vazina, Eli Yona, Yair Molad, and Micha J Rapoport. Increased erk and jnk activation and decreased erk/jnk ratio are associated with long-term organ damage in patients with systemic lupus erythematosus. *Rheumatology*, 53(6):1034–1042, 2014.

[219] Benjamin Lai, Chien-Hsiang Wu, and Jenn-Haung Lai. Activation of c-jun n-terminal kinase, a potential therapeutic target in autoimmune arthritis. *Cells*, 9(11):2466, 2020.

[220] Peter Angel, Kazue Hattori, Tod Smeal, and Michael Karin. The jun proto-oncogene is positively autoregulated by its product, jun/ap-1. *Cell*, 55(5):875–885, 1988.

[221] ID Federation. IDF Diabetes Atlas, Tenth. *International Diabetes*, 2021.

[222] Benjamin M Leon and Thomas M Maddox. Diabetes and cardiovascular disease: epidemiology, biological mechanisms, treatment recommendations and future research. *World Journal of Diabetes*, 6(13):1246, 2015.

[223] Djamel Lebeche, Amy J Davidoff, and Roger J Hajjar. Interplay between impaired calcium regulation and insulin signaling abnormalities in diabetic cardiomyopathy. *Nature Clinical Practice Cardiovascular Medicine*, 5(11):715–724, 2008.

[224] Shirley Rubler, Joel Dlugash, Yusuf Ziya Yuceoglu, Tarik Kumral, Arthur Whitley Branwood, and Arthur Grishman. New type of cardiomyopathy associated with diabetic glomerulosclerosis. *The American Journal of Cardiology*, 30(6):595–602, 1972.

[225] Guanghong Jia, Michael A Hill, and James R Sowers. Diabetic cardiomyopathy: an update of mechanisms contributing to this clinical entity. *Circulation Research*, 122(4):624–638, 2018.

[226] Angelo Avogaro, Saula Vigili de Kreutzenberg, Christian Negut, Antonio Tiengo, and Roldano Scognamiglio. Diabetic cardiomyopathy: a metabolic perspective. *The American Journal of Cardiology*, 93(8):13–16, 2004.

[227] Sihem Boudina and E Dale Abel. Diabetic cardiomyopathy revisited. *Circulation*, 115(25):3213–3223, 2007.

[228] David L Severson. Diabetic cardiomyopathy: recent evidence from mouse models of type 1 and type 2 diabetes. *Canadian Journal of Physiology and Pharmacology*, 82(10):813–823, 2004.

[229] Indu G Poornima, Pratik Parikh, and Richard P Shannon. Diabetic cardiomyopathy: the search for a unifying hypothesis. *Circulation Research*, 98(5):596–605, 2006.

[230] Ding An and Brian Rodrigues. Role of changes in cardiac metabolism in development of diabetic cardiomyopathy. *American Journal of Physiology-Heart and Circulatory Physiology*, 291(4):H1489–H1506, 2006.

[231] Lina T Al Kury. Calcium homeostasis in ventricular myocytes of diabetic cardiomyopathy. *Journal of Diabetes Research*, 2020, 2020.

[232] G Gilbert, K Demydenko, E Dries, RD Puertas, X Jin, K Sipido, and HL Roderick. Calcium signaling in cardiomyocyte function, cold spring harb. *Perspect. Biol*, 1(2), 2020.

[233] Claire J Fearnley, H Llewelyn Roderick, and Martin D Bootman. Calcium signaling in cardiac myocytes. *Cold Spring Harbor Perspectives in Biology*, 3(11):a004242, 2011.

[234] Yuanhua Tang, John L Stephenson, and Hans G Othmer. Simplification and analysis of models of calcium dynamics based on ip3-sensitive calcium channel kinetics. *Biophysical Journal*, 70(1):246–263, 1996.

[235] Andrew P Landstrom, Dobromir Dobrev, and Xander HT Wehrens. Calcium signaling and cardiac arrhythmias. *Circulation Research*, 120(12):1969–1993, 2017.

[236] Phonindra Nath Das, Ajay Kumar, Nandadulal Bairagi, and Samrat Chatterjee. Effect of delay in transportation of extracellular glucose into cardiomyocytes under diabetic condition: a study through mathematical model. *Journal of Biological Physics*, 46(3):253–281, 2020.

[237] Christoph Maack and Brian O'Rourke. Excitation-contraction coupling and mitochondrial energetics. *Basic Research in Cardiology*, 102(5):369–392, 2007.

[238] Dan Shao and Rong Tian. Glucose transporters in cardiac metabolism and hypertrophy. *Comprehensive Physiology*, 6(1):331, 2015.

[239] Nathalie Rosenblatt-Velin, René Lerch, Irène Papageorgiou, and Christophe Montessuit. Insulin resistance in adult cardiomyocytes undergoing dedifferentiation: role of glut4 expression and translocation. *The FASEB Journal*, 18(7):872–874, 2004.

[240] Guanghong Jia, Vincent G DeMarco, and James R Sowers. Insulin resistance and hyperinsulinaemia in diabetic cardiomyopathy. *Nature Reviews Endocrinology*, 12(3):144–153, 2016.

[241] Mònica Zamora and Josep A Villena. Contribution of impaired insulin signaling to the pathogenesis of diabetic cardiomyopathy. *International Journal of Molecular Sciences*, 20(11):2833, 2019.

[242] Kaushik Dutta, Marybeth W Carmody, Steven E Cala, and Amy J Davidoff. Depressed pka activity contributes to impaired serca function and is linked to the pathogenesis of glucose-induced cardiomyopathy. *Journal of Molecular and Cellular Cardiology*, 34(8):985–996, 2002.

[243] Amy J Davidoff, Michael B Davidson, Marybeth W Carmody, Mari-Elena Davis, and Jun Ren. Diabetic cardiomyocyte dysfunction and myocyte insulin resistance: role of glucose-induced pkc activity. *Molecular and Cellular Biochemistry*, 262(1):155–163, 2004.

[244] Y Shimoni, L Firek, D Severson, and W Giles. Short-term diabetes alters k+ currents in rat ventricular myocytes. *Circulation Research*, 74(4):620–628, 1994.

[245] Jie Yu, Hai-feng Zhang, Feng Wu, Qiu-xia Li, Heng Ma, Wen-yi Guo, Hai-chang Wang, and Feng Gao. Insulin improves cardiomyocyte contractile function through enhancement of serca2a activity in simulated ischemia/reperfusion. *Acta Pharmacologica Sinica*, 27(7):919–926, 2006.

[246] Marion Berenguer, Yannick Le Marchand-Brustel, and Roland Govers. Glut4 molecules are recruited at random for insertion within the plasma membrane upon insulin stimulation. *FEBS Letters*, 584(3):537–542, 2010.

[247] D Jaquet, H Vidal, R Hankard, P Czernichow, and C Levy-Marchal. Impaired regulation of glucose transporter 4 gene expression in insulin resistance associated with in utero undernutrition. *The Journal of Clinical Endocrinology & Metabolism*, 86(7):3266–3271, 2001.

[248] Ariel Zisman, Odile D Peroni, E Dale Abel, M Dodson Michael, Franck Mauvais-Jarvis, Bradford B Lowell, Jørgen FP Wojtaszewski, Michael F Hirshman, Antti Virkamaki, Laurie J Goodyear, et al. Targeted disruption of the glucose transporter 4 selectively in muscle causes insulin resistance and glucose intolerance. *Nature Medicine*, 6(8):924–928, 2000.

[249] Polly A Hansen, Eric A Gulve, Bess Adkins Marshall, Jiaping Gao, Jeffrey E Pessin, John O Holloszy, and Mike Mueckler. Skeletal muscle glucose transport and metabolism are enhanced in transgenic mice overexpressing the glut4 glucose transporter. *Journal of Biological Chemistry*, 270(4):1679–1684, 1995.

[250] Joseph T Brozinick Jr, Scott C McCoid, Thomas H Reynolds, Nancy A Nardone, Diane M Hargrove, Ralph W Stevenson, Samuel W Cushman, and E Michael Gibbs. Glut4 overexpression in db/db mice dose-dependently ameliorates diabetes but is not a lifelong cure. *Diabetes*, 50(3):593–600, 2001.

[251] Yasuhiro Nishino, Tetsuji Miura, Takayuki Miki, Jun Sakamoto, Yuichi Nakamura, Yoshihiro Ikeda, Hironori Kobayashi, and Kazuaki Shimamoto. Ischemic preconditioning activates ampk in a pkc-dependent manner and induces glut4 up-regulation in the late phase of cardioprotection. *Cardiovascular Research*, 61(3):610–619, 2004.

[252] Shinya Yamaguchi, Hiroshi Katahira, Sachihiko Ozawa, Yoko Nakamichi, Toshiaki Tanaka, Tatsuhiro Shimoyama, Kazuto Takahashi, Katsuhiko Yoshimoto, Mica Ohara Imaizumi, Shinya Nagamatsu, et al. Activators of amp-activated protein kinase enhance glut4 translocation and its glucose transport activity in 3t3-l1 adipocytes. *American Journal of Physiology-Endocrinology and Metabolism*, 289(4):E643–E649, 2005.

[253] Jing Yang and Geoffrey D Holman. Long-term metformin treatment stimulates cardiomyocyte glucose transport through an amp-activated protein kinase-dependent reduction in glut4 endocytosis. *Endocrinology*, 147(6):2728–2736, 2006.

[254] Eman Adel Zayed, Afaf A AinShoka, Kamal A El Shazly, and Hekma A Abd El Latif. Improvement of insulin resistance via increase of glut4 and pparγ in metabolic syndrome-induced rats treated with omega-3 fatty acid or l-carnitine. *Journal of Biochemical and Molecular Toxicology*, 32(11):e22218, 2018.

[255] Geneviève Dupont, Laurent Combettes, Gary S Bird, and James W Putney. Calcium oscillations. *Cold Spring Harbor Perspectives in Biology*, 3(3):a004226, 2011.

[256] Alexander Skupin, Helmut Kettenmann, Ulrike Winkler, Maria Wartenberg, Heinrich Sauer, Stephen C Tovey, Colin W Taylor, and Martin Falcke. How does intracellular ca2+ oscillate: by chance or by the clock? *Biophysical Journal*, 94(6):2404–2411, 2008.

[257] Alexander Skupin, Helmut Kettenmann, and Martin Falcke. Calcium signals driven by single channel noise. *PLoS Computational Biology*, 6(8):e1000870, 2010.

[258] Ahmad R Sedaghat, Arthur Sherman, and Michael J Quon. A mathematical model of metabolic insulin signaling pathways. *American Journal of Physiology-Endocrinology and Metabolism*, 283(5):E1084–E1101, 2002.

[259] Christophe Montessuit and René Lerch. Regulation and dysregulation of glucose transport in cardiomyocytes. *Biochimica et Biophysica Acta (BBA)-Molecular Cell Research*, 1833(4):848–856, 2013.

[260] Daniel J Fazakerley, Scott P Lawrence, Vladimir A Lizunov, Samuel W Cushman, and Geoffrey D Holman. A common trafficking route for glut4 in cardiomyocytes in response to insulin, contraction and energy-status signalling. *Journal of Cell Science*, 122(5):727–734, 2009.

[261] P Shen and R Larter. Chaos in intracellular ca2+ oscillations in a new model for non-excitable cells. *Cell Calcium*, 17(3):225–232, 1995.

[262] Gérald Houart, Geneviève Dupont, and Albert Goldbeter. Bursting, chaos and birhythmicity originating from self-modulation of the inositol 1, 4, 5-trisphosphate signal in a model for intracellular ca2+ oscillations. *Bulletin of Mathematical Biology*, 61(3):507–530, 1999.

[263] James Watras, Barbara E Ehrlich, et al. Bell-shaped calcium-response curves of lns (l, 4, 5) p3-and calcium-gated channels from endoplasmic reticulum of cerebellum. *Nature*, 351(6329):751–754, 1991.

[264] Phonindra Nath Das, Gabriele Pedruzzi, Nandadulal Bairagi, and Samrat Chatterjee. Coupling calcium dynamics and mitochondrial bioenergetic: an in silico study to simulate cardiomyocyte dysfunction. *Molecular BioSystems*, 12(3):806–817, 2016.

[265] Enrique Alvarez-Lacalle, Blas Echebarria, Jon Spalding, and Yohannes Shiferaw. Calcium alternans is due to an order-disorder phase transition in cardiac cells. *Physical Review Letters*, 114(10):108101, 2015.

[266] Ursula Kummer, Borut Krajnc, Jürgen Pahle, Anne K Green, C Jane Dixon, and Marko Marhl. Transition from stochastic to deterministic behavior in calcium oscillations. *Biophysical Journal*, 89(3):1603–1611, 2005.

[267] Geneviève Dupont and Huguette Croisier. Spatiotemporal organization of ca2+ dynamics: A modeling-based approach. *HFSP Journal*, 4(2):43–51, 2010.

[268] Donald M Bers. Cardiac excitation–contraction coupling. *Nature*, 415(6868):198–205, 2002.

[269] J Andrew Taylor. Heart rate variability standards. *Circulation*, 95:280–281, 1997.

[270] Amish Asthana and William S Kisaalita. Biophysical microenvironment and 3d culture physiological relevance. *Drug Discovery Today*, 18(11-12):533–540, 2013.

[271] Stéphane Swillens and Dany Mercan. Computer simulation of a cytosolic calcium oscillator. *Biochemical Journal*, 271(3):835, 1990.

[272] Valeska Ormazabal, Soumyalekshmi Nair, Omar Elfeky, Claudio Aguayo, Carlos Salomon, and Felipe A Zuñiga. Association between insulin resistance and the development of cardiovascular disease. *Cardiovascular Diabetology*, 17(1):1–14, 2018.

[273] Cecilia Granéli, Ryan Hicks, Gabriella Brolén, Jane Synnergren, and Peter Sartipy. Diabetic cardiomyopathy modelling using induced pluripotent stem cell derived cardiomyocytes: recent advances and emerging models. *Stem Cell Reviews and Reports*, 15(1):13–22, 2019.

[274] Li Zhi, Zhu Yuzhang, Huang Tianliang, Ichiro Hisatome, Tetsuya Yamamoto, and Cheng Jidong. High uric acid induces insulin resistance in cardiomyocytes in vitro and in vivo. *PloS One*, 11(2):e0147737, 2016.

[275] Anthony Saxton, Muhammad Ali Tariq, and Bruno Bordoni. Anatomy, thorax, cardiac muscle. In *StatPearls [Internet]*. StatPearls Publishing, 2021.

[276] Ann Louise Olson. Regulation of glut4 and insulin-dependent glucose flux. *International Scholarly Research Notices*, 2012, 2012.

[277] Qi Zhou, Xinzhou Yang, Mingrui Xiong, Xiaolan Xu, Li Zhen, Weiwei Chen, Yan Wang, Jinhua Shen, Ping Zhao, and Qing-Hua Liu. Chloroquine increases glucose uptake via enhancing glut4 translocation and fusion with the plasma membrane in l6 cells. *Cellular Physiology and Biochemistry*, 38(5):2030–2040, 2016.

[278] Ping Zhao, Di Tian, Guanjun Song, Qian Ming, Jia Liu, Jinhua Shen, Qing-Hua Liu, and Xinzhou Yang. Neferine promotes glut4 expression and fusion with the plasma membrane to induce glucose uptake in l6 cells. *Frontiers in Pharmacology*, 10:999, 2019.

[279] Zhen Qi, Renrong Wang, Rongheng Liao, Song Xue, and Yongyi Wang. Neferine ameliorates sepsis-induced myocardial dysfunction through anti-apoptotic and antioxidative effects by regulating the pi3k/akt/mtor signaling pathway. *Frontiers in Pharmacology*, page 1899, 2021.

[280] Gurusamy Lalitha, Paramasivan Poornima, Arjunan Archanah, and Viswanadha Vijaya Padma. Protective effect of neferine against isoproterenol-induced cardiac toxicity. *Cardiovascular Toxicology*, 13(2):168–179, 2013.

[281] Xue Liu, Xiuhui Song, Jianjun Lu, Xueying Chen, Ershun Liang, Xiaoqiong Liu, Mingxiang Zhang, Yun Zhang, Zhanhui Du, and Yuxia Zhao. Neferine inhibits proliferation and collagen synthesis induced by high glucose in cardiac fibroblasts and reduces cardiac fibrosis in diabetic mice. *Oncotarget*, 7(38):61703, 2016.

[282] Lohanathan Bharathi Priya, Rathinasamy Baskaran, Chih-Yang Huang, and Viswanadha Vijaya Padma. Neferine ameliorates cardiomyoblast apoptosis induced by doxorubicin: possible role in modulating nadph oxidase/ros-mediated nfκb redox signaling cascade. *Scientific Reports*, 7(1):1–13, 2017.

[283] Chung-Chi Yang, Yen-Ling Hung, Wen-Chin Ko, Yi-Ju Tsai, Jia-Feng Chang, Cher-Wei Liang, Der-Chen Chang, and Chi-Feng Hung. Effect of neferine on dncb-induced atopic dermatitis in hacat cells and balb/c mice. *International Journal of Molecular Sciences*, 22(15):8237, 2021.

[284] Hui Ye, Yanan He, Chuan Zheng, Fang Wang, Ming Yang, Junzhi Lin, Runchun Xu, and Dingkun Zhang. Type 2 diabetes complicated with heart failure: Research on therapeutic mechanism and potential drug development based on insulin signaling pathway. *Frontiers in Pharmacology*, 13, 2022.

[285] Wenguang Chang, Ming Zhang, Jing Li, Zhaojie Meng, Shengnan Wei, Hongwei Du, Li Chen, and Grant M Hatch. Berberine improves insulin resistance in cardiomyocytes via activation of 5$'$-adenosine monophosphate-activated protein kinase. *Metabolism*, 62(8):1159–1167, 2013.

[286] Ning Hou, Yunpei Mai, Xiaoxia Qiu, Wenchang Yuan, Yilang Li, Chengfeng Luo, Yun Liu, Guiping Zhang, Ganjiang Zhao, and Jian-dong Luo. Carvacrol attenuates diabetic cardiomyopathy by modulating the pi3k/akt/glut4 pathway in diabetic mice. *Frontiers in Pharmacology*, 10:998, 2019.

List of Publications

List of publications related to thesis

Published

1. **Halder, S.**, Chatterjee, S., & Bairagi, N. (2018). Unravelling the sensitivity of two motif structures under random perturbation. *Trends in Biomathematics: Modeling, Optimization and Computational Problems*, 245-263.

2. **Halder, S.**, Ghosh, S., Chattopadhyay, J., & Chatterjee, S. (2021). Bistability in cell signalling and its significance in identifying potential drug-targets. *Bioinformatics*, 37(22), 4156-4163.

3. **Halder, S.**, Ghosh, S., Chattopadhyay, J., & Chatterjee, S. (2022). Understanding noise in cell signalling in the prospect of drug-targets. *Journal of Theoretical Biology*, 555, 111298.

4. **Halder, S.**, & Chatterjee, S. (2023). Bistability regulates TNFR2-mediated survival and death of T-regulatory cells. *Journal of Biological Physics*, https://doi.org/10.1007/s10867-023-09625-3.

Communicated

1. **Halder, S.**, Das, P.N., Ghosh, S., Bairagi, N., & Chatterjee, S. Studying the role of random translocation of GLUT4 in cardiomyocytes on calcium oscillations.

List of Other Publications

Published

- Das, P. N., **Halder, S.**, Bairagi, N., & Chatterjee, S. (2020). Delay in ATP-dependent calcium inflow may affect insulin secretion from pancreatic beta-cell. *Applied Mathematical Modelling*, 84, 202-221.

Conferences

Poster Presentations

- **The 106th Indian Science Congress**, January 2019, at Lovely Professional University, Phagwara, Jalandhar.